Monitoring, modelling and quantification of accumulation of damage on masonry structures due to recursive loads

UNIVERSITY OF LEEDS

Dimitrios Dais

Submitted in accordance with the requirements for the degree of
Doctor of Philosophy

The University of Leeds
School of Civil Engineering

September, 2021

The candidate confirms that the work submitted is his own, except where work which has formed part of jointly-authored publications has been included. The contribution of the candidate and the other authors to this work has been indicated explicitly below. The candidate confirms that appropriate credit has been given within the thesis where reference has been made to the work of others.

Journal (Bal et al. 2019b) and conference (Bal et al. 2018) publications were prepared on the investigation of seismic records from induced seismicity. These two papers are relevant to this PhD study since they deal with induced seismicity, but they do not fall directly within the scope of the PhD. Thus, their results are only briefly mentioned in the Introduction (Chapter 1). The contribution of the candidate was on the data collection and processing; and writing/editing the papers.

The main conclusions from Chapter 3 regarding the work on the structural health monitoring of Fraeylemaborg, a monument which suffered damage along the recent seismic activity in the Groningen region of the Netherlands, were presented in journal (Bal et al. 2021a) and conference (Dais et al. 2019b) publications. The candidate was responsible for the continuous operation of the installed monitoring system; data collection and processing; development and calibration of the numerical model and investigation of different loading scenarios; writing and editing the papers. The supervisory team was in charge of funding acquisition, managing and coordinating the research project; maintaining collaborations with other parties to obtain additional data such as soil properties, tilt measurements, architectural details etc.; processing of the data, writing and editing the papers.

The work presented in Section 4.1 regarding the use of artificial intelligence to automatically detect cracks from photographs of masonry surfaces was published as journal paper (Dais et al. 2021a). The candidate was responsible for the methodology; conceptualization; data collection; training of the artificial intelligence model; and writing and editing the corresponding paper. The supervisory team contributed in terms of conceptualization; and writing and editing the corresponding paper.

The development of invisible infrared markers for crack monitoring, demonstrated in Section 4.2, was published as journal paper (Bal et al. 2021b). The candidate worked on different trials with the infrared markers to improve the obtained accuracy; developed the code to process the images; assisted in the selection of the appropriate methodology to evaluate the accuracy of the markers and wrote and edited the paper. The idea to utilize invisible infrared markers was

proposed by the supervisory team while they also coordinated the supply of the appropriate equipment (infrared camera; markers; flash etc.). Furthermore, the supervisory team contributed on testing the accuracy of the proposed method; and helped in writing and editing the paper.

The work on the modelling and quantification of damage evolution in masonry walls subjected to induced seismicity was published in two journal (Sarhosis et al. 2019b, 2021) and one conference (Sarhosis et al. 2019c) paper. Evidence of damage accumulation were highlighted from experimental campaigns found in the literature (presented in Chapter 2) and the findings were further enriched with a course of numerical exercises (exhibited in Section 5.1). The candidate undertook the required literature review and collected the experimental data from previous experimental campaigns. Additionally, the candidate processed the numerical results and worked on the quantification of damage. The candidate contributed to the writing and editing of the papers. The supervisory team performed the analysis with the single degree of freedom model (Sarhosis et al. 2019b); conceptualized the UDEC model (Sarhosis et al. 2019c, b, 2021) and executed the numerical exercises and assisted to the processing of the numerical results. The supervisory team also worked on the writing and editing of the papers.

Acknowledgements

I would like to thank my supervisory team for their invaluable support and guidance throughout my PhD study. I had the great opportunity to collaborate with Dr. Vasilis Sarhosis along the four years of my PhD research. He was always full of ideas and eager to help with any obstacle that I faced. Also, I worked with Dr. İhsan Engin Bal and Dr. Eleni Smyrou for the last seven years. Apart from the period of PhD study, I had the great chance to be mentored by them as part of a research project and my Master's degree while in Istanbul. I was involved in different projects and gained priceless experience that prepared me for the next steps of my career. Overall, if it was not for my supervisory team, I would not be where I am today and for this I am really grateful.

The staff members of the Schools of Civil Engineering at the Universities of Newcastle and Leeds are gratefully acknowledged for their support and hard work. Special thanks go to Hanze University[1], Groningen, the Netherlands, which gave me the chance to pursue my PhD and funded this research and in particular to people from the Kenniscentrum NoorderRuimte for their invaluable support along the last four years. It is also important to thank the members of the research groups at Newcastle, Leeds and Hanze University for the fruitful discussions and collaboration along my research and different projects.

I feel obligated to express my gratitude to George Papageorgopoulos who has helped to shape my career since the day I submitted my application to enter the University to study Civil Engineering. The PhD time has its ups and downs and there are moments that it gets tough. I cannot thank enough my friends that were always there for me and made the limited free time I had to be worthy giving me energy to continue. Special mention is due to my dear friend Nektarios Lianos who helped me take a turn in my career towards the exciting world of artificial intelligence. My family has always provided a solid foundation for building my life on and I am grateful for this.

Last but not least, I wish that one day I will be able to thank enough my partner Simla for being in my life.

---

[1] Hanze University of Applied Sciences

Hanze
University of Applied Sciences
Groningen

Abstract

The use of induced seismicity is gaining in popularity, particularly in Northern Europe, as people strive to increase local energy supplies. The local building stock, comprising mainly of low-rise domestic masonry structures without any aseismic design, has been found susceptible to these induced tremors. Induced seismicity is generally characterized by frequent small-to-medium magnitude earthquakes in which structural and non-structural damage have been reported. Since the induced earthquakes are caused by third parties liability issues arise and a damage claim mechanism is activated. Typically, any damage are evaluated by visual inspections. This damage assessment process has been found rather cumbersome since visual inspections are laborious, slow and expensive while the identification of the cause of any light damage is a challenging task rendering essential the development of a more reliable approach. The aim of this PhD study is to gain a better understanding of the monitoring, modelling and quantification of accumulation of damage in masonry structures due to recursive loads.

Fraeylemaborg, the most emblematic monument in the Groningen region dating back to the 14th century, has experienced damage due to the induced seismic activity in the region in recent years. A novel monitoring approach is proposed to detect damage accumulation due to induced seismicity on the monument. Results of the monitoring, in particular the monitoring of the effects of induced seismic activity,, as well as the usefulness and need of various monitoring data for similar cases are discussed. A numerical model is developed and calibrated based on experimental findings and different loading scenarios are compared with the actual damage patterns observed on the structure.

Vision-based techniques are developed for the detection of damage accumulation in masonry structures in an attempt to enhance effectiveness of the inspection process. In particular, an artificial intelligence solution is proposed for the automatic detection of cracks on masonry structures. A dataset with photographs from masonry structures is produced containing complex backgrounds and various crack types and sizes. Moreover, different convolutional neural networks are evaluated on their efficacy to automatically detect cracks. Furthermore, computer vision and photogrammetry methods are considered along with novel invisible markers for monitoring cracks. The proposed method shifts the marker reflection and its contrast with the background into the invisible wavelength of light (i.e. to the near-infrared) so that the markers are not easily distinguishable. The method is thus particularly

suitable for monitoring historical buildings where it is important to avoid any interventions or disruption to the authenticity of the basic fabric of construction..

Further on, the quantification and modelling of damage in masonry structures are attempted by taking into consideration the initiation and propagation of damage due to earthquake excitations. The evaluation of damage in masonry structures due to (induced) earthquakes represents a challenging task. Cumulative damage due to subsequent ground motions is expected to have an effect on the seismic capacity of a structure. Crack patterns obtained from experimental campaigns from the literature are investigated and their correlation with damage propagation is examined. Discontinuous modelling techniques are able to reliably reproduce damage initiation and propagation by accounting for residual cracks even for low intensity loading. Detailed models based on the Distinct Element Method and Finite Element Model analysis are considered to capture and quantify the cumulative damage in micro level in masonry subjected to seismic loads.

Finally, an experimental campaign is undertaken to investigate the accumulation of damage in masonry structure under repetitive load. Six wall specimens resembling the configuration of a spandrel element are tested under three-point in-plane bending considering different loading protocols. The walls were prepared adopting materials and practices followed in the Groningen region. Different numerical approaches are researched for their efficacy to reproduce the experimental response and any limitations are highlighted.

Table of Contents

List of Tables

List of Figures

List of Abbreviations

CDP   Concrete Damaged Plasticity

CE   Cross entropy

CNN   Convolutional neural network

CoV   Coefficient of variation

CPT   Cone penetration test

DEM   Distinct Element Method

DIC   Digital image correlation

DL   Damage Limitation

DSLR   Digital single-lens reflex

FC   Fully connected

FCN   Fully convolutional network

FEM   Finite Element Method

FN   False negative

FP   False positive

FPN   Feature Pyramid Networks

GPU   Graphics processing units

IDA   Incremental dynamic analysis

ISD   Inter-story drift

KNMI   The Royal Dutch Meteorological Institute

LVDT   Linear variable differential transformer

ML   Local magnitude

NC   Near Collapse

NDT	Non-destructive testing
NE	Northeast
NIR	Near-infrared
NW	Northwest
PGA	Peak Ground Acceleration
RC	Reinforced concrete
ReLU	Rectified linear unit
SD	Significant Damage
SDOF	Single degree of freedom
SHM	Structural health monitoring
StDev	Standard deviation
TN	True negative
TP	True positive
TUD	Delft University of Technology
TUE	Eindhoven University of Technology
URM	Unreinforced masonry
UV	Ultraviolet
WCE	Weighted cross entropy

List of Notations

$(x, \quad y)$,   Coordinates of a set of corresponding points in two images related with
(x', y') the homography matrix

c Cohesion

D Damage variable

d_c Damage variable in compression

DI Damage index

DI_{crack} Ratio of failed mortar joints over the total mortar joints of a masonry wall

DI_{drift} Drift ratio (δ) divided by a drift limit value (δ_{Limit})

DI_{open} The length of joints that opened due to tension divided by the total length of joints

DI_{slip} The length of joints slipped (or at shear limit) due to shear divided by the total length of joints

d_t Damage variable in tension

E Young's modulus

E_0 Initial (undamaged) elastic stiffness

f User-defined factor which controls the timestep

f_b Normalized compressive strength of masonry units

f_c Compressive strength of mortar

$f_{c,m}$ Compressive strength of masonry perpendicular to bed joints

f_s Shear strength

f_t Tensile strength

f_w Bond strength of masonry

G Shear modulus

g_t	Gradient vector
H	Height
H	Homography matrix (used in Section 4.2.1.5)
H_0	Shear span
i_{open}	Length of joints opened
i_{slip}	Length of joints slipped
K	Bulk modulus
K_c	Ratio of the second stress invariant on the tensile meridian
K_n	Overall stiffness of the units and contacts
k_n	Normal stiffness
$k_{n,c}$	Normal stiffness in compression
$k_{n,t}$	Normal stiffness in tension
k_s	Shear stiffness
L	Length
LA_{ij}	Actual distance between marker ''i' and marker 'j'
L_{CE}	Cross entropy loss function
LM_{ij}	Pixel-wise distance measured in the image processing algorithm between marker 'i' and marker 'j'
L_{wCE}	Weighted cross entropy loss function
M_n	Nodal mass
m_t	First (mean) biased moment estimate of the gradients
$\widehat{m}_t$	First (mean) bias-corrected moment estimate of the gradients
p	Density of masonry
p_b	Density of bricks

s	Scale factor
t	Thickness
$tan\varphi$	Internal friction coefficient
u_n	Normal displacement
u_n^f	Normal displacement at complete failure
u_n^{max}	Maximum normal displacement attained during the loading history
u_n^o	Normal displacement at damage initiation
u_s	Shear displacement
u_s^f	Shear displacement at complete failure
u_s^{max}	Maximum shear displacement attained during the loading history
u_s^o	Shear displacement at damage initiation
v	Poisson's ratio
v_t	Second (uncentered variance) biased moment estimate of the gradients
$\hat{v}_t$	Second (uncentered variance) bias-corrected moment estimate of the gradients
w	Model weights
$y, \hat{y}$	Ground truth and prediction
α	Learning rate
β	Weight of the positive class
β_1, β_2	Exponential decay rates for the moment estimates
Δ	Geometric error
Δt_n	Timestep
Δu_n	Change in normal displacement
Δu_s	Change in shear displacement

$\Delta\sigma_n$	Change in normal stress
$\Delta\tau_s$	Change in shear stress
δ	Drift ratio
δ_{limit}	Drift limit value
ε_c	Uniaxial compressive strain
ε_c^{el}	Equivalent compressive elastic strain
ε_c^{pl}	Equivalent compressive plastic strain
ε_t	Uniaxial tensile strain
ε_t^{el}	Equivalent tensile elastic strain
ε_t^{pl}	Equivalent tensile plastic strain
μ	Residual friction coefficient
σ_{b0}	Initial equibiaxial compressive yield stress
σ_c	Uniaxial compressive stress
σ_{c0}	Initial uniaxial compressive strength
σ_n	Normal stress
σ_t	Uniaxial tensile stress
σ_{t0}	Initial uniaxial tensile strength
σ_v	Precompression
τ_s	Shear stress

Chapter 1
Introduction

1.1 Overview

Masonry as construction material

Brick masonry is one of the main structural components in modern and historical structures around the world. Numerous old masonry buildings still exist proving that, when well-preserved, the life cycle of such structures may be significantly extended (Tomazevic 1999). In many cases, historical masonry structures have been found to be vulnerable to seismic excitations and thus thorough damage assessment is required to propose suitable restoration schemes, when necessary (Dais et al. 2019a, 2021b). Moreover, masonry has been widely used in modern structures in countries with low or no seismicity. Masonry structures subjected to induced seismicity, like the ones in the north of the Netherlands, have been found to be susceptible to seismic excitations given the fact that they were constructed without any seismic design (Bal et al. 2021a). As another example of vulnerable masonry structural systems, arch bridges are the most common single bridge type on the UK rail network, most of which are now over than 100 years old and showing significant signs of distress. The importance to develop improved analysis and assessment methods for these bridges was highlighted (Gilbert 2009). In brief, masonry structures need to be properly inspected to detect any defects on early stage or after an extreme event in order to safeguard them.

Induced seismicity and damage claims

In the last decade, with the pressure to increase local energy supplies by unlocking the energy potential of the ground, induced seismicity in the northern part of Europe has considerably increased (Foulger et al. 2018). At the same time, the existing building stock in the region was not designed to sustain such seismic demands. Consequently, structural and non-structural damage in buildings has been observed. For example, in Switzerland magnitudes of up to 3.5 Richter have been reported, due to enhanced geothermal systems, resulting in cracks on walls alongside non-structural damage (Abbiati et al. 2018). The resulted damage claims are in excess of 7-20 million Swiss Francs. Similar situations is also described in Groningen, the Netherlands. In this case, the seismicity is related to the hydraulic fracturing process for the extraction of natural gas from deep geological formations. Back in 1991, the first induced seismicity was recorded in the Groningen gas field with local magnitude (ML) 2.4. In the subsequent years, more than 1,300 small in magnitude earthquakes have been reported in the region, the largest of which was the one in 2012 with

magnitude equal to ML 3.6 (van Thienen-Visser and Breunese 2015). Along the period of seismic shakings in the Groningen gas field, the damage claims from citizens increased. For example, for the period 2012 to 2016, an average of € 374 million per year was spent on compensation for damage as consequence of gas extraction, which accounts for approximately 3% of the average revenues from gas extraction during the same period (Mulder and Perey 2018). On top of this, issues related to devaluation of the real estate market and buyout of properties, expenses for the seismic retrofit of the structures and cost of lawsuits need to be accounted for (Bal et al. 2019a).

Structural health monitoring

Structural health monitoring (SHM) has been used extensively to reliably assess the condition of structures affected by different types of loading originating from earthquakes, vibrations, soil movements, environmental changes etc. SHM entails the deployment of various sensors like accelerometers, tiltmeters, potentiometers, environmental sensors, etc. combined in different ways depending on the needs of each monitoring case (Ramos et al. 2010b; Ceravolo et al. 2017; Kita et al. 2020; Makoond et al. 2020). SHM can be one-time, periodic or permanent recording continuously, at given intervals or triggered by an event. These measurements provide valuable information for the identification of any structural changes that might compromise the structural integrity of the building stock. In particular for the Groningen region, despite the high concentration of historical buildings in the gas field, their seismic vulnerability and the past damage, other than Fraeylemaborg, which is monitored for the sake of this PhD study, no additional historical masonry buildings exist in the region where standard seismic SHM methods are applied. Though there are some sensors installed for different purposes in various ways in some other historical buildings in the region (Bal 2018), interestingly enough no other heritage structure has a complete monitoring system, while at the same time there are accelerometer sensors in more than 400 houses, together with more than 50 strong ground motion stations of the Royal Dutch Meteorological Institute (KNMI) (KNMI 1993).

Visual inspection of structures

Other than SHM, assessment of structures heavily relies on visual damage inspection based on data mostly obtained visually. Visual inspection is the most common practice due to its simplicity and the lack of reliable alternatives. Nevertheless, this practice is rather laborious, slow and expensive when accounting for the man-hours required to be invested in the field and at the office to process the obtained data. On top of that, the quality of the process can be subjective since it relies heavily on the skills and the physical condition of the inspector as well as lack of experience or tiredness could easily lead to ill-reported damage. Visual inspection can raise safety concerns since there are parts of structures with access restrictions and difficult to reach. Visual inspection becomes particularly difficult for the post-

event cases, such as in the catastrophic aftermath of a strong earthquake, when a high number of buildings need to be inspected with limited resources in a short time. Apart from the efficiency, reliability is another aspect to be considered when inspecting masonry structures visually. Significant variability in the routine inspection documentation of structural conditions was previously reported (Phares et al. 2004; Laefer et al. 2010). Discrepancy was observed both for the assignment of condition ratings but also for the prepared documents, e.g. field inspection notes, photographs, etc. Specifically, on average between four and five different condition rating values were assigned to each structural component, with a maximum of six being assigned (Phares et al. 2004). In order to address the drawbacks of visual inspection, vision-based assessment and monitoring of civil infrastructures are gaining ground (Spencer et al. 2019). In particular, computer vision for crack detection has interested researchers for quite some time. Vision-based crack detection is a perfect example of a non-destructive assessment technique, which can be useful especially for historical structures where strict regulations apply and even simple interventions, such as placing crack-rulers, are not permitted by the conservation authorities. Moreover, the automated crack detection from photographs of structures could benefit tools developed for the rapid post-earthquake assessment and interpretation of the sustained damage (Novelli and D'Ayala 2015, 2019). Vision-based crack monitoring has been enhanced with the usage of photogrammetric techniques to accurately measure the crack width (Nishiyama et al. 2015; Germanese et al. 2018; Wojnarowski et al. 2019).

Damage accumulation due to recursive load on unreinforced masonry

Most of the building stock in the seismic region of Groningen consists of low-rise unreinforced masonry (URM) constructions (Crowley et al. 2017). URM is a brittle material that responds to cyclic load reversals in a non-ductile way. The recent quakes in the Groningen region have a significant impact on the URM buildings that were not designed according to any seismic design criteria and are characterized by very slender cavity walls, absence of reinforcement, and little structural continuity between walls and floors. Due to the increased amount of induced seismicity activity in the Groningen region in the last two decades, extensive experimental campaigns have been undertaken to verify the properties of local building stock (Graziotti et al. 2017; Tomassetti et al. 2019; Korswagen et al. 2019, 2020a; Esposito et al. 2019; Messali et al. 2020; Arslan et al. 2021). The interest of the scientific community regarding URM structures was mainly focused on the identification of the capacity of the structural elements and damage that occurs in large load amplitudes associated with partial or total collapse. Response of URM to recursive, frequent but low-amplitude seismic loads, on the other hand, is a relatively overlooked topic that needs experimental and analytical investigation and validation.

Numerical representation of unreinforced masonry

Numerical modelling is a widely applied technique to evaluate the condition of structures by computational simulations of different loading scenarios (Asteris et al. 2015; de Felice et al. 2016). Masonry, a complex material consisting of units and mortar joints following a certain pattern, is heterogeneous and anisotropic in nature. Different approaches and scales exist in the literature for the numerical representation of masonry (D'Altri et al. 2019b). In particular, ways to numerically reproduce the accumulation of damage in URM has interested the research community (Mouyiannou et al. 2014; Casolo 2017; Iervolino et al. 2020). A reliable representation of the damage onset and evolution will enable a precise assessment of our infrastructure and will allow us to capture damage at its initial stages before it becomes threating. Detailed numerical modelling is often required to robustly capture different crack patterns and nonlinear phenomena expressed at the level of masonry units and joints (Lourenço 1996; D'Altri et al. 2019a). Furthermore, it is of paramount importance for the numerical simulations to account for the cyclic response of masonry under recursive loading (Oliveira and Lourenço 2004).

1.2 Aim and objectives

Induced seismicity in Groningen, despite being characterised by low magnitude events, has led to substantial damage claims and compensation costs as well as public unrest (refer to Section 2.1). Typical examples of damage in buildings in the Groningen gas field are shown in Figure 1-1. Commonly the damage is expressed as thin hairline cracks spreading along various structural components of the buildings although higher damage levels are possible (refer to Section 2.1). Therefore the research interest lays on the initiation of damage as well as its further evolution. Fraeylemaborg, a monumental structure in the Groningen region, has experienced damage due to the seismic activity in the last decade (for additional clarification refer to Chapter 3). The Director of the Conservation Committee described the damage evolution in the monument as follows: "About five years ago it began to dawn on us, when our staff said: the building is suddenly aging very quickly". Since the earthquakes are of small magnitude, any sings of damage are not easily traceable and therefore it is difficult to identify the cause of any (micro) damage. Moreover, the effect of the frequent earthquakes of small to moderate magnitude on the structural condition of the masonry structures, which constitute the main building stock in Groningen, is not clear.

Figure 1-1: Typical examples of damage in buildings in the Groningen gas field. Photographs taken by Dimitrios Dais.

In order to address the aforementioned issues this PhD study aims to gain a better understanding of the monitoring, modelling and quantification of accumulation of damage in masonry structures due to recursive loads.

The objectives of this PhD research project are as follows:

1) Showcase the potential of seismic events of low magnitude to cause damage to the built environment
2) Monitor the damage initiation and propagation in masonry structures with the use of remote sensing
3) Investigate and quantify the damage evolution in masonry walls subjected to in-plane recursive load
4) Reproduce numerically the accumulation of damage in masonry under repetitive load
5) Evaluate the effect of repetitive load on damage evolution and numerically reproduce any findings

1.3 Methodology

The methodology that is followed to address the aforementioned objectives is described below. For each objective different tasks (T) are defined.

Initially, a literature review is undertaken (Chapter 2) to a) gain enough understanding concerning the seismicity of the region and the damage claims, b) investigate experimental studies on the building stock of the Groningen region and indications of accumulation of damage, c) scrutinize numerical techniques for the response of URM under seismic excitation

and d) examine the existing computer vision algorithms for detection and monitoring of cracks.

Fraeylemaborg, a monumental masonry structure in the Groningen region is selected as case study in order to showcase the potential of seismic events of low magnitude to cause damage to the built environment (Chapter 3). A thorough structural condition assessment of the monument is initially regarded and any signs of damage are highlighted (T1.1). A novel monitoring approach is considered to continuously monitor the monument (T1.2). Measurements from accelerometers, a tiltmeter, analogue crack rulers, meteorological data as well as the ground water level are collected continuously. SHM takes place for over a year in order to capture any seasonal influences. Moreover, a numerical model is calibrated based on experimental findings and different loading scenarios are considered (T1.3). Combining the monitoring data with the numerical results and the findings from the inspections of the monument after the earthquake events will allow to reliably trace any inflicted damage and link this damage to the low seismicity of the Groningen region.

Since monitoring each structure with sensors is not a viable solution, monitoring of the damage initiation and propagation in masonry structures with the use of remote sensing is attempted (Chapter 4). To achieve this objective automatic crack detection with the use of artificial intelligence (Section 4.1) (T2.1) and crack width monitoring with invisible markers (Section 4.2) (T2.2) are attempted. In particular, an artificial intelligence solution is developed to automatically detect and measure cracks on images of masonry structures. A dataset of photographs from masonry surfaces with cracks are collected (T2.1.1) and different CNNs are trained and tested on their accuracy to automatically detect cracks (T2.1.2). Furthermore, invisible infrared markers are used to allow for accurate monitoring of the crack width. Two types of markers (tape and paint markers) are tested under various configurations (T2.2.1). Photogrammetric and image processing techniques are used to verify the potential of the developed invisible markers to be used for crack monitoring (T2.2.2). The developed monitoring solutions are implemented (T2.1.3 and T2.2.3) on the case study and the experimental campaign to reliably monitor the development of cracks under induced seismicity (Fraeylemaborg) and repetitive load (experimental campaign).

Furthermore, the damage evolution in masonry walls subjected to in-plane recursive load is investigated and quantified. A numerical exercise on the quantification of damage evolution with the Distinct Element Method (DEM) is considered in Section 5.1 (T3.1) while an extensive database of in plane quasi static cyclic experiments in masonry walls found in the literature is evaluated for the quantification of damage (Section 5.2) (T3.2).

Within the numerical exercise, wall panels representing common typologies of house façades of URM buildings in the Northern European region, i.e. Groningen gas field, are numerically investigated under dynamic load (T3.1.1). The accumulated damage within the seismic

response of the masonry walls is investigated by means of representative harmonic load excitations and an incremental dynamic analysis (IDA) based on induced seismicity records from Groningen. A damage indexing equation is proposed with drift ratio and cracking characteristics used as damage parameters to quantify the damage evolution (T3.1.2). Using the results of the developed DEM numerical model, the suitability of the proposed damage indexing equation to realistically represent the level of damage and its sensitivity to low amplitude loading is demonstrated.

The examined database of cyclic experiments accounts for different types of real-case masonry piers since various aspect ratios, boundary conditions and values of overload are covered (T3.2.1). Measurements are obtained regarding the crack extent at various stages of the tests to study the initiation of cracks and their evolution. A damage index is proposed to quantify the damage propagation for different drift levels (T3.2.2). Trends associated with different failure modes are highlighted while cracking levels are correlated with limit states.

To further the results from the DEM analyses and overcome any limitations, a micro-modelling solution is developed with the Finite Element Method (FEM) software ABAQUS to reliably reproduce and quantify the damage accumulation in masonry structures (Section 5.3). Due to the lack of suitable constitutive law implemented in ABAQUS, a subroutine is developed for the sake of this study to describe the response of mortar joints under cyclic load (T4.1). The numerical model is verified against a challenging set of experimental studies in terms of hysteresis loop and failure mechanism (T4.2). A concise methodology to correctly calibrate the mechanical properties of the implemented micro-model is proposed. The quantification of damage propagation is numerically evaluated with the use of the introduced damage index based on the crack extent (T4.3). Measurements of crack width, which are not commonly reported in experimental studies are retrieved numerically due to the detailed representation of crack propagation. The crack width measurements are considered for the quantification of damage evolution.

Finally, an experimental campaign is undertaken to investigate the accumulation of damage in masonry under repetitive load (Chapter 6). Six wall specimens, prepared adopting materials and practices followed in the Groningen region, are tested considering different loading protocols, i.e. (a) monotonic; (b) cyclic with one cycle per amplitude; and (c) cyclic with multiple cycles per amplitude (T5.1). The effect of the cyclic load on the capacity of the walls is highlighted (T5.2). Measurements of deformations along the tested specimens are used to trace any signs of accumulation of (micro) damage due to the application of repetitive load. For the numerical representation of the experimental campaign three different models are considered (T5.3). In particular, a macro-modelling simulation and two variations of the simplified micro-modelling approach are regarded. The different numerical approaches are

evaluated for their efficacy to reproduce the experimental findings and any limitations are presented.
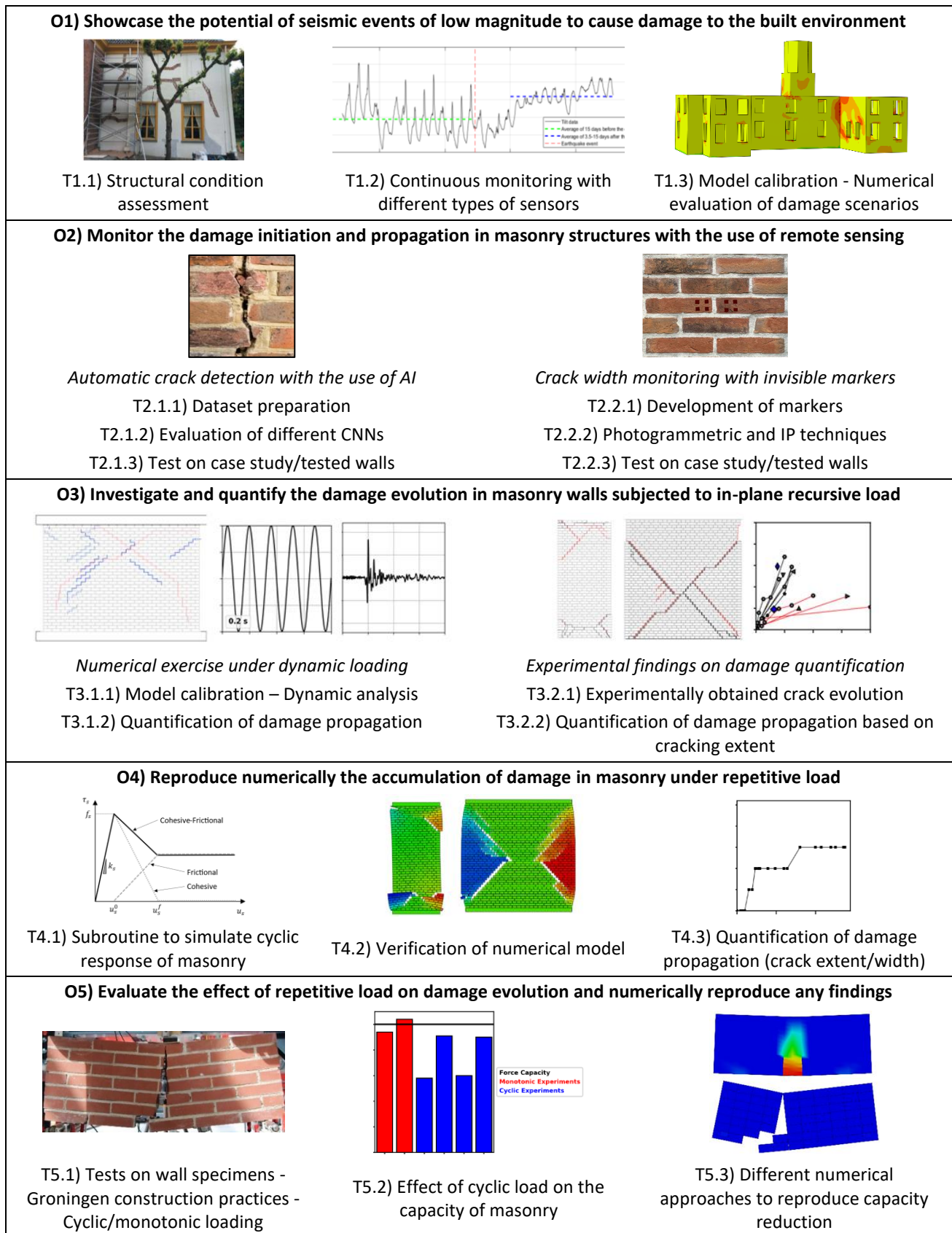
Figure 1-2: Illustrative representation of the objectives along with the corresponding tasks according to the prescribed methodology. O and T stand for objective and task respectively. AI: artificial intelligence, CNN: convolutional neural network, IP: image processing.

1.4 Thesis outline

Chapter 2 provides a detailed literature review on the topics that are further investigated along this study. In particular, an insight is illustrated regarding induced seismicity focusing on its implications for the Groningen region. Practices of SHM for monuments with particular interest in masonry monuments are highlighted. Techniques for the vision based assessment of structures are evaluated for their potential to be further developed to perform well for masonry constructions. Experimental findings are scrutinized for evidence of damage accumulation while modelling strategies are evaluated for the efficacy to estimate damage propagation.

In Chapter 3, a novel monitoring approach to detect damage accumulation due to induced seismicity implemented on a case study monument is presented. For Fraeylemaborg, a historical building in Groningen, the Netherlands, which experienced damage due to the seismic activity in the region along the recent years, a tailor-made SHM system is implemented. Results of the monitoring, particularities of the monitoring in case of induced earthquakes, as well as the usefulness and need of various monitoring data for similar cases are discussed. Weak soil properties dominate the structural response in the region; thus, the ground water monitoring as well as the interaction of soil movements with the structural response has also been scrutinized. The effect of the changes in the environmental conditions and its relevance to monitoring in case of induced seismicity are discussed.

In Chapter 4, vision-based techniques to detect damage accumulation in masonry structures are introduced. In particular, in Section 4.1 different artificial intelligence techniques for crack detection on images from masonry structures are evaluated. A dataset with photographs from masonry structures is produced containing complex backgrounds and various crack sizes. Different deep learning networks are considered and by leveraging the effect of transfer learning crack detection on masonry surfaces is performed both on patch and pixel level. This is the first implementation of deep learning for pixel-level crack segmentation on masonry surfaces. Finally, a comparative study is performed where a segmentation network trained on masonry images is tested on photographs with cracks taken from concrete surfaces in order to evaluate the ability of convolutional neural networks (CNN) to generalize over different materials. To complement the automatic detection of cracks, novel invisible markers for monitoring the crack width are additionally developed (Section 4.2). In more detail, a proof of concept for monitoring masonry structures using two different types of markers which are not easily noticeable by human eye but exhibit high reflection when subjected to near-infrared (NIR) wavelength of light is displayed. The first type is a retroreflective marker covered by a special tape that is opaque in visible light but translucent in NIR, while the second marker is a paint produced from infrared reflective pigments. The reflection of these markers is captured by a special camera-flash combination and processed using image processing

algorithms. A series of experiments are conducted to verify their potential to monitor crack development.

In Chapter 5, quantification and modelling of damage evolution in masonry walls subjected to in-plane recursive load is investigated. Initially, a numerical exercise on the quantification of damage evolution with the DEM is presented (Section 5.1). A damage index equation is proposed considering the inter-story drift (ISD) and the numerically represented crack evolution. The evolution of damage in masonry wall panels under different loading scenarios is estimated with the application of the introduced damage indexing methodology. To further extend the findings and overcome any limitations from the numerical exercise with the DEM, an extensive database of experimental campaigns is regarded (Section 5.2). Experimental evidence of damage propagation is evaluated and quantified for different configurations (i.e. wall types, precompression levels, material properties and boundary conditions). Finally a numerical simulation with the micro-modelling approach is developed to address any weaknesses of the DEM and further investigate the quantification of crack propagation for different wall configurations (Section 5.3).

In Chapter 6, the experimental campaign undertaken for the sake of this study is demonstrated. The effect of cyclic load on the response of masonry structures is examined focusing on the damage propagation as expressed through deformations and crack onset. Six wall specimens resembling the configuration of a spandrel element are tested under three-point in-plane bending. The walls are prepared adopting materials and practices followed in the Groningen region. Different numerical approaches are considered to simulate the tested specimens and are evaluated on their efficacy to reproduce the experimental findings.

In Chapter 7, concluding remarks are summarized along with suggestions for future investigation in order to overcome any limitations encountered and to further build upon any findings of this research study.

Chapter 2
Literature review

2.1 Induced seismicity and the Groningen gas field

Induced seismicity accounts for quakes and tremors which are triggered by human activities, such as coastal engineering, quarrying, extraction of groundwater, coal, minerals, gas, oil and geothermal, fluids, excavation of tunnels, etc., that change the stresses and strains on the Earth's crust (Foulger et al. 2018). These human activities cause a rate of energy release which is unexpectedly high given the common level of historical seismic rate. This alteration of the seismicity rates might be expressed as an increase in the annual events or in the recorded magnitudes as well. The seismic activity due to human activities is characterized by events of generally low magnitude although moderate intensities have been recorded as well (Foulger et al. 2018; Bal et al. 2019b). Contrary to the common practice of examining a single isolated event, Taylor et al. (2018) suggested that a multievent loading scenario could potentially generate cumulative damage effects or fatigue which exceeds the design loads. Zuzulock et al. (2021) investigated the potential of small magnitude events of induced seismicity to lead to soil fatigue. Regulations regarding the gas production rates have been proposed to pertain the seismic risk to acceptable levels (Vlek 2018). Traffic light protocols were recommended in order to effectively manage the growing concern over induced earthquakes caused by hydraulic fracturing (Baisch et al. 2019; Schultz et al. 2020) while improvements of these protocols with the use of machine learning were introduced (He et al. 2020).

Groningen is the largest on-land gas field in the world and is being exploited since 1963, with gas initially in place of close to 3000 billion m^3 (van Thienen-Visser and Breunese 2015). Almost 3 quarters of the gas has been extracted since then resulting in a maximum soil compaction of 30 cm in the heart of the gas field (NAM 2016). The compaction and the decrease of internal pressure in the reservoir inflicted earthquakes since early 90s. More than 1,300 earthquakes have been recorded in the region all attributed to the gas extraction activities since the region was totally silent in terms of prior seismic activity (van Thienen-Visser and Breunese 2015). The largest earthquake recorded so far was of ML 3.6 in 2012 with the largest horizontal peak ground acceleration (PGA) of 0.08 g, and the largest ever horizontal PGA recorded as 0.11 g during an event of ML 3.4 in January 2018. Groningen has been turned into the spearhead of the research related to induced seismicity in the recent years as it is the most intensely populated area in the world with many man-made earthquakes. A brief history of the earthquakes in the region as well as of the social and political developments afterwards can be found in Bal, Smyrou, and Bulder (2019), while a more detailed overview is given by van den Beukel and van Geuns (2019). Although it is often

claimed, but not supported by evidence, that the earthquakes in Groningen are *"different"*, induced earthquakes are similar to small-magnitude shallow earthquakes in several aspects relevant to structural response (Bal 2018; Bal et al. 2019b).

Despite the rather small magnitude of these earthquakes, the weak soil characteristics, the ground water table very close to the surface, as well as the non-seismic design and construction methods, render the building stock vulnerable (Rots et al. 2017; van Elk et al. 2017; Tomassetti et al. 2019). More than 80% of the buildings in the region are URM, 2/3 of which are built by using cavity walls (i.e. two-leaf slender masonry walls with 7-10 cm air gap in between) (Crowley et al. 2017). This construction method is particularly vulnerable to seismic loading because of the weak connection between the two layers, the low axial load on the external layer, unusually large openings, as well as the high out-of-plane slenderness of the bearing walls. Most structures sit on piles or deep foundations, which is not always the case for historical buildings either because the piles were not placed in the first place or have deteriorated over time. There are more than 2,000 registered historical monuments in the Groningen region, the earthquake safety and structural integrity of which during these repeated small-magnitude induced earthquakes is a major concern for the authorities, local communities and owners. The cultural heritage structures in the region consist of the traditional Dutch farm houses inherited from generation to generation, churches together with surrounding premises belonging to them, public and administrative buildings of importance, residential houses, towers and noble houses (*"borg"* structures).

Due to the fact that the earthquakes are of small magnitude, their manifestation is not easily traceable neither by eye nor by sensitive equipment. Even if some movement, which may be the cause of the damage, is detected, the same amount of movement could also be caused by a number of other factors, such as subsidence and thermal effect. Masonry is a brittle material with low strength threshold before presenting actual plastic deformations (Zucchini and Lourenço 2009; Vasconcelos and Lourenço 2009). This fact raises the question whether the small and sometimes invisible plastic deformations prior to a major earthquake play a significant role in the overall final response of masonry structures or not. This question has become an important issue especially in induced seismicity areas, such as Groningen. In case of a significant earthquake, a damage claim mechanism is activated, rendering the question of possible previous damage prior to the main earthquake critical. Since the induced earthquakes are caused by third parties, liability issues arise and the handling of all consequences is expected to be undertaken by the licensee companies and/or government.

2.2 Structural health monitoring

Historical masonry buildings are often complex structures in the sense of use of non-standardized materials and largely varying construction practices. This is reason why a case-

specific SHM scheme ought to be developed to obtain a precise structural assessment. A SHM strategy should include long term plans, preferably a year and more if possible, so that changes in environmental conditions can be reflected in measurements. As an example, although slightly less than a yearlong monitoring was conducted, Kita et al. (2019) successfully investigated temperature effects on the static and dynamic response of an iconic Italian monumental palace. Data from crack and temperature measurements were combined with a continuous modal identification system and a calibrated numerical model for over a year course providing a better insight of the initial condition of the structure and enabling an accurate damage detection process. They have combined the crack amplitudes with temperature and the vibration results. Another example in environmental effects and the use of the SHM strategy in combination with those effects is the study by Ramos et al. (2010) where results were reported from two complex historical structures consisted of continuous measurements of vibration temperature and relative air humidity. In their study, the dynamic characteristics of the structures are obtained by operational modal analysis and subsequently statistical analysis are performed to evaluate the environmental effects on the dynamic response allowing the detection of damage at an early stage. Ceravolo et al. (2017) showed results from a long-term monitoring where 10-year monitoring results provided conclusions regarding a strengthening measure that took place in the past. The effect of the environmental changes on structural response as well as the efficacy of past structural strengthening were evaluated based on the monitoring data.

Given the necessity to preserve the authentic style of the monumental structures invasive test techniques are not usually allowed. When permission is granted by the preservation authorities, non-destructive testing (NDT) techniques are implemented to complement the findings from SHM (Gonçalves et al. 2017). Particularly, in case of a post-earthquake diagnosis the geometric survey and visual inspections are used in parallel with ambient vibration tests, sonic and flat-jack tests and the monitoring of vibration and temperature act as a seismic early warning system (Rossi and Rossi 2015; Saisi and Gentile 2015). Extensive structural monitoring networks have been deployed in regions with high seismic activity focusing on historical structures (Çaktı and Şafak 2019), while decisions for seismic retrofitting of historical structures are based on the monitoring data in an example by Erdik (2018). It should also be stated that continuous measurements could provide valuable information for damage diagnosis, and help to develop a smart maintenance plan (Coïsson and Blasi 2015; Cigada et al. 2017).

2.3 Vision-based assessment of structures

In order to enhance the inspection process, significant research has focused on the development of automatic vision-based procedures. In particular, artificial intelligence

solutions have been investigated for the detection of cracks for concrete and asphalt surfaces (Section 2.3.1) whereas research on masonry is rather limited (Section 2.3.2). Remote sensing techniques with the use of photogrammetry have been introduced for the monitoring of cracks (Section 2.3.3).

2.3.1 Convolutional neural networks for crack detection

Deep learning, which is a subfield of artificial intelligence, and its representative tool, namely CNN have proven their efficacy in object detection (Zhao et al. 2019). Unlike traditional machine learning approaches, deep learning does not require any hand-crafted features and thus provides end-to-end classifiers which internally learn features and can automatically detect objects (Rosebrock 2017). This attribute of deep learning algorithms along with the recent development of the graphics processing units (GPU) which allowed for very fast computations have boosted their usage in different fields. For the case of crack detection from images, the user only provides as input different photographs and receives as output any detected cracks in these photographs without the necessity for any manual intervention. Deep learning for crack detection has found different case studies such as on inspection of bridges (Kim et al. 2018), gas turbines (Mohtasham Khani et al. 2020) and asphalt surfaces (Zhang et al. 2018a).

Image classification with CNN can be categorized into three types: image patch classification, boundary box regression and semantic segmentation (Zhang et al. 2019). In image patch classification the image is divided in patches and each patch is labelled with a class (Figure 2-1a). When boundary box regression is considered, a box bounds the detected object, that is a crack, and reveals its position and boundaries (Figure 2-1b). These two classification techniques have been extensively used to detect cracks and other defects, and have shown promising results (Cha et al. 2017, 2018; Feng et al. 2019; Mohtasham Khani et al. 2020). Nevertheless, these techniques are implemented at block level rather than at pixel level. On the contrary, semantic segmentation provides information about the exact location, width or length of any defects/cracks since each pixel is assigned to a class label (Figure 2-1c) (Chen et al. 2018a; Li et al. 2018; Liu et al. 2019a; Choi and Cha 2020). Pixel-wise image segmentation has gained ground in the recent years over image patch classification and boundary box regression. A review on deep learning methods for semantic segmentation applied to various application areas was presented in Garcia-Garcia et al. (2018).
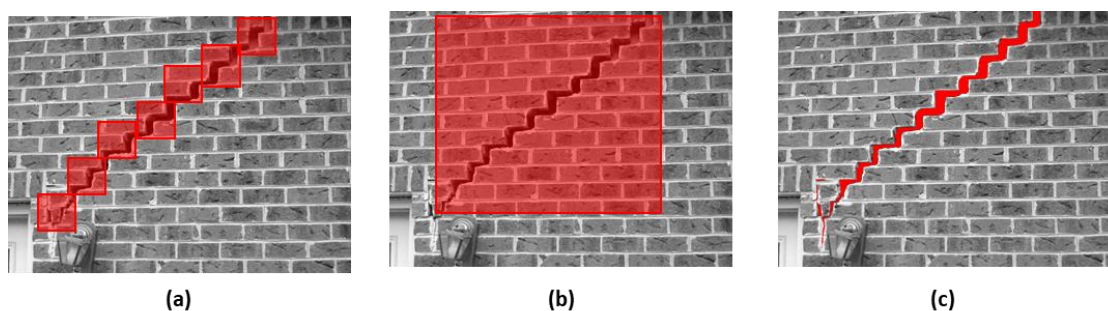
Figure 2-1: Crack detection with (a) image patch classification, (b) boundary box regression and (c) semantic segmentation. The output of each crack detection technique is denoted with red.

Recently Fully Convolutional Networks (FCNs), which are end-to-end networks, have been extensively used for semantic segmentation (Long et al. 2015). FCNs performed as an extended CNN where the final prediction was an image with semantic segmentation instead of a class identification. In a recent study, FCNs have been implemented for semantic segmentation on concrete crack images by evaluating several pre-trained network architectures serving as the backbone of FCN encoder (Dung and Anh 2019). FCNs were also used by Yang et al. (2018) to semantically identify and segment crack pixels with different scales and were combined with morphological operations to extract geometric characteristics, such as length and width, directly from images without manual measurement. An automatic crack segmentation method based on CNN and consisting of the extended FCN and the Deeply-Supervised Nets (DSN) was introduced by Liu et al. (2019). Special care was given to produce a dataset of photographs from asphalt and concrete surfaces with cracks in multi-scale and multi-scene to evaluate the crack detection systems. A modified FCN with fine-tuning the DenseNet-121 (a densely connected CNN) was implemented by Li et al. (2019) to provide pixel-level detection of multiple damage, i.e. crack, spalling, efflorescence and holes, found on concrete surfaces. The suggested method outperformed the results obtained from a method based on SegNet (a deep convolutional encoder–decoder architecture trained to classify urban street pictures at pixel level) while producing smaller sizes of trained models as well. An FCN was implemented to simultaneously identify material type (concrete, steel, asphalt), as well as fine (cracks, exposed rebar) and coarse (spalling, corrosion) structural damage (Hoskere et al. 2020).

U-net is a deep FCN that was developed for biomedical image segmentation and outperformed other state of the art networks (Ronneberger et al. 2015). Since then, U-net has become a benchmark for image segmentation in different fields and its efficacy to detect thin edges resulted in its wide implementation on the inspection of structures. In particular, U-net was implemented for crack detection on pavement surfaces (David Jenkins et al. 2018; Konig et al. 2019). Another showcase for U-net was presented Liu et al. (2019) for concrete crack detection, where the U-net performed better than the other FCN methods (Yang et al. 2018; Dung and Anh 2019) while being trained on significantly smaller training sets. Note that

in order to solve the sample imbalance problem, the focal loss function was selected in the study by Liu et al. (2019). A deep learning algorithm based on U-Net and a CNN with alternately updated clique (CliqueNet), called U-CliqueNet, was proposed to separate cracks from background in tunnel images (Li et al. 2020). The system obtained promising results and was able to separate cracks from images with noise similar to cracks, such as patchwork joints, wires, etc. It is noted that, while other studies were based on datasets of couple of hundreds of images, the proposed network was trained on an extensive dataset consisting of 50,000 and 10,000 images of 496 x 496 pixels for training and testing respectively.

Feature Pyramid Networks (FPN) (Lin et al. 2017) is a typical model architecture to generate pyramidal feature representations for object detection. This architecture extracts features at different scales and then fuses them which reportedly provides predictions of higher accuracy (Lin et al. 2017). FPN achieved state of the art single-model results on the COCO detection benchmark and has been implemented as a generic feature extractor in several applications such as object detection and instance object segmentation (He et al. 2017; Redmon and Farhadi 2018). FPN was combined with an hierarchical boosting module to perform pavement crack segmentation obtaining high accuracy and generalizability (Yang et al. 2020a). The cutting-edge single-stage object detector YOLOv3 adopting FPN was utilized to detect multiple concrete damage of highway bridges (Zhang et al. 2018b). Multiscale feature maps were obtained by a generic pretrained CNN model and fused by implementing FPN in order to apply crack segmentation on concrete images (Ni et al. 2019).

Furthermore, transfer learning in deep learning has been extensively implemented on different fields of computer vision with remarkable results and is considered suitable when the training dataset is small allowing for better performance and less computational effort (Chollet 2017; Rosebrock 2017). The intuition behind transfer learning for image classification is that if a model is trained on a large and general enough dataset, this model will effectively serve as a generic model of the visual world (Abadi et al. 2016). CNN utilizing transfer learning have been used extensively for image classification and semantic segmentation in the field of crack detection (Li et al. 2019; Bang et al. 2019; Yang et al. 2020b; Choi and Cha 2020). Transfer learning was implemented in image-based structural recognition to perform component type identification, spalling condition check, damage level evaluation, and damage type determination (Gao and Mosalam 2018).

Lately, different studies obtained noteworthy results in crack segmentation by implementing region proposal networks followed by algorithms for pixel-level crack detection (Kalfarisi et al. 2020; Kang et al. 2020). In particular, such a hybrid method was proposed by Kang et al. (2020) where crack regions detected by Faster R-CNN were processed by a modified tubularity flow field algorithm to segment the crack pixels. As reported by Kang et al. (2020), the advantages of this method is that Faster R-CNN can detect crack regions very well even

on complex backgrounds while only a dataset of images with bounding boxes of cracks is required which drastically reduces the time to prepare a dataset. As stated by Kang et al. (2020), the proposed method is useful for concrete surfaces only and its applicability on different materials might be limited. Moreover, Chen et al. (2019) implemented an encoder-decoder architecture and proposed a switch method to distinguish between the negative and positive sample automatically and skip the decoder module when the sample is negative to save the inference time.

2.3.2 Vision-based assessment on masonry surfaces

As shown in Section 2.3.1, vision-based and, in particular, deep learning methods for crack detection have been widely applied for concrete surfaces or asphalt. On the contrary, little research has been done on vision-based assessment and specifically for defect detection applied to masonry surfaces. Inarguably, the surface of masonry is less homogeneous and significantly noisier as compared to concrete or asphalt (Brackenbury et al. 2019). On top of that, studies have shown that deep learning models are sensitive to material. In other words, deep learning models that were trained on a specific surface type failed to achieve the same level of accuracy when the material was different. The development of deep learning models that could be robustly applied to infrastructure inspection images for both concrete and asphalt pavement was attempted but crack detection models trained on one material did not necessarily work on other materials and significant performance degradation would be expected when testing on other materials (Alipour and Harris 2020). In another study, various CNN were trained on images from concrete structures for crack detection and their transferability of learned features to photographs from different materials was examined by Özgenel & Sorguç (2018). Brickwork images were found to be the most challenging among the tested cases since brickwork jointing and background textures constitute challenging noises. Moreover, it was concluded that the level of variance in the dataset was more important than the number of samples.

Point clouds were obtained with laser scanning and photogrammetry techniques and were combined to detect different types of defects on ashlar masonry walls by using machine learning classification based on geometry and colour information (Valero et al. 2019). U-net (Ronneberger et al. 2015) was used for brick segmentation in masonry walls (Ibrahim et al. 2019). Najimi et al. (2014) used a system that combined different types of sensors (multiple high-resolution cameras, laser scanning and inertial measurement unit) for tunnel inspection. Digital image correlation (DIC) techniques were utilized to automatically trace any changes in between consecutive inspections and subsequently an operator would appropriately classify them among a list of defects (Najimi et al. 2014). Thus, the defect detection process is not fully automatized and human intervention is still required.

CNN to classify different defect types, such as cracking, spalling, mortar loss, and vegetation, from images of masonry structures was used by Brackenbury et al. (2019). In detail, photographs were taken from masonry bridges and corrected for perspective distortion and then resized to ensure a constant resolution. Defect classification was implemented on patches of 100 x 100 pixels. It was suggested that by firstly detecting and segmenting mortar joints, and then classifying defects, defected and defect-free areas of the masonry could be all predicted with more confidence and better accuracy.

A novel damage identification architecture to detect two types of damage (efflorescence and spalling) in historic masonry buildings based on the Faster R-CNN ResNet101 model was proposed by Wang et al. (2019). In particular, two orthophotographs were extracted from a historical structure and were segmented into small patches of 500 x 500 pixels. The produced patches were annotated with bounding boxes marking the investigated damage types. Quick identification and detection of the surface damage was achieved. The necessity for the expansion of the database with wider range of distances and angles and more types of structural samples was reported.

An automatic vision-based crack detection system using CNN was proposed by Ali (2019) to ease the inspection of masonry structures. The feature extraction process was done by CNN from colour images and three classifiers were studied, namely the CNN itself, SVM and Random Forest. False negative areas were found since the system would confuse the grout lines with cracks. Finally, since the cracks on masonry structures could not be easily identified, extreme care was needed when annotating the dataset.

A common limitation observed in the existing literature for vision-based assessment on masonry surfaces is that the developed methods regarded only a single structure and therefore their ability to generalize when tested on more diverse data remains to be evaluated.

2.3.3 Crack monitoring with markers

Continuous monitoring of masonry structures can be done in various forms with the help of SHM solutions (Ramos et al. 2010b; Ceravolo et al. 2017; Kita et al. 2020; Makoond et al. 2020), NDT techniques (Gonçalves et al. 2017) or the use of technologies like DIC, photogrammetry or laser scanning (Salmanpour et al. 2015; Riveiro et al. 2016; Acikgoz et al. 2018a; D'Altri et al. 2018b; Napolitano and Glisic 2019; Korswagen et al. 2020b; Kassotakis et al. 2020). Although these techniques, provide crucial information on the damage identification and quantification, they cannot be rapidly employed when screening of numerous structures is required after an event. It is simply not feasible to perform testing on every structure excited during an earthquake to assess any residual damage. Furthermore, the vast majority of structures does not have a monitoring scheme installed, while vision-based techniques usually require expensive equipment and skilled personnel to operate

them. In particular, the DIC approaches entail a cumbersome procedure (surface preparation, lighting conditions, DIC algorithms etc.) and thus are mainly limited to laboratory conditions (Kallioras et al. 2018; Senaldi et al. 2020). Due to these drawbacks, the assessment of structures relies heavily on visual damage inspection based on data mostly obtained visually. Nevertheless, this practice is rather laborious, slow, and expensive when accounting for the man-hours required to be invested in the field and at the office to process the collected data. Moreover, visual inspection can raise safety concerns, since there are parts of structures with access restrictions that are difficult to reach.

Bal et al. (2021a) introduced a tailor-made SHM scheme for a historical masonry structure subjected to induced-seismicity events and the importance of crack monitoring for a reliable damage assessment was showcased (refer to Chapter 3). Carrillo et al. (2017) and Farhidzadeh et al. (2013) emphasized that the characteristics of cracks as obtained from the inspection process, e.g. length, width, pattern and distribution, are important indicators of structural damage, while a quantification of damage based on residual cracks was performed numerically (Sarhosis et al. 2019b). While the significance of monitoring of the crack characteristics was established, it is highlighted that the methods for automatic crack detection from photographs lack the ability to detect the crack width accurately (Cho et al. 2018; Yang et al. 2018; Dais et al. 2021a), especially in the sub-millimetre region, a parameter that can provide crucial information on the severity and the progression of the damage. Without surface preparation, the information reflected in the photograph highly depends on the photographic conditions, especially on the amount and angle of the light, while the accurate width measurement of thin edges, such as cracks, is hard to be achieved. Various methods were developed in the past to overcome this problem, relying on monitoring certain type of markers around the cracks instead of monitoring the crack itself (Nishiyama et al. 2015; Germanese et al. 2018; Cho et al. 2018; Zhang et al. 2018a; Wojnarowski et al. 2019). It is stressed that these markers are highly visible and especially for the cases of monumental structures, where strict regulations apply, even simple interventions, such as placing crack-rulers, are not permitted by the conservation authorities. AI techniques for automatic crack segmentation and measurement have been presented (Yang et al. 2018; Kang et al. 2020) for rather homogeneous surfaces, such as asphalt and concrete, but their applicability to complex surfaces, that is masonry, might be limited.

2.4 Damage accumulation in masonry

Structural materials subjected to repeated cyclic loading present weakening, an issue known as fatigue (Schijve 2009). Some of the available research treats the effect of cumulative loading in masonry from the fatigue point of view. For example, a rainflow algorithm was applied to experimental and numerical results of masonry specimens, in an effort to quantify

non-structural damage in URM walls due to induced earthquakes in Basel and in St. Gallen, Switzerland (Didier et al. 2017). In cases where the load amplitudes are relatively high (still below the design values) but the number of cycles is low (typically lower than a few hundred thousand), the phenomenon is called low-cycle fatigue. There is an immense number of elastic cycles in high-cycle fatigue, while both elastic and small plastic deformations can be observed in much lower number of cycles in low-cycle fatigue. Past earthquakes with limited plastic deformations, in combination with pre-earthquake static loads and support settlements, are structural effects that resemble low-cycle fatigue in masonry (Elnashai and Di Sarno 2008); for a discussion on the low-cycle fatigue and its effects on structures refer to Chai (2005). In this thesis the term fatigue is being used to describe the accumulation of micro damage in masonry structures due to repetitive load leading to premature failure at load levels below the capacity obtained for the application of monotonic excitation (for further clarification refer to the results of the experimental campaign in Chapter 6). The accumulation of micro damage is expressed as residual deformations prior to the formation of visible cracks and will be referred to hereafter as plastic deformations. It should be noted that the term "plastic deformation" here refers to masonry as a composition, as in (Zucchini and Lourenço 2009; Vasconcelos and Lourenço 2009), rather than to the behaviour of the individual materials, such as the mortar or brick units.

Seismic events often take place in sequences over a short period of time not allowing for any repair or strengthening actions in the meantime possibly leading to damage accumulation (Iervolino et al. 2020). The cumulative damage caused by multiple, consecutive seismic shakings was investigated by Grimaz & Malisan (2017). It was pinpointed that greater damage level could be attained when a repetition of two shocks with the same PGA was considered instead of accounting only for a unique shock. Furthermore, damage increase could occur also after a second shock with intensity lower than the first one, if the previous shock caused damage (Grimaz and Malisan 2017). Di Sarno (2013) examined the case of multiple earthquakes occurring in a short period of time, and the effect of such phenomena on the seismic response of structures. For the case study analysed, it was shown that the seismic force demands on a structure can be thrice as compared to a single event, especially for structural periods above 1.0 s. It was further observed that multiple earthquakes warrant extensive and urgent studies, giving indications of the levels of lack of conservatism in the safety of conventionally-designed structures when subjected to multiple earthquakes. Different types of structures were excited under seismic sequences and greater damage accumulation was reported with respect to only one event (Fragiacomo et al. 2004; Hatzivassiliou and Hatzigeorgiou 2015; Oggu and Gopikrishna 2020). The performance of two historic centres under the effect of the Central Italy earthquake sequence was studied (Putrino and D'Ayala 2019a, b). A procedure was proposed where the masonry structures were reproduced with bilinear curves and their characteristics, such as stiffness and ductility,

were updated for every seismic excitation. Following this procedure, it was possible to capture the damage evolution through the two main events of the seismic sequence (Putrino and D'Ayala 2019a). It is noted that the latter studies mainly focused on medium–strong intensity earthquakes. The recent work of Nievas et al. (2020) highlighted the potential of small-to-medium magnitude earthquakes to be damaging. This is particularly interesting for induced seismicity which is characterized by frequent events of such magnitude. As shown in Section 2.1, man-made earthquakes have been proven able to cause damage to the built environment, although the impact of the repetitive low/moderate magnitude excitations is not yet clear.

Damage accumulation in masonry structures have interested the research community. In particular, DIC techniques have been widely used recently to reliably monitor propagation of stresses and strains along experimental campaigns for the definition of damage states (Heerema et al. 2015; Bolhassani et al. 2017). DIC and acoustic emission were combined to identify the onset of crack initiation and development of critical crack growth in an attempt to quantify progressive damage development in reinforced concrete (RC) masonry walls (Vanniamparambil et al. 2014). Tomor et al. (2013) investigated the deterioration process of brick masonry through small-scale laboratory tests under compression and shear. With the help of acoustic emission methods, they identified three different stages of accumulation of damage, i.e. compaction, micro-cracking and macro-cracking for compression loading, but were not able to detect a trend of damage accumulation for shear loading. An acoustic emission-based method was utilized to quantify the progressive damage in masonry under cyclic compressive loads (Shetty et al. 2019). NDTs (i.e. infrared thermography and ground-penetrating radar) were utilized to correlate structural damage and damage of attached artistic assets on stone masonry walls (Calderini et al. 2015). An overview of the capabilities and limitations in the use of microscopy for diagnosing a number of forms of deterioration of brick masonry was presented (Larbi 2004). Furthermore, the progressive change of modal characteristics has been used to identify any accumulated damage in masonry structures (Ramos et al. 2010a; Graziotti et al. 2017; Kouris et al. 2019). Such dynamic based methods have been found to perform well on the identification of damage at global level, although fail to account for local failures. Changes in the environmental conditions (e.g. humidity and temperature) can lead to fluctuations of the identified natural frequencies making hard the detection of minor damage (Kita et al. 2019; Zonno et al. 2019b, a).

Although the above-mentioned assessment techniques have shown promising results on the quantification of damage propagation for masonry structures, they are not readily available since they require special equipment and controlled conditions to perform well, thus limiting their implementation mostly to laboratory applications or structures with a monitoring system installed. In practice, structural assessment commonly relies on the inspection of cracking distribution along a structure. Petry & Beyer (2015b) examined a set of tested URM walls and

defined qualitative limit states based on local crack patterns differentiating between flexure and shear mode. Vintzileou et al. (2020) argued that establishing a quantitative classification based on cracking level would be beneficial, although additional quantitative experimental data would be required. For a literature review on the crack-based assessment of structures refer to Section 2.6. Techniques for quantification of damage based on crack patterns are particularly beneficial considering the recent boost on the usage of automated techniques to detect cracks from structures (see Section 2.3.1). Additionally, such techniques could be implemented on numerical results with the micro-modelling approach where any damage can be traced at a local level (i.e. mortar joint or unit cracking) (see Section 5.1.1).

2.5 Evidence of accumulated damage in experiments

The vast majority of research on masonry provides only indirect information about the accumulation of damage as it does not constitute the main topic in those studies. Traces of cumulative damage from the available, though limited, experimental evidence in the literature were highlighted here.

Tests conducted at Delft University of Technology (TUD) (Rots et al. 2017) on masonry specimens resembling Groningen structures showed that the compressive behaviour is highly nonlinear starting from very low stress levels (i.e. 10% of the strength and above). Repeated compression tests on masonry wallets (Graziotti et al. 2015) demonstrated that there is residual plastic deformation on the samples at 10% of the strength, and this deformation is close to the peak deformation attained in that loading half-cycle. The ratio of the residual displacement to the maximum displacement of the relevant half cycle decreased gradually (note that the residual displacement value increased in absolute terms) reaching up to 70% at the maximum load.

Two masonry piers, one slender and one squat dominated by flexure and shear behaviour respectively, tested at EUCENTRE (Graziotti et al. 2015, 2017). The first cycles of the lateral loading for the two specimens are provided in Figure 2-2a in a normalized format, where force and lateral deformation of the wall specimens in the first loading cycle have been divided to the overall wall strength and to the wall yield displacement, respectively. The first loading cycle is approximately 25–30% of the strength of the wall, resulting in 10–15% of the yield displacement. Both specimens exhibited residual displacement approximately 2–3% of the yield displacement at zero load crossing, thus at 20% of the peak displacement of the first cycle. This is a highly plastic behaviour, at component level, even though it is only the first loading cycle with relatively small forces and displacements attained. Further tests that took place at TUD (Ravenshorst and Messali 2016) verified that the initiation of crack formation on wall piers (squat or slender) happened for very small values of drift. Similar conclusions were drawn from a series of quasi-static cyclic tests on masonry panels; crack onset took

place for almost all the examined walls for rather small drift level (i.e. 0.025%) and was associated with the first reduction of stiffness (Petry and Beyer 2015a). An experimental campaign was undertaken to study the degradation of masonry shear walls subjected to harmonic shear loads (Nichols 2000). It was found that the reduction of the effective stiffness starts for strain level of 25 microns while the onset of cracking was observed at 200 micro-strains. Thus, the degradation of the properties of masonry takes place before the formation of any visible cracks showcasing the development of micro-damage.

A 3D full-scale test specimen, similar to the Groningen cavity-wall terrace houses, was tested under sequential shake table excitations of increasing intensity (Graziotti et al. 2015, 2017). The residual displacements at the first and second floor and the roof level are presented in Figure 2-2b. The residual displacement is not cumulative towards one direction, meaning that it changes sign during the experiments. For example, application of 150% of EQ2 resulted in 4.5 mm residual displacement at roof while the next applied record, 200% of EQ2, resulted in 3 mm residual displacement in the opposite direction. Observations on the crack width at the first and second floor of the same specimen were also presented (Graziotti et al. 2017); a continuously increasing pattern in crack width was revealed, suggesting that the cumulative damage may manifest itself in different forms when residual system displacements or specific structural cracks are monitored.

Cyclic tests on a full-scale two-storey Groningen house resulted in residual structural cracks up to 1 mm width at limited drift level (i.e. 0.055%) and incrementally their opening became greater, providing a clear visualization of the accumulation of damage (Esposito et al. 2016). Kallioras et al. (2020, 2018) performed full scale shake table tests on URM buildings and highlighted that the damage limit state accounting for minor structural damage, linked to hairline cracks with less than 1 mm width, was attained for drift values 0.05-0.2%. The appearance of minor structural damage was associated with elongation of the first period of the tested structure from 0.15 s to 0.19 s while residual drift was negligible (Kallioras et al. 2020). Although period elongation can be considered suitable for damage identification, it can be argued that such measurements are not available for every structure due to lack of installed monitoring. On the other hand, inspecting cracks is a more accessible solution and provides a clear demonstration of the inflicted damage.

Based on the observations from previous experimental studies presented above, for masonry nonlinear response initiates for very small amplitude of deformations. This behaviour so far is being overlooked or ill reported, since the focus of the experimental campaigns is the response of the URM specimens close to their ultimate state. Moreover, it was concluded that by using the data of the full-scale shake table tests the cumulative damage does not monotonically increase in case overall structural parameters, such as top displacement or floor displacements, are monitored. For instance, the damage level corresponding to minor

structural might be reached (i.e. formation of hairline cracks along the structure) while the residual inter-storey drift remains zero. Thus, it can be inferred that using only the residual ISD as damage indicator would be misleading since the already inflicted cracks would not be accounted for. Monitoring of cracks seems to be a better tool as cracks provide steady increase in measured damage linked to the application of additional earthquake loads on the structure.

(a)

(b)
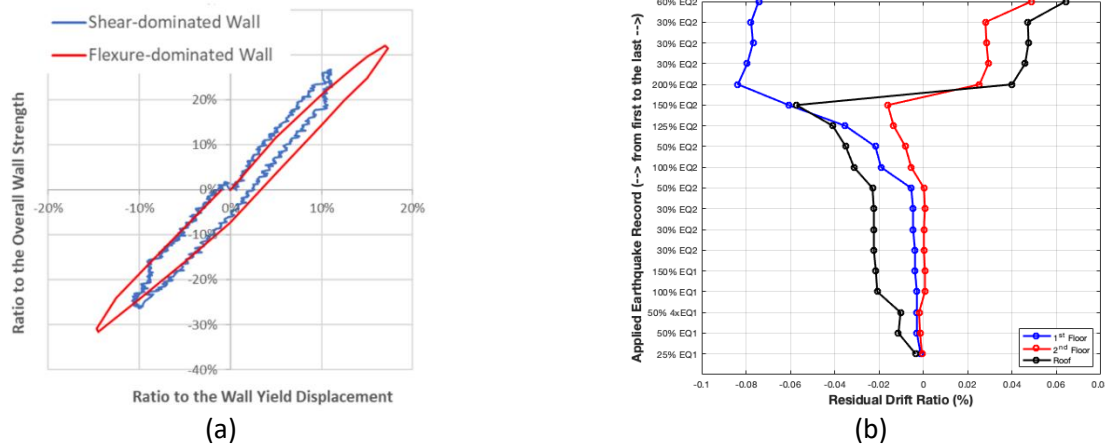
Figure 2-2: (a) First cycles from the quasi-static tests on calcium silicate specimens (Graziotti et al. 2015); (b) residual displacements from sequential shake table tests on the full-scale specimen (modified from Graziotti et al. (2015)), where 'y' axis shows the sequentially applied earthquake records).

2.6 Crack-based assessment of structures

(FEMA 307 1998; Farhidzadeh et al. 2013; Carrillo et al. 2017; Bal et al. 2021a) emphasized that the characteristics of cracks as obtained from the inspection process, e.g. length, width, pattern and distribution, are important indicators of structural damage. In order to provide a quantitative assessment of shear-cracked RC structures, a crack-based analysis procedure has been presented by Zaborac et al. (2020). The suggested methodology utilized a combination of measured and estimated concrete cracking data (e.g. crack widths, spacing of cracks, inclination of cracks etc.) as primary input to predict the residual shear capacity of a RC beam (Zaborac et al. 2020). Acceptance limits of the structural response of RC walls were suggested based on ISD ratios, residual crack width and total damaged area (i.e. the area of cracks) (Carrillo and Alcocer 2012). Regression models, capable of estimating the maximum lateral drift experienced by a damaged RC column based solely on quantitative data extracted from images of any cracks were developed (Lattanzi et al. 2016). A computer vision approach was followed to generate a quantitative assessment of damage and load levels based on surface crack patterns for RC structural elements (Davoudi et al. 2018). The results obtained were set as a baseline for the potential of the proposed method and its limitations were elucidated (Davoudi et al. 2018).

Furthermore, several studies have proposed an automatic process for quantitative assessment based on the evaluation of fractal dimensions as measured from crack patterns. Fractal geometry has been used to measure rough or irregular surfaces (Mandelbrot and Wheeler 1983; Falconer 2003). Fractal dimension has been characterized as a measure of the space-filling capacity of a pattern that tells how a fractal, i.e. a crack, scales differently from the space it is embedded in, i.e. a wall. In an early study, Xiao & Jiang (1994) pointed out that the fracture surfaces contain a lot of information regarding the micromechanics of brick masonry. The relationship between fracture energy and fractal dimension associates the macroscopic behaviour with the microscopic structure (Xiao and Jiang 1994). Using results of six quasi-static cyclic tests on unreinforced brick masonry walls with different failure modes, predictions of the stiffness and strength degradation were extracted based on the crack patterns (Dolatshahi and Beyer 2019). The proposed approach worked better for higher damage levels (Dolatshahi and Beyer 2019). Similar process was followed on an experimental study on two large-scale RC shear wall (Farhidzadeh et al. 2013). In particular, the produced damage index based on the fractal dimensions of the observed cracks could estimate any stiffness loss of the tested specimens with acceptable accuracy. Further on, it was concluded that extra test specimens with different shape and size would be required to verify the robustness of the proposed approach (Farhidzadeh et al. 2013). A recent study based on literature research and experimental data on concrete and masonry walls reviewed how different parameters of the fractal analysis, such as box size interval, scale factor etc., affect the computed fractal dimensions (Rezaie et al. 2020). A damage index for rapid evaluation of the damage state was developed based on the fractal dimensions as computed from experiments on RC walls (Carrillo et al. 2017). Even though the assessment of structural components based on fractural analysis has yielded promising results, limitations have been pointed out as well; the results appeared to be case specific and thus extensive parametric studies were highly recommended (Ebrahimkhanlou et al. 2019).

DIC can be used as a non-destructive method for damage identification and quantification. DIC is an optical method that employs tracking and image registration techniques for accurate full filed measurements of displacements and strains (Ghorbani et al. 2015; Salmanpour et al. 2015; Acikgoz et al. 2018b; Shafiei Dizaji et al. 2018). DIC along with acoustic emission were utilized in the past to detect, monitor and quantify damage propagation (Vanniamparambil et al. 2014; Shetty et al. 2019). In particular, different studies utilized DIC techniques for the quantification of the development of damage caused by small to moderate seismicity. Abbiati et al. (2018) undertook an experimental campaign attempting to produce a probabilistic model for quantifying plaster cracks on URM structures due to induced seismicity. In order to quantify the initiation and accumulation of damage, a "damage score" was proposed based on Von Mises strain field estimations (Abbiati et al. 2018). More recently, Korswagen et al. (2019) carried out an experimental campaign to quantify light damage in

URM structures due to repeated horizontal loads. DIC methods were utilized to precisely capture the initiation and propagation of cracks during the experiments. A dimensionless damage parameter was introduced based on the number of cracks, and their width and length (Korswagen et al. 2019). The produced equation defining the damage parameter is applicable for the limited cases treated in the study and thus its applicability to serve as a damage indicator for a wider range of cases needs to be investigated further (Korswagen et al. 2019). A DIC technique was utilized on a small-scale physical model of a masonry structure to translate the measured displacement fields to crack characteristics, i.e. length and width (Nghiem et al. 2015). It was concluded that for a reliable damage quantification based on crack length, the failure mode needs to be taken into consideration (Nghiem et al. 2015).

In conclusion, evaluating crack distribution and evolution appears to provide invaluable information for the reliable assessment of the condition of a structure. In particular, for masonry constructions limited research has been undertaken and information about cracks are usually not reported at all or ill-documented in experimental studies hindering thus the development of a crack-based assessment procedure (Vintzileou et al. 2020).

2.7 Influence of load history on the response of masonry structures

As discussed in Section 2.1, the building stock in Groningen, mainly consisting of masonry constructions, has been proven vulnerable to the recent induced seismicity of the region. These structures along the last decade received multiple load cycles due to the frequent low to medium earthquakes. Therefore, it is critical to investigate the effect of load history on the performance of these masonry structures.

Godio et al. (2019) considered quasi-static shear-compression tests to study the effect of load history on the behaviour of stone masonry walls. Varying the number of loading cycles has negligible influence on the stiffness and the force capacity of the walls, whereas the ultimate drift was observed to be very sensitive to the load history, being larger when the walls were subjected to monotonic loading than when they were subjected to cyclic loading (Godio et al. 2019). Similar observations were made by experimental (Korswagen et al. 2019) and numerical (Wilding et al. 2017) studies. In particular for the latter research (Wilding et al. 2017), for shear controlled walls under cyclic excitations the ultimate drift capacity was approximately half the one obtained for monotonic load, while the drift capacity of flexure dominated specimens was found insensitive to the load history.

The behaviour of clay-unit masonry was found to be influenced significantly by repeated compressive forces (Abrams et al. 1985). Results showed that reductions in static strengths as large as 30% were possible for as little as 40 cycles of loading at a relatively small amplitude of alternating force (Abrams et al. 1985). Specimens with stronger mortar were more sensitive to repeated loadings than those with weaker mortar (Abrams et al. 1985).

Finally, additional experimental investigations were suggested for the establishment of a mechanical model for masonry subjected to repeated stresses with the consideration of reduction factors for the splitting strength of brick units due to cyclic forces (Abrams et al. 1985).

The mechanical behaviour of masonry triplets subjected to monotonic and cyclic shear loadings was experimentally and numerically studied (Barattucci et al. 2020). Shear tests on triplets show that cyclic loading significantly reduces the peak shear strength (typically around 18%) with respect to monotonic loads, regardless of the mortar composition. Numerical results highlight that cyclic shear strength reduction can be attributed to the progressive formation of cracks in the mortar layers along with the cyclic loading (Barattucci et al. 2020).

Masonry is susceptible to cumulative damage demands; in other words its force and/or displacement capacities are a function of the number of loading cycles until failure is attained (Beyer et al. 2014). A systematic study on the effect of loading protocol on the behaviour of masonry is required to propose a correction for the capacity of masonry accounting for loading history (Beyer et al. 2014).

A masonry spandrel was excited under cyclic load and the damage evolution was traced with various monitoring techniques (Verstrynge et al. 2018). In particular, displacement sensors were placed along the length of the spandrel with only one of them located on the wall part where a crack was formed at the final stage of the test. The latter sensor measured considerably greater deformations than the rest of the sensors prior to the initiation of any visible crack. This is an indication of the sustained micro-damage signifying that a crack would be expected at this location along the coming cycles. Consequently, measuring deformations on a loaded masonry structure can provide valuable information on the damage accumulation. It is highlighted that, although multiple load cycles were applied, no conclusions can be drawn regarding the effect of load history since no monotonic test was considered to perform as reference.

Korswagen et al. (2019, 2020a) undertook an extensive experimental campaign on the assessment of light damage in masonry structures. In particular, masonry spandrels were tested under monotonic and cyclic load to study the damage propagation. The investigation of damage accumulation focused on the force reduction along repetitive loads without considering the evolution of deformations that lead to damage. It can be argued that for a real structure it is hard to monitor the applied load cycles or reliably evaluate its strength. On the other hand, measuring deformations at various locations is more straightforward. Consequently, correlation of cumulative damage to deformation levels instead of force level or wall strength appears desirable.

Actions like expansion/shrinkage due to environmental conditions and structural deformations due to soil movements can be considered as recursive load cycles along the

life span of a structure. As a consequence of the climate change buildings are exposed to more severe and frequent extreme weather conditions such as floods and wind driven rainstorms (Stephenson and D'Ayala 2019). An novel experimental investigation was performed to measure the impact of cyclic wind driven rain and flood exposure on the lateral stiffness and strength of masonry infilled timber frames (Stephenson and D'Ayala 2019). Empirical data indicated losses in elastic stiffness exceeding 75% as a result of exposure while further investigation of the effect of meteorological conditions on the response of masonry structures was recommended.

Based on the literature review, additional research is required to better understand the relationship between load history and damage accumulation for masonry structures. In particular, loading wall panels in a cyclic manner and comparing the response to monotonically tested specimens is recommended. Monitoring deformations along the tested walls prior to formation of visible crack would illustrate any accumulation of micro-damage.

2.8 Modelling strategies for estimation of damage accumulation

At this point, the available modelling tools were scrutinized in terms of their advantages and limitations in modelling cumulative damage in masonry. For a detailed review of modelling strategies for the computational analysis of masonry structures refer to (Roca et al. 2010; Asteris et al. 2015; Shadlou et al. 2020; D'Altri et al. 2020).

In order to study the effect of repeated seismic loads on structures, Hatzigeorgiou & Beskos, (2009) conducted an extensive number of analyses on single degree of freedom (SDOF) systems that resemble a variety of structural typologies and presented a simple approach for representing the inelastic displacement ratio of structures under recursive earthquakes. They found that repeated earthquakes have a significant effect on the inelastic displacement ratio and hence on the maximum inelastic displacement of the SDOF systems. In a similar but comparatively much more limited study, Aschheim & Black (1999) performed nonlinear analyses on SDOF systems where Takeda hysteresis model (Takeda et al. 1970) was used, without being able to identify a strong effect of previous earthquakes in these analyses, a result attributed to the nature of such hysteresis models, as explained further below.

Mouyiannou et al. (2014) on the other hand, studied the cumulative damage in masonry from repeated shocks, such as seismic sequence or multiple events and after-shocks affecting an unrepaired structure. An approach was proposed in which derivation of state-dependent fragility curves is possible, considering cumulated seismic damage, whilst neglecting possible ageing effects. Their approach was based on running cyclic analysis by imposing displacements up to the existing state of the structure and running the nonlinear time-histories after that state. After running SDOF models with real earthquake sequences from Christchurch in 2010 and 2011, it was concluded that running fragility models only based on

the main shock is inappropriate, since it provides missing information regarding the actual response of the structure.

Iervolino et al. (2013) approached the matter from a reliability perspective, introducing the gamma process, often used for finding the remaining life cycle of reliable systems. A set of compatible equations and case study applications were considered to illustrate that the gamma process can be used to find the remaining strength and life time of structures after recursive earthquakes take place.

Chai (2005) proposed a low-cycle fatigue model into duration-dependent inelastic design spectra in order to allow for the effect of longer or repetitive earthquakes in the design process. The introduced approach was based on the premise that, in order to ensure satisfactory performance of a structure, the cyclic plastic strain energy capacity of the structure must be larger than or equal to the portion of seismic input energy contributing to cumulative damage.

Three typology buildings from Groningen gas field were modelled as SDOFs to investigate the possibilities of modelling the cumulative damage (Sarhosis et al. 2019b). Crowley & Pinho (2017) calibrated the SDOF backbone curves by using dynamic hysteresis loops representing the peak base shear of each analysis and the corresponding attic floor displacement (i.e. the highest level of the building). The parameters for the SDOF models had to be slightly modified to be able to reproduce the experimental response where often nonlinearities take place even in the small pre-yield load and displacement amplitudes, as shown in Section 2.5, while strength degradation was additionally taken into account (Sarhosis et al. 2019b).

MDOF properties of a real building can be coined into a single SDOF curve after a number of assumptions and simplifications are made. This is a rather standard procedure used for generating an SDOF system that would respond similarly to its MDOF counterpart in terms of top displacement and base shear force. SDOF models representing real buildings are often preferred for faster yet efficient way of deriving results from large number of time-histories analyses. Previous efforts of modelling cumulative damage in SDOF models (Aschheim and Black 1999; Elnashai and Di Sarno 2008; Hatzigeorgiou and Beskos 2009; Di Sarno 2013; Mouyiannou et al. 2014; Dais et al. 2017) show that such simplified models are not able to accurately capture the accumulation of damage if sequential time-history analyses are run, unless stiffness and strength degradation issues are properly addressed. Even in this case, the start of the next earthquake from the point the previous one has left the structure is not a straightforward issue since the residual displacements from a previous earthquake are numerically wiped, thus "forgotten", once larger displacements are attained in the next earthquake. A user intervention is needed to accurately model the sequence in the accumulation of residual displacements (Mouyiannou et al. 2014; Sarhosis et al. 2019b).

In overall, SDOF models can be useful for detecting tendencies in cases that more complicated analyses are not feasible. The major drawback of using SDOF models is that the simulated cumulative damage is sensitive to the degradation parameters, which require calibration against experimental data. To address these limitations, more elaborate analyses were considered in this study for the simulation of damage accumulation in masonry structures.

Depending on the level of accuracy and the simplicity desired, different modelling strategies can be adopted (Lourenço 1996) (Figure 2-3):

- Detailed micro-modelling: units and mortar in the joints are represented by continuum elements whereas the unit-mortar interface is represented by discontinuous elements
- Simplified micro-modelling: expanded units are represented by continuum elements whereas the behaviour of the mortar joints and unit-mortar interface is lumped in discontinuous elements
- Macro-modelling: units, mortar and unit-mortar interface are smeared out in the continuum
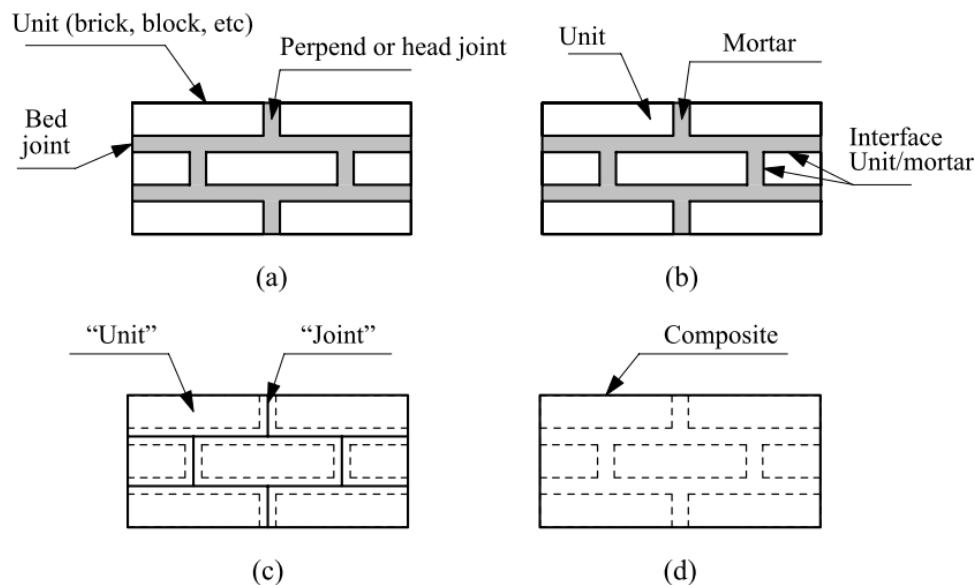
Figure 2-3: Modelling strategies for masonry structures: (a) masonry sample; (b) detailed micro-modelling; (c) simplified micro-modelling; (d) macro-modelling. Figure was reproduced from Lourenço (1996).

In larger structures due to concerns regarding the increased computational cost and convergence issues, the masonry units and the mortar joints are commonly represented by homogenous elements following the macro-modelling approach (Gambarotta and Lagomarsino 1997a; Milani 2011). A limitation of the macro-modelling approach is that it fails to reproduce the anisotropy in the inelastic range that characterises masonry (Milani 2011). The mortar joints act as planes of weakness and thus the arrangement of bricks/blocks influences the orthotropic response of masonry (Milani and Tralli 2011; Valente and Milani

2016a). Milani & Lourenço (2010) in order to address this limitation examined representative elements of masonry walls with different orientations of the bed joints and the in-plane masonry strength was stochastically assessed. A continuum damage model was introduced by Pelà et al. (2011) in which the orthotropic behaviour was simulated using the concept of mapped stress tensor. While such sophisticated numerical models exist in the literature, it is commonly accepted for damage-plasticity isotropic models mainly designed for concrete to be utilized to simulate masonry structures (Valente and Milani 2016b). These isotropic models neglect any orthotropic effects but they have been found to reproduce accurately the overall behaviour of a structure (Valente and Milani 2016b; Castellazzi et al. 2017; Milani et al. 2018; Meoni et al. 2019; D'Altri et al. 2020; Dais et al. 2021b). For this study the macro-modelling method was adopted for the simulation of a two-storey URM monument where the location of the expected cracks was examined for different loading scenarios (see Chapter 3).

The overall results of numerical models, such as SDOF residual displacement or floor lateral displacements, may be misleading in understanding the damage accumulation (refer to Section 2.5). On the other hand, detailed discrete-element modelling has been found to be computationally expensive but more consistent in terms of providing insights in real damage accumulation (Sarhosis et al. 2019b). When higher detail is requested and the focus lays on the simulation of failure at local level, such as joint tensile cracking and slipping, the micro-modelling method is preferred (Sarhosis and Lemos 2018). Comparative studies between continuous and discrete models concluded that both methods could reproduce the failure mechanisms adequately, although only the latter were able to reproduce with high fidelity the cracking distribution (Bejarano-Urrego et al. 2018; Malena et al. 2019; Pepe et al. 2020; Ferrante et al. 2021a). The micro-modelling approach enables an accurate representation of the complex response of masonry and account for the different failure mechanisms both at joint and unit level (Lourenço 1996; Gambarotta and Lagomarsino 1997b; Chaimoon and Attard 2007; Petracca et al. 2017). Here, micro-modelling approaches implemented with the DEM and the FEM analysis were considered for the numerical evaluation of damage propagation in masonry structures.

One of the first implementations of FEM for discrete modelling of masonry was attempted by (Page 1978). Masonry was considered as an assemblage of elastic brick continuum elements acting in conjunction with linkage elements simulating the mortar joints (Page 1978). Since then, numerous applications of the method have been reported in the literature (Stavridis and Shing 2010; Kumar and Barbato 2019). In particular for the finite element software ABAQUS (ABAQUS 2013), the provided traction-separation law combined with frictional behaviour has been implemented for the micro-modelling of different material types like polymer-matrix composites, masonry pillars reinforced with fibre reinforced polymer strips and different configurations of masonry wallets (Alberto et al. 2011; Abdelmoneim Elamin Mohamad and

Chen 2016; Abdulla et al. 2017; Nian et al. 2018; Bertolesi et al. 2018; Nasiri and Liu 2020; Naciri et al. 2021). In order to better approximate the response of mortar joints with discontinuous elements elaborate subroutines were developed within ABAQUS using either implicit or explicit analysis to allow for more sophisticated constitutive laws to be reproduced (Zucchini and Lourenço 2009; Nazir and Dhanasekar 2014; Aref and Dolatshahi 2013; Nazir and Dhanasekar 2013; Dolatshahi et al. 2014; Yuen et al. 2016; Dolatshahi and Aref 2016; Serpieri et al. 2017; Andreotti et al. 2018, 2019; D'Altri et al. 2018a, 2019a; Kumar and Barbato 2019; Lin et al. 2019). For additional information on the discrete modelling of masonry with FEM refer to Section 5.3 where a simplified micro-modelling approach was developed in ABAQUS. In particular, the continuum elements simulating masonry units were governed by damaged elasticity in combination with tensile and compressive plasticity while cohesive-frictional behaviour was incorporated in the interfaces representing mortar joints with the development of an elaborate subroutine.

According to Giordano et al. (2002), two major concerns arise when the micro-modelling approach is implemented within the framework of FEM. Firstly, block mesh and joint mesh must be connected together, so that they have to be compatible, which is possible only if interface joints are identically located. This compatibility is very difficult to ensure when complex block arrangements are to be handled, like in 3D structures. Secondly, the joint element is intrinsically able to model the contact only in the small displacement field. When large motion are to be dealt, is not possible to provide easy remeshing in order to update existing contacts and/or to create new ones.

The DEM has been found able to overcome the aforementioned limitations (Giordano et al. 2002). The contacts are not fixed, like in the FEM with discontinuous elements, so that during the analyses blocks can lose existing contacts and make new ones. Once every single block has been modelled both geometrically and mechanically, and the volume and surface forces are known, the time history of the block's displacements is determined by explicitly solving the differential equations of motion (Giordano et al. 2002). DEM was initially developed for problems of sliding and crashing rocks (Cundall 1971). DEM for the simulation of masonry (Lemos 2007) has been widely implemented through the commercial software packages UCEC and 3DEC (ITASCA 2011). DEM has been widely used for the simulation of dry (Smoljanović et al. 2013, 2015a; Bui et al. 2017; Ehresman et al. 2021; Pulatsu et al. 2021) or mortar joint (Ulrich et al. 2015; Adhikari and D'Ayala 2020; Pulatsu et al. 2020a) masonry constructions under cyclic load. Additionally, DEM techniques were considered to study the effects of size and position of openings on in-plane capacity of URM walls (Liu and Crewe 2020) and examine the influence of material parameters on the response of low bond strength masonry (Sarhosis and Sheng 2014; Sarhosis et al. 2015). DEM was used to reliably reproduce the results of experimental campaigns with masonry walls of different scale (Malomo et al. 2019b, a; Pulatsu et al. 2020a, 2021; Malomo and DeJong 2021). The DEM

approach has been also utilized to model the complex geometry of masonry arch and vaults (Tóth et al. 2009; Pulatsu et al. 2018; Fang et al. 2019; Kassotakis et al. 2021), masonry towers (Pulatsu et al. 2020c; Kassotakis et al. 2020; Ferrante et al. 2021b), as well as historical monuments under various loading types (Sarhosis et al. 2016, 2019a; Çaktı et al. 2016, 2020; Tavafi et al. 2019; Napolitano et al. 2019; Erdogmus et al. 2020; Mordanova and de Felice 2020). DEM generally neglects the deformability of the masonry elements, thus failing to properly account for masonry crushing, which can be, in some cases, crucial in the mechanical response of masonry structures (Sarhosis and Lemos 2018; D'Altri et al. 2020). To address this limitation, the finite-discrete element method proposed by Munjiza (2004) has been adopted for the simulation of masonry constructions (Smoljanović et al. 2015b, 2018; Miglietta et al. 2017; Pepe et al. 2020). The approach relies on a combination of FEM and DEM where discrete elements are meshed into finite elements with embedded crack elements that activate whenever the peak strength is reached. In this way, elastic deformation in the continuum is accounted by finite elements, while interaction, fracture, and fragmentation processes are modelled by discrete elements (Pepe et al. 2020). The robustness and effectiveness of the DEM to handle contact problems has allowed researchers to consider more elaborate discretization in order to assess the response of masonry at the micro level. In particular, Sarhosis & Lemos (2018) introduced an innovative discrete element modelling strategy in which masonry units and mortar joints were represented as an assemblage of densely packed discrete irregular deformable particles bonded together by zero thickness interface laws. The significant advantage of this approach was to model cracking as a real discontinuity among particles and not as a modification in the material properties. Similar modelling within the DEM has been adopted by more recent studies (Pulatsu et al. 2019, 2020d, b; Barattucci et al. 2020).

Extra clarification for the DEM with masonry structures is provided in Section 5.1, where the DEM was adopted for a numerical exercise on the quantification of damage evolution in masonry wallets.

Chapter 3
Case study: Novel monitoring approach to detect damage accumulation due to induced seismicity

In this Chapter the research on the development of a novel monitoring approach to detect damage accumulation due to induced seismicity for the case study monument, Fraeylemaborg, is presented. Section 3.1 provides an introduction to the investigated structure. The SHM system adopted is explained and any recent findings are reported in Section 3.2. A numerical model was calibrated based on experimental measurements and different loading scenarios were evaluated to identify the causation of the observed damage in the monuments (Section 3.3). The conclusions of the Chapter along with suggestions for future research are presented in Section 3.4.

3.1 Case study structure: Fraeylemaborg in Slochteren

Fraeylemaborg is a noble house built inside a manmade lake and is regarded as the most emblematic monument in the Groningen region (Figure 3-1). The structure is located in the middle of the town of Slochteren which gave its name to the largest gas field in the world upon its discovery in 1959. Gas extraction has caused small-magnitude shallow earthquakes during the last decade, damaging not only the residential inventory but also the historical structures in the area. For additional information regarding the seismic activity in the Groningen region refer to Section 2.1.

Fraeylemaborg is located in an estate of more than 0.23 km^2. The house dates back to the 14th century and reached its current form at the end of the 18th century. The structure was built in the 14th century as a stone house, a defensive dwelling, and grew into an impressive residence by an influential resident. After 1670 the two wings were added giving its current U-shaped form (Figure 3-2). Following a change of owners and a major restoration in 1972, Fraeylemaborg became a museum.

The estate includes a large park behind the main structure that is visited by more than 30,000 visitors per year. The complex is developed in the English style where the main house, the cowshed (now a restaurant) and the coach house (used as office, exhibition area and the museum shop) are in use by the museum administration to host events and exhibitions. The buildings are completed with 17th and 18th century sandstone garden ornaments in the park. The rooms reflect the character of mid-20th century, the era in which the home was last privately occupied. The Large Hall (Grote Zaal) is used for concerts and receptions, while the Small Hall (Kleine Zaal) is used as a wedding room (Figure 3-2).
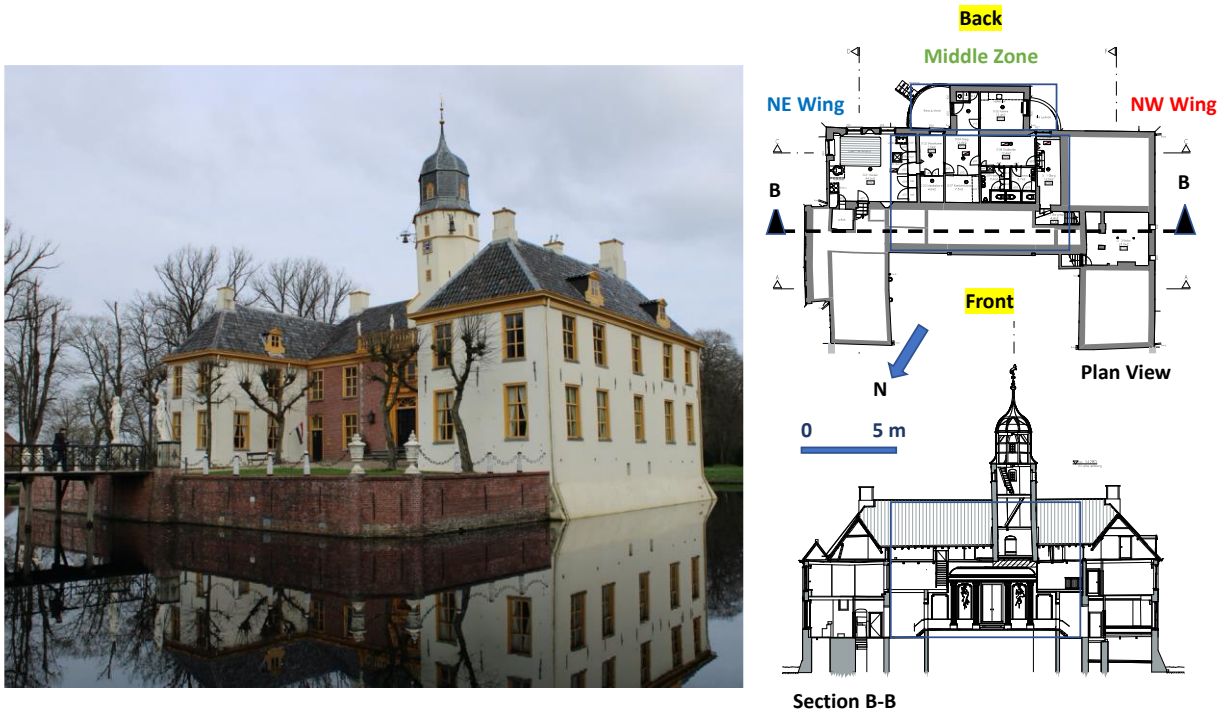
Figure 3-1. Left: Photograph of Fraeylemaborg (looking from West towards East); right: plan view (top) and section (bottom).

Figure 3-2: Construction phases of the building.

The structure is surrounded by a manmade lake with a water depth of approximately 1.5 m. The main structure has a U-shaped plan consisting of a partial basement, two floors, roof attic and a clock tower (Figure 3-1). The plan of the building is 28.6 m long and 22.6 m wide while the top of the tower reaches 20 m height. The construction material of the load bearing walls is clay brick with additions of stones in the corners, and metal ties and timber elements in the roof.

The brick-walls are solid and are of varying thickness (40 to 80 cm) in different parts of the structure and the bricks are laid in English bond pattern. Six bricks, retrieved during the previous restoration works, were subjected to compression tests. Their compressive strength was 2.5 MPa in average (Dais et al. 2019b), a value considerably lower than those obtained from recent experimental studies (Graziotti et al. 2017, 2019; Messali et al. 2018; Esposito et al. 2019) on clay bricks currently used in the construction in Groningen. These findings highlight the low capacity of the masonry walls of the structure and raise the question of seismic vulnerability.

The timber elements of the floors (Figure 3-3a-b) are poorly connected to each other and thus a diaphragmatic action is not ensured. Numerous steel anchors exist at various locations of the structure (Figure 3-3c-d) in order to connect the floors to the peripheral walls. The structural elements of the roof are timber beams transferring the loads to the peripheral walls.

(a)

(b)

(c)

(d)

Figure 3-3: Details from the timber floors (a-b) and steel anchors (c-d) around the monument.

The structure went through a serious renovation in 1973, including structural interventions in the retaining walls outside as well as in the floors and connection details inside the building. There is no written report from that period, but photographs of a personal archive have been

used to identify the nature of the structural interventions. As shown in Figure 3-4, bricks from damaged masonry walls were removed and replaced, however the cause of these damage are unknown. The foundations at the perimeter of the building are also made of brick masonry. They were repaired by using new bricks. A RC floor was added above the main entrance, right below the tower. Steel profiles were added at the base of the tower to stabilize it. Finally, all masonry retaining walls were repaired, missing parts were added, and new steel anchors were placed behind the walls.

(a)

(b)

(c)

(d)
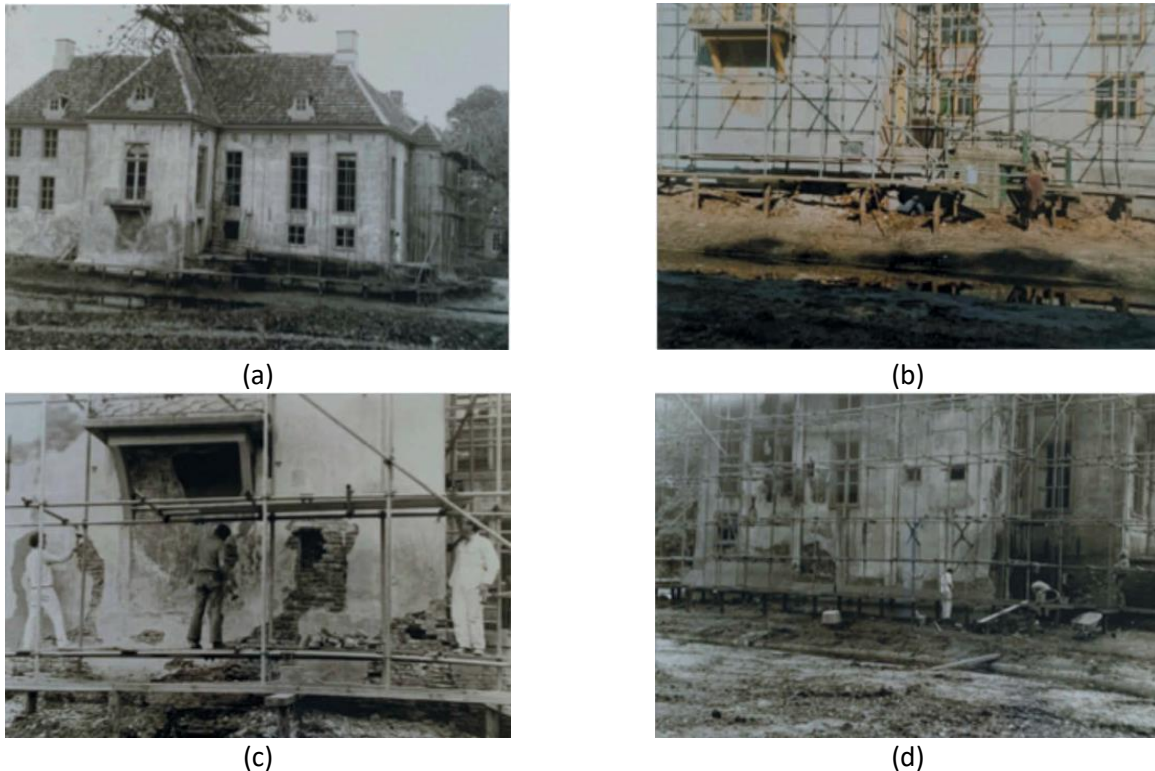
Figure 3-4: Photographs from the restoration works in 1973, (a) a general view from the building under restoration, (b) works at foundations along the perimeter, (c) mason works on the brick walls, and (d) works on the walls and the foundations.

The latest major restoration works took place at the end of 2015 and the beginning of 2017, mostly due to the damage caused by the induced earthquakes in the area. It is highlighted that in 2015 the onset of damage in the structure was recorded while before that no damage was observed. The restorations in 2015-2017 included some structural repair, that was mostly removal and replacement of bricks from the cracked parts of the load bearing walls. These parts were plastered afterwards.

It is noted that Fraeylemaborg was first visited for the sake of this study by the end of 2017. Therefore, at that moment no cracks could be detected along the structure since they had been repaired along the previous restoration courses. Nevertheless, visual inspections around the monument and its retaining walls revealed traces of damage. In particular, around the entrance of the basement located at front Northwest (NW) wing cracks were observed

along the stairs and the brickwalls while detachment was noticed between the staircase and the walls (Figure 3-5). The walls siting above the basement at the NW wing suffered damage from the 2015 earthquake while new cracks appeared after the 2018 seismic event as shown below. Moreover, cracks could be seen around the front retaining wall and detachment of the steel anchors was reported (Figure 3-6). Based on these findings it was obvious that soil movements around the basement and the retaining walls had taken place possibly leading to differential displacements/settlements. It was considered important to include these evidence of damage due to soil movements in the structural assessment of the monument in order to obtain a clear picture of the cause of cracks along the building. Further elaboration on the causation of damage in the structure and the investigation of different loading scenarios are presented in Section 3.2 and 3.3.

Figure 3-5: Signs of damage around the entrance of the basement located at the front NW wing.

Figure 3-6: Cracks along the front retaining wall (left) and detachment of the steel anchors (right).

There have been 24 earthquakes above magnitude ML 2.0 since 2012, in epicentral distances 3 to 23 km from the structure. Structural damage and cracks were observed in an increasing pace between 2014 and 2015. The 2015 restoration included interventions on the front façade of the structure where extensive cracks had been formed (Figure 3-7), while the cracks on the internal walls of the structure were repaired during the 2017 restoration. These cracks were mostly vertical and partly horizontal and diagonal, concentrated on the NW wing as well as on the front façade of the middle zone (see Figure 3-1) of the structure. The cracks were as wide as a couple of millimetres in some regions. The plaster was removed and the damaged bricks were replaced during the 2015 restoration.
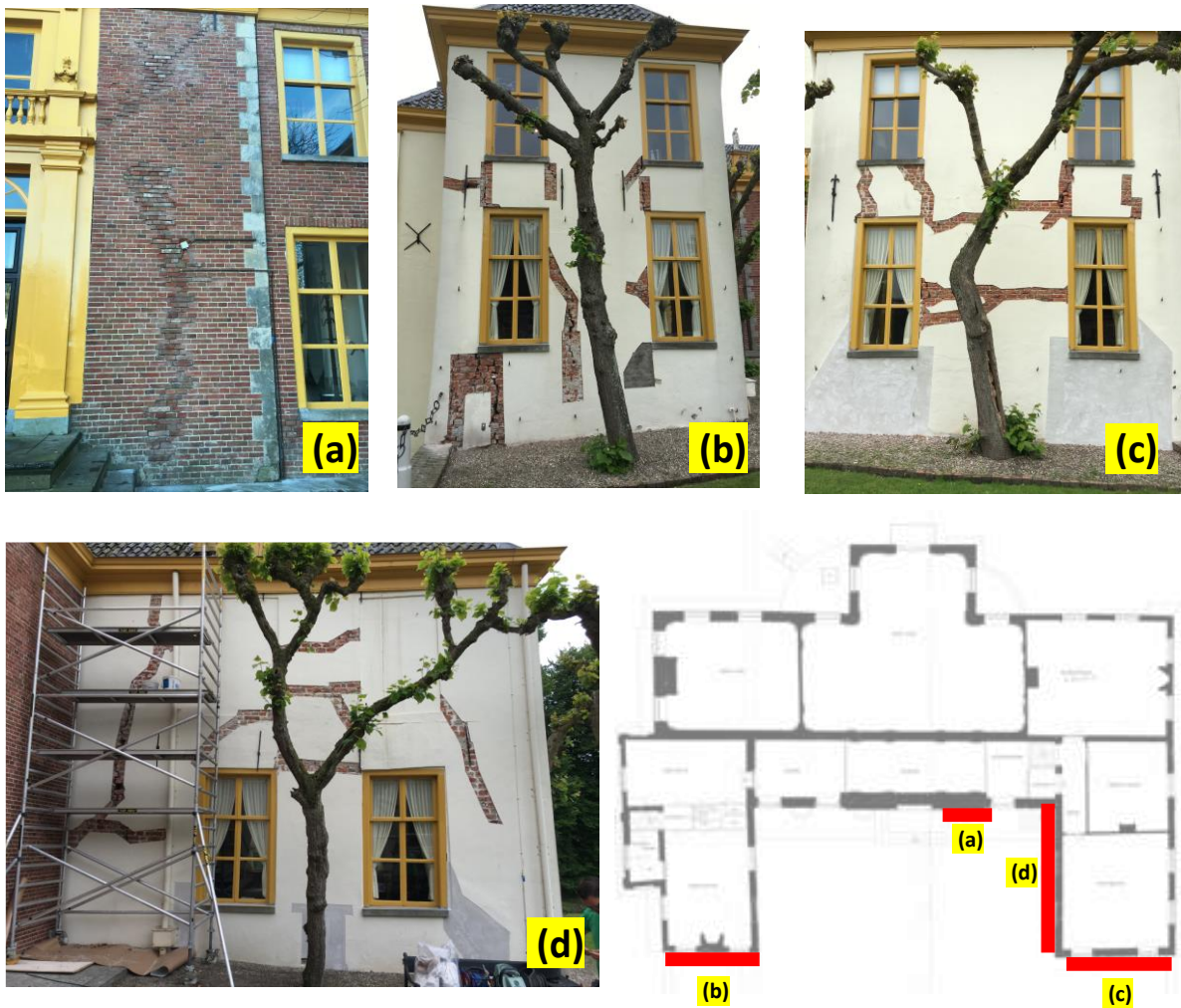
Figure 3-7. Cracks registered during the 2015 restoration; the red lines on the right-corner plan view denote external walls subjected to damage. For the dimensions of the building refer to Figure 3-1.

Although the increased seismic activity went hand in hand with increased number of cracks, the shape and location of latter did not resemble earthquake-related cracks. Most of them were in vertical direction, with a larger width close to the base and smaller widths in higher elevation, while diagonal X-shaped cracks, the standard sign of in-plane masonry response to lateral earthquake loading, were not observed in the structure. The existing cracks reminded more cracks caused by soil movements rather than by seismic load. After the end of restoration the manifestation of new cracks in the summer of 2018 in the most problematic part of the structure, i.e. the façades of the NW wing (Figure 3-8), was a puzzlement given the relative limited seismic activity in the respective period. However, after monitoring results have been combined together with finite element analyses and observations in the field, it was possible to reach a plausible explanation for the old (prior to 2015 and in 2015) and the new (summer 2018) damage in the building, as discussed further in Section 3.2 and 3.3.
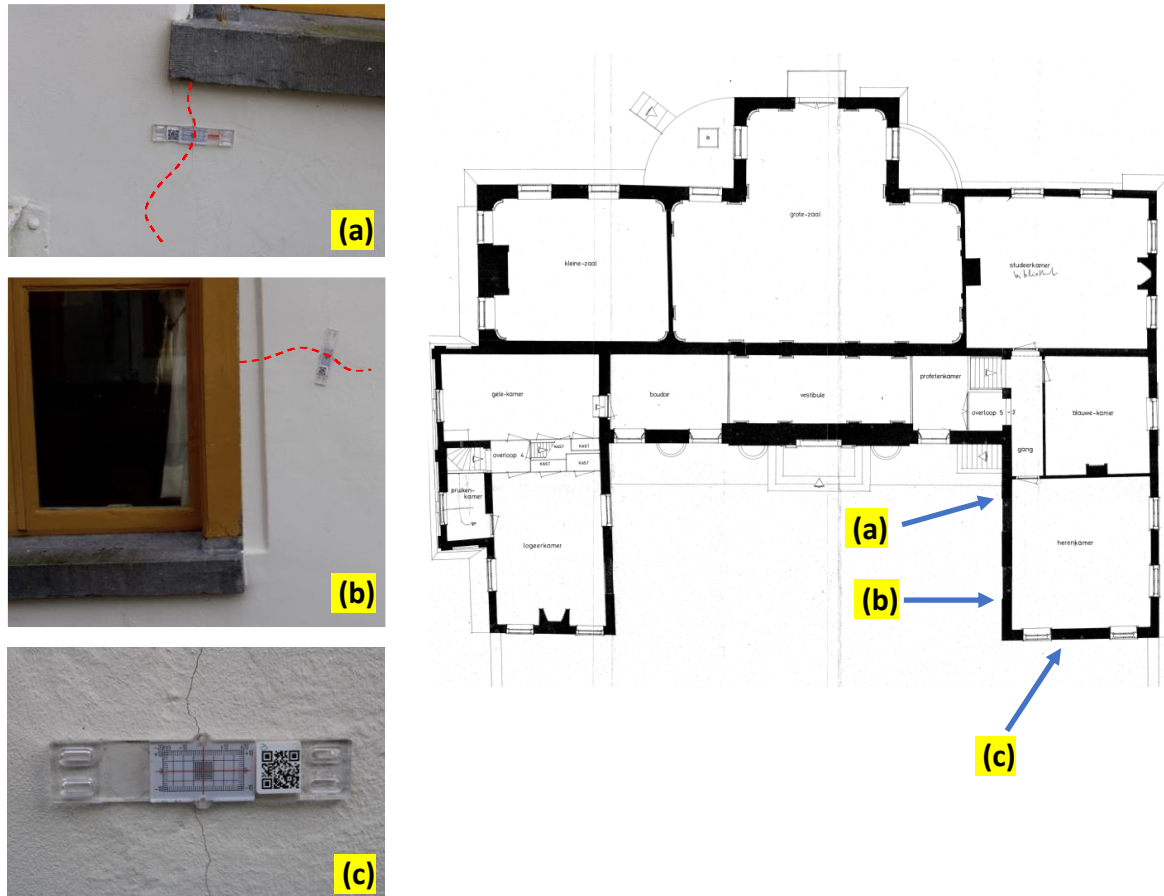
Figure 3-8. Minor cracks appeared in August 2018 at the façades of the NW wing of Fraeylemaborg.

Fraeylemaborg is being monitored by a tiltmeter at the base since mid-2014, with five 3-axes accelerometers since March 2018, and by analogue crack-rulers since January 2019. Ground water data is available starting from mid-2015 while meteorological data is available for more than 10 years. Supplementary to the monitoring activities at Fraeylemaborg (see Section 3.2 for details), soil investigations were also conducted (see Figure 3-14). Eight boreholes were drilled around the structure, right outside of the structure and inside the manmade lake after it was drained (Fugro 2018). The boreholes were opened up to 32 m depth at 6 locations and up to 12 m depth at two locations. The upper layers (the first 2-6 m) consist of multiple layers of clay, silty loam, impermeable pot-clay ("potklei" in Dutch) and sand, while a uniform sand layer exists after 6-8 m depth. Most of the cone penetration test (CPT) values are below 2 MPa and partly below 4 MPa in the first 5 m. During the soil investigations, the foundation at the perimetry of the structure were inspected measuring its dimensions and depth but no information was collected about the existence or condition of any piles.

3.2 Structural health monitoring at Fraeylemaborg and recent findings

The SHM scheme applied at Fraeylemaborg comprises various information channels, i.e. accelerometers, a tiltmeter, analogue crack rulers, meteorological data as well as ground

water level measurements. The simultaneous use of multiple channels of information is necessitated by the nature of the induced earthquakes as explained so that reliable conclusions are drawn. The methodology followed is often based on excluding some of the possible causes and focusing on the most plausible scenarios with the help of multiple sensing data.

Studies have highlighted the of effect of the environmental conditions, such as temperature, humidity, wind etc, on the response of the structure (Ramos et al. 2010a; Kita et al. 2019; Stephenson and D'Ayala 2019). Taking this into consideration, the outside ambient temperature, the rain rate as well as the ground water level are monitored for the case study to reliably capture any effects of the environmental conditions on the structural response of the monument.

The distribution and mounting of accelerometers and the tiltmeter can be seen in Figure 3-9. The accelerometers used in the seismic SHM system are force-balance type with ultra-low noise levels of 130 ng/Hz$^{0.5}$. The bandwidth of the sensors is 0.1-120 Hz, with a range of +-2 g. More information can be found in the technical sheets of the producer[2]. The analogue sensors are connected to a 16-channel digitizer. The data are collected into a computer on site and continuously mirrored in a network mapped hard-drive on a virtual machine. Some example data from a recent ML 3.2 earthquake in May 2019 (Bal and Smyrou 2019a) and the accelerometer and tiltmeter data from 2018 August (Bal and Smyrou 2019b) are digitally available.

Although electronic displacement sensors (potentiometers) were designed for monitoring existing or potential cracks, their installation was avoided due to aesthetic concerns. Instead, crack rulers (see Figure 3-8 for a clear close-up photo) were placed in January 2019 and monitoring takes place by regularly photographing these crack rulers since then. No movement has been detected since January 2019.

There is a meteorological station in Slochteren the data of which are available online by KNMI. The station data consist of temperature, humidity and rain rate. The station is in less than a kilometre distance from the site.

The ground water level is very well monitored in the region due to significance for the agricultural activities. There are several monitoring wells around the site, but the one that is 600 m south of the site, was particularly useful. The level of the ground water is being monitored since April 2015 in this well with 2 hours intervals.

---

[2]   See   product   technical   specifications   at:
http://www.teknikdestek.com.tr/tr/urun/13/sensebox702x-703x-?category_id=5

The tiltmeter is an accelerometer-based sensor that detects the inclination of the two perpendicular axes in respect to the vertical axis, by making use of the gravitational acceleration in the vertical direction. The tiltmeter at the basement records in high and low sampling rates. The high sampling rate is 0.01 sec (100 Hz) while the low sampling rate is 15 sec. More data on the technical specifications of the tiltmeter can be found on the technical documentation of the producer (StabiAlert 2019).
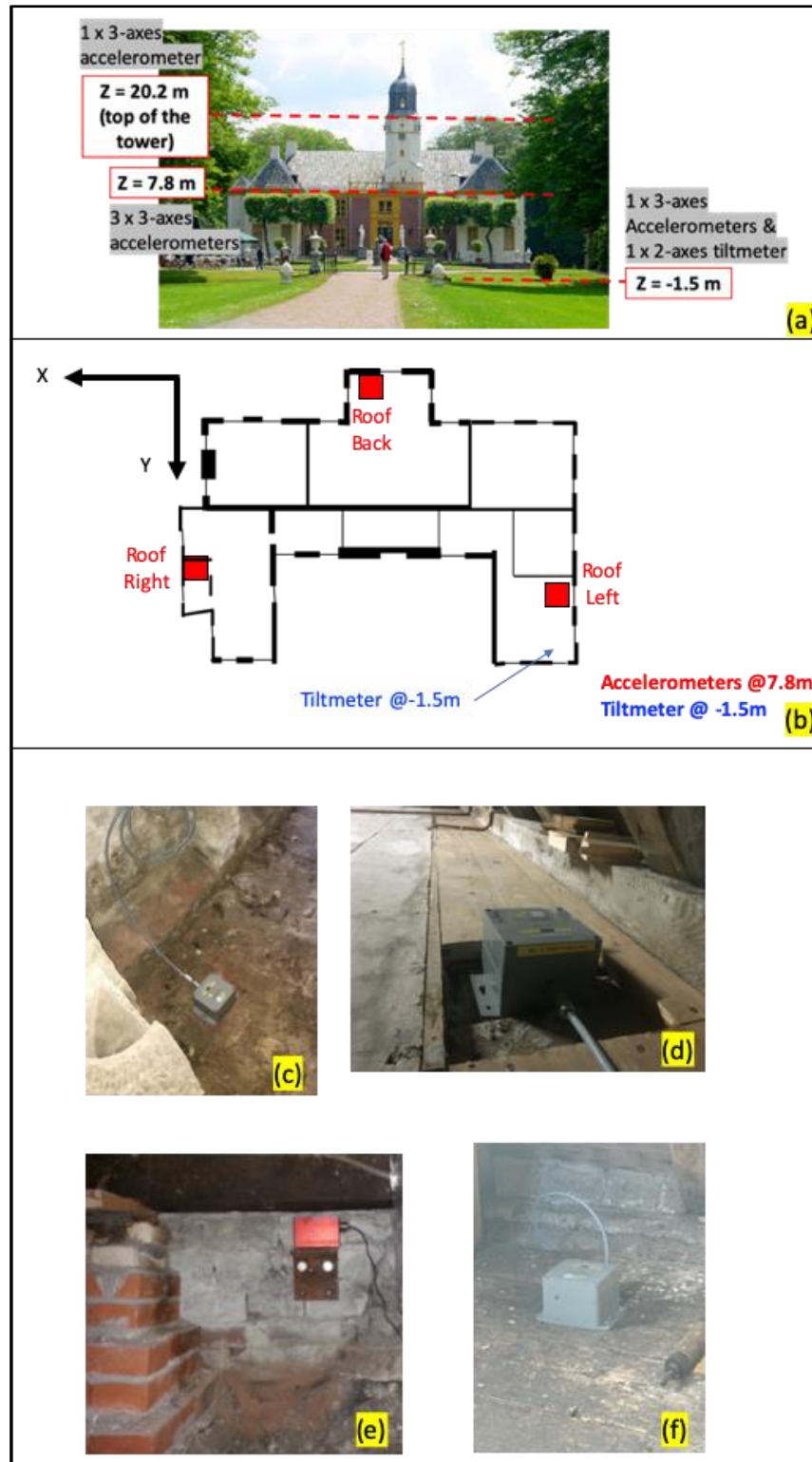
Figure 3-9. (a) Elevation of the sensor locations; (b) sign convention for the accelerometers and the tiltmeter sensor; (c) accelerometer at the basement; (d) accelerometer on top of the bearing walls at 7.8 m elevation; (e) tiltmeter at the basement; and (f) accelerometer on the tower floor.

The tiltmeter data since 2014 are given in Figure 3-10. It should be noted that there was a local repair work in January 2015 and in December 2015 that has shifted the tilt values around both axes. The data jumps around the restoration periods are because of this. In overall, it is

evident since the beginning of the monitoring (sometime mid-2014) until the end of the structural restoration and repair (beginning of 2016) that the tilt values systematically increased with the exception of the major structural restoration period that took place right after the Hellum Earthquake of ML 3.1 that occurred just 3 km from the structure. Furthermore, the significant earthquakes (magnitude above 3) recorded during the monitoring period do not present evident effects on the overall plot, however, this may be because the changes in tilt during or after these earthquakes are not big enough and remain concealed by the temporal changes and noise of the tilt measurements. Thus, as explained further later, the evaluation of the structural response to each event needs to be done individually. Finally, it is also observed (Figure 3-10) that the tilt around Y axis is stabilized around a virtual baseline after the restoration and repair works, as only fluctuations for the seasonal changes can be observed after that date. On the contrary, the tilt around X axis exhibits an increasing trend since the end of the restoration and repair works.
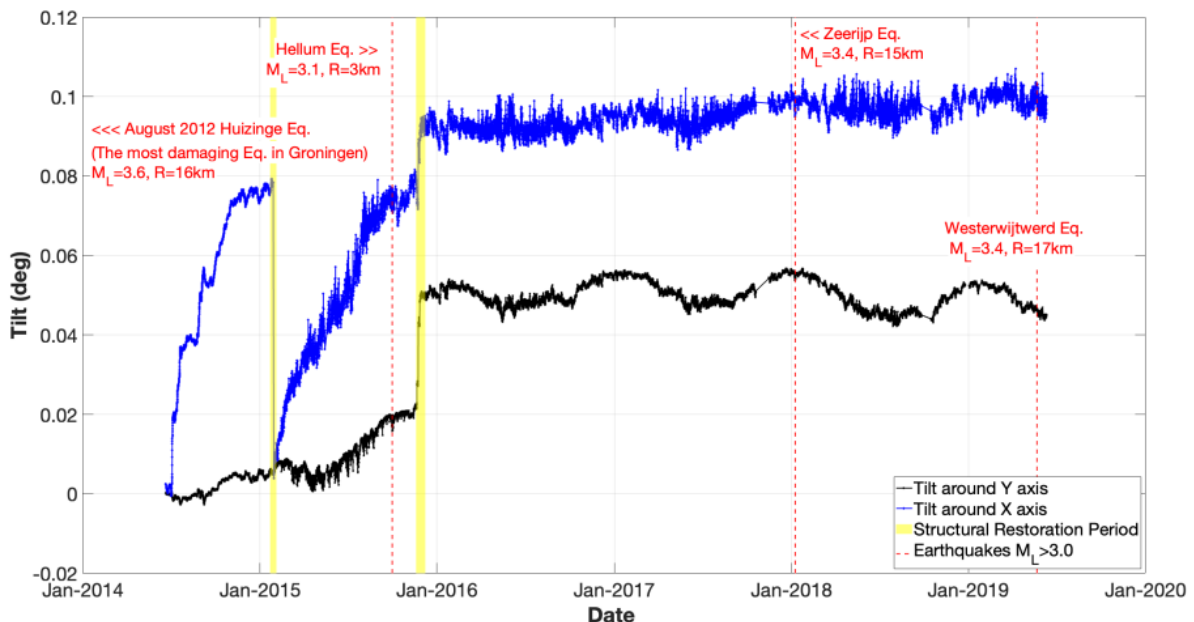
Figure 3-10. Tiltmeter measurements since 2014, together with significant earthquakes and restoration periods.

Although an earthquake event usually precedes the appearance or deterioration of cracks, it is difficult to establish such an association from the overall plot of tilts. However, focusing on event-based results, better explanations can be obtained that highlight too the difference in monitoring when small induced earthquakes are concerned. Two earthquakes were selected: the 8th of August 2018 Appingedam Earthquake with magnitude ML 1.9 and an epicentral distance of 12 km from the site in the North-East of the Groningen gas field, and the 22nd of May 2019 Westerwijtwerd Earthquake of ML 3.4 in an epicentral distance of 16 km from the site in the NW of the gas field. After the former some damage was reported (see Figure 3-8), while the day of the latter, as well as a week before and a week after, the crack rulers were

photographed, with no movement or additional crack being detected. In order to discuss the different methodologies needed in seismic SHM in case of induced earthquakes, these two earthquake events constitute a good comparative example as explained below in detail.

The 2018 Appingedam Earthquake (ML 1.9) was recorded by the accelerometers in the building (the full dataset is available online in open source by Bal and Smyrou (2019b)). The time-histories at the basement, at the roof level, on the two wings of the structure as well as at the tower are given in Figure 3-11. The presented time-histories are baseline corrected and bandpass Butterworth filtered between 0.1-20 Hz. The motion was detected by the sensors although the maximum accelerations do not exceed 1 cm/sec^2 (0.001 g). The tower amplified the input motion approximately 3 times, while the structure itself amplified it 2 times, both still remaining well below the horizontal acceleration levels that would normally cause any cracks.
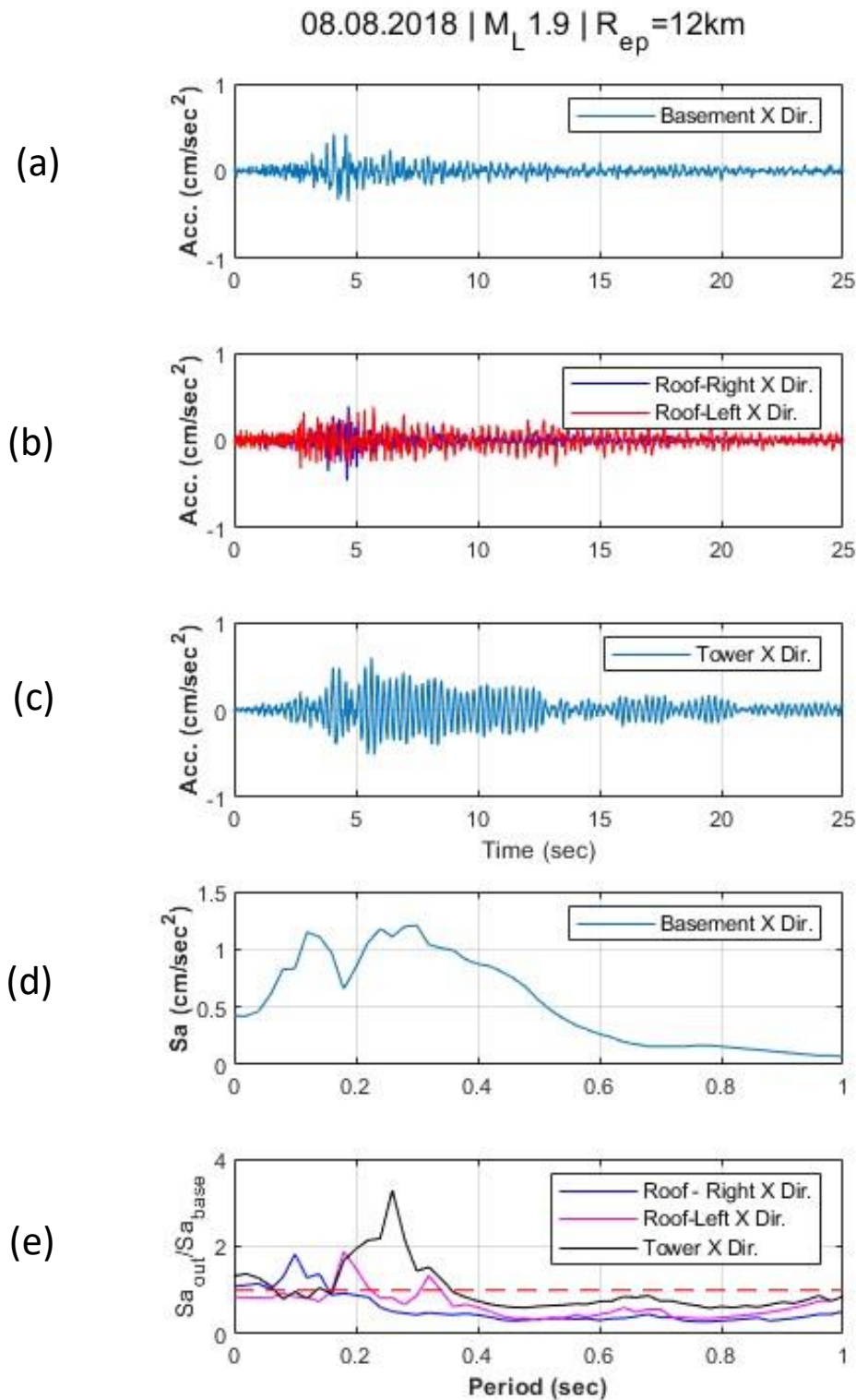
Figure 3-11: For the 8th of August 2018 Appingedam Earthquake of ML 1.9 in epicentral distance of 12 km are presented: acceleration time-histories (Acc.) in the X direction for the sensors at (a) the basement level, (b) the roof level (right and left side of the structure, shown in Figure 3-9b), and (c) the tower, (d) 5% damped spectral acceleration (Sa) as obtained from the sensor at the basement in the X direction, and (e) transfer functions (spectral acceleration on the structure (Sa_out) divided by the spectral acceleration at the base (Sa_base)).

During the seismic excitation the fluctuation of tilt recorded was rather insignificant. Thus, only examining real-time tilt data would not offer an insight into the degree of damage that

actually led to the formation of new cracks. In order to better understand the cause of damage, low sampling rate tiltmeter data have also been examined (Figure 3-12). For the last 15 days before the earthquake the daily temperature cycles oscillate on average around a baseline but the motion builds up in a way in the three days following the earthquake. From the 4th to 15th day after the earthquake tilt values in both axes increase significantly jumping to a new baseline. Furthermore, the range of angles in daily temperature changes also decreases causing the tilt values to fluctuate in a narrower band. A new baseline of tilt values indirectly signifies a certain level of plastic deformation, indicating that damage took place.
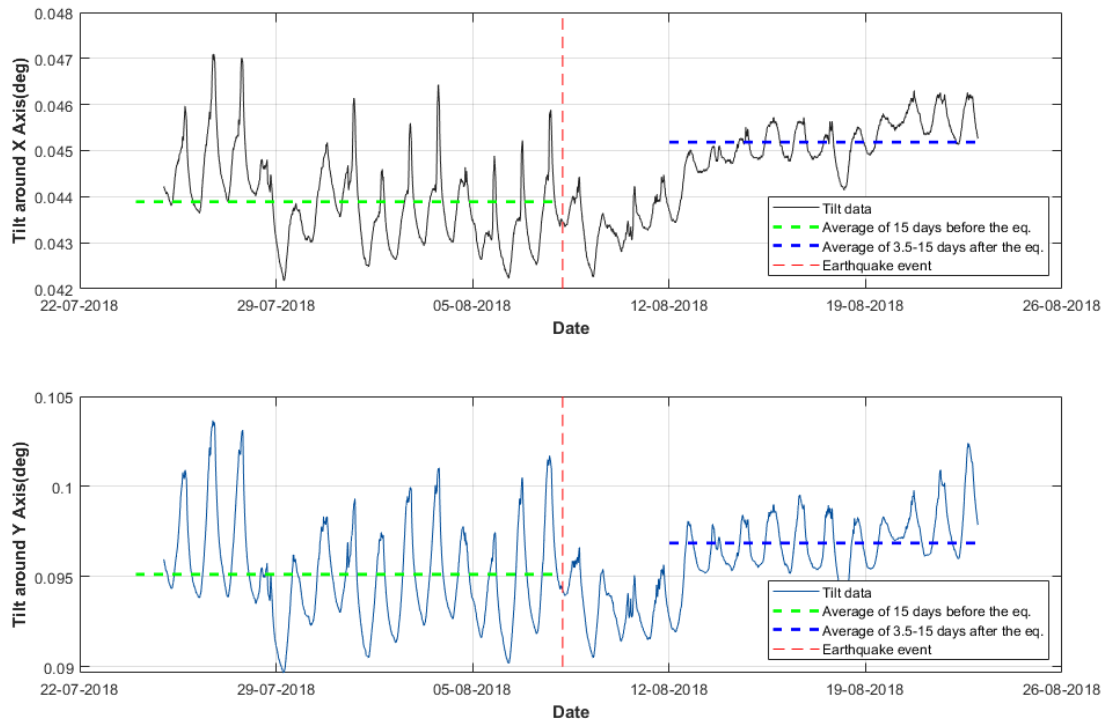
Figure 3-12. Low sampling rate tiltmeter data 15 days before and 15 days after the earthquake of 08.08.2018 Appingedam (ML 1.9).

It is naturally expected that the tilt values are highly influenced by the temperature changes. In order to decouple the temperature effects from the measurements, plots in Figure 3-13 were prepared where the 30-day period (15 days before and 15 days after the earthquake) have been plotted against the measured ambient temperature. Furthermore, in order to understand the progress of the tilt values, the exact same 30-day periods are also plotted for one and two years before (2017 and 2016 respectively) for the same period of the year. These data are used to understand the relevance of the observed damage with the 2018 Appingedam Earthquake of ML 1.9. The first and striking observation is that the temperatures in 2018 were much higher than the prior two years, which led to a different correlation between the ambient temperature and the tilt values in the range of 25 ºC to 30 ºC. Furthermore, it was shown that the relationship between the tilt values and the temperature is within an expected range 15 days before the earthquake (green lines) and 3 days following

the earthquake (orange lines), while 4th to 15th days after the earthquake a different relationship is observed (red lines), where the tilt values increase independent of the temperature values. In brief, it is concluded that the change of baseline in the tilt values is not related to the ambient temperature.
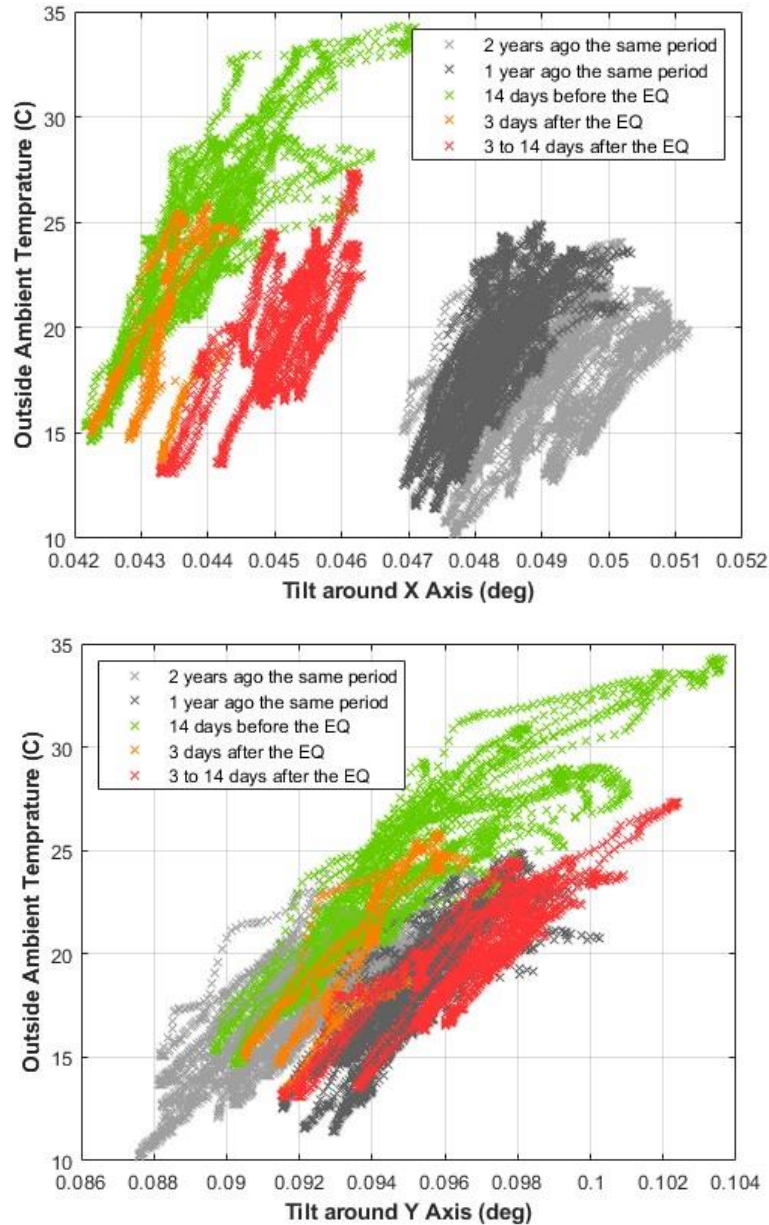
Figure 3-13: Tilt angles recorded +-15 days from the earthquake and last two years before around X (top) and Y axis (bottom) (the axis are shown in Figure 3-9b).

The tiltmeter data, in combination with the accelerometers data from 8th of August 2018 event, indicate that the foundation of the NW wing and the soil beneath have played an important role in the cracks that appeared in August 2018. It is difficult to explain the exact contribution of soil-related parameters since fundamental data, such as the potential existence and the situation of piles, are unknown. Speculation about possible explanations regarding the soil effects are provided below.

As mentioned before, soil properties of the site were determined by using 8 boreholes and CPT tests (see Figure 3-14). The borehole right next to the NW wing, where the damage concentration occurred, revealed a different soil profile in the first 10 m from that in the Northeast (NE) side. The clay/pot-clay layers are more prevailing for the NW side while the sand layers were more extensive for the first 3 m at the NE (Figure 3-14).
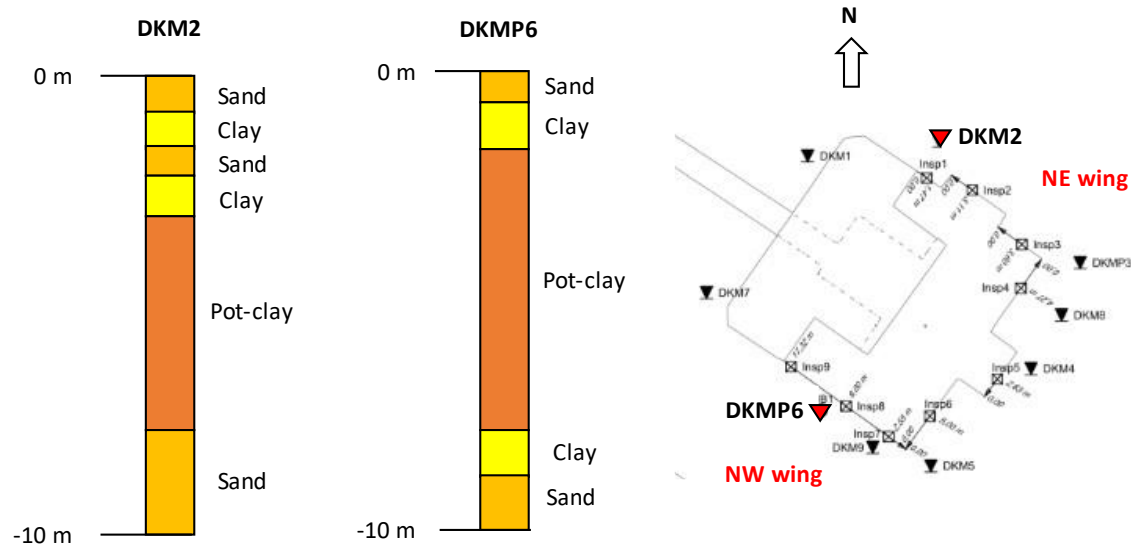
Figure 3-14: Soil stratigraphy for depth 0-10 m as obtained from boreholes for the NW (DKM2) and NE (DKMP6) wing.

The shrinking or/and the expansive behaviour of the clay layers may be responsible for the structural cracks considering that clay soils can be responsive to moist cycles. Certain clay types are expansive soils, and early studies have identified potential problems for the foundations sitting on such soils (Popescu 1986; Nelson and Miller 1992). When shrinking or swelling, certain clay soils apply a level of pressure to the environment, including structural foundations (Basma et al. 1995). Specific clay types can also crack due to lack of water, up to some metres of depth (Morris et al. 1992), decreasing the bearing capacity substantially. There are several regions with similar soils in the Netherlands (Bouma 1980).

Based on the borehole findings, part of the NW wing of the structure is sitting on pot-clay layers of several metres thick, a highly impermeable and stiff clay material. Swelling tests conducted on pot-clay layers in the region[3] show that expansion can be limited to less than 1% in volume but considerable shrinking is possible when the layers dry out completely. Due to the high impermeability water is hindered and thus the expansion is limited. Shrinkage, however, can still be an issue for pot-clay.

---

[3] Personnal communication with Onno Dijkstra from Fugro in Groningen.

Another possible explanation may be related to the piles under the foundation. Due to the weak soil conditions in the region, it is almost impossible to construct any structure without piles. It is thus expected that Fraeylemaborg, being a relatively heavy structure as compared to the modern ones, would also be sitting on some sort of pile grid. Because of the historical identity of the building access to certain parts is not allowed, thus the existence of the piles is not confirmed. Nevertheless, the common construction practice in the region dictates that some wooden piles must exist under the foundations. If this is the case, especially the old wooden piles need to be under water for protection from deterioration. It is known that drought causes adverse effects on wooden piles in historical buildings.

The scenarios for relating the soil response to structural cracks given above are based on water conditions. One may consider that the structure is surrounded by a manmade lake thus the soil layers are always under water. However this is not granted since the dominating layers are highly impermeable clays.Thus, the soil layers right beneath the foundations may still be dry in case of drought.

The ground water movement in the same days was also investigated. The rain rate is plotted in Figure 3-15 together with the ground water measurements, in order to decouple possible ground water raise due to the earthquake action. The ground water is monitored in the monitoring well with approximately 4 m total depth. Due to the monitoring setup, the sensors used and the sampling rate (2 hours), the monitoring data can provide only slow movements of ground water and not the changes during the seconds of the earthquake motion.

Figure 3-15 reveals a very dry period from mid-March to mid-August in 2018, reported as a disastrous period for the farmers in the region due to the extremely dry soil. It was also witnessed in soil drilling works that the clay layers were hard and dry due to lack of rain for a very long period. As seen in Figure 3-15 the start of the rainy period coincides with the earthquake (in fact, a couple of days later). When other rainy periods in the data are examined, tiltmeter data are found mostly insensitive to the rain. Furthermore, the out-of-the-ordinary movement (i.e. change in tilt baseline) in the tiltmeter data starts right after the earthquake, proving that the movement is related to the earthquake motion too.
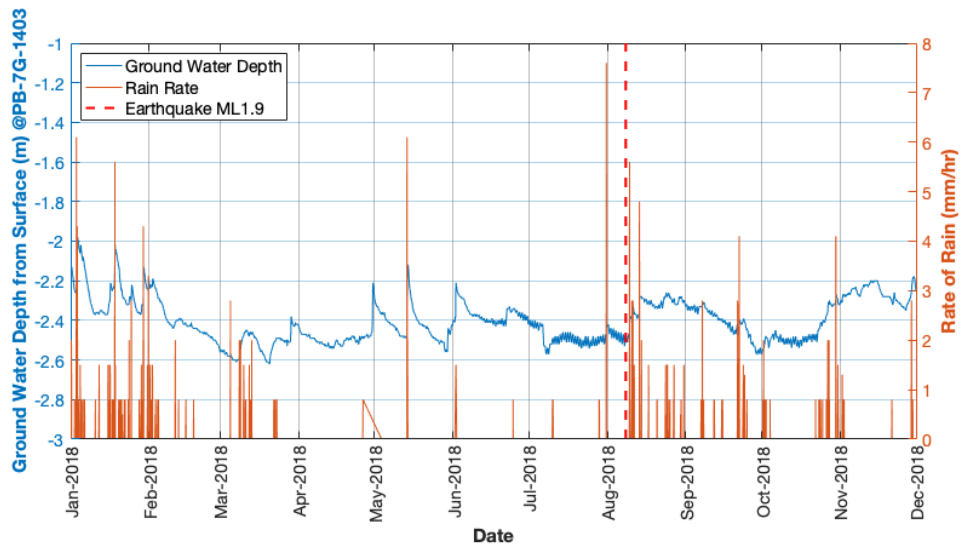
Figure 3-15. Ground water depth from the surface and the rate of rain in 2018 in the monitoring well 600 m south of the site.

Based on all available data, the most plausible scenario for explaining the damage in August 2018 is studied. The structure has light floors and a light timber roof, while the bearing walls are relatively thick. In-plane cracks would not be expected in this structure during such small earthquakes. One possible explanation is that the soil parameters such as shrinking of water-sensitive soil layers and/or response of piles, in combination with a small distant earthquake, caused settlements and/or increased the stress levels on foundations. In other words, the soil effects might have superimposed with the earthquake motion and caused the small cracks. Nonlinear finite element analyses have also been run for supporting this scenario, as presented further in Section 3.3.

If the monitoring results constituted merely by acceleration measurements, one could argue that the structure should have had much more cracks after the 22nd of May 2019 earthquake of ML 3.4 since the accelerations at the base, on the structure and at the tower were much higher than the respective of the event in the 8th of August 2018 (Bal and Smyrou 2019a). Note that the horizontal PGA at the basement was 0.004 g and the maximum absolute horizontal acceleration at the tower was recorded as 0.03 g. Although still very small, these accelerations are larger more than an order of magnitude as compared to the acceleration levels of the August 2018 event (Figure 3-16). A detailed check on the photographs of the crack rulers showed that no significant movement took place during this earthquake. When the tilt data of 15 days before and 15 days after were examined, no change of tilt baseline or any other out-of-the-ordinary movement was observed. Had the seismic SHM system relied only on the accelerometer data, the fact that August 2018 earthquake caused damage while the stronger in terms of acceleration May 2019 earthquake caused no damage would be inexplicable.
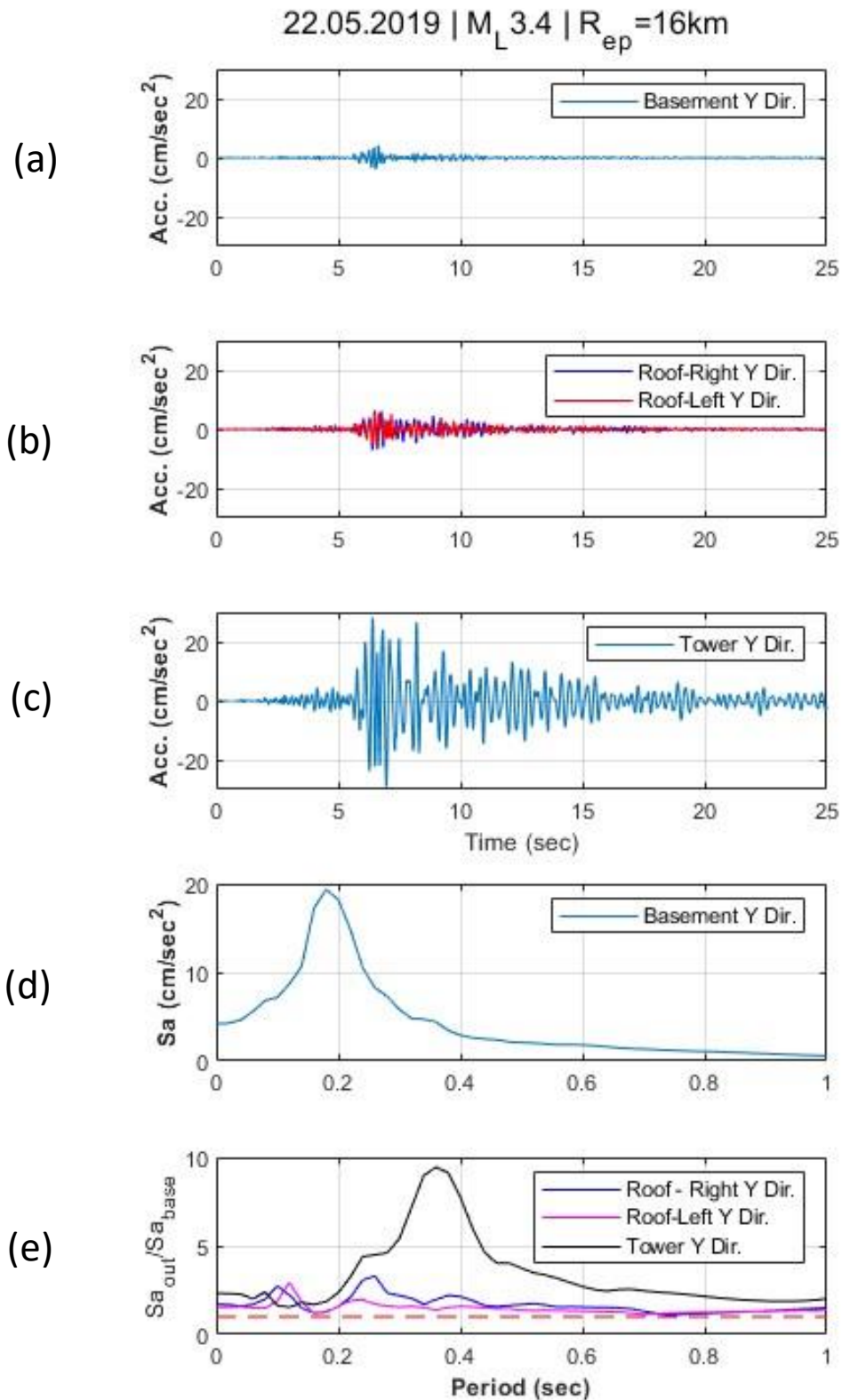
Figure 3-16: For the 22nd of May 2019 Westerwijtwerd Earthquake of ML 3.4 in epicentral distance of 16 km are presented: acceleration time-histories (Acc.) in the Y direction for the sensors at (a) the basement level, (b) the roof level (right and left side of the structure, shown in Figure 3-9b), and (c) the tower, (d) 5% damped spectral acceleration (Sa) as obtained from the sensor at the basement in the Y direction, and (e) transfer functions (spectral acceleration on the structure (Sa_{out}) divided by the spectral acceleration at the base (Sa_{base})).

3.3 Damage scenario, field measurements and numerical model

In order to better understand the damage mechanism of the structure, a numerical model of Fraeylemaborg was developed and calibrated based on in situ measurements and possible damage scenarios were examined. A nonlinear three-dimensional FEM (Figure 3-17) based on the macro-modelling approach was simulated in the commercial code ABAQUS (ABAQUS 2013). The complex geometry of the monument was precisely incorporated in the numerical model while special care was given to realistically reproduce its structural elements.
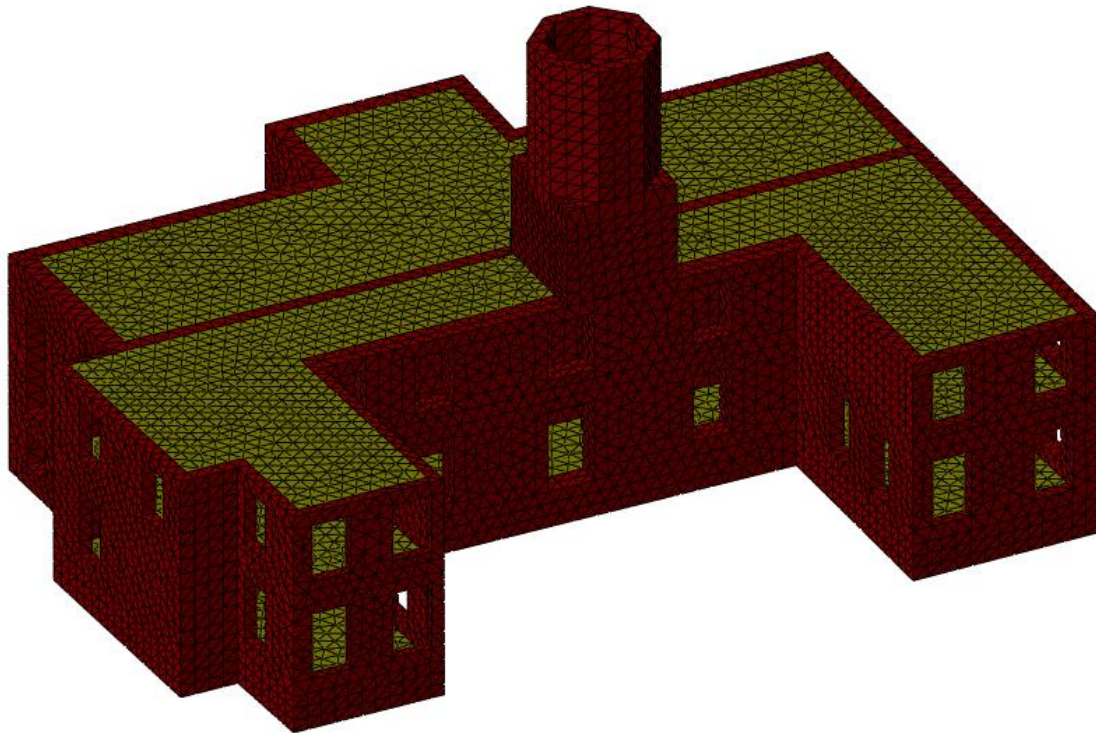
Figure 3-17: The three-dimensional numerical model of Fraeylemaborg (clay brick walls in maroon colour, wooden floor in yellow).

The structural members of the monument, i.e. masonry walls and timber slabs, were simulated with 3D solid continuum elements. The timber slab elements are characterized by the lack of proper connections to each other and to the walls (Figure 3-3a-b), and thus there is absence of diaphragmatic action. This behaviour was incorporated in the model by accounting for rather low stiffness for the slabs. Given the fact that no damage has been observed in the timber elements, the timber slabs were modelled as linear elastic.

The masonry walls were simulated with the Concrete Damaged Plasticity (CDP) model which uses concepts of isotropic damaged elasticity in combination with isotropic tensile and compressive plasticity (ABAQUS 2013). This nonlinear constitutive law is suitable for the analysis of quasi-brittle materials, such as masonry, subjected to cyclic loads and to reproduce the main failure mechanisms of masonry, that is cracking in tension and crushing

in compression. This is a common numerical approach that has been used extensively to simulate historical masonry structures (Milani et al. 2018; Valente and Milani 2019; D'Altri et al. 2020; Dais et al. 2021b). The CDP constitutive law assumes different yield strength in tension and compression and stiffness degradation is incorporated in the post-yield phase. The degradation of the elastic stiffness is characterized by two damage variables, d_c and d_t for compression and tension respectively, and their evolution is a function of the plastic strains (Table 3-2). If E_0 is the initial (undamaged) elastic stiffness of the material, the stress-strain ($\sigma - \varepsilon$) relations under uniaxial tension and compression loading are, respectively:

$$\sigma_t = (1 - d_t)\, E_0\, (\varepsilon_t - \varepsilon_t^{pl}) \tag{3.1}$$

$$\sigma_c = (1 - d_c)\, E_0\, (\varepsilon_c - \varepsilon_c^{pl}) \tag{3.2}$$

where ε^{pl} is equivalent plastic strain; the subscripts 't' and 'c' denote tension and compression respectively. The damage variables can take values from zero, representing the undamaged material, to one, which represents total loss of strength. In the developed model the damage variables reach up to 0.9 in order to allow for limited residual strength. Under uniaxial load the stress-strain response follows a linear elastic relationship until the value of the failure stress, σ_{t0} and σ_{c0} respectively for tension and compression, is reached (Figure 3-18). The value of compressive and tensile strength for the brick walls were chosen equal to 1 MPa and 0.075 MPa respectively (Table 3-2). The failure stress corresponds to the onset of micro-cracking. Beyond the failure stress the formation of micro-cracks is represented macroscopically with a softening stress-strain response, which induces strain localization. The CDP model assumes non-associated potential plastic flow. The flow potential used for this model is the Drucker-Prager hyperbolic function (ABAQUS 2013). The parameters to define the flow potential, yield surface and viscosity are given in

Table 3-3. In particular, σ_{b0}/σ_{c0} is the ratio of initial equibiaxial compressive yield stress to initial uniaxial compressive yield stress; the default value 1.16 was used. The parameter K_c denotes the ratio of the second stress invariant on the tensile meridian to that on the compressive meridian for the yield function with default value 0.666 (Figure 3-19). This value distorts the Drucker-Prager surface rendering it closer to the Mohr-Coulomb criterion. The dilation angle was assumed as 10° in accordance to experimental (van der Pluijm et al. 2000) and numerical studies (Valente and Milani 2019; D'Altri et al. 2020; Dais et al. 2021b). The default flow potential eccentricity was implemented, that is 0.1, which implies that the material has almost the same dilation angle over a wide range of confining pressure stress values. Material models exhibiting softening behaviour and stiffness degradation often lead to severe convergence difficulties in implicit analysis programs. A common technique to overcome some of these convergence difficulties is the use of a visco-plastic regularization of the constitutive equations. In this study the viscosity parameter was 0.0005.
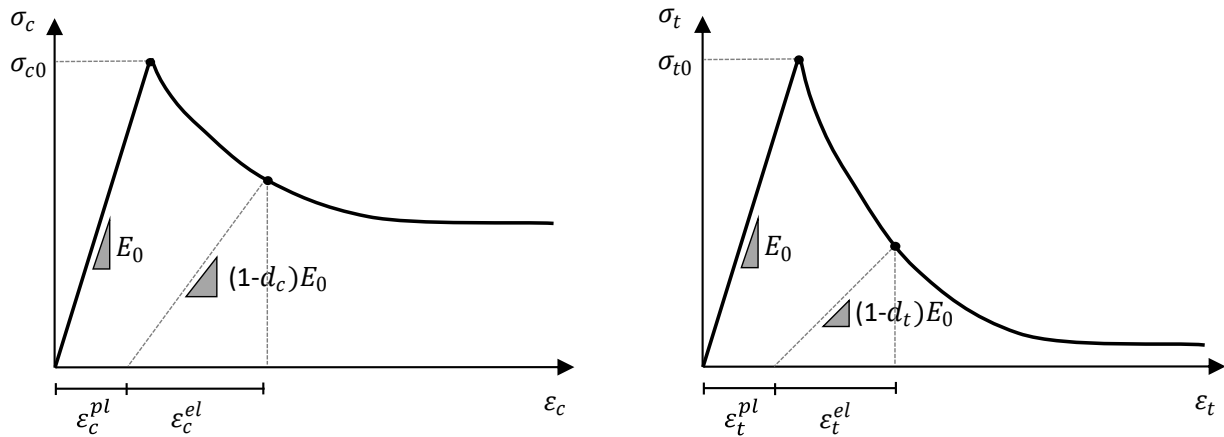
Figure 3-18: Schematic representation of the response of Concrete Damaged Plasticity to uniaxial loading in compression (left) and tension (right).
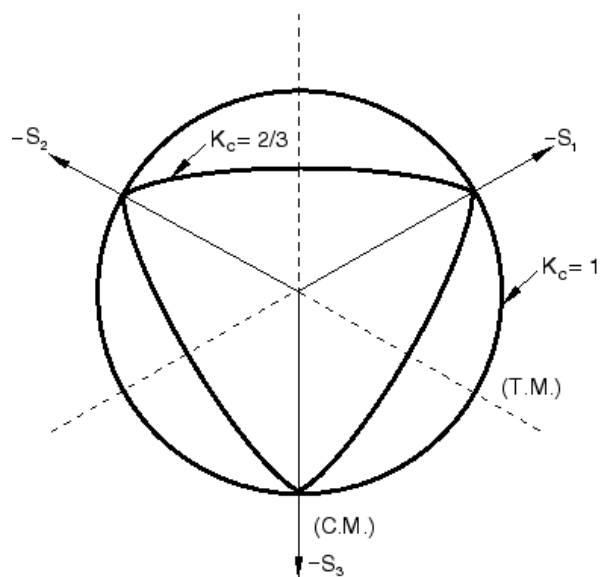
Figure 3-19: Yield surfaces in the deviatoric plane, corresponding to different values of K$_c$ (ABAQUS 2013). C.M.: compressive meridian. T.M.: tensile meridian.

Table 3-1: Summary of mechanical properties adopted in the numerical model.

Material	Density [kg/m^3]	Young's modulus [MPa]	Poisson's ratio [-]
Masonry	2,000	1,000	0.2
Timber	800	2,000	0.3

Table 3-2: Nonlinear uniaxial response of the Concrete Damaged Plasticity in compression (left) and tension (right).

Compression			Tension		
ε_c^{pl}	σ_c [MPa]	d_c	ε_t^{pl}	σ_t [MPa]	d_t
0	1	0	0	0.075	0
0.01	0.8	0.9	0.005	0.005	0.9

Table 3-3: The main parameters for the Concrete Damaged Plasticity model.

Dilatation angle [°]	Eccentricity	σ_{b0}/σ_{c0}	K_c	Viscosity
10	0.1	1.16	0.666	0.0005

The elastic properties of the model were calibrated against ambient vibration tests that took place on site. For the ambient vibration measurements extra accelerometers were used in addition to the permanent monitoring system installed on the structure. In particular, five extra sensors were placed at the roof level to reproduce better local phenomena along the structure due to the lack of rigid slabs (Figure 3-20). The ambient vibration measurements were processed with ARTEMIS software (ARTEMIS 2016). Operational modal analysis was carried out by means of Frequency Domain Decomposition technique (Brincker et al. 2001)enabling the acquisition of the natural frequencies (Figure 3-21) and the corresponding mode shapes, directly from the raw measured time series data of the structure under natural conditions.
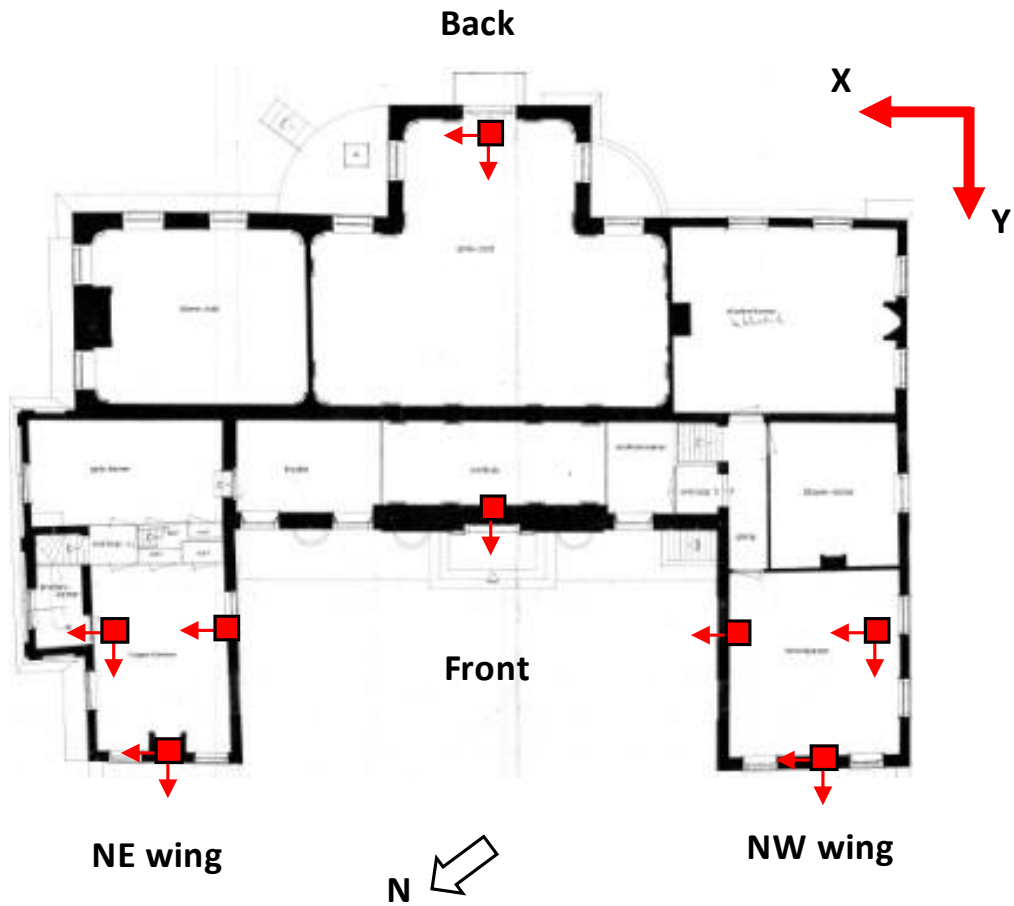
Figure 3-20: The position of the accelerometers along the roof level (7.8 m height) used for the ambient vibration measurements. The horizontal recording axes are denoted with red arrows for each sensor.
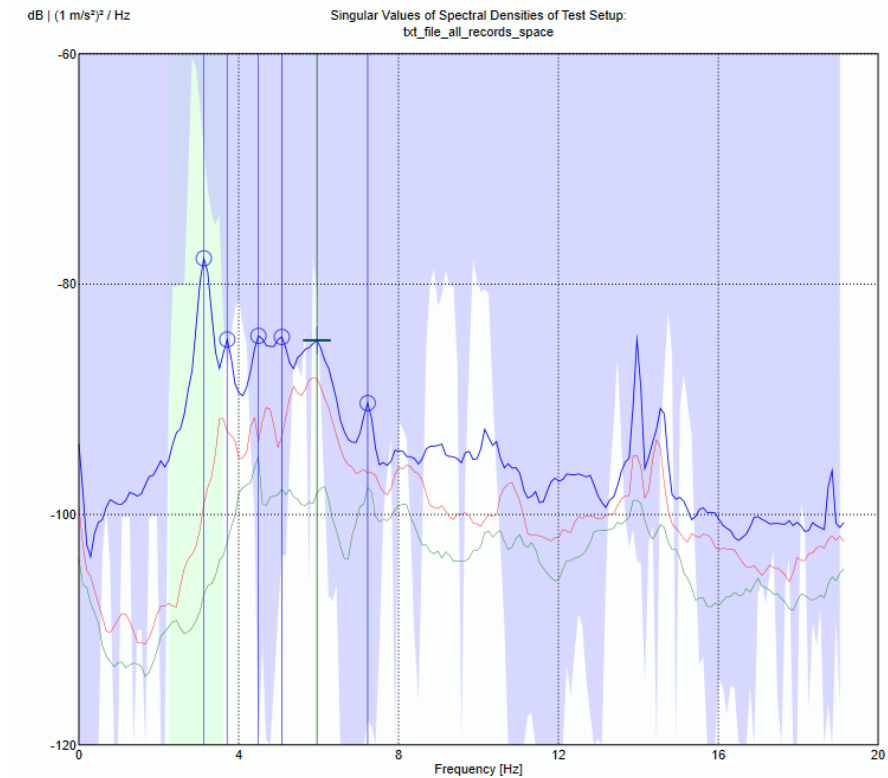
Figure 3-21: The first six natural frequencies of the model as obtained with ARTEMIS software by means of Frequency Domain Decomposition.

The numerical model was then calibrated to match the experimentally obtained natural periods and mode shapes. The modulus of elasticity was derived as 1,000 MPa and 2,000 MPa for masonry walls and timber slabs respectively (Table 3-1). It is noted that values in the range of 5,000 MPa for modulus of elasticity were estimated from experimental campaigns on Groningen resembling masonry wall specimens (Graziotti et al. 2017; Messali et al. 2020; Kallioras et al. 2020). It is justifiable that a historical structure will be characterized by lower properties due to material degradation and lack of modern construction practices. Moreover, while a common value of approximately 12,500 MPa is assigned as modulus of elasticity for timber elements, theobtained values were significantly lower. Nevertheless, this low value, i.e. 2,000 MPa, calculated from the model calibration seems suitable since the lack of diaphragm action leads to flexible response of the timber slabs.

In particular, good agreement was attained in terms of natural periods from the calibrated ABAQUS model and the ARTEMIS modal analysis (Figure 3-22); the first eigen-period of the structure obtained numerically and experimentally was 0.35 s and 0.32 s respectively. In particular, the first mode is translational primarily along the Y axis of the structure while the X component is negligible, and thus the latter is not presented in Figure 3-23. The displacement values corresponding to the deformed shape of the first mode were normalized with respect to the maximum value of displacement obtained at the roof level. As shown in Figure 3-23, satisfactory match between field measurements (ARTEMIS) and numerical

analysis (ABAQUS) was achieved. The first mode shape from the calibrated numerical model is displayed in Figure 3-24. It is evident that the tower does not follow the main structure in the Y direction, while in X direction its displacements are negligible (Figure 3-24). Such a response is explained by considering the connection of the tower to the rest of the structure; only two sides of the tower are directly connected to the adjacent walls of the structure while the other two sides simply sit on the wooden floor.
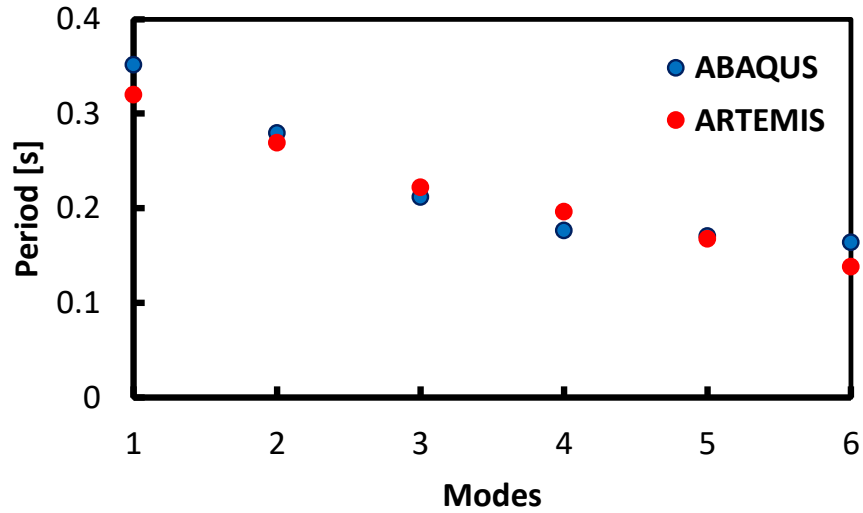
Figure 3-22: Comparison of the natural periods for the first six modes as calculated with ABAQUS and ARTEMIS software.
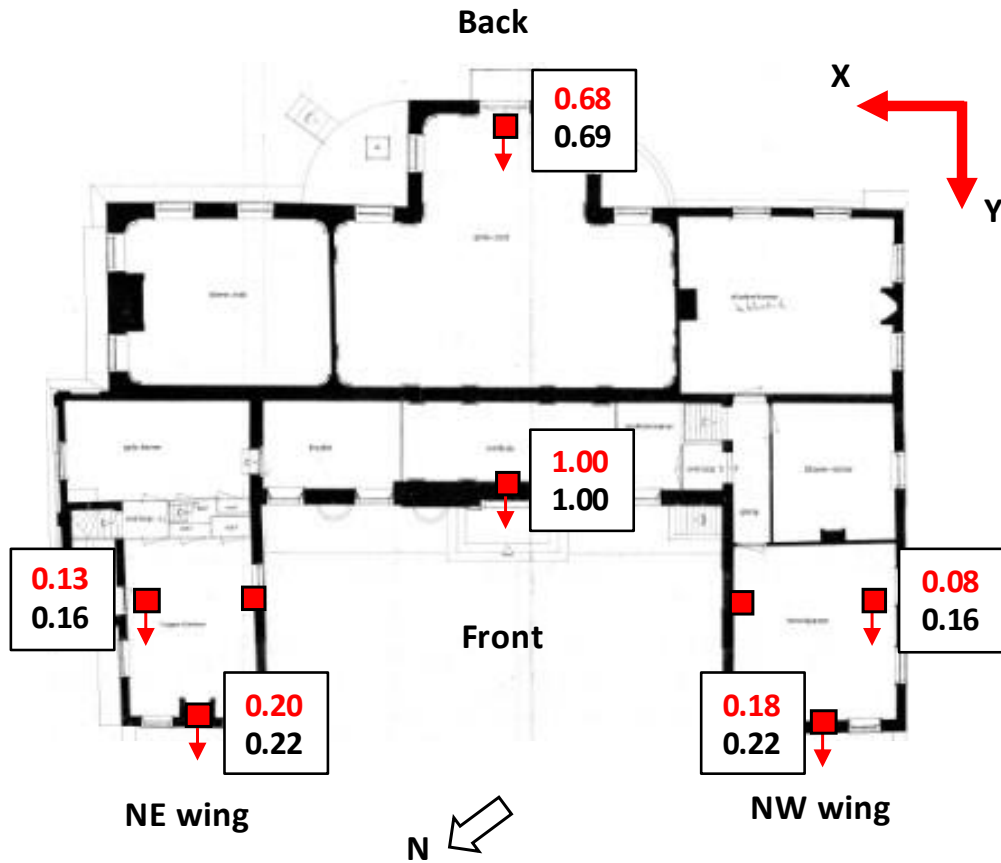
Figure 3-23: Normalised modal displacements in Y direction for the first mode shape derived from the ambient vibration measurements (red) and the numerical modal analysis (black).
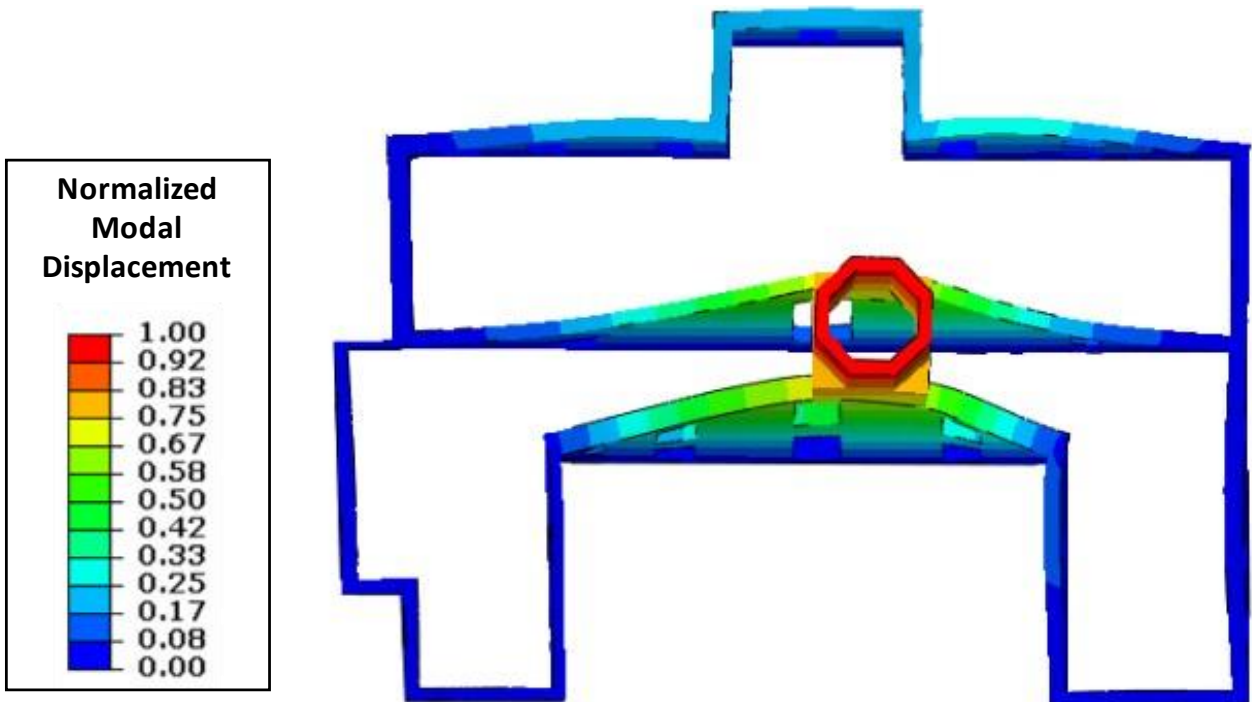
Figure 3-24: The first mode shape from the calibrated numerical model. The contours demonstrate the normalized modal displacement.

Upon calibration, the nonlinear numerical model was subjected to different scenarios to see if a correlation can be established between the analytical findings and the past damage. As explained in Section 3.1, there are findings (i.e. crack patterns, concentration of damage) in the structure that support the occurrence of soil settlement in the NW wing, thus a settlement profile was applied in that wing analytically. In particular, a 0 to 0.5 cm vertical settlement is applied on the NW wing (i.e. 0.5 cm at the edge, 0 cm at the connection with the main zone) and the response of the structure is shown in terms of tensile maximum principal stresses (Figure 3-25). In case of the scenario of only-settlement, although some of the cracks prior to the renovation and repair in 2015 (Figure 3-7) were captured, the results were not satisfactory in overall. Match between the damage distribution and the observed damage was not achieved. When an earthquake load is applied in conjunction with the settlement, the location of the cracks in the NW wing and at the front façade of the main zone were captured successfully (see the comparison in Figure 3-25). The earthquake load is applied as incremental lateral equivalent static force proportionally to the mass from 0 to 0.08 g. The earthquake load is applied in the short direction of the structure because this was the dominant direction of the 2015 Hellum Earthquake of ML 3.1 (i.e. the direction perpendicular to the travel path). Hellum Earthquake was reported as the reason of the damage in the structure in 2015 and the crack photographs presented in Figure 3-7 belong to a period right after that earthquake.

The point of this numerical exercise is to show the distribution of cracks derived after the combination of two actions. In more detail, when settlements are applied, concertation of damage is observed at the wall shown in Figure 3-7d and beneath the tower. After the superposition of seismic load, further damage appears at the walls as also shown in Figure 3-7a, b and c.
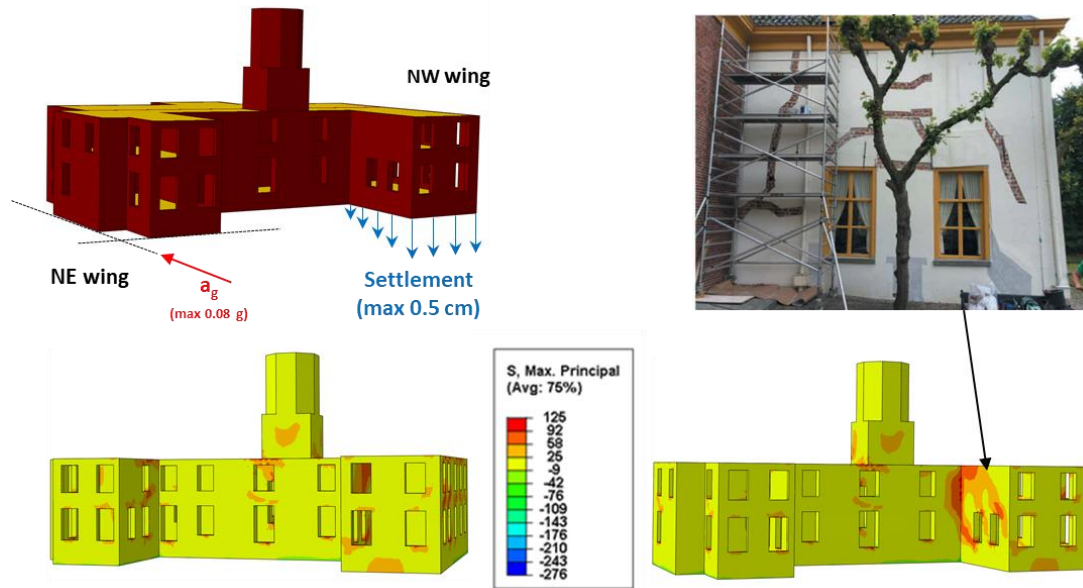
Figure 3-25: Distribution of maximum principal stresses from the nonlinear static analyses in the scenario of 0.5 cm maximum vertical settlement at the NW wing superposed with lateral earthquake equivalent static load of 0.08 g and comparison with the observed damage.

3.4 Conclusions

The increasing number of deep underground energy exploitation projects around the world is associated with induced earthquakes, which are usually small in magnitude and recursive. In most cases, they occur in areas without prior seismic activity, meaning that the building stock is inherently vulnerable to seismic loads.

Due to their effects on the built environment, induced earthquakes in the Groningen gas field in the north Netherlands have triggered intense research on the response of URM to induced earthquakes. An extended seismic monitoring network has also been established. Although there are more than 2,000 historically registered buildings in the region, only a single building is being monitored by using standard seismic SHM techniques, that is the monument used as case study here. The monitoring results of that historical building, Fraeylemaborg in Slochteren, were presented here to create a basis of discussion on what would be the main differences when monitoring historical buildings in case of induced earthquakes.

Two earthquakes and the relevant monitoring data were used to better explain the goals of this work. First, a small and distant earthquake with reported slight damage was investigated by using accelerometer, tiltmeter, soil investigation, ground water monitoring and meteorological data. Second, a recent earthquake with much higher recorded accelerations in the structure, but without any reported damage was studied. The seemingly controversial nature of the damage effect of these two cases was discussed by using supporting monitoring data and FEM analysis. Although conclusions on causes of damage cannot be of absolute

certainty, that is normal in induced seismicity, plausible scenarios were proposed and discussed in detail. In this way, it was shown that measurements that are based on a single source of sensors, such as only tiltmeters or only accelerometers, would not be enough to provide reasonable explanations. Furthermore, it was also shown that the meteorological data play a critical role in developing damage scenarios in case of induced seismicity. From the above it is evident that the potential to employ continuous, real-time and automatic SHM system is beneficial for the detection of causes of damage but also for the early detection of a potentially dangerous situation for the structure and its occupants. There are several available choices to use today, and the best measurement strategy provided by the monitoring system is crucial. It is anticipated that a compromise between the need of information, complexity of the measuring system and the related costs needs to be made.

In brief, Fraeylemaborg was used here as an exemplary case to exhibit that the effects of induced small-magnitude earthquakes may not be immediately evident or may be overshadowed or concealed with other causes. Furthermore, it was also shown that in case of induced small earthquakes, seemingly misleading monitoring results may have meaning, thus even the data that seem irrelevant should be examined with an open-minded approach. It was highlighted that, in case of damage to historical masonry due to small recursive earthquakes, combination of techniques and tailor-made solutions are needed.

As a side note, and relevant to the climate adaptation problems in the world in recent years, it was shown that the changing climate ultimately can play a role in structural damage, even to the structures that have survived hundreds of years.

Based on all available data, the damage at Fraeylemaborg were studied. It was concluded that the in-plane cracks would not be expected in this structure during such small earthquakes. One explanation could be that the soil parameters, such as shrinking of water-sensitive soil layers and/or response of piles, in combination with a small distant earthquake, caused settlements and/or increased the stress levels on foundations. The soil effects might have superimposed with the earthquake effects causing small cracks.

In the future, the work in Fraeylemaborg will continue to better understand the nature of the damage. As part of that effort, a nonlinear numerical model with a properly modelled soil box is prepared and will be run to investigate further the soil-structure interaction phenomena associated with induced seismicity events. Furthermore, in order to better capture the ground water movements during the earthquake, two monitoring wells are planned to be installed exactly on the site, right outside of the artificial lake. These monitoring spots will provide pore pressure data and ground water height data with 100 Hz sampling.

Chapter 4
Vision-based techniques to detect damage accumulation in masonry structures

As shown in Chapter 3, SHM can provide a reliable assessment of structures. Nevertheless, it is not possible to install such systems to every structure. Therefore, currently the structural condition of structures is still predominantly visually inspected which is a laborious, costly and subjective process. Cracks provide a clear manifestation of the inflicted damage in a structure and thus crack monitoring is deemed beneficial. With developments in computer vision, there is an opportunity to use digital images to automate the visual inspection process. In order to enhance the process of visual inspection of infrastructure, vision-based techniques to monitor crack propagation were introduced allowing a reliable assessment of damage accumulation. An artificial intelligence solution was introduced for the automatic detection of cracks on masonry structures (Section 4.1) and novel invisible markers for monitoring cracks were additionally developed (Section 4.2).

4.1 Automatic crack classification and segmentation on masonry surfaces using convolutional neural networks and transfer learning

The different steps considered to utilize CNNs to automatically detect cracks on photographs of masonry structures are demonstrated in Figure 4-1. Firstly, the dataset is prepared by collecting data (i.e. images from masonry structures) from different sources and consequently annotating the data by labelling any cracks on the images. The dataset is then split in training and validation sets. In the process of training artificial intelligence networks, different neural network architectures and loss functions are evaluated. This process is iterative, that is each network is trained for different configurations (learning rate, batch size, etc.), a procedure that is called hyperparameter tuning. The different architecture and parameter configurations are evaluated based on suitable performance metrics. Once the segmentation error on the validation set is small, the best performing network is used and the correctness of the segmentations on different images is further verified. At that stage it is being checked whether the network performs poorly on specific data types. Once the performance of the trained network is verified, it is further tested on real world data. In the case that the performance is poor, the further expansion of the training dataset and the consideration of additional neural networks need to be investigated. Further clarification on these steps is provided in the following Sections.

| **1. Prepare dataset** |
| Collect data |
| Annotate data |
| Split dataset (training/validation) |

| **2. Train AI network** |
| Evaluate different neural network architectures and loss functions |
| Select suitable performance metrics |
| Hyperparameter tuning (learning rate, batch size etc) |

| **3. Evaluate performance of trained AI network** |
| Verify that error is adequately low on validation set |
| Evaluate segmentations on different images |
| Check if the network performs poorly on specific data types |

| **4. Test performance of trained AI network on real cases** |
| Decide whether is accurate |
| If performance is poor consider expanding the training dataset (Step1.) |
| and/or testing additional neural network architectures (Step 2.) |

Figure 4-1: Flowchart of the followed procedure for the implementation of neural networks.

In order to address the lack of data in the literature, a dataset with photographs from masonry structures was produced containing complex backgrounds and various crack types and sizes (Section 4.1.1). Since for masonry structures little work has been done for crack detection it was deemed beneficial to train networks both for patch classification (Section 4.1.2) and pixel-level segmentation (Section 4.1.3) in order to examine the efficacy of different techniques and broadcast the feasibility of deep learning methods on crack detection for masonry surfaces. Furthermore, a comparative study was performed where a segmentation network trained on masonry images was tested on photographs with cracks taken from concrete surfaces in order to evaluate the ability of CNN to generalize over different materials (Section 4.1.4). Conclusions from the work on the automatic crack detection with the use of artificial intelligence algorithms are elucidated in Section 4.1.5.

4.1.1 Dataset preparation

In order to address the lack of data in the literature, a dataset with photographs from masonry structures is produced containing complex backgrounds and various crack types and sizes. Deep learning networks are data-driven techniques, thus they heavily rely on the quality and amount of data (Zhang et al. 2020). Before preparing the masonry dataset for this study, an

extensive literature review is performed to spot good and bad practices when collecting data for crack detection. It is highlighted that the goal of training a network is to enhance its ability to generalize when fed with diverse data.

Special care is frequently paid when collecting data so that photographs are taken in a homogeneous way keeping constant conditions, such as distance, angle etc. (Dorafshan et al. 2018; Li et al. 2019; Mei et al. 2020). Moreover, it is common for datasets for crack detection to be custom-made and manually pre-processed to exclude noisy background and for images to be carefully selected to focus on the cracks (Mei et al. 2020). Nevertheless, a common criticism over developed deep learning methods is that they attain remarkable results when tested on monotonous backgrounds, but their accuracy severely drops when deployed on images with complex backgrounds. Choi & Cha (2020) observed that when a CNN trained on images of monotonous background and subsequently tested on a more complex dataset the performance drastically decreased; precision dropped from 0.874 to 0.231. Several studies have emphasized the necessity for more complex datasets (Zhang et al. 2019; Alipour et al. 2019; Tabernik et al. 2020). The issue they raised is particularly important for the context of this study since masonry surfaces consist of brick or stone materials, possibly with mortar joints, with several complex objects around, such as windows, doors, ornaments, labels, lamps, cables, vegetation etc. which can be characterized as noise for the crack detection process. Other materials, such as concrete or asphalt that crack detection methods have been widely investigated, provide a relatively smooth and flat surface. On the contrary, masonry surface is usually rough and uneven since mortar might protrude around the bricks or some gaps might exist in the interface between mortar joints and brick units. These anomalies might create shadows in the photographs especially when the photographs are taken with acute angles, causing the network to falsely consider these regions as cracks. Moreover, cracks are usually covered with dust or colour-paints. Therefore, it is deemed that a database as generic as possible would lead to higher chances of developing a tool that is able to perform accurately in real cases.

Taking all these into consideration a masonry dataset is prepared for this study. Photographs were collected from different sources. Various images of masonry walls containing cracks were obtained from the Internet. Additionally, photographs were taken from different masonry buildings in the Groningen region, the Netherlands. In fact, in order to simulate the scenario where different users will contribute in the data collection by taking photographs with devices of different characteristics, various members of our research group were asked to photograph cracks from masonry walls with their phones or digital single-lens reflex (DSLR) cameras after providing them with simple guidelines. It is noted that photographs from masonry surfaces with (Figure 4-2a-b) and without (Figure 4-2c-d) cracks were taken under similar conditions (angle, distance, etc.) in order to enrich further the non-crack class.
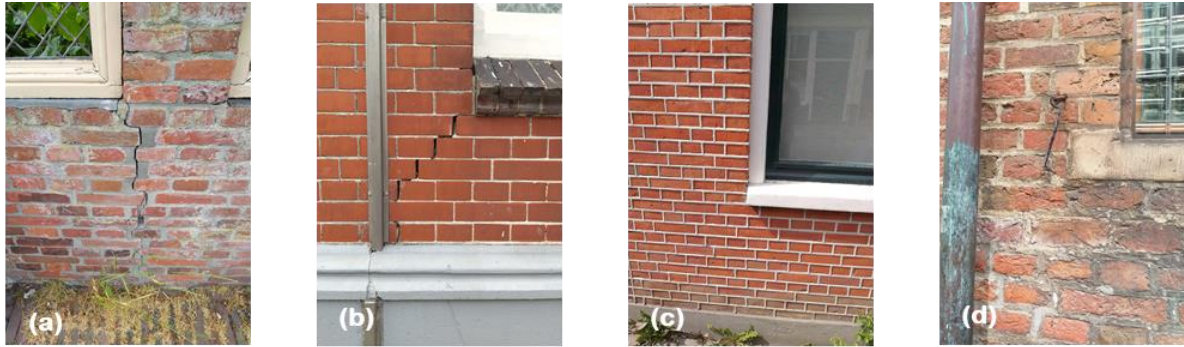
Figure 4-2: Images from masonry surfaces (a-b) with and (c-d) without cracks.

The created dataset will be referred to as "masonry dataset". In total 351 photographs containing cracks and 118 without any crack were gathered from masonry surfaces. These photographs were divided in patches of 224 x 224 pixels, which leads to 4,057 patch containing cracks while extra 7,434 non-crack patches were randomly selected from the gathered photographs. A sample of photographs from the masonry dataset with cracks is presented in Figure 4-3. A wide range of scales and resolutions was considered. The crack patches depicture from small (couple of bricks) to larger (whole masonry walls) field of views. Cracks might extend over the joints, the bricks or both. Cracks appearing as straight lines, zigzag or complex shapes were examined. A diverse type of cracks in terms of length, width and shape were included in the masonry dataset. Moreover, the crack patches included different types of noisy background, such as windows, plants, lamps and signs (Figure 4-3). Further examples of objects that typically exist around masonry façades and are included in the non-crack patches are shown in Figure 4-4.
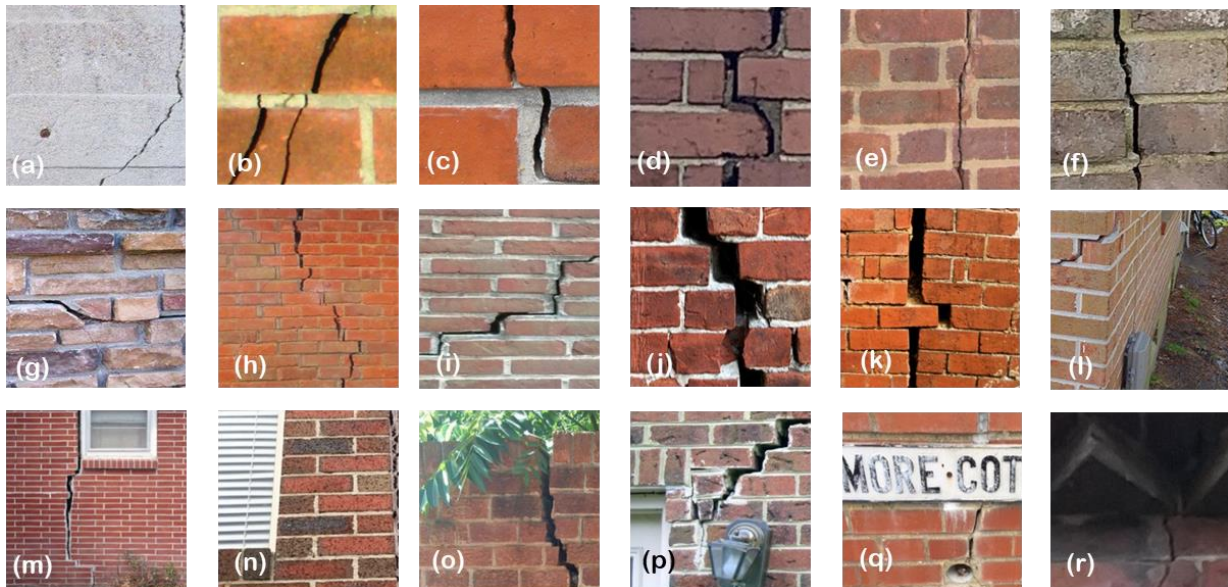
Figure 4-3: Images from the masonry dataset containing cracks.

Figure 4-4: Images depicturing various 'non-crack' objects included in the masonry dataset for the training of the classification network.

Along the development of this study, while collecting new data the different networks were run with the available dataset each time. It was observed that the metrics were improving as the masonry dataset was being enriched. The greatest improvement was recorded in the precision value; while extra types of background objects were included in the dataset the easier it was for the networks to learn to accurately negate them. Therefore, by improving how closely the dataset represents the real world the better would be the performance of the networks.

4.1.2 Image patch classification for crack detection

4.1.2.1 Convolutional neural networks for crack image classification

Image patch classification for crack detection was implemented by leveraging the effect of transfer learning via fine-tuning. The technique of fine-tuning was implemented by discarding the fully connected (FC) layers at the top of a pretrained network and training new, freshly initialized FC layers on the new data with a low learning rate (Rosebrock 2017). In detail, a FC layer with 128 features and rectified linear unit (ReLU) activation was added followed by batch normalization and a dropout layer with a probability of 0.5. Batch normalization is a technique that improves the speed, performance, and stability of artificial neural networks and was used to normalize the input layer by adjusting and scaling the activations while dropout temporarily disconnects the neural connections between connected layers during training. Finally, a FC layer with softmax activation was placed to classify the images as crack or non-crack.

Different state of the art CNN pretrained on ImageNet (1.2 million images with 1,000 categories) were examined for their efficacy to classify images from masonry surfaces on patch level as crack or non-crack. The considered networks were: VGG16 (Liu and Deng 2015), MobileNet (Howard et al. 2017), MobileNetV2 (Sandler et al. 2018), InceptionV3 (Szegedy et al. 2016), DenseNet121 (Huang et al. 2017a), DenseNet169 (Huang et al. 2017a), ResNet34 (He et al. 2016), ResNet50 (He et al. 2016). The configuration of ResNet34

and the pre-trained weights were obtained from Yakubovskiy (Yakubovskiy 2019), while for the rest of the networks the configuration and the weights were extracted from Keras (Chollet 2015). The details of the different networks are shown in Table 4-1. All the models were deposited in the GitHub repository: github.com/dimitrisdais/crack_detection_CNN_masonry.

At this point the architecture of MobileNet is highlighted since it obtained the best results as will be shown below (Section 4.1.2.3). MobileNet is a lightweight network destined to run on computationally limited platforms; it achieved accuracy comparable to VGG16 on ImageNet with only 1/30 of the computational cost and model size (Huang et al. 2017b). A standard convolution both filters and combines inputs into a new set of outputs in one step. MobileNet is based on depthwise separable convolutions which is a form of factorized convolutions (see Figure 4-5); the depthwise convolution applies a single filter to each input channel and the pointwise convolution then applies a 1 × 1 convolution to combine the outputs of the depthwise convolution. This factorization (Figure 4-5) has the effect of drastically reducing computation and model size. MobileNet comprises of multiple factorized layers with depthwise convolution, 1 × 1 pointwise convolution, batch normalization and ReLU activation (Figure 4-6a) instead of layers of regular convolutions followed by batch normalization and ReLU activation (Figure 4-6b). The MobileNet architecture has two hyper-parameters that is width and resolution multipliers in order to easily produce smaller versions of the network. For both hyper-parameters the default value is selected, that is 1, which means than no shrinking is applied to the model (Chollet 2015; Howard et al. 2017).

(a)   (b)   (c)
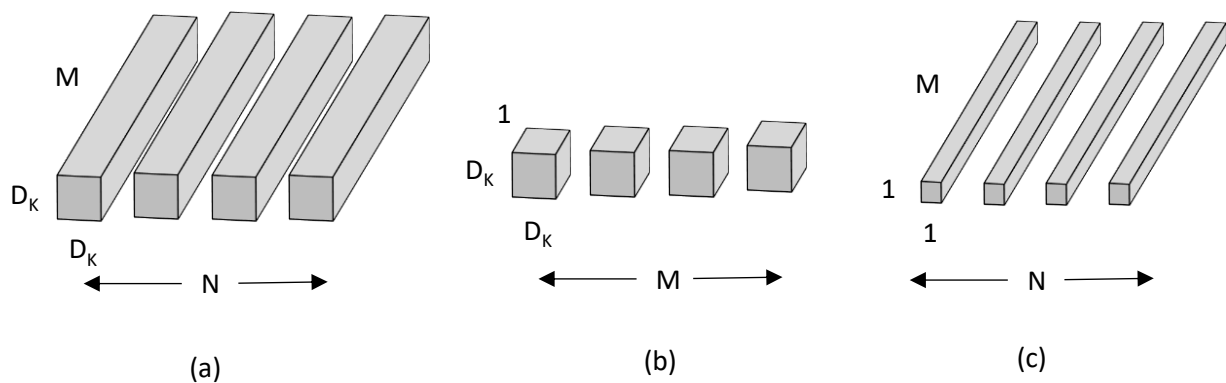
Figure 4-5: Schematic representation of (a) standard convolutional filters, (b) depthwise convolutional filters, and (c) 1 x 1 convolutional filters called pointwise convolution. M, N and D_K stand for the number of input channels, the number of output channels and kernel size respectively.
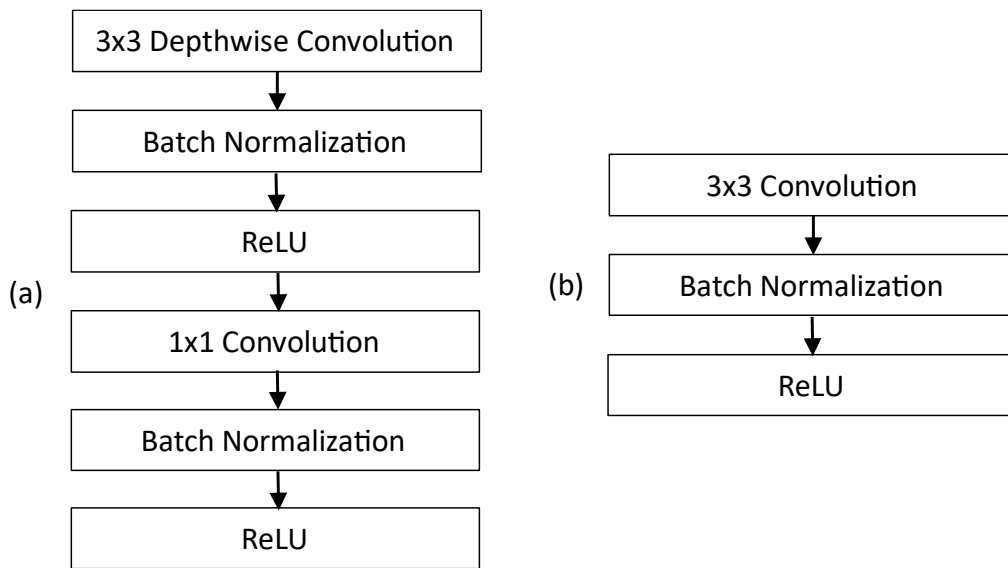
Figure 4-6: (a) Factorized layer with depthwise convolution, 1 × 1 pointwise convolution, batch normalization and ReLU activation. (b) Standard convolutional layer followed by batch normalization and ReLU activation.

MobileNet or networks that made use of depthwise separable convolution have been implemented in recent studies for crack detection. Single Shot MultiBox Detector (Liu et al. 2016), an object detection framework, was combined with MobileNet to detect different damage types on road surfaces (Maeda et al. 2018). MobilneNet performed as the encoder of a semantic segmentation network based on DeepLab (Chen et al. 2018a) for real-time tunnel crack analysis (Song et al. 2019). The depthwise separable convolution was used to reduce computational complexity and improve computational efficiency of image classification for crack detection (Xu et al. 2019). Depthwise convolutions have been successfully used for pixel-level segmentation of cracks on concrete surfaces (Choi and Cha 2020).

4.1.2.2 Training configuration

The networks for image classification are allowed to train for a great number of epochs, with a minimum of 50 epochs, until the accuracy (see Eq. (4.7)) on the validation set does not increase any further. The data are fed to the network with a batch size of 10.

Optimization in deep learning networks updates the weight parameters to minimize the loss function. The Adam method (Adaptive Moment Estimation) was found to outperform other stochastic optimization methods (Kingma and Ba 2015), i.e. it converges faster, and is selected as the optimizer of the network. Adam is an algorithm for first-order gradient-based optimization of stochastic objective functions, based on adaptive estimates of lower-order moments (Kingma and Ba 2015). The method is straightforward to implement, is computationally efficient, has little memory requirements, is invariant to diagonal rescaling of the gradients, and is well suited for problems that are large in terms of data and/or parameters

(Kingma and Ba 2015). The hyperparameters have intuitive interpretations and typically require little tuning. The weight update with Adam optimizer is described as follows:

$$m_t = \beta_1 m_{t-1} + (1 - \beta_1) g_t \tag{4.1}$$

$$v_t = \beta_2 v_{t-1} + (1 - \beta_2) g_t^2 \tag{4.2}$$

$$\hat{m}_t = \frac{m_t}{1 - \beta_1^t} \tag{4.3}$$

$$\hat{v}_t = \frac{v_t}{1 - \beta_2^t} \tag{4.4}$$

$$w_t = w_{t-1} - \alpha \frac{\hat{m}_t}{\sqrt{\hat{v}_t} + \varepsilon} \tag{4.5}$$

where t is the timestep, g_t is the gradient vector, m_t and v_t are the first (mean) and second (uncentered variance) biased moment estimates of the gradients respectively, $\hat{m}_t$ and $\hat{v}_t$ are the first (mean) and second (uncentered variance) bias-corrected moment estimates of the gradients respectively, β_1 and β_2 are the exponential decay rates for the moment estimates, α is the learning rate, w is the model weights and $\varepsilon = 10^{-8}$. The default values 0.9 and 0.999 are taken for β_1 and β_2 respectively (Chollet 2015; Kingma and Ba 2015). The networks are trained with a constant learning rate α equal to 0.001.

In the context of an optimization algorithm, a loss function is used to evaluate a candidate solution (i.e. a set of weights) that will minimize the prediction error. The cross entropy (CE) loss function (L_{CE}) is utilized hereand is given as:

$$L_{CE} = - \left(y \, log(\hat{y}) + (1 - y) \, log(1 - \hat{y}) \right) \tag{4.6}$$

where y is the ground truth, $\hat{y}$ is the prediction. y can take values equal to 0 (non-crack) or 1 (crack) while $\hat{y}$ can be in the range of 0 to 1.

The performance of the networks is evaluated based on the values of accuracy which is defined as:

$$Accuracy = \frac{TP + TN}{TP + TN + FP + FN} \tag{4.7}$$

where TP, TN, FP and FN correspond to true positive, true negative, false positive and false negative, respectively. The classification is binary with non-crack and crack cases corresponding to negative and positive class respectively. Thus, TP implies that a crack image is correctly classified while TN means that a non-crack image is predicted accurately. While accuracy performs as an average of the performance of the two classes, TP and TN

provide a better insight on the classification error for each class individually and thus are reported as well.

For the training of the image classification networks the 4,057 crack and the 7,434 non-crack patches of the masonry dataset are used. 60% and 40% of the patches are used for training and validation respectively. The networks are implemented on Keras (Chollet 2015), a high-level neural network API, written in Python and by utilizing TensorFlow as back-end. The networks are run on a laptop with Intel i7 processor with 2.20 GHz, 16 GB RAM and Nvidia GPU GeForce(R) RTX 2060 with 6 GB.

4.1.2.3 Results for crack image classification

In this section the results from the trained networks for image classification are presented. The obtained metrics from the trained models on the validation set are enlisted in Table 4-1 for the epoch that the highest accuracy is reached for each case. While all the considered networks obtain high accuracy on the validation set, that is 88% or more, MobileNet outperforms the rest by scoring accuracy 95.3% (Table 4-1). In order to examine the benefit of transfer learning, MobileNet is also evaluated without pretraining with its weights randomly initialized (Chollet 2015). Indeed, the accuracy of MobileNet drops from 95.3% to 89.0% which reveals that transfer learning offers a significant boost to the performance of the network. In more detail, when random initialization is considered, the ratio of TN remains high, that is 96.4%, however TP declines considerably from 89.8% to 75.8%. Consequently, without pretraining the network struggles to differentiate edges corresponding to the crack class and tends to label them as non-crack.

Table 4-1: Details and metrics of the networks used for image classification. The metrics are presented for the validation set.

Network	Pretrained[a]	Parameters[b] [millions]	Weight[c] [MB]	Accuracy [%]	TN [%]	TP [%]	Analysis Time[d] [hours]	Best Epoch[e]
VGG16	Yes	17.9	70.1	88.0	89.3	85.8	2.2	28
ResNet34	Yes	24.5	96.1	91.6	96.8	82.3	0.7	84
ResNet50	Yes	36.4	142.7	86.5	94.4	72.3	1.1	49
DenseNet121	Yes	13.5	53.5	92.4	95.8	86.2	2.3	48
DenseNet169	Yes	23.1	91.4	89.9	93.3	83.6	2.5	50
InceptionV3	Yes	28.4	111.5	88.4	94.7	77.0	1.7	50
MobileNet	Yes	9.7	37.9	**95.3**	98.4	89.8	1.1	32
	No			89.0	96.4	75.8		95
MobileNetV2	Yes	10.3	40.6	89.7	93.7	82.7	1.2	58

TN: true negatives, TP: true positives
[a] Whether the encoder of a network is pretrained on ImageNet.
[b] The total number of parameters of a network.
[c] Size of the file where the weights of a network are stored.
[d] Analysis time required to run a network for 50 epochs.
[e] Epoch where the highest accuracy was obtained for the validation set.

In Figure 4-3 and Figure 4-4 representative images of the masonry dataset are presented. Based on the accuracy of the model it can concluded that the network learns rich features that allow for correct classifications on the dataset produced. A closer look to the performance of MobileNet is highlighted in the produced confusion matrix (Figure 4-7). It is inferred that MobileNet excels in predicting correctly the non-crack case with only 1.6% error while the error in the crack class is higher, that is 10.2% of the crack images are classified as non-crack. Different cases of FP and FN predicted with MobileNet from the validation set are displayed in Figure 4-8 and Figure 4-9 respectively. Part of a pipe (Figure 4-8a), joints without mortar (Figure 4-8b, g-h), edges around doors (Figure 4-8e-f), and blurry or dark edges (Figure 4-8c-d) are wrongly classified as cracks. Evidently, a further expansion of the masonry dataset should take into consideration a better representation of the cases that yielded FP so that the network will learn their features and correctly classify them. On the other hand, crack images taken with acute angle (Figure 4-9a) or with great field of view capturing thin cracks (Figure 4-9b-d) are misclassified. Moreover, there are cases of close-up images of thin (Figure 4-9e-j) or well-shaped cracks (Figure 4-9k-m), crack with missing mortar (Figure 4-9n) and crack in dark background (Figure 4-9o) that the network falsely negates them to the non-crack class.
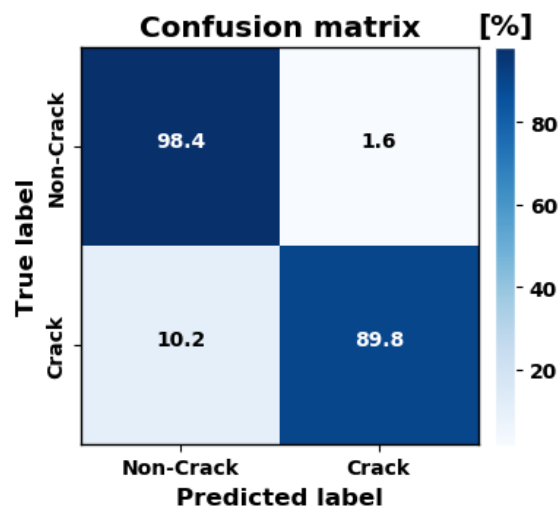
Figure 4-7: Confusion matrix obtained with the MobileNet on the validation set.
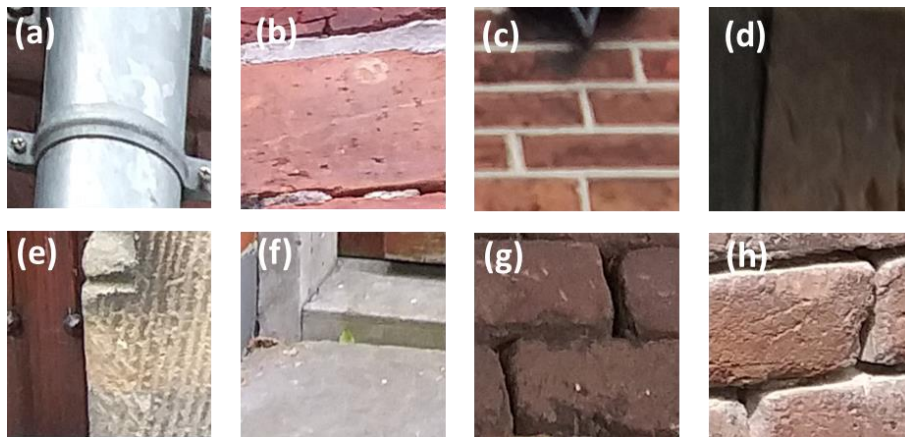
Figure 4-8: Non-crack images classified as crack (false positive) by implementing MobileNet on the validation set.
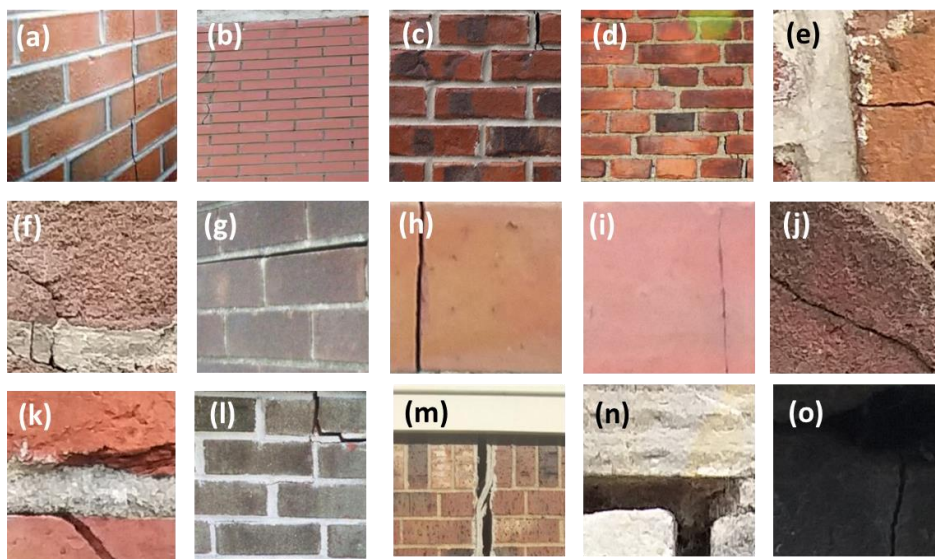
Figure 4-9: Crack images classified as non-crack (false negative) by implementing MobileNet on the validation set.

4.1.3 Crack segmentation on pixel level

4.1.3.1 Convolutional neural networks for crack segmentation

As per Long et al. (2015) "semantic segmentation faces an inherent tension between semantics and location: global information resolves what while local information resolves where". Recently FCNs (Long et al. 2015), which are end-to-end networks, have been extensively used for semantic segmentation and in particular for crack segmentation, as highlighted above (section 2.3.1). FCNs perform as an extended CNN where the final prediction is an image with semantic segmentation instead of a class identification. FCNs adopt architectures with pyramidal shapes; they follow the usual contracting path (encoder) of image classification networks and replace any FC layers with convolutional layers while on top of the encoder an expanding path (decoder) is added with successive convolutional layers followed by upsampling operators. The encoder captures context while the decoder enables

precise localization. In order to avoid loss of low-level information, skip connections are used to allow the decoder to access the low-level features obtained by the encoder branch. A schematic representation of the encoder-decoder architecture of FCNs is shown in Figure 4-10. U-net (Ronneberger et al. 2015), a deep FCN, and FPN (Lin et al. 2017), a generic pyramid representation, are considered and combined with different CNN performing as the backbone of the encoder part of the network. FPN in fact adopts a similar architecture with U-net, but FPN performs predictions independently at different stages of the expanding path and subsequently concatenates these predictions while U-net only produces predictions at the last stage. The implementation of the U-net and FPN based models with different CNN as backbone is in accordance with the work of Yakubovskiy (2019) and is further elucidated in the next paragraphs. Furthermore, different networks that were successfully used in the literature for crack segmentation are examined in an extensive comparative study.
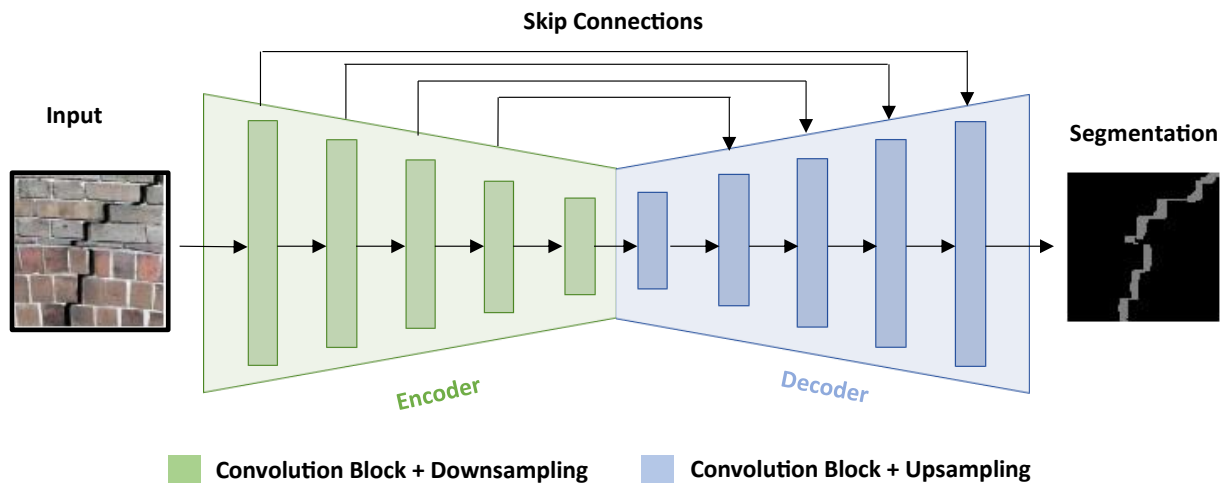
Figure 4-10: Schematic representation of the encoder-decoder architecture of Fully Convolutional Networks.

U-net (Ronneberger et al. 2015) built upon the original implementation of FCN (Long et al. 2015) by increasing the number of feature channels in the upsampling part, which allow the network to propagate context information to higher resolution layers. As a result, in U-net the expansive path is almost symmetric to the contracting path yielding a U-shaped architecture. In the encoder there are repeated blocks of two 3 x 3 convolutional layers and each of them is followed by batch normalization and ReLU activation. These blocks are referred to as ConvBlock. ConvBlocks are followed by a 2 x 2 max pooling layer with stride 2 which halves the dimensions of the images and doubles the number of feature channels, a process that is called downsampling. In the decoder, a 2 x 2 deconvolution layer succeeds each ConvBlock. The deconvolution layer, usually referred to as transpose convolution layer, upsamples the images, meaning it doubles its size and halves the number of feature channels. The final deconvolution layer restores the original size of the image. Then, a 1 x 1 convolution with sigmoid activation follows which yields the final prediction for each pixel of the image. In total

the network has 23 convolutional layers. Same-level ConvBlocks between the encoder and the decoder are merged with skip connections (Figure 4-11).
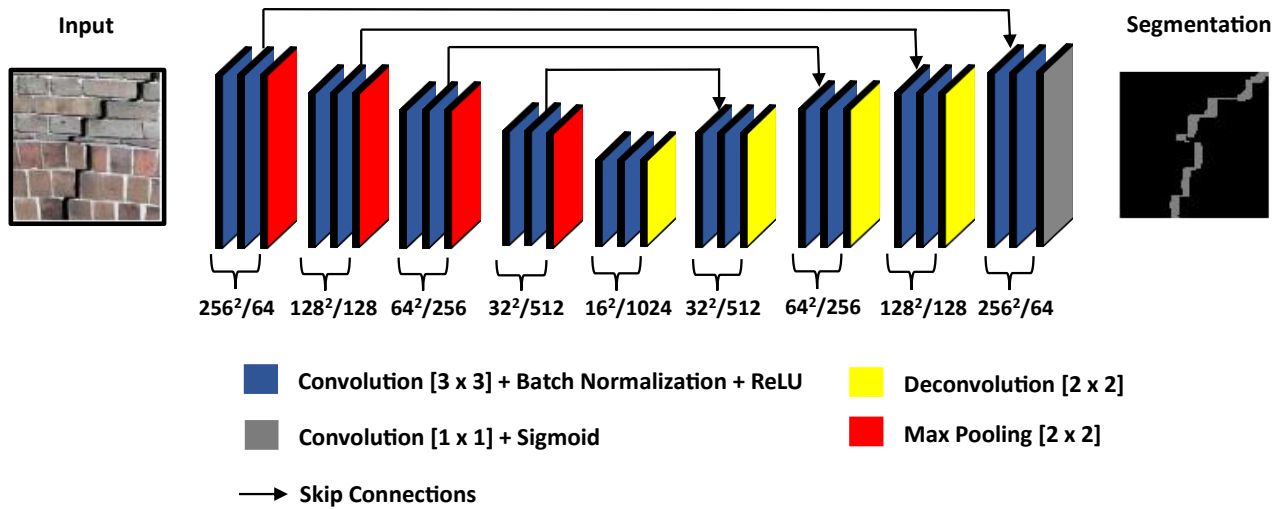
Figure 4-11: Illustration of the architecture of U-net as implemented in this study. The numbers below the layers denote their size/feature channels respectively.

FPN (Lin et al. 2017) is a typical model architecture to generate pyramidal feature representations for object detection. FPN is independent of the backbone network and its architecture makes it easily configurable to receive different CNN as the backbone of the encoder. In particular, FPN adopts a convolutional architecture as its backbone, typically designed for image classification, and builds a feature pyramid with a bottom-up pathway, a top-down pathway and lateral connections. The high-level features, which are semantically strong but lower resolution, are upsampled and combined with higher resolution features to generate feature representations that are both high resolution and semantically strong. The upsampling layer repeats the rows and columns of the input features by 2 x 2 and fills in the new rows and columns by using the nearest neighbour algorithm (Chollet 2015). The bottom-up pathway which is the feed-forward computation of the backbone CNN produces a feature hierarchy consisting of feature maps at several scales with a scaling step of 2. Layers producing output maps of the same size are considered in the same network stage and for each stage one pyramid level is defined. The top-down pathway obtains higher resolution features by upsampling by a factor of 2 spatially coarser, but semantically stronger, feature maps from higher pyramid levels. These features are then enhanced by element-wise addition with features from the bottom-up pathway which undergo a 1×1 convolutional layer to reduce channel dimensions. Further on, 3×3 convolutions are appended on each merged feature map and the produced maps from the different stages are concatenated. A schematic representation of FPN is displayed in Figure 4-12.
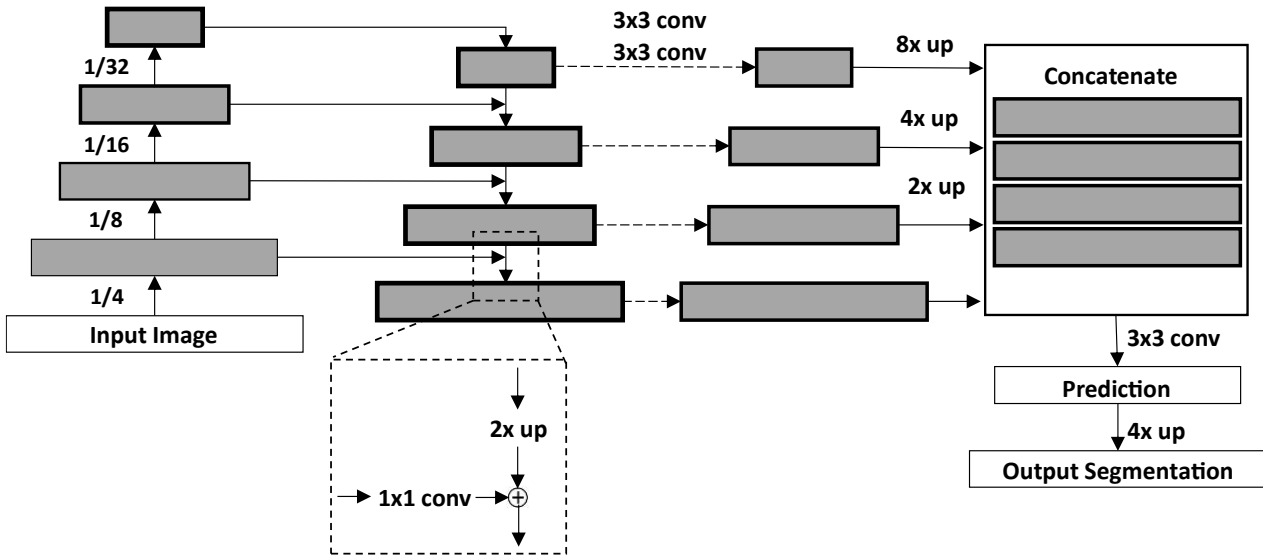
Figure 4-12: Schematic representation of Feature Pyramid Network. The rectangles with grey hatch correspond to feature maps and the thicker outlines denote semantically stronger features. The lateral connections and the top-down pathway are merged by addition as shown in the detail (denoted with dashed line). conv and up strand for convolution and upsampling respectively.

The CNN that were tested for image classification in Section 4.1.2 are utilized as the encoder for U-net and FPN in order to perform crack segmentation on pixel level this time. In particular, the considered networks are: VGG16 (Liu and Deng 2015), MobileNet (Howard et al. 2017), MobileNetV2 (Sandler et al. 2018), InceptionV3 (Szegedy et al. 2016), DenseNet121 (Huang et al. 2017a), DenseNet169 (Huang et al. 2017a), ResNet34 (He et al. 2016), ResNet50 (He et al. 2016). It is noted that U-net is also considered as a standalone network configured as explained above (Figure 4-11). For further reference, the models based on U-net and FPN will be called with the base-model followed by the backbone network, e.g. U-net-MobileNet uses U-Net as base-model with MobileNet as backbone. Moreover, apart from U-net, other networks found in the literature and performed well in crack segmentation are examined as well. In particular, DeepLabv3+ (Chen et al. 2018b), DeepCrack (Liu et al. 2019a), and FCN based on VGG16 (will be referred to as FCN-VGG16) (Long et al. 2015). All the networks used in this study for segmentation are listed in Table 4-2 and can be found in the GitHub repository: github.com/dimitrisdais/crack_detection_CNN_masonry.

4.1.3.2 Training configuration

The segmentation networks are allowed to train for a great number of epochs, with a minimum of 100 epochs, until the F1 score (see Eq. (4.11)) on the validation set does not increase any further. The data are fed to the network with a batch size of 4. Similar to the image classification case, the networks for crack segmentation are trained with Adam as optimization algorithm and the learning rate is kept constant equal to 0.0005. The Adam algorithm is further explained above (Section 4.1.2.2).

Datasets for image segmentation on crack detection are characterized by severe class imbalance i.e. the background class occupies the greatest part of photographs while cracks extend over limited pixels. Due to this imbalance, if special measures are not taken, the network tends to become overconfident in predicting the background class which could lead to misclassifications of cracks and numerous false negatives. To overcome this, the weighted cross entropy (WCE) loss function is implemented. In particular, misclassifications of the crack class are penalized with a higher weight. The WCE loss function (L_{wCE}), utilized here, is given as:

$$L_{wCE} = -\left(\beta\, y\, log(\hat{y}) + (1 - y)\, log(1 - \hat{y})\right) \tag{4.8}$$

where y is the ground truth, $\hat{y}$ is the prediction, and β is the weight of the positive class (i.e. crack) chosen as 10. Also, y can take values equal to 0 (background) or 1 (crack); while $\hat{y}$ can be in the range of 0 to 1. In order to evaluate the effect of the loss function to the performance of the network, different loss functions are examined, i.e. CE, F1 score and focal loss. CE and F1 score correspond to the loss functions obtained from Eq. (4.6) and (4.11) respectively while focal loss reshapes CE to down-weight easy examples and thus focus training on hard negatives (Lin et al. 2020). It is noted that the focal loss is implemented with the default values suggested by Lin et al. (Lin et al. 2020).

The evaluation of the network is on the values of precision, recall and F1 score. These metrics are given as:

$$Precision = \frac{TP}{TP + FP} \tag{4.9}$$

$$Recall = \frac{TP}{TP + FN} \tag{4.10}$$

$$F1\ score = \frac{2\ x\ Precision\ x\ Recall}{Precision\ + Recall} \tag{4.11}$$

where TP, FP, TN, FN correspond to true positive, false positive, true negative and false negative, respectively.

Another common metric in image segmentation is accuracy which denotes the correctly predicted pixels over the total number of pixels. When there is class imbalance, accuracy is not considered suitable to evaluate the performance of the network since accuracy will yield a score close to its maximum value, that is 1, even if the whole image is classified as the prevailing class (i.e. background). Therefore, accuracy is ignored and is not reported.

Precision regards the correct positive predictions over the total number of the positive predictions and measures the efficiency of the network to negate crack-like objects in the background. Recall considers the completeness of the positive predictions i.e. how many of

the actual crack pixels are correctly classified. Precision and recall frequently conflict with each other (Zhang et al. 2017). In other words, usually high recall values lead to low precisions and vice versa. F1 score is the harmonic mean of precision and recall.

Requesting the model to segment the exact width of the crack has been found to be rather strict and hard to achieve. Different approaches have been implemented in order to overcome this limitation. In particular, connectivity constraints were incorporated in the loss function to take into consideration the relationship among annotations of neighbouring pixels (Mei et al. 2020). Other suggested solution was to apply post-processing to isolate noisy parts (Chambon and Moliard 2011). A common approach was to allow for some tolerance in the evaluation of the crack detection. Thus, background pixels predicted as cracks (FP) were considered as TP if they were a few pixels apart from the annotated cracks (Chambon and Moliard 2011; Shi et al. 2016; Zou et al. 2019; Mei et al. 2020). The latter proposed approach is followed in this study.

For the training of the segmentation networks the 4,057 crack patches of the masonry dataset were used. In particular, 60% and 40% of the patches were used for training and validation respectively. The crack patches were fed to the networks along with pixel-level annotated labels. Similar to the classification networks, the segmentation models were implemented on Keras (Chollet 2015) by utilizing TensorFlow as back-end and were run on the same computing laptop (see Section 4.1.2.2 for details).

4.1.3.3 Results for crack segmentation

In this section the segmentation results from the trained networks are presented. The obtained metrics from the trained models on the validation set are shown in Table 4-2 for the epoch that the highest F1 score is reached for each case. From Table 4-2, a high value of recall does not necessarily mean high precision and vice versa. Thus, F1 score, the average between recall and precision, is deemed the most indicative metric to decide which networks perform better. Thus, U-net-MobileNet and FPN-InceptionV3 attain the highest F1 score, that is 79.6%, and FPN-MobileNet follows with 79.5%.

Table 4-2: Details and metrics of the networks used for segmentation. The metrics are presented for the validation set.

Network	Pretrained[a]	Loss	Parameters[b] [millions]	Weight[c] [MB]	F1 score [%]	Recall [%]	Precision [%]	Analysis Time[d] [hours]	Best Epoch[e]
DeepCrack	No	WCE	29.5	115.5	74.0	80.1	71.6	5.2	28
DeepLabv3+	No	WCE	41.3	162.2	74.9	79.0	73.8	5.6	26
FCN-VGG16	No	WCE	27.8	108.8	75.6	76.6	76.9	2.5	95
U-net	No	WCE	34.5	135.1	75.7	78.9	75.7	5.8	75
U-net-VGG16	Yes	WCE	46.1	180.2	77.2	81.2	76.2	6.0	37
U-net-ResNet34	Yes	WCE	48.0	188.1	77.6	78.3	79.5	4.9	61
U-net-ResNet50	Yes	WCE	73.7	288.5	76.3	80.9	74.8	6.8	45
U-net-Densenet121	Yes	WCE	41.6	163.5	78.1	80.7	78.1	6.2	55
U-net-Densenet169	Yes	WCE	54.3	213.4	78.5	83.5	76.2	7.1	63
U-net-InceptionV3	Yes	WCE	68.5	268.1	77.7	79.2	78.9	6.8	31
U-net-MobileNet	Yes	WCE	37.8	147.9	**79.6**	79.9	81.4	4.8	45
	No	WCE			75.4	80.7	73.4		36
	Yes	CE			76.6	73.0	83.0		36
	Yes	F1-score			78.2	77.1	82.0		29
	Yes	Focal Loss			71.2	61.1	89.4		85
U-net-MobileNetV2	Yes	WCE	39.5	154.9	77.7	76.6	81.9	5.3	58
FPN-VGG16	Yes	WCE	32.2	125.8	77.9	82.0	76.2	5.6	79
FPN-ResNet34	Yes	WCE	38.3	150.2	78.0	81.5	77.2	5.2	36
FPN-ResNet50	Yes	WCE	42.1	164.8	77.2	81.4	75.8	5.8	27
FPN-Densenet121	Yes	WCE	24.6	97.0	79.0	83.6	77.2	6.1	31
FPN-Densenet169	Yes	WCE	30.6	120.8	78.6	80.0	79.5	6.6	59
FPN-InceptionV3	Yes	WCE	40.0	157.2	**79.6**	81.3	80.1	5.7	34
FPN-MobileNet	Yes	WCE	20.8	81.4	79.5	79.5	81.7	4.6	40
FPN-MobileNetV2	Yes	WCE	19.9	78.3	78.5	76.7	82.7	4.8	49

WCE: weighted cross entropy, CE: cross entropy
[a] Whether the encoder of a network is pretrained on ImageNet.
[b] The total number of parameters of a network.
[c] Size of the file where the weights of a network are stored.
[d] Analysis time required to run a network for 100 epochs.
[e] Epoch where the highest F1 score was obtained for the validation set.

Firstly, the effect of the loss function on the performance of the networks was evaluated. U-net-MobileNet was trained, apart from WCE, with CE, F1 score and focal loss as loss function. It is noted that similar results were extracted for the other networks but for brevity only results for U-net-MobileNet are presented. The performance of U-net-MobileNet for the different loss functions is displayed in Table 4-2 and the evolution of the metrics is shown in detail in Figure 4-13. As shown in Table 4-2, the best performance is reached when WCE is utilized; the obtained F1 score is 79.6%, 76.6%, 78.2% and 71.2% for WCE, CE, F1 score and focal loss respectively. Precision is in the range of 90% for CE (Figure 4-13b) and focal loss (Figure 4-13d) while recall remains significantly lower, i.e. in the range of 60% to 70%. Thus, these two loss functions are not able to handle the class imbalance problem for crack segmentation since the network becomes overconfident in predicting background while neglecting the

minority class, that is crack. When WCE (Figure 4-13a) and F1 score (Figure 4-13c) are used as loss function the discrepancy between precision and recall is less profound. Specifically for WCE, in the first epochs, the recall value ranks approximately 90% while further on converges to 80% and from the 80th epoch onwards decreases to 70%. On the other hand, precision follows an opposite path, starting from 50% and gradually increasing up to 85% in the final epochs. F1 score in the beginning of training is 60% and then converges to value close to slightly below 80%. The highest F1 score is attained in the 45th epoch. The performance of the three metrics indicates that in the beginning, the system is overconfident to predict cracks. In this process, it misclassifies background as cracks. Similar behaviour was reported by (Liu et al. 2019b; Mei et al. 2020). As Zhang et al. (2017) pointed out, precision and recall frequently conflict with each other and a compromise between recall and precision is made to select the best model. In order to visualize the meaning of different values of recall and precision, predictions with U-net-MobileNet for different images are exhibited for the epochs 3 and 45 which correspond to the highest recall and F1 score respectively (Figure 4-14). All the examples in Figure 4-14 rank a recall value close to 100% (i.e. maximum value) at epoch 3. Nevertheless, precision and F1 score remain significantly lower. Taking a closer look at the predictions at epoch 3, large parts of the background have been misclassified as cracks (Figure 4-14). Regarding the predictions on epoch 45, recall slightly drops while precision significantly increases since the network learns to negate greater parts of the background (Figure 4-14).
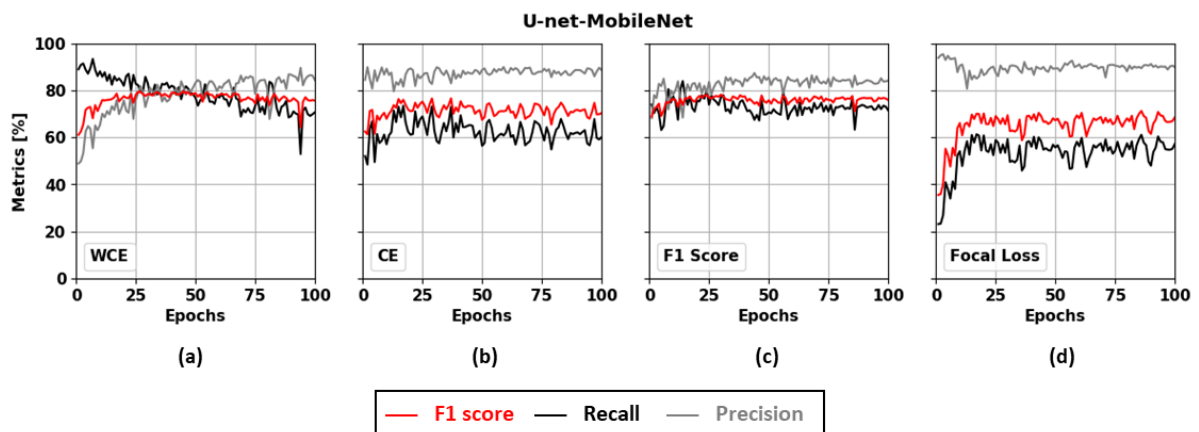
Figure 4-13: The metrics F1 score, Recall and Precision as obtained from the pretrained U-net-MobileNet for different loss functions: (a) weighted cross entropy (WCE), (b) cross entropy (CE), (c) F1 score, and (d) focal loss.
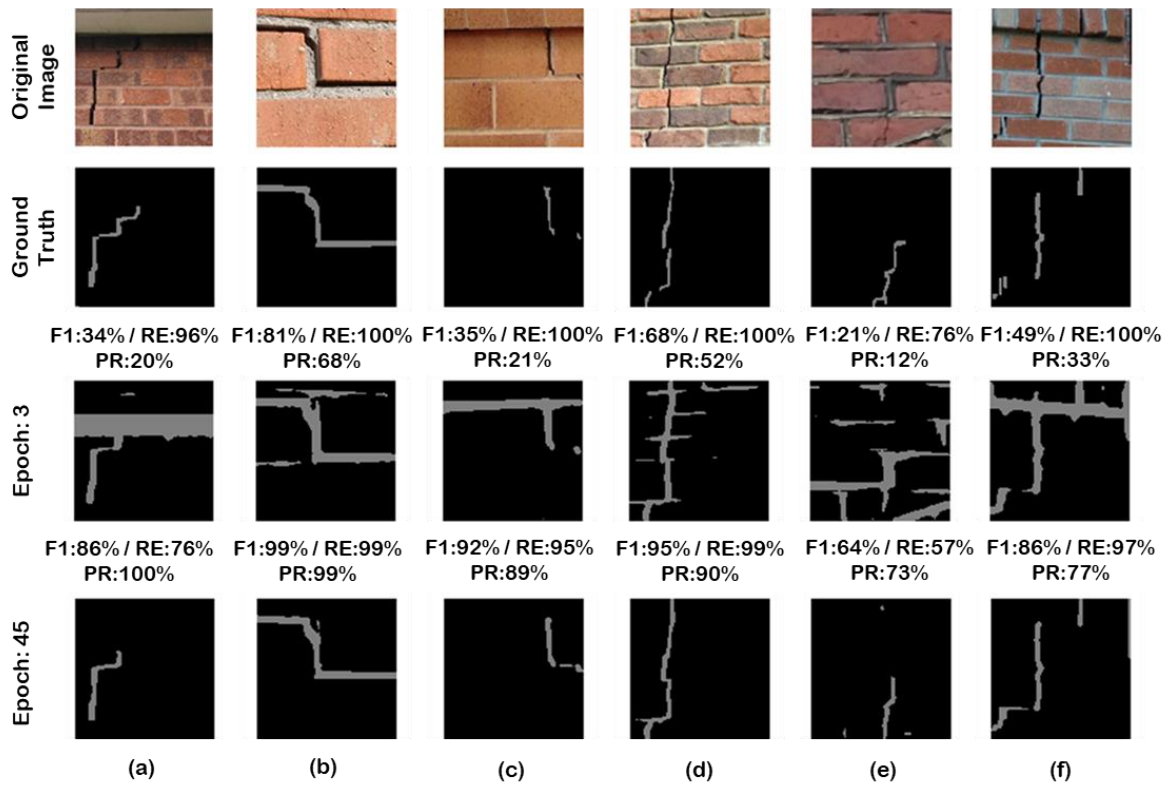
Figure 4-14: The original image, the ground truth and the predictions with U-net-MobileNet at epochs 3 and 45 are displayed for different images from the masonry dataset. At the top of each prediction the calculated metrics (F1: F1 score, RE: recall, and PR: precision) are highlighted.

Furthermore, the networks found in the literature, that is DeepCrack, DeepLabv3+, FCN-VGG16 and U-net, have similar performance in terms of F1 score, i.e. from 74% to 75.7%. U-net outperforms the other networks obtained from the literature achieving F1 score 75.7% with FCN-VGG16 following closely with F1 score 75.6%. Moreover, regarding the performance of the networks found in the literature except for FCN-VGG16, significant discrepancy is observed between the recall and precision values; the networks favour the recall which lead to lower values of precision. The models based on U-net and FPN with a pretrained CNN as backbone attain F1 score from 77.2% to 79.6% which means that they surpass the F1 score, that is 75.7%, of the models found in the literature and are implemented without pretraining. Furthermore, in Table 4-2 can be observed that U-net and U-net-MobileNet without pretraining reach similar F1 score, that is 75.7% and 75.4% respectively, while the pretrained U-net-MobileNet yields F1 score 79.6%. This observation highlights the effect of pretraining on the performance of the networks; F1 score is boosted by 4.2% when pretraining is considered for U-net-MobileNet. The U-net-MobileNet without pretraining in terms of F1 score records performance similar to FCN-VGG16 and U-net and outperforms DeepCrack and DeepLabv3+. The models based on FPN in general score higher than the corresponding ones built on U-net while the highest F1 score is obtained with U-net-MobileNet and FPN-InceptionV3 (Table 4-2). It is noted that the models based on FPN have almost half the size of the ones with U-net in terms of model parameters and memory size of

the stored weights (Table 4-2). Thus, FPN models match the performance of the U-net counterparts while being significantly more lightweight networks.

In Figure 4-15 different examples from the validation set are presented with predictions obtained with DeepCrack, DeepLabv3+, U-net, U-net-MobileNet (with and without pretraining) and FPN-InceptionV3. In particular, images with edges around openings (Figure 4-15a-e), crack-like mortar joints (Figure 4-15f-i), shadows (Figure 4-15k) and dark spots (Figure 4-15l) are displayed. While the pretrained U-net-MobileNet and FPN-InceptionV3 are able to negate different types of noisy background, the rest of the networks (Figure 4-15) score lower in terms precision.

Images from the validation set with predictions obtained using U-net-MobileNet have already been presented in Figure 4-14 and Figure 4-15 while extra examples are shown in Figure 4-16. The network successfully segments cracks with different crack size, scale and background complexity; close-up photographs (Figure 4-16a-c), images with a larger field of view (Figure 4-16d-f) and with unwanted objects (i.e. windows and colour-paints) (Figure 4-16g-i). Apparently, there are cases that the network failed to perform crack segmentation accurately. For example, in Figure 4-16j-k the network fails to detect parts of the cracks. Moreover, Figure 4-16l-r displays examples where the model does not manage to negate noisy types of background.

	(a)	(b)	(c)	(d)	(e)	(f)
Original Image						
Ground Truth						
DeepCrack	F1:24% / RE:82% PR:14%	F1:14% / RE:44% PR:9%	F1:26% / RE:47% PR:15%	F1:38% / RE:96% PR:23%	F1:34% / RE:99% PR:20%	F1:70% / RE:78% PR:64%
DeepLabv3+	F1:43% / RE:84% PR:28%	F1:33% / RE:72% PR:22%	F1:17% / RE:54% PR:10%	F1:91% / RE:91% PR:90%	F1:43% / RE:100% PR:28%	F1:70% / RE:81% PR:61%
U-net	F1:19% / RE:83% PR:11%	F1:28% / RE:52% PR:20%	F1:27% / RE:81% PR:16%	F1:28% / RE:99% PR:17%	F1:56% / RE:100% PR:40%	F1:78% / RE:75% PR:81%
U-net-MobileNet	F1:86% / RE:76% PR:98%	F1:77% / RE:75% PR:78%	F1:80% / RE:81% PR:80%	F1:73% / RE:98% PR:57%	F1:62% / RE:100% PR:45%	F1:78% / RE:64% PR:99%
U-net-MobileNet (without pretraining)	F1:41% / RE:82% PR:27%	F1:20% / RE:42% PR:13%	F1:55% / RE:57% PR:51%	F1:48% / RE:98% PR:32%	F1:42% / RE:100% PR:27%	F1:71% / RE:72% PR:69%
FPN-InceptionV3	F1:82% / RE:73% PR:94%	F1:46% / RE:66% PR:35%	F1:55% / RE:56% PR:54%	F1:76% / RE:92% PR:64%	F1:74% / RE:95% PR:61%	F1:75% / RE:71% PR:80%

(Continues)

Figure 4-15: The original image, the ground truth and the prediction with different netwroks are displayed for different images from the masonry dataset. At the top of each prediction the calculated metrics (F1: F1 score, RE: recall, and PR: precision) are highlighted.
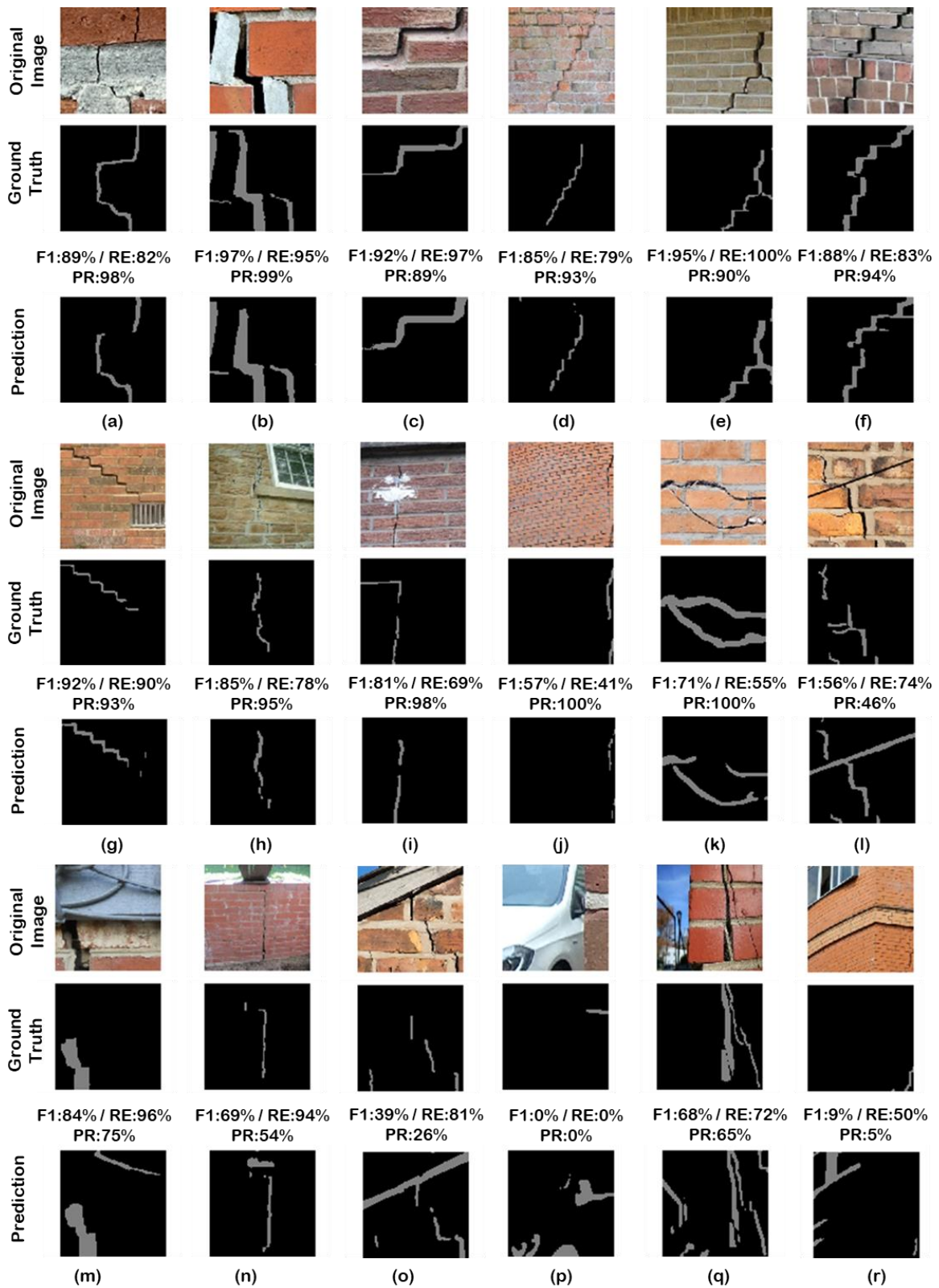
Figure 4-16: The original image, the ground truth and the prediction with U-net-MobileNet are displayed for different images from the masonry dataset. At the top of each prediction the calculated metrics (F1: F1 score, RE: recall, and PR: precision) are highlighted.

4.1.4 Comparative study

In a previous study for crack detection on concrete surfaces it was concluded that when a deep learning network was trained on images of monotonous background and subsequently tested on a more complex dataset the performance drastically decreased (Choi and Cha 2020). In more detail, precision from 87.4% fell to 23.1%. Moreover, deep learning networks trained on concrete images found to perform poorly when tested on masonry images because they are rather complex (Özgenel and Sorguç 2018). This behaviour of CNN was explained by Thompson et al. (2019); the transferability of features decreases as the distance between the base task (i.e. training dataset) and target task (i.e. testing dataset) increases. To build up on these findings, U-net-MobileNet trained on the masonry dataset is tested on images from concrete surfaces in order to evaluate the ability of CNN to generalize over different materials.

In particular, the open source dataset prepared by Yang et al. (2018) is selected and will be referred to as the "concrete dataset". The dataset consists of 776 concrete images containing different crack types. Examples of images in the concrete dataset with their labelled cracks are presented in Figure 4-17. An FCN was trained and morphological transformations were applied to further improve the crack segmentation. The reported F1 score, recall and precision were 80%, 79% and 82% respectively (Yang et al., 2018).

When U-net-MobileNet is tested on the concrete dataset it ranks 74.7%, 70.9%, 91.2% for F1 score, recall and precision respectively. The network does not perform satisfactorily in terms of recall value while excels in terms of precision. These results can be explained by taking a closer look on the predictions on the concrete dataset (Figure 4-17). In fact, the network performs exceptionally segmenting cracks with complicated shapes (Figure 4-17a-d) obtaining 79% recall or above and a minimum of 94% in terms of precision. On the other hand, the network fails to detect cracks like in Figure 4-17e-f but it is noted that these defects look like spalling and do not have a typical crack-like shape; similar defects do not exist in the masonry dataset. Additionally, precision is high which implies that the network can easily negate the background. This could be attributed to the fact that concrete surfaces are rather homogeneous and less complex than masonry surfaces. Consequently, the performance of U-net-MobileNet trained on the masonry dataset deteriorates, i.e. F1 scores declines from 79.6% to 74.7%, when tested on the concrete dataset but not as drastically as reported in the literature when networks trained on concrete images were consequently tested on masonry photographs. As explained above (Section 2.3.2), masonry surfaces are more complex than concrete ones. It is noted that in the literature there are various datasets of concrete surfaces while only limited data for masonry exist. Thus, when crack segmentation on concrete surfaces is requested, it is recommended to train a model solely on concrete images instead of relying on models trained on masonry data. On the other hand, for cases

where only few data exist, e.g. timber surfaces, a model trained on a dataset with complex backgrounds like the masonry dataset produced herecould be an alternative.
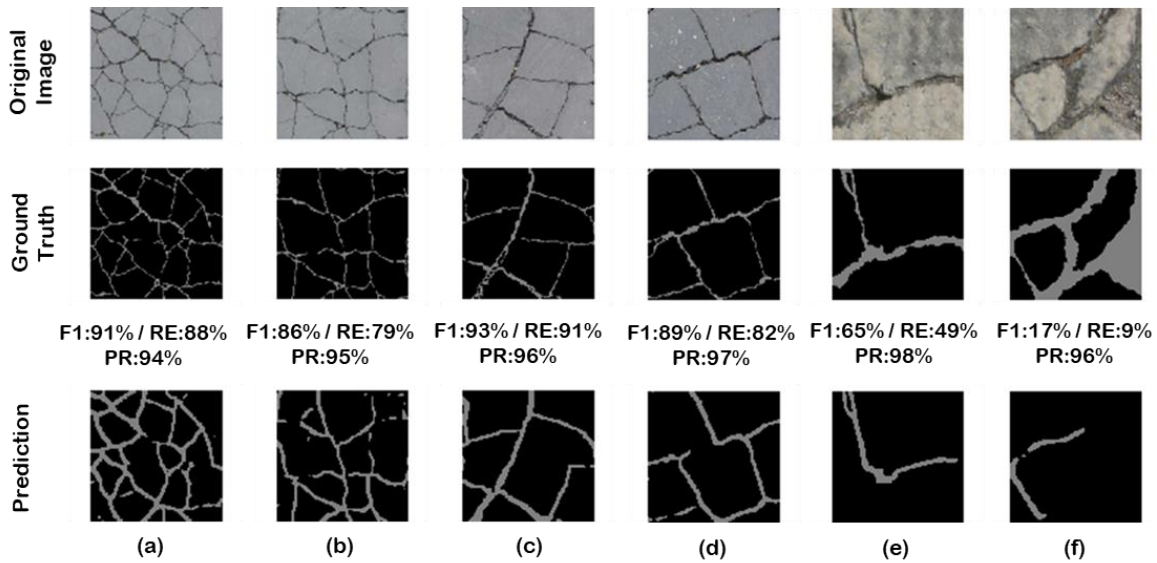
Figure 4-17: Results obtained when U-net-MobileNet is trained on the masonry dataset and tested on photographs from the concrete dataset (Yang et al. 2018). For each image, the original image, the ground truth and the prediction are displayed. At the top of each prediction the calculated metrics (F1: F1 score, RE: recall, and PR: precision) are highlighted.

4.1.5 Conclusions

In this study the feasibility of deep learning techniques for crack detection on images from masonry walls is investigated. Even though masonry surfaces have been reported to be rather complex for CNN on crack detection, this study showcases that deep learning algorithms are able to accurately detect cracks from images of real masonry surfaces. In order to address the lack of data in the literature, a dataset with photographs from masonry structures was produced containing complex backgrounds and various crack types and sizes. Different deep learning networks are considered and by leveraging the effect of transfer learning crack detection on masonry surfaces is performed both on patch and pixel level. To the author's best knowledge, this is the first implementation of deep learning for pixel-level crack segmentation on masonry surfaces. State of the art CNN pretrained on ImageNet are examined for their efficacy to classify images from masonry surfaces on patch level with MobileNet obtaining the highest accuracy, that is 95.3%. U-net, a deep FCN, and FPN, a generic pyramid representation, are combined with different pretrained CNN performing as the backbone of the encoder part of the network to perform pixel level crack segmentation. U-net-MobileNet and FPN-InceptionV3 attain the highest F1 score, that is 79.6%, and outperform other networks for crack segmentation from the literature. In particular, for U-net-MobileNet, when the backbone CNN is considered without pretraining, F1 score declines from 79.6% to 75.4%, which demonstrates the beneficial effect of transfer learning. The ability of CNN to generalize over different materials is evaluated. The performance of U-net-

MobileNet trained on the masonry dataset deteriorates, i.e. F1 scores declines from 79.6% to 74.7%, when tested on concrete images but not as drastically as reported in the literature when networks trained on concrete images were consequently tested on masonry photographs. Codes, data and networks relevant to this study can be found in the GitHub repository: github.com/dimitrisdais/crack_detection_CNN_masonry.

Although the proposed deep learning algorithms achieved promising results, further improvements are required to achieve a fully automated vision-based assessment of masonry surfaces. The current study focuses on the detection of cracks but in the future the annotations of the masonry dataset could be updated to consider other defect types as well. The results of deep learning methods heavily rely on the quality of data. Thus, the expansion of the current masonry dataset is highly recommended with special care for the inclusion of even broader background types. In particular, including photographs under low-lighting conditions and further evaluating the accuracy of the crack detection is highly recommended. With the increasing accessibility to high quality camera sensors it is advised that the research community develops ways to further mobilize engineers, practitioners and citizens to contribute in the data collection process and provide them with guidelines and automatic procedures that will render the gathered data reliable. Significant research has been devoted to the automatic semantic segmentation of photographs coming from building façades, a technique known as façade parsing. Further studies are advised to evaluate whether façade parsing could be utilized to preliminarily detect objects like doors, ornaments, etc. and negate them so that the network would search for defects only on masonry surfaces. In this study, networks based on U-net and FPN architectures were implemented. Recent studies have come up with updated versions of these architectures which outperformed the original implementations. A further investigation whether these updated versions could improve the accuracy of the suggested deep learning algorithms for crack detection is encouraged. The best performing networks implemented here scored better than other networks which have already been successfully used in the literature for crack segmentation on concrete or asphalt surfaces. Thus, it is highly recommended that the best architectures used here are implemented on other types of surfaces as future research.

4.2 Novel invisible markers for monitoring cracks on masonry structures

Although the methods developed in Section 4.1 for automatic crack detection from photographs capture with acceptable accuracy the length of the detected cracks, the predictions regarding the crack width fail to reliably measure the actual value, especially in the sub-millimetre region. Crack width is a parameter that can provide crucial information on the severity and the progression of the damage and therefore obtaining such measurements

appears crucial. As discussed in Section 2.3.3, solutions that require surface preparation or placing markers around the cracks are highly visible and especially for the cases of monumental structures, where strict regulations apply, even simple interventions, such as placing crack-rulers, are not permitted by the conservation authorities. To overcome these limitations and complement the automatic detection of cracks, novel invisible markers were introduced for the monitoring of cracks with the use of computer vision and photogrammetry. The proposed method here shifts the marker reflection and its contrast with the background into the invisible wavelength of light (i.e. to the NIR) so that the markers are not easily distinguishable. The method is thus particularly suitable for monitoring historical buildings. Time-stamped continuous monitoring is possible since the digital photograph files automatically contain additional information on the location of the object, camera exposure and intrinsic parameters, as well as the date and time stamp. The method is also suitable for automatized monitoring of a large inventory of structures where the data can be collected by non-technical people or citizens and uploaded on a web server for further processing. Three main challenges are attempted to be addressed by the crack monitoring with the novel NIR markers: providing continuous and low-cost monitoring without needing high technical skills, focusing on cracks and progression of damage, and being discrete enough to be appropriate for applications on real structures.

In Section 4.2.1, the novel infrared markers are presented while clarification on the camera, flashlight and test setup used and the perspective correction technique are provided. The image processing procedure and the undertaken experiments are explained in Section 4.2.2. Finally, conclusions and recommendations for future research for the use of the newly introduced invisible markers are highlighted in Section 4.2.3.

4.2.1 NIR markers and crack measurement

Square markers are used in this study. The square shape of the marker is more in line with the masonry texture, making the markers even more invisible. Furthermore, a group of 4 markers is used for forming a gauge on each side of a crack. The 4-marker configuration decreases the errors and renders the marker setup more durable in case of loss of a marker.

As shown in Figure 4-18a, two groups of markers, each group consisting of 4 identical markers, are designed to be placed on both sides of a crack. Unlike conventional sensors, such as linear variable differential transformers (LVDTs) or potentiometers, which only measure along their axis, the proposed approach can detect deformations along any direction in the plane of the markers. Image processing algorithms can filter out the shining markers by creating a binary (i.e. black & white) photo from an image like in Figure 4-18d, a process explained in Section 4.2.2. In this process, the centroid of each marker is calculated pixel-wise, and then the centroid of each marker group is calculated by averaging the coordinates of each group of markers (i.e. left and right quadruple). The vertical and the horizontal

distance between the two centroids of markers quadruples is then used to monitor the crack in between.

The procedure described here is designed so that a non-technical person can also place the markers and take the photographs. This will allow citizen involvement, a procedure that can tremendously increase the amount of data while decreasing the costs. In order to replicate this in the tests presented here, three issues have been taken care of:

1. Material commercially available and easily accessible in the market are used (including the camera and the flashlight)
2. The photographs are taken by holding the camera always in hand, without a tripod
3. Instead of large and fixed flash sources, commonly used in laboratory applications, a simple hot-shoe NIR flash attached on the camera as the main light source

Two types of markers were tested: i) tape markers, and ii) reflective paint markers. The tape markers are intended for use directly on clay brick surfaces without any surface preparation. The reflective paint markers are for plastered and painted surfaces. Details of these markers are given in Sections 4.2.1.2 and 4.2.1.3. Both types of markers, although they do not match perfectly with the background colour, exhibit colours tones very close to the background making it hard to be distinguished by human eye.
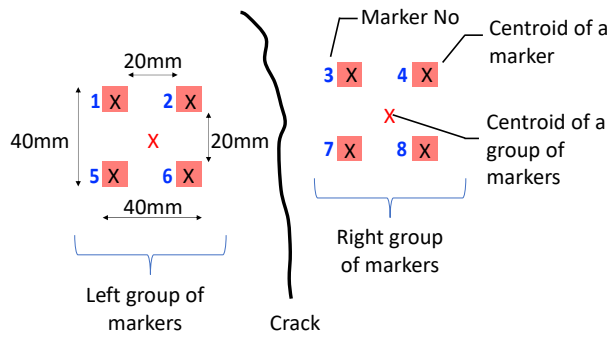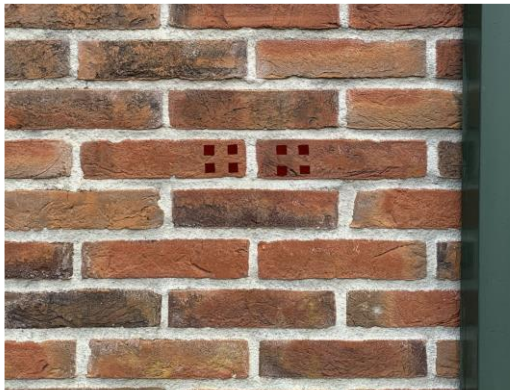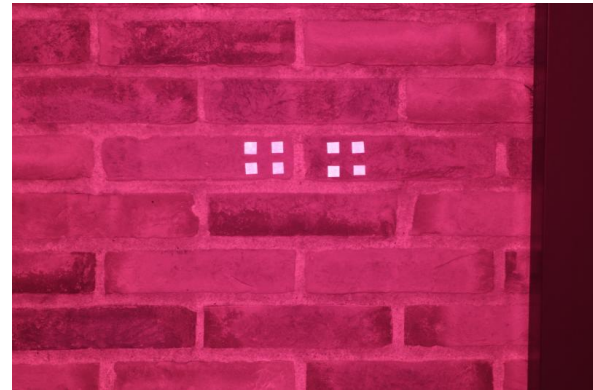
Figure 4-18. (a) Schematic view of the proposed marker setup and the marker numbering, (b) NIR markers on the outer wall of a real house, (c) close-up view of the NIR markers in the visible light, and (d) close-up photo of the markers captured with special NIR camera.

4.2.1.1 NIR camera and hot-shoe flashlight

The NIR images used in this study were taken by a commercially available DSLR type camera and a compatible hot-shoe flashlight. The camera and the flashlight were modified to be able to work only in the NIR region of light. A commercially available 24 MP DSLR consumer camera was modified by using a longpass filter (Hoya RM90) that transmits 50% of light at 920 nm. Longpass filter means that the filter will allow only above a certain wavelength of light to pass. Besides that, the flash attached on the camera has a longpass filter that is rated as 715 nm (i.e. 50% of light passes at 715 nm wavelength). The relation of the sensitivity areas of the camera and the flash in respect to the visible light can be seen in Figure 4-19.
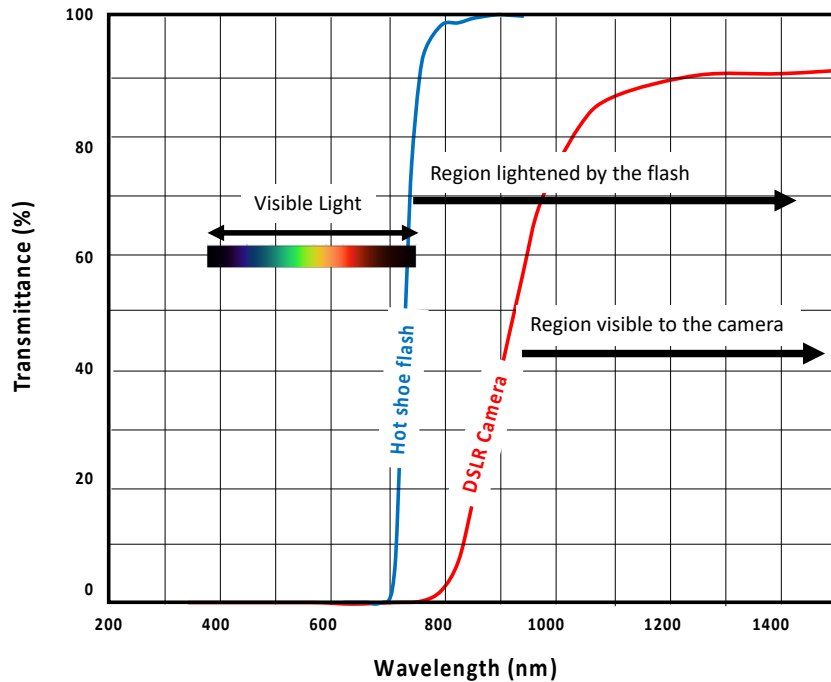
Figure 4-19. Comparison of the wavelength of the visible light, the visible region for the modified DSLR camera and the modified hot-shoe flash used in this study.

The camera intrinsic parameters and the photograph exposure play a major role in the accuracy and precision of the procedure. The key parameters that were evaluated are i) focal length, ii) shutter speed, iii) brightness (ISO), iv) aperture (F), and v) flash intensity. The focal length is set to 55 mm and kept constant in all photographs; this is because in this setting the distortion of the planar view due to the lens is minimized. The shutter speed, which defines the duration the camera lens stays open, is also set to a constant value as 125 (i.e. 1/125th of a second) which allows sufficient time so that enough light falls on the camera sensor but short enough not to lead to blurry edges when a tripod is not used. The rest of the parameters are set according to the marker type and the camera distance.

The NIR tape markers are used directly on clay brick surfaces while infrared reflective paint is used on painted surfaces. When tape markers are used, the clay is also an infrared reflective material, thus when a clay brick surface is subjected to infrared flashlight it shines more than a normal surface. In order to keep the contrast between the clay brick background and the tape markers, F18 and ISO 400 settings are used in all photographs taken from the tape markers in order to achieve smaller brightness for the background.

The painted surfaces absorb more NIR light than the clay brick surfaces and appear relatively dark in the photographs. This is also one of the main reasons why infrared reflective paints are used widely in automotive and construction industry. The infrared part of the sunlight is reflected back thanks to the infrared reflective pigments, which are also called "cool pigments" keeping the indoors cooler in hot summer days. This reflection keeps the surfaces painted

with this special pigment cooler than the surfaces painted with a normal paint. In the case of the reflective paint markers, more light needs to be emitted on the surface to create an acceptable level of contrast between the normal painted background and the reflective markers. This is the reason why F10/ISO 1000 is used for the photographs for the NIR reflective paint markers. The difference between the two settings (i.e. F18/ISO 400 for the tape markers versus F10/ISO 1000 for the paint markers) is evident when Figure 4-21 is compared to Figure 4-20. The binary photographs are mostly dark in Figure 4-20 (tape markers) while the background is white in Figure 4-21 (paint markers).

The flashlight used in this application is able to produce light in varying intensities. The intensity of the flash can automatically be detected by the flash depending on the distance from the object. However, this function does not work well in the NIR flash and camera combination. Instead, the flash intensity was set manually, by trying several options and finding manually a range of acceptable flash intensities for each camera distance. It is further discussed later that the flash intensity plays a major role in the accuracy and precision of the method, since it is the prime source of light produced in the NIR region. It is shown below that if the flash is either too strong or too weak, the accuracy deteriorates significantly. The flash intensity can be set from 1.0 (100%) to 1/2 (50%), 1/4 (25%) and so on. There are also three steps between these flash intensities, i.e. between 100% and 50%.

4.2.1.2 NIR tape markers

The idea behind the NIR tape markers is simple as the main reflective material is a retro-reflective tape, similar to those used in laboratory applications of structural testing (Kallioras et al. 2018). The retro-reflection allows the flashlight emitted by the reflector to always return to the camera, a property that minimizes the errors caused by varying camera angles. These are white stickers that are visible in daylight and shine in dark when subjected to any source of light. They are thus not directly usable for applications in real structures as they would create a disturbing view both in day and night. To avoid that, the retroreflective material is covered with a special tape used in photography, made of a derivation of plastic (PV1 – polyvinyl). This material is opaque in the visible light and becomes translucent in the NIR region. The lower layer of retroreflective material is covered with a sticky layer beneath for application on the wall surfaces. These 3-layer markers are then cut 10 mm x 10 mm dimensions and placed in the configuration as shown in Figure 4-18a.

The PV1 tapes are available in the market exclusively in ruby colour. If these markers be produced massively, then varying colours to better match the background brickwork texture can be produced. The tape markers would become even less visible in this case.

Another issue with the application of these markers is making perfect shapes. The markers used were manually produced and applied on brick samples. This yielded into a non-perfect

configuration of marker arrangement and also imperfect marker dimensions. If these parameters be industrialized, further accuracy and precision can be achieved.

Finally, the tape markers were applied on the brick surfaces with simple glued industrial paper, which is not necessarily durable enough for outdoor applications. Furthermore, the markers were used for short term measurements without actually being tested in terms of ultraviolet (UV) resistance. Application details of this sort need to be addressed before applying the technology on actual structures.

The actual view of the test setup from varying distances, as well as the NIR photographs and the processed binary photographs from the specimens with the tape markers can be found in Figure 4-20.

		Marker group centroid / Marker centroid
photo from 0.5m		
1.0m		
1.5m		
2.0m		
2.5m		
3.0m		
(a) Conventional camera	(b) NIR modified camera	(c) Processed image
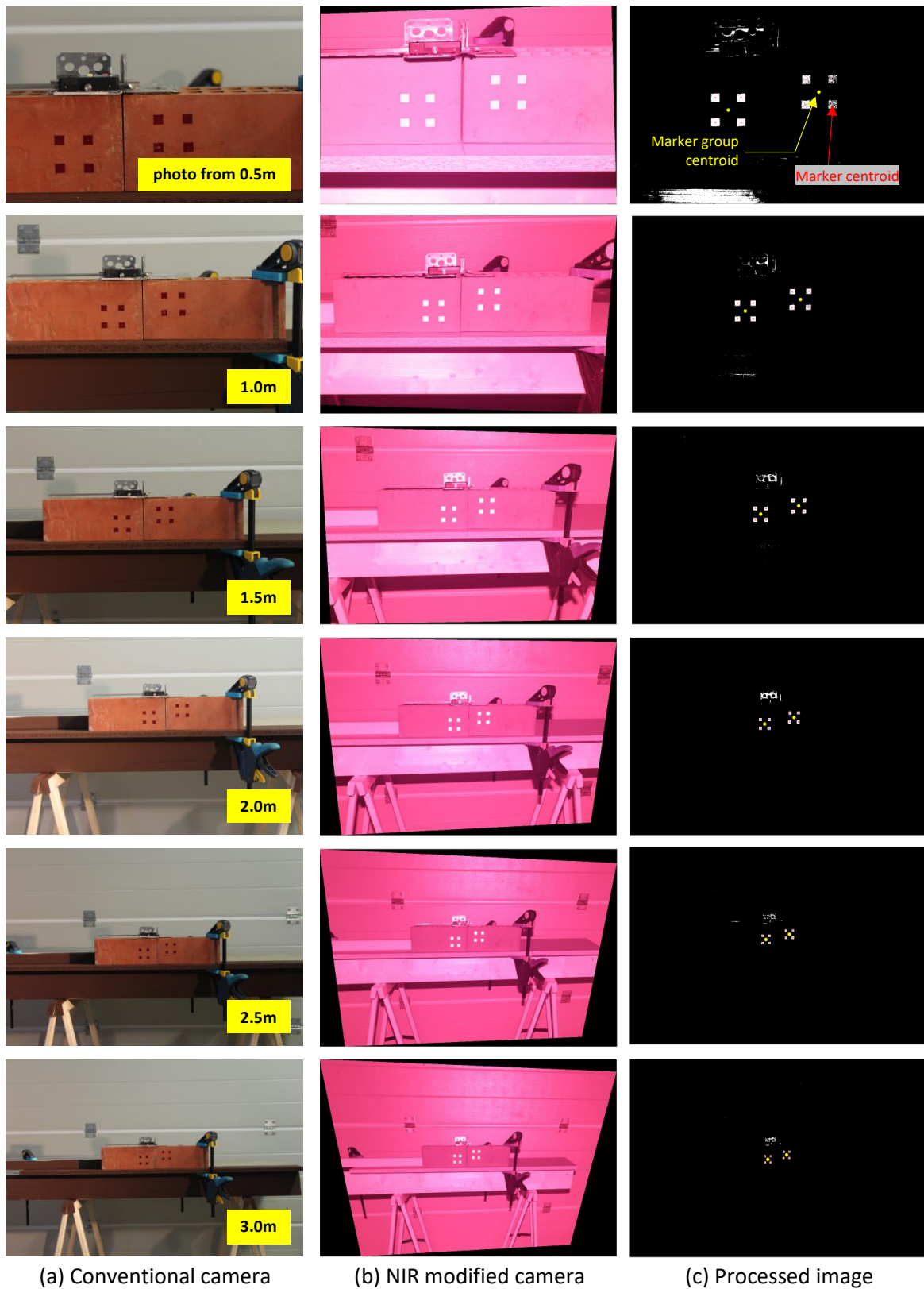
Figure 4-20. Photographs taken by a conventional camera (a), photographs taken by the NIR modified camera and perspective correction is applied (b), and binary (black & white) photographs created by the image processing procedure from the perspective corrected photographs (c) for the NIR tape markers.

4.2.1.3 NIR reflective paint markers

NIR reflective paint markers are applied on already painted surfaces (Figure 4-21). There are various colours available in the market. For the purposes of this study dark brown colour is used for the paint markers. The background was painted with a similar colour of paint suitable for outdoor applications. A template was cut from glued paper, placed on the painted brick surfaces, and then the infrared reflective paint was applied on the brick surface with a home-type paint spray to make sure a homogenous spread of paint material within the markers. A similar configuration to that of the tape markers is kept also in the paint markers.

(a) Conventional camera   (b) NIR modified camera   (c) Processed image
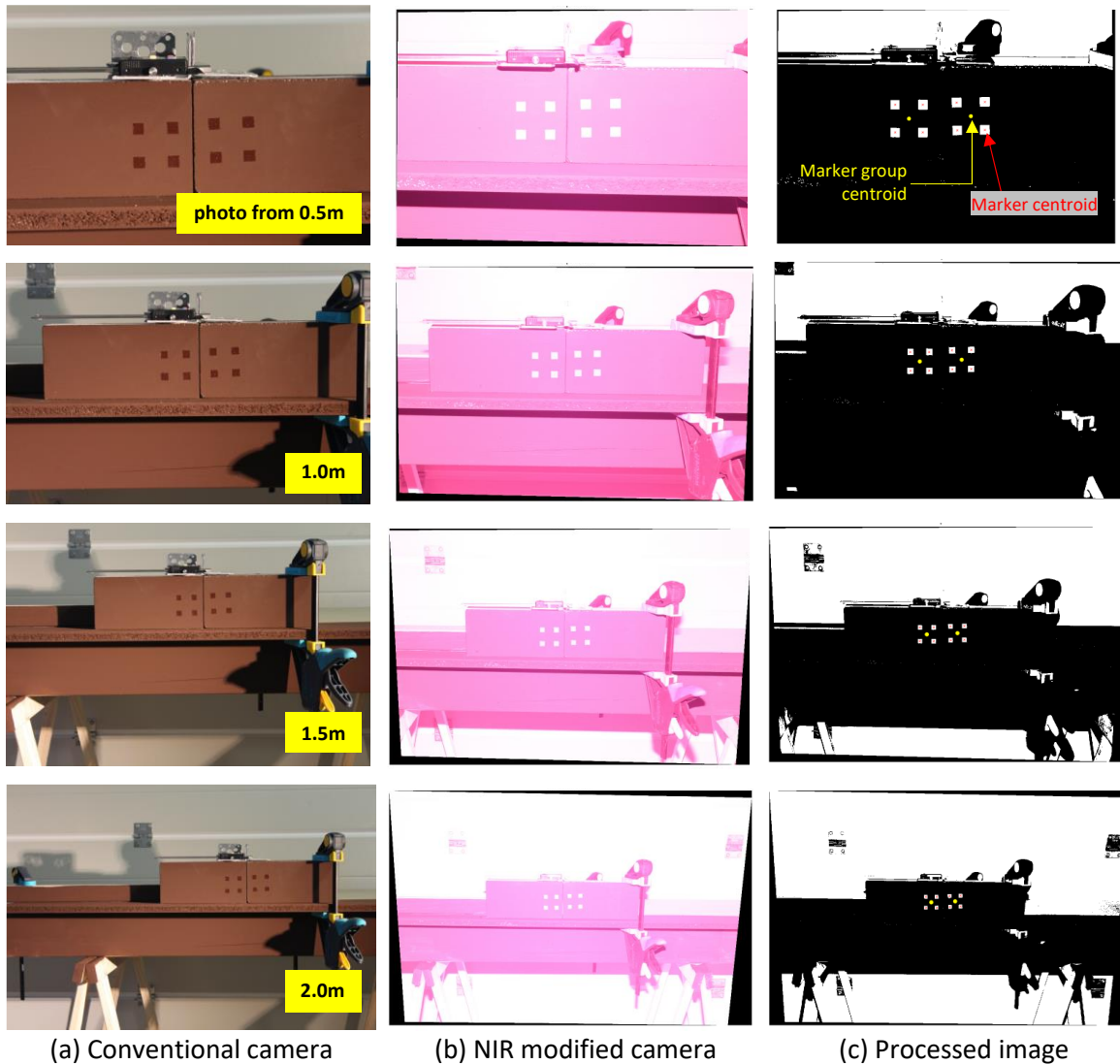
Figure 4-21. Photographs taken by a conventional camera (a), photographs taken by the NIR modified camera and perspective correction is applied (b), and binary (black & white) photographs created by the image processing procedure from the perspective corrected photographs (c) for the NIR paint markers.

Infrared reflective pigments are available in the market as dust. They need to be mixed with a correct type of binder (a liquid epoxy-based mixture) to become a paint and be able to adhere on the surface of application. The NIR light reflection ability of pigments depends on

the colour since the colour is the outcome of the material the pigments are produced from. Although a variety of colours is available commercially, these pigments are intended for industrial use and sold only in large quantities. It was rather difficult to get small sample quantities for the purposes of this study, so only one colour (dark brown) is tested here. However, various other colours can also be used in the exact same configuration, better matching the painted colour of the background.

The main advantage of the paint markers is that the application is very simple and the impact on the structure is almost none. Because the paint is only a very thin layer, it is also more difficult to be distinguished as compared to the tape markers, which need special attention on how to stick to the brick surface and how to provide UV protection.

The NIR paint markers were also tested directly on clay brick surfaces. However, as mentioned before, clay is also an infrared reflective material, thus the reflection from the paint markers does not create a large enough contrast with the background.

4.2.1.4 Test setup

Both types of markers, i.e. tape and reflective paint markers, were applied on brick surfaces by using the configuration presented in Figure 4-18a. Properties of the two marker types are listed in Table 1. Photographs were then taken at camera distances of 0.5, 1.0, 1.5, 2.0, 2.5 and 3.0 meters. In each distance, two or three different flash intensities were used as shown in Table 4-4.

The test setup consists of two bricks as shown in Figure 4-22. One of the bricks is fixed while the other is slightly moved to the sideway in each set of photographs. The two marker quadruples are then separated from each other, simulating a crack in a real-life example. The movement of one brick in respect to the other was measured with a digital calliper with mm/100 precision. The moving brick was moved along a guide in order to keep the movement within the marker plain. A set of photographs were taken first without any separation between the bricks, where the calliper was set to zero. Separations of 0.23, 0.56, 1.20, 1.80, 2.40, 3.53 and 5.00 mm were applied on the setup of the tape markers while 0.25, 0.53, 1.18, 1.91, 2.59, 3.70 and 5.04 mm separations were imposed in the case of paint markers.

Distances were marked on the floor and a photo was taken by hand (i.e. without the use of tripod) from each distance, following the flash intensity ranges shown in Table 4-4. As shown in Figure 4-20 and in Figure 4-21 (middle column), the photographs were taken from arbitrary horizontal and vertical angles as expected result of a manual process of photo taking.
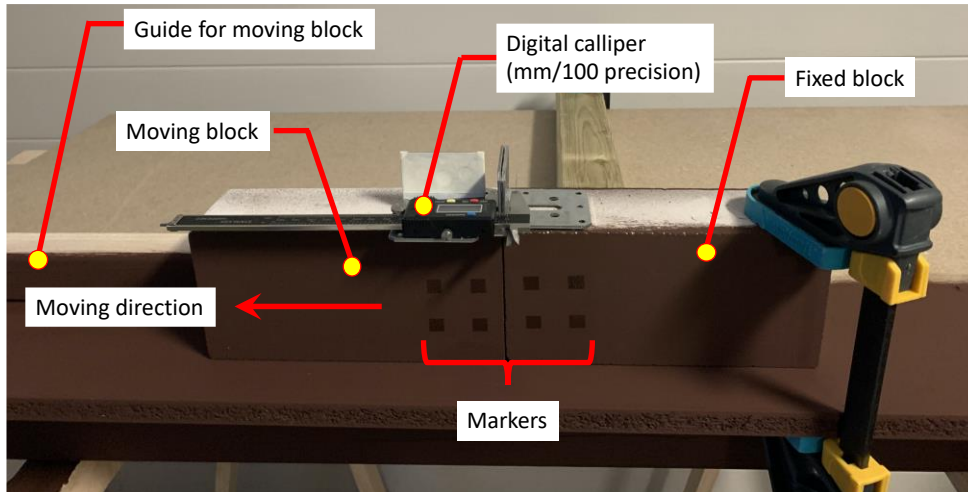
Figure 4-22. Test setup used in this study to evaluate the accuracy of the measurements with the NIR markers.

Table 4-3. Properties of the tape and paint markers.

Marker property	Tape marker	Paint marker
Material	From brick surface to outwards composed of 3 layers as: adhesive tape, retroreflective tape, NIR translucent tape	NIR reflective dust pigments mixed with epoxy-based bonding agent
Configuration	2 marker groups on each side of the crack, each group with 4 markers at the corners of a square (see Fig. 1a)	
Marker dimensions	10 mm x 10 mm	
Application to the surface	Stuck with an adhesive tape	Painted with a spray paint gun, over a custom-made template
Surfaces suitable	Naked brick, plastered or painted surfaced	
UV protection	No	Yes

Table 4-4. Camera distances and flash intensities used in the tests.

Camera distance [m]	Flash intensity notation	Flash intensity [%]
3.0	1/1	100
2.5	1/1	100
2.0	1/1	100
	1/1 - 0.3	85
1.5	1/1 - 0.3	85
	1/1 - 0.7	65
	1/2	50
1.0	1/2	50
	1/2 - 0.3	42.5
	1/2 – 0.7	32.5
0.5	1/4	25
	1/4 – 0.3	21.25

4.2.1.5 Perspective correction

Crack monitoring entails revisiting a location multiple times to extract measurements. Given the fact that the camera is kept in hand and not fixed to a constant point, corrections need to be accounted for the camera pose of each measurement (see Figure 4-23 for an example). In other words, a so-called homography transformation (a 3 × 3 matrix) is performed to map the points in one image to the corresponding points in a reference image (Hartley and

Zisserman 2004; Szeliski 2011; MATLAB 2019). The planar homography matrix relates the transformation between two planes (up to a scale factor) with the following relationship:

$$s \begin{bmatrix} x' \\ y' \\ 1 \end{bmatrix} = H \begin{bmatrix} x \\ y \\ 1 \end{bmatrix} \tag{4.12}$$

where s is the scale factor, H the homography matrix, and (x, y) and (x', y') the coordinates of a set of corresponding points in the two images. The homography transformation aligns any image taken with random camera pose to a reference image, while the scale factor translates pixel coordinates to a metric system, thus allowing to correctly measure any distances along the reference plane defined by the markers. The scale factor is calculated based on the distance of the markers which is predefined by the user.

Original Image   *Perspective Corrected Image*
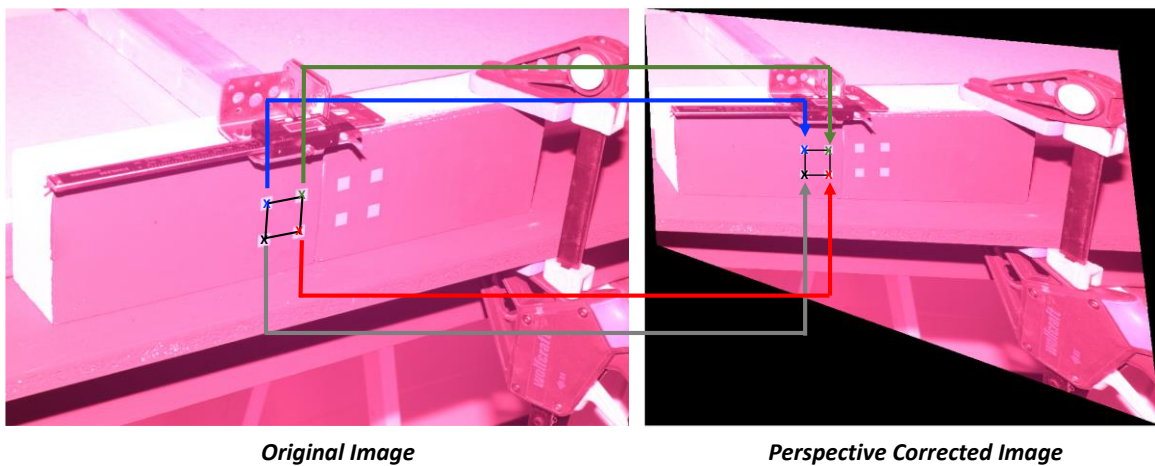
Figure 4-23. An example of perspective correction with the test setup used in this study.

4.2.2 Image processing procedure and experiments

The images taken from the test setup are then processed to find the position of the marker areas within each photo. The image processing code was developed in the MATLAB environment (MATLAB 2019). The procedure is as follows:

1. The image is turned into a gray-scale photo where the intensity of each pixel is between 0 (black) and 1 (white). An example of such a picture is shown in Figure 4-24 in step 1.
2. Because the markers are shining, they present high values of intensity, i.e. values close to 1, in the grayscale picture (see the 2nd step in Figure 4-24). In an iterative procedure, several thresholds of intensity values are used ranging from 0.6 to 1.0.
3. In each step of this iteration, pixels below the threshold value are turned into black and the rest into white. A binary (i.e. black and white) image is obtained in this way.
4. In the binary image, boundaries are defined. A boundary is an island of connected white pixels in a black background.

5. A geometric compatibility check is applied on each boundary. According to this, too large or too small boundaries, boundaries that are not square-like, or boundaries that are not towards the middle of the photo are eliminated.

6. If exactly 8 boundaries remained after the geometric compatibility check, and if the distance ratios between these boundaries are similar to those distance ratios of the actual markers, then this iteration with this light intensity factor is flagged as appropriate.

7. Marker positions obtained from an iteration flagged as appropriate, are then used for calculating the geometric error, d, as shown in Eq.(4.15). The light intensity factor which gives the smallest geometric error (Δ) is accepted as the best iteration, and the rest of the steps are conducted by using this light intensity limit obtained from this iteration. For instance, in the example image of Figure 4-24, the value of 0.96 was estimated as the best intensity limit. If the image in the second step of Figure 4-24 is vertically cut at 0.96, then the plot in the third step of the same figure is obtained. In the third step, the markers are detected together with other shining surfaces, but the geometric tests eliminate the non-compliant surfaces and filter out the markers only. The geometric error (Δ) is calculated as:

$$\delta_{left} = \left| \frac{\left(\frac{LM_{52}}{LM_{61}} - \frac{LA_{52}}{LA_{61}} \right)}{(LA_{52}/LA_{61})} \right| \tag{4.13}$$

$$\delta_{right} = \left| \frac{\left(\frac{LM_{74}}{LM_{83}} - \frac{LA_{74}}{LA_{83}} \right)}{(LA_{74}/LA_{83})} \right| \tag{4.14}$$

$$\Delta = \frac{\left(\delta_{left} + \delta_{right} \right)}{2} \tag{4.15}$$

where LM_{ij} is the pixel-wise distance measured in the image processing algorithm between marker 'i' and marker 'j', LA_{ij} is the actual distance between the same markers of ''i' and 'j'. These distances are measured between the diagonals of each marker quadruple (see Figure 4-18a for the marker numbering). In an ideal situation, the geometric error (Δ) should equal to zero. The higher values departing from zero translate to higher errors of the measurement.

8. Once the best threshold value is determined iteratively, then the marker positions, centroids and quadruple centroids are calculated pixelwise. One of the marker quadruples is used for perspective correction of the image as explained in Section 4.2.1.5. The centroids of the four markers in one quadruple are defined as a perfect

square and the image is aligned in respect to the reference image forming a perfect square at the location of the quadruple.

9. A new and perspective-corrected image is obtained. Geometric compatibility checks are once more applied on the perspective-corrected image and the new positions and the pixel coordinates of the 8 markers are re-calculated along the reference plane.

10. Pixel coordinates are translated to a metric system. A pixel-to-metric scale factor is calculated based on the distance of the markers which is predefined by the user. By using this conversion, actual dimensions and the separation between the marker quadruples are calculated along the plane of the markers.

The results are presented in terms of the agreement of the measured separation with the actual separation of the brick blocks. In order to evaluate the reliability of the measurements two metrics are used, i.e. accuracy (Eq. (4.16)) and precision (Eq. (4.17)). Accuracy is the correctness of a measurement, while precision shows the statistical dispersion of the results. A higher dispersion means less precise results, in other words, higher measurement-to-measurement variations. The formulae for accuracy and precision are given below in Eq. (4.16) and Eq. (4.17) (see Nishiyama et al. (2015) for a similar approach).
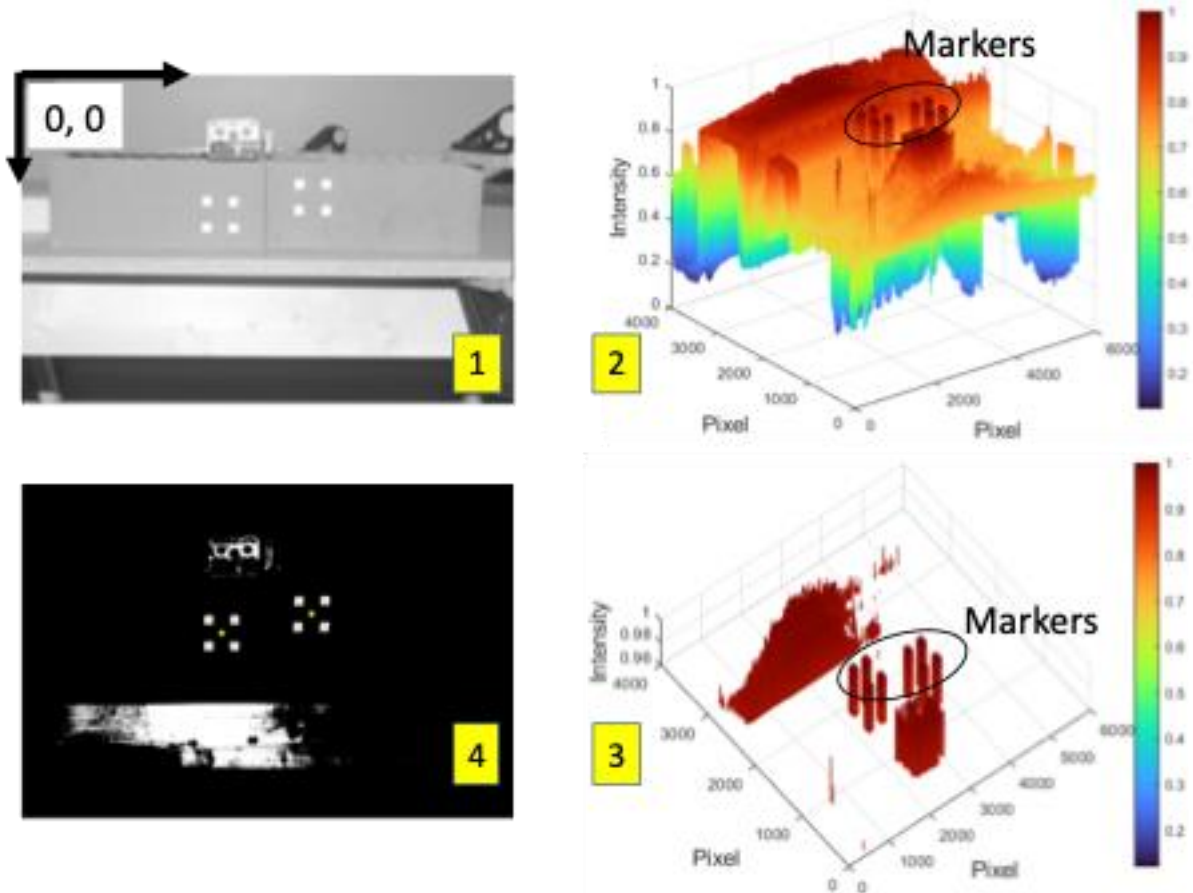
Figure 4-24. Steps of the image processing method; (1) grayscale image, (2) intensity distribution in the grayscale image from 0 to 1, (3) pixels with intensity lower than the threshold value of 0.96 are discarded, and (4) binary image created by using 0.96 as intensity threshold, and the markers automatically spotted by using the geometric compatibility checks.

$$Accuracy = \sqrt{\frac{\sum(x - x_0)^2}{n}} \tag{4.16}$$

$$Precision = \sqrt{\frac{\sum\left(x - \frac{\sum_{i=1}^{n} x}{n}\right)^2}{n}} \tag{4.17}$$

where n the is the number of measurement data, and x and x_0 are the measured and actual separations respectively. Comparison of the measured versus actual separation is satisfactorily good as shown in Figure 4-25. It would normally be expected that the closer the camera to the markers, the better the measurement would be. This may be correct in normal markers, since a closer photo means a larger number of pixels fitting into a marker boundary, minimizing the pixel-wise errors. Nevertheless, this is not the case in the NIR markers since the photo is illuminated with a strong NIR flash and the reflection amount is dominated by the intensity and the angle of the flashlight on the surface. This issue can be more clearly seen in Figure 4-26 where accuracy and precision of measurements are presented for each

distance. The accuracy values are worse for the closest distance (0.5 m) in both marker types. The reason for this is that the strong flash creates a strong reflection on the surfaces of the object, creating a noise around the edges of the markers. These arbitrary edges then shift the centroid of the marker boundaries, leading thus to an error in the measurements. The best picture distance is 1.5 m in the tape markers and 1.0 m in the painted markers, provided that the exposure parameters are used as described above. This is a very practical information since approaching the walls more than 1-1.5 m is most of the times not possible or allowed. It is reminded that for the whole set of experiments the focal length is kept equal to 55 mm in an 18 x 55 lens, while the larger distances could also work with a lens with a higher zoom capability.

Another observation is that the painted markers perform better than the tape markers both in terms of accuracy and precision. It is possible to obtain 0.05 mm accuracy and 0.04 mm precision with the painted markers. The accuracy and precision can be 0.05 mm and 0.052 mm respectively in the case of tape markers, respectively. Considering that the crack widths start to be noticeable by the human eye from 0.1 mm (Burland and Wroth 1974), accuracy and precision of both markers are satisfactory for practical use in masonry brick or plastered and painted masonry surfaces, thus the proposed method can reliably replace crack monitoring sensors.

(a) Tape markers
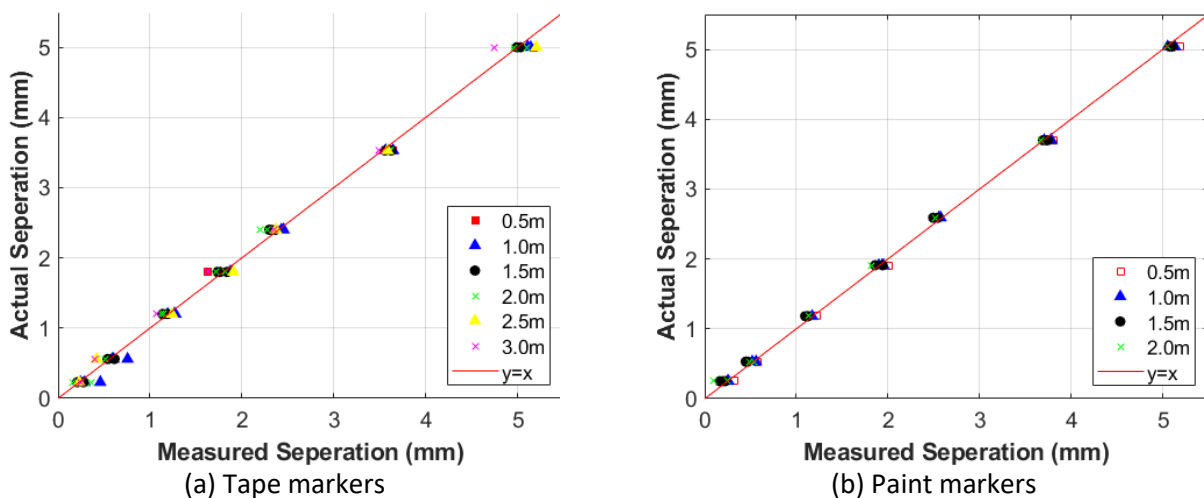
(b) Paint markers

Figure 4-25. Comparison of the measured vs actual separation of the brick blocks; tape markers (a), and the paint markers (b).
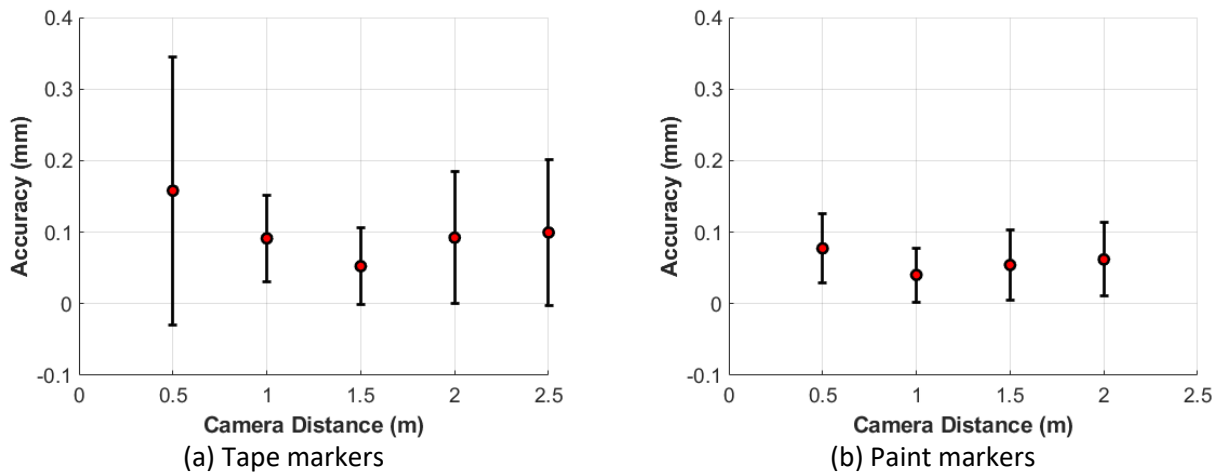
Figure 4-26. Accuracy of the measurements from multiple photographs with a varying range of flash intensities (vertical lines represent the precision of the measurement); tape markers (a), and the paint markers (b).

4.2.3 Conclusions

Historical buildings with acute structural problems, aging masonry structures and infrastructure inventory (masonry arch bridges, tunnels, viaducts etc.) need increasingly more attention. Higher operational loads, change of their use, extreme loads like induced or natural earthquakes and strains imposed by the climate change are the major threats to our aging masonry built stock. Failure of such structures and infrastructure could lead to significant direct and indirect costs to the economy and society and could hamper rescue and recovery efforts. The cost of replacing masonry infrastructure in Europe alone would run into tens of billions of euros. Last but not least, in most cases the aesthetic and heritage value of masonry infrastructure is significant.

Visual inspection is a manual process that has been used internationally for keeping track of the health condition of masonry structures and monitoring the progress of damage. However, the method is time consuming and subjective (giving rise to variance in standards and quality) which makes the task of prioritising renewal or refurbishment schemes extremely difficult. Human-based inspections are also highly costly and difficult to manage when a large number of structures needs to be assessed.

Alternative technological methods, such as photographic techniques, which are more efficient and reliable, could help meeting the challenges of examining of these structures; especially the identification and monitoring of crack development. Although there are very sensitive DIC techniques widely available for the laboratory applications and for experiments, they need surface preparation or require markers that are easily visible, disturbing the aesthetic look of a structure. Furthermore, in such laboratory applications, the camera needs to remain in a fixed position. When dealing with real structures and particularly with historical buildings, aesthetically acceptable methods with minimum intervention are needed.

Here a technique was proposed for measuring cracks in masonry structures using a digital camera. Two different types of markers, which are not easily noticeable by human eye but exhibit high reflection when subjected to NIR wavelength of light, were used. The first type of marker was a retroreflective one covered by a special tape that is opaque in visible light but translucent in NIR. The second marker was a paint produced from infrared reflective pigments. The markers were placed at areas of interest and digital camera images of the targets were processed by photogrammetry and image processing. A series of experiments were conducted to verify the potential of approach and the measurement accuracy and precision. Measurements obtained from image processing were measured against the ones obtained from manual measurements. From the results analysis, it was shown that:

- Separation distance of bricks, representing cracks, was measured by image processing and compared to the actual separations.
- A camera, held in hand and up to 2.5 m distance to the brick surface, was able to capture photographs that provide high accuracy, which was below 0.1 mm in average in most cases.
- The accuracy values were worse for the closest distance (0.5 m) in both marker types
- The best picture distance is 1.5 m away from the target for the tape markers, and 1.0 m for the painted markers, provided that the proposed camera settings were used.
- The painted markers perform better than the tape markers both in terms of accuracy and precision.
- The variation of the accuracy in the case of tape markers was minimum 0.06 mm and maximum 0.17 mm for 1.5 m and 0.5 m camera distances, respectively.
- The variation of the accuracy in the case of paint markers was much smaller, 0.04 mm at minimum and 0.06 mm at maximum, for 1.0 m and 0.5 m camera distances, respectively.
- For both painted and tape markers, the accuracy could be in the range of 0.05 mm < 0.1 mm (crack widths noticeable by the human eye) which verifies the suitability of the approach to measure cracks in masonry walls or plastered and painted masonry surfaces.

The proposed technique is fast and reliable in measuring changes in the crack length and width. The method is especially useful for historical buildings, for monitoring progression of damage also in slow acting events such as foundation settlements. The technique could also be used by non-technical people. So, citizen involvement is also possible in collecting data from the field.

In the future, the effects of angle to the wall on the accuracy of the method will be evaluated. Lenses with higher focal length will be examined in the future to allow for measurement from longer distances. In addition, performing further research and taking measurements on actual

sites with the aim to assess reliability and durability of the markers to weathering and improve efficiency of the proposed system are already planned.

Chapter 5
Quantification and modelling of damage evolution in masonry walls subjected to in-plane recursive load

In this Chapter, quantification and modelling of damage in URM structures was attempted by taking into consideration the initiation and propagation of damage due to earthquake excitations. The evaluation of damage in masonry structures due to (induced) earthquakes represents a challenging task. Cumulative damage due to subsequent ground motions is expected to have an effect on the seismic capacity of a structure. Based on the literature review (Section 2.6), even though crack-based assessment has attracted the interest of the research community, relevant studies on URM are rather limited. Experimentally obtained crack patterns were investigated and their correlation with damage propagation was examined (Section 5.2). As highlighted by the findings of the literature review (Section 2.8), analytical tools may be a solution to shed light on the repeated earthquakes and their damage in the masonry structures. Discontinuous modelling techniques are able to reliably reproduce damage initiation and propagation by accounting for residual cracks even for low intensity loading. Detailed models based on the DEM (Section 5.1) and FEM analysis (Section 5.3) were considered to capture and quantify the cumulative damage in micro level in masonry subjected to seismic loads.

5.1   Numerical exercise on the quantification of damage evolution with the Distinct Element Method

Detailed models were created employing the DEM approach in UDEC software (ITASCA 2011), a tool based on discontinuous modelling that can simulate the response of discontinuous media subjected to either static or dynamic loading. A damage indexing equation was proposed to quantify the damage evolution based on the numerical exercise undertaken with the DEM (Section 5.1.1). An overview of the DEM for modelling masonry walls is provided in Section 5.1.2. In particular, the representation of masonry units (Section 5.1.2.1) and mortar joints (Section 5.1.2.2) along with the numerical solution (Section 5.1.2.3) and the implementation of the damage indexing equation in the DEM (Section 5.1.2.4) are elucidated. The developed numerical model was validated against a series of full-scale experimental tests obtained from the literature (Section 5.1.2.5). The accumulated damage within the seismic response of the masonry walls was investigated by means of representative harmonic load excitations (Section 5.1.3) and an IDA based on induced seismicity records from the Groningen region (Section 5.1.4). Conclusions and limitations on the quantification of damage evolution in masonry structures are exhibited while recommendation for future research are regarded in Section 5.1.5.

5.1.1 Damage indexing equation

Existing masonry structures, especially historical ones, are usually characterized by their low bond strength. Low bond strength masonry refers to masonry in which the tensile and shear bond at the unit-mortar interface is so low that it has a dominant effect on the mechanical behaviour of masonry, including the formation of cracks and the formation of the collapse mechanisms (Giamundo et al. 2014). Therefore, any damage indexing scheme for masonry should consider the proportion of joints that have undergone inelastic slip or tensile/shear opening (i.e., cracking) of the mortar joints. Also, when a structure is subjected to lateral loads, it sustains lateral deflections. At structural element level, drift can be estimated as the difference in lateral deformation between two stories of a structure due to the application of later loads (such as seismic loads). In its simple format, for a single-story building, lateral drift equals the amount of horizontal displacement at the top. Lateral drift is an important indicator of the level of damage in a building after an earthquake (FEMA 2000). Also, based on the ISD ratio (relative displacement divided by the inter-storey height), the building can be classified as serviceable, safe, or unsafe. Typically, the ISD ratio should not pass a certain drift limit to keep it at a certain performance level (EN-1998-1 2005; ASCE 2017).

The introduced damage index (DI) equation can be used to quantify damage evolution on URM structures subjected to seismic excitations. The DI equation consists of three damage parameters which include: a) the extent of drift ratio (DI_drift); b) the length of joints opened (DI_open); and c) the length of joints at shear failure (or slippage) (DI_slip):

$$DI = 1 - \left(1 - DI_{drift}\right) \times \left(1 - DI_{open}\right) \times \left(1 - DI_{slip}\right) \qquad (5.1)$$

$$DI_{drift} = \frac{\delta}{\delta_{limit}} \qquad (5.2)$$

$$DI_{open} = \frac{Length\ of\ joints\ opened}{Total\ length\ of\ joints} \qquad (5.3)$$

$$DI_{slip} = \frac{Length\ of\ joints\ slipped}{Total\ length\ of\ joints} \qquad (5.4)$$

where, DI_drift is the drift ratio (δ) by a drift limit value (δ_limit) which refers to the Near Collapse (NC) state of the structure under investigation. Messali & Rots (2018) investigated the in-plane drift capacity at NC of rocking URM piers and the average ultimate drift for the piers failing with flexural mode was found 2%. This value was considered as the drift limit that the drift ratio was normalized with, since the examined walls (Section 5.1.3 and 5.1.4) were characterized by flexural failure. DI_open and DI_slip relate to the length of joints that opened due to tension and the length of joints slipped (or at shear limit) due to shear respectively, divided by the total length of joints. In this way, the DI_open and DI_slip are normalized metrics

of the cracks along the surface of the wall and are independent of the dimensions of the structural element. According to Burland et al. (1977), cracks greater than 0.1 mm in width are visible to the naked eye. This value of inelastic relative displacement at the joint was adopted as the criterion for registering a joint as 'opened'. The value of the calculated DI and the individual components DI_{drift}, DI_{open}, and DI_{slip} ranges from 0 (no damage) to 1 (catastrophic collapse or all joint failed or drift limit reached).

5.1.2 Overview of the Distinct Element Method for modelling masonry walls

The proposed damage indexing scheme was integrated to a modelling approach based on the DEM to study the mechanical behaviour of masonry structures under seismic loading. The DEM belongs to the discontinuum analysis approaches. UDEC is a two-dimensional command driven software that was developed by Cundall (1971) in early 1970s for solving problems related to sliding of rock masses and falls within the DEM. Since then, the code has been used with success to simulate the static and dynamic behaviour of blocky systems including masonry structures e.g. (Lemos 2007; Sarhosis and Sheng 2014). The code's framework is different to that of the well-known FEM. Within UDEC, a masonry wall can be considered as a series of distinct blocks separated by zero thickness interfaces. Such zero-thickness interfaces can open and close depending on the stresses they sustain (Sarhosis and Lemos 2018). Masonry units are represented by blocks which could have any geometric shape and can be assigned different mechanical properties even in the same model. The DEM can be used to realistically represent geometrical, physical, and mechanical characteristics of a masonry structure as opposed to the numerical methods in which continuity theories exists and masonry is considered as a simplification into an unrealistic continuum (Sarhosis and Lemos 2018). Another characteristic of the DEM is that large displacements and rotations of the masonry units are allowed and that detection of contacts between neighbouring masonry units and updating of contacts is occurring simultaneously and as the simulation proceeds (ITASCA 2011). In addition, the DEM can make use of an explicit dynamic solution algorithm scheme which allows real dynamic analysis to be undertaken.

5.1.2.1 Representation of the masonry units in a masonry wall

When defining the model in UDEC, a single block covering the domain to be analysed is considered. The geometric features of the model are then introduced by discretizing the block into smaller ones (e.g., masonry units) whose boundaries represent discontinuities (e.g., mortar joints). It is these discontinuities which allow the interaction between blocks to take place as the simulation proceeds. Since the mortar joints are simulated by a zero-thickness interface, the size of the masonry units has to be expanded slighted (e.g. half of the mortar thickness in each direction) to accommodate this. In general, blocks can take any geometry and could differ from each other in size and shape. Individual blocks can be rigid or

deformable. Rigid blocks can be used when the behaviour of the system is dominated by the joints (i.e., in cases where masonry units are strong, the mortar joints are weak, and failure is a result of debonding of masonry units to mortar joints or failure of the mortar joints). Deformable blocks are used when deformation of masonry units plays a role in the mechanical response of the system or when internal stresses in masonry units needs to be estimated. The complexity of the deformation of the blocks depends on the number of zone elements into which they are divided (i.e., finite discretization), and the constitutive law assigned to them. The constitutive model assigned to the zones could be either linear elastic or non-linear elastic and the strain for each separate block can be estimated. The material parameters for the linear elastic model are the unit weight of the brick, the bulk modulus (K) and the shear modulus (G) are given as:

$$K = \frac{E}{3(1 - 2v)} \tag{5.5}$$

$$G = \frac{E}{2(1 + v)} \tag{5.6}$$

where E is the Young's modulus and v is the Poisson's ratio of the brick. Also, the size of simulation is limited by the number of masonry units which is a function of the available computational power.

5.1.2.2 Representation of mortar joints in a masonry wall

Within the DEM, mortar joints are represented by zero-thickness interfaces. At each interface, masonry units are connected cinematically to each other by contacts; the so called contact hypothesis approach (Cundall and Hart 1993). These contact points are positioned at the outside perimeter of the masonry units. For deformable blocks, the contact points are located at the edges or corners of the blocks and the zones. In this way, geometric interaction between the blocks is allowed. A significant advantage of the contact hypothesis method is its ability to mesh the block independently without the need to match nodal points. So, the more the number of contact points, the higher the accuracy of the stress distribution in the blocks. The contact points in UDEC are "soft". This means that the contact forces are generated as a result of interpretation of adjacent blocks. The amount of interpenetration is controlled by the user and does influence the computational time. At each contact point there are two spring connections. The springs allow the transfer of a normal force or a shear force from one block to the other. The joints constitutive laws used in the present study are displayed in Figure 5-1. In the normal direction, the mechanical behaviour of mortar joints can be represented using the following equation:

$$\Delta\sigma_n = -k_n \cdot \Delta u_n \tag{5.7}$$

where k_n is the normal stiffness of the contact (stress deformation characteristic), $\Delta\sigma_n$ $\Delta\sigma_n$ is the change in normal stress and Δu_n is the change in normal displacement. Similarly, in the shear direction the mechanical behaviour of the joints is controlled by constant shear stiffness k_s using the following expression:

$$\Delta\tau_s = -k_s \cdot \Delta u_s \tag{5.8}$$

where $\Delta\tau_s$ $\Delta\tau_s$ is the change in shear stress and Δu_s Δu_s is the change in shear displacement along the joint. Stresses calculated at grid points along contacts are submitted to the Mohr-Coulomb failure criterion which limits shear stresses along joints. The following parameters are used to define the mechanical behaviour of the contacts: the normal stiffness (k_n), the shear stiffness (k_s), the internal friction angle (φ), the cohesion (c) and the tensile strength (f_t). The dilation angle was assumed zero, as per Sarhosis & Sheng (2014).
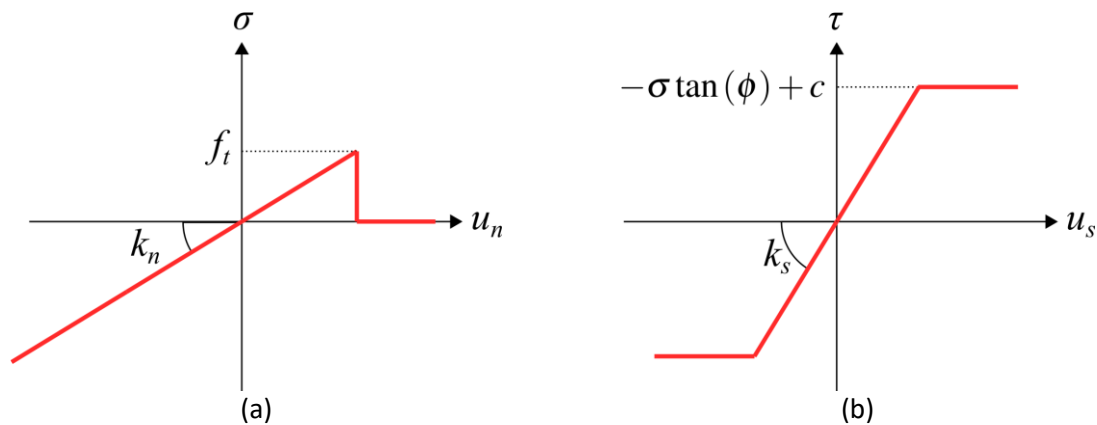
Figure 5-1: Joints constitutive laws used in the present study: (a) joint behavior in the normal direction; and (b) joint behaviour in the shear direction.

A problem often encountered when modelling masonry is the unrealistic response when brick interaction occurs close to or at two opposing brick contacts. At this point, numerically, blocks may be locked or hung-up due to the modelling assumptions that brick corners are sharp or have infinite strength. In a real masonry structure this will only occur because of stress concentrations. Simulating such a phenomenon is impractical. A realistic representation can be achieved by rounding the corners of the blocks so that they can smoothly slide past one another when two opposing corners interact. A short corner rounding length (e.g. 1% of the block's length) gives a good level of accuracy.

5.1.2.3 Numerical solution

Estimation of motion in masonry units is made using the force displacement law at all contacts and the Newton's Second Law of motion at each time increment using the central difference method. Contact forces can be obtained from the force-displacement law. Similarly, the motion of the masonry units can be obtained from the known forces acting on the nodes using the Newton second law. For the numerical solution, a dynamic relaxation procedure is

adopted. Adaptive damping is used for convergence to static solution. A limit step can be defined by the user which helps to avoid numerical instabilities. The timestep can be calculated using the equation below:

$$\Delta t_n = 2f \sqrt{\frac{M_n}{K_n}} \qquad (5.9)$$

where and K_n is the overall stiffness of the units and contacts connected to the node, M_n is the nodal mass, and f is a user-defined factor which controls the timestep (ITASCA 2011). The length of the computational effort can be minimized by parallel processing, scaling up the number of units and scaling up the length of simulation.

A characteristic feature of UDEC is the geometric non-linearity of the intact bricks to be modelled. In other worlds, the displacement of the bricks due to shear and opening up of the interface can be immediately included in the calculations. So, it is possible that bricks which were originally adjacent to each other could either become partially or entirely loosened from each other, or new contact points could be formed between bricks that were initially not next to each other. This is significant feature of UDEC when modelling problems involving discontinuities such as low bond strength masonry, where the predominant failure mechanism is due to the de-bonding of the bricks or blocks from the mortar, as the location and the magnitude of surface crack widths within a masonry structure can be determined realistically. Detecting and updating brick contacts in a numerical model is the most time-consuming part of the software's calculation.

5.1.2.4 Implementation of damage indexing equation in the Distinct Element Method

Mortar joints can open, close and slip depending on the stresses acting on them (Figure 5-2). Criteria for joint opening and slip are based on the magnitude of normal displacement or on the shear stresses levels. Joint opening occurs when the normal stress σ_n at a contact exceeds the tensile strength f_t, a condition expressed by the equation:

$$\sigma_n \geq f_t \qquad (5.10)$$

The value of f_t is defined by the user and can be taken experimentally by undertaking small scale testing e.g. crossed brick couplets. Upon reaching this condition, the normal stress is reduced to zero and the tensile strength of the interface vanishes. According to the relative displacement threshold of 0.1 mm established, joints are marked as opened when this threshold is exceeded. However, this threshold value can be assigned by the user.

Slippage between the units will occur when the shear force at a contact reaches a critical value f_s defined by the Mohr-Coulomb criterion:

$$\tau_s \geq -tan\varphi \cdot \sigma_n + c = f_s \qquad (5.11)$$

where τ_s is the shear stress at the joint, c is the cohesion and $tan\varphi$ is the internal friction coefficient. The value of cohesion and friction can be obtained from small scale tests such as triplet shear tests.
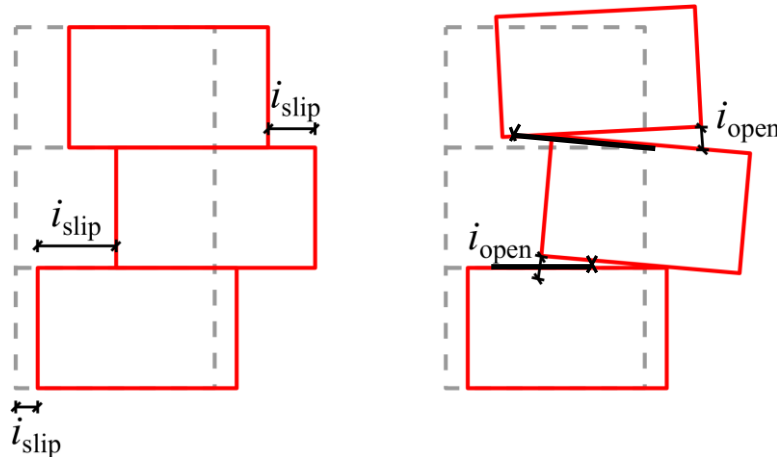
Figure 5-2: Representation of joints opening and joint at shear limit. Parameters i_{slip} (length of joints slipped) and i_{open} (length of joints opened) recorded during the simulation.

5.1.2.5 Validation of the Distinct Element Method for masonry walls

A two-dimensional numerical model based on DEM was developed to estimate and understand the extent of damage accumulation in masonry walls with and without openings subjected to induced seismicity events. All walls had dimensions equal to 4 m width and 2.75 m height (Figure 5-3), typical in Dutch construction practice. One solid (Figure 5-3a) and two perforated walls, either symmetric (Figure 5-3b) or asymmetric (Figure 5-3c), were examined. The size of the opening was set to 2 m by 2.5 m. Such large openings on the façade are quite common in the building inventory within the Groningen gas field. The vertical sides of the wall were left free. In addition, the top of the wall was also free to rotate creating a cantilever condition. A vertical pre-compression equal to 0.3 N/mm^2 was applied at the top of the wall during loading. Each brick of the masonry wall panel was represented by a deformable block separated by zero thickness interfaces at each mortar bed and perpendicular joint. To allow for the 10 mm thick mortar joints in the real wall panels, each deformable block was based on the nominal brick size increased by 5 mm in each face direction resulting in a model block size of 225 mm × 102.5 mm × 75 mm.
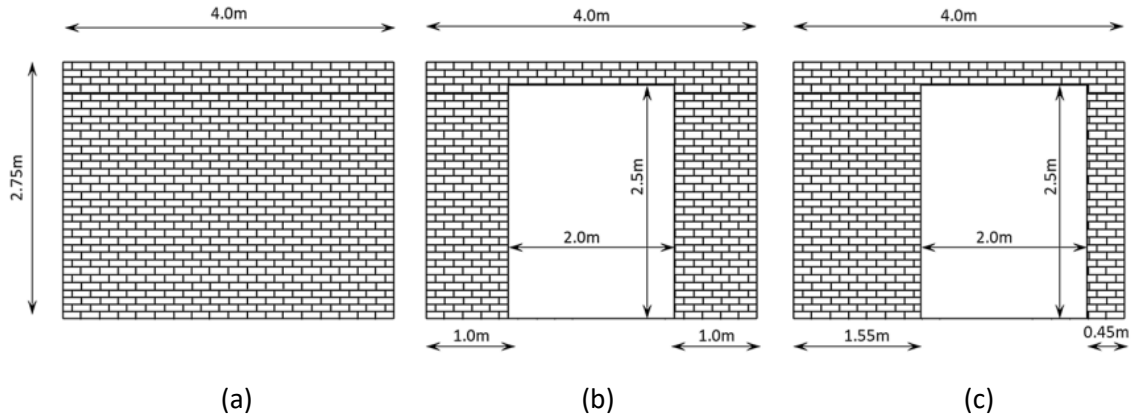
Figure 5-3: The geometry of the models developed: (a) wall panel with no opening/solid wall; (b) wall panel with symmetric opening; (c) wall panel with asymmetric opening.

The developed model was validated against experimental results obtained from Graziotti et al. (Graziotti et al. 2017). The material properties of the zero-thickness interfaces and the masonry units are presented in Table 5-1 and Table 5-2 respectively. A comparison between the experimentally obtained behaviour and the numerical model is illustrated in Figure 5-4 in terms of initial stiffness and hysteretic behaviour. Overall, good agreement was obtained, with the stiffness and peak force being approximated with very good accuracy and the unloading/reloading stiffness being reasonably well reproduced. A comparison of the experimental against the numerically predicted crack patterns is shown in Figure 5-5. Considering the inherent variability of masonry, the numerical model was able to capture the failure mode fairly accurately.

Table 5-1: Material properties of the zero-thickness interfaces used in the numerical model.

Normal stiffness, k_n [N/m³]	Shear stiffness, k_s [N/m³]	Internal friction angle, φ [°]	Tensile strength, f_t [N/m²]	Cohesion, c [N/m²]
12 x 10¹¹	4 x 10¹¹	32	0.21 x 10⁶	0.24 x 10⁶

Table 5-2: Material properties of the masonry units used in the numerical model.

Young's modulus, E [N/m²]	Bulk Modulus, K [N/m²]	Shear Modulus, G [N/m²]
5.20×10^9	2.90×10^9	2.16×10^9
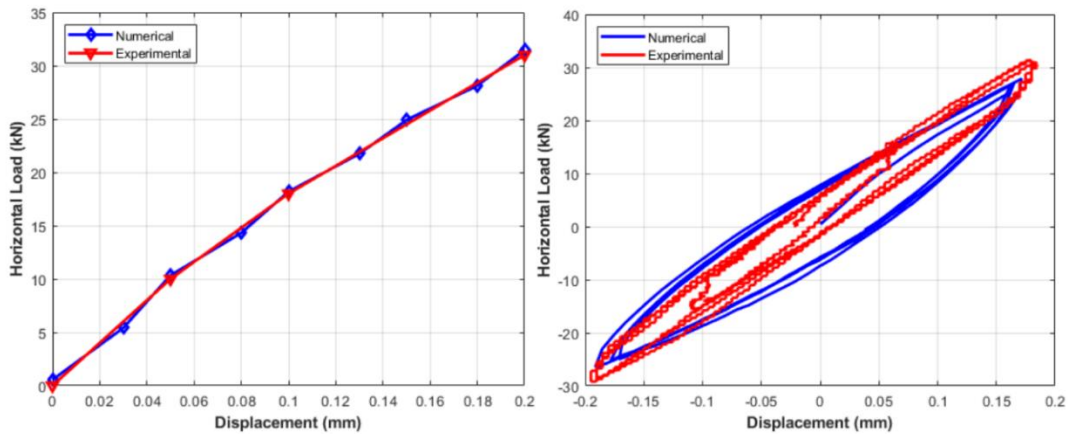
Figure 5-4: Comparison of experimental against numerical results in terms of the initial stiffness for the squat model (left) and the first loading cycles (right).
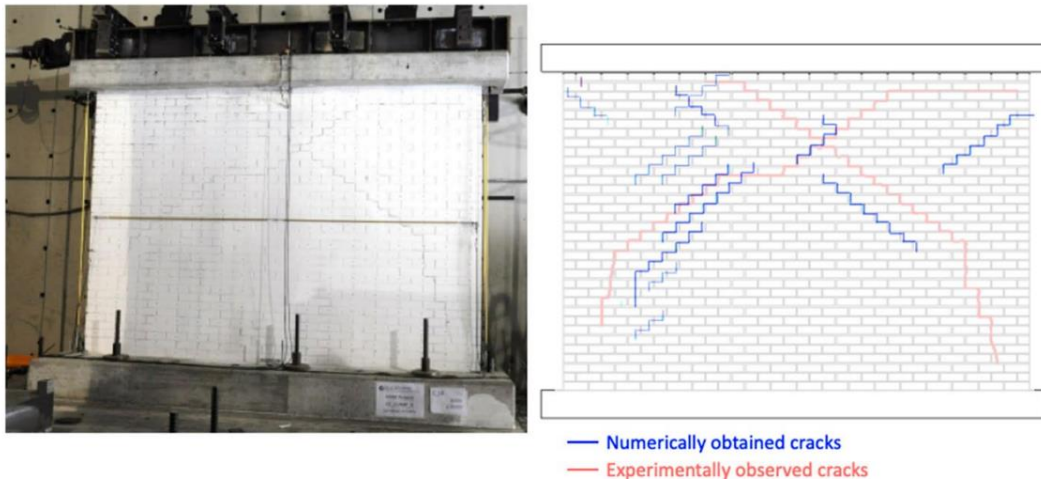
Figure 5-5: Comparison of experimental (left) against numerical (right) failure mode.

5.1.3 Application of damage indexing in walls under harmonic loading

Using the DI equation Eq. (5.1), estimates of the evolution of damage in masonry wall panels subjected to harmonic loading of different amplitudes and periods were estimated. The solid wall has a natural period of 0.06 s, while the period of the perforated wall panels is approximately 0.2 s. The models were subjected to sinusoidal acceleration loading with varying amplitude (0.01 g, 0.025 g, 0.05 g, 0.075 g and 0.1 g) and excitation periods (0.06 s, 0.2 s, 0.33 s and 1 s). The acceleration amplitude was up to 0.1 g. This is an acceptable level of acceleration considering that the highest PGA ever recorded in the Groningen gas field was 0.11 g in the 2018 Zeerijp Earthquake (Figure 5-10b). The applied harmonic loadings are presented in Figure 5-6. From the results of the analyses, it was concluded that, there was slight damage in the solid wall when subjected to low amplitude harmonic loadings and thus, for the sake of brevity, only the results from the perforated wall panels will be presented.
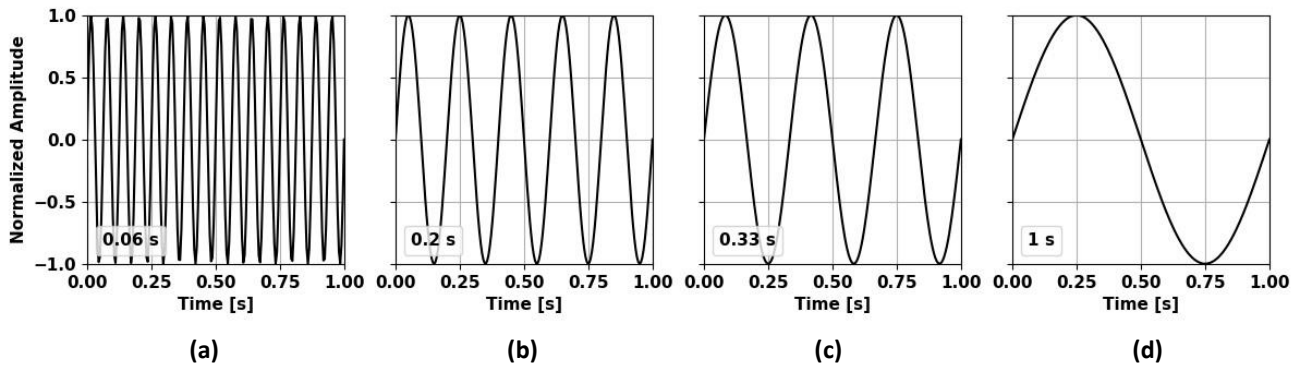
Figure 5-6: The harmonic loadings applied in the numerical analyses with excitation period (a) 0.06, (b) 0.2, (c) 0.33 and (d) 1 s.

Figure 5-7 shows the evolution of DI and its components (DI_{drift}, DI_{slip} and DI_{open}) over time for the URM wall with a symmetric opening when subjected to acceleration amplitudes equal to 0.025 and 0.1 g and excitation periods 0.33 s and 0.2 s. These accelerations correspond to low and moderate acceleration amplitude, respectively. The period of 0.2 s matches the natural frequency of the perforated walls, while the period 0.33 s is slightly higher of that of the natural frequency and thus resonance is not expected to occur in this case. When the wall was excited to a period of 0.33 s and acceleration amplitude equal to 0.025 g, the inflicted damage was negligible (Figure 5-7a). When dynamic motion with period 0.33 s and acceleration 0.1 g was applied, the maximum value of DI was attained during the first cycle of the excitation and in the upcoming cycles the same value of DI was reached but this was not exceeded (Figure 5-7a). For the wall subjected to a period of 0.2 s, the achieved maximum DI increased for every cycle of the harmonic signal for both acceleration amplitudes (see Figure 5-7b). Similar response was obtained for the wall with asymmetric opening. Consequently, even slight difference between the frequency of the signal and the natural frequency of the modelled wall significantly altered the response of the structure. When resonance occurred, even for low acceleration, damage propagated further during the successive cycles, while when there was no period matching only for higher acceleration some extent of damage was recorded and did not spread additionally along consecutive load cycles.
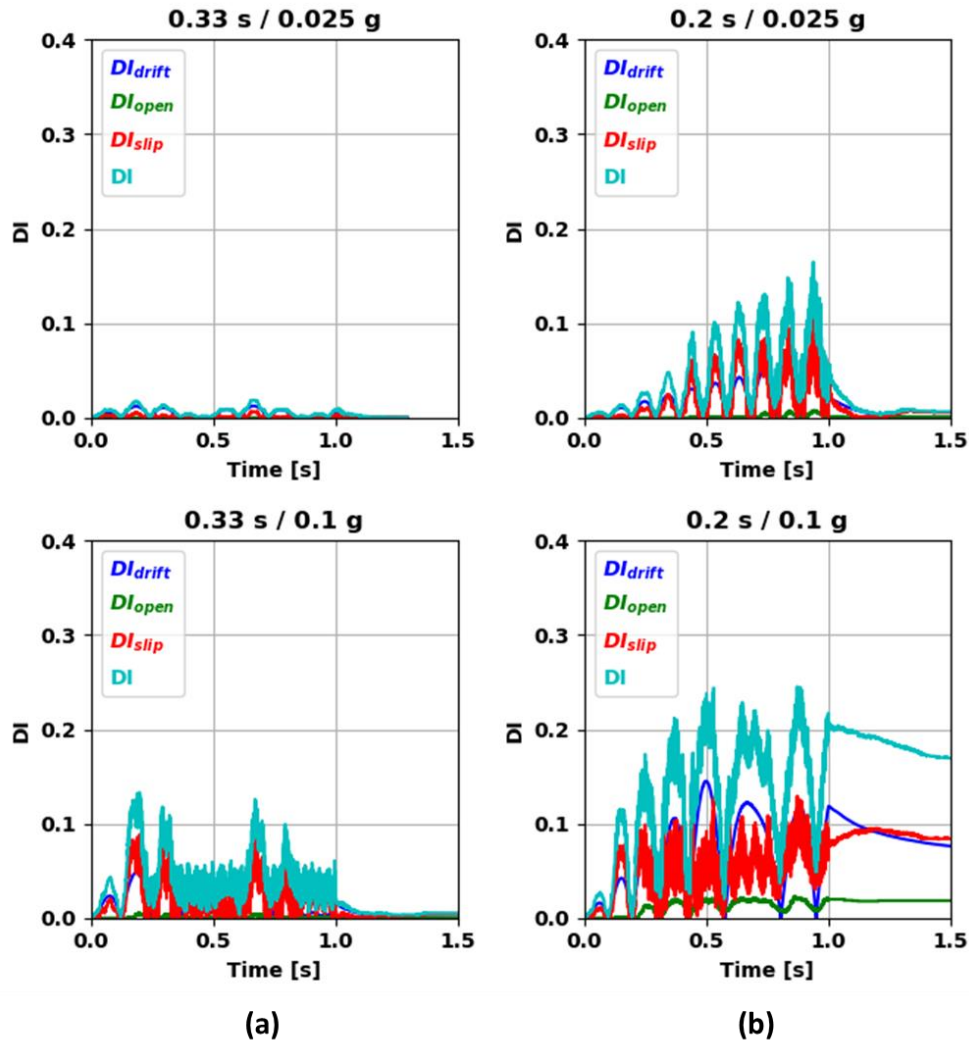
Figure 5-7: The evolution of the damage indices DI_{drift}, DI_{open}, DI_{slip} and DI for the symmetric model for acceleration amplitudes 0.025 and 0.1 g and periods of excitation (a) 0.33 and (b) 0.2 s.

Figure 5-8 shows the maximum and residual values of the damage indices DI_{drift}, DI_{open}, DI_{slip} and DI for the wall with symmetric opening for the excitation periods considered. The asymmetric wall presents similar behaviour as the symmetric one and thus it was not deemed essential to be included here. When the wall was excited to a period of 0.06 s only slightly damage was recorded; even for higher amplitudes of acceleration. For the cases of period 0.33 s and 1 s, the maximum DI reported increased linearly as stronger motions were applied while residual damage was negligible. Since period 0.2 s falls closer to the natural period of the wall, higher damage was observed in terms of DI for the corresponding excitations. In particular for period 0.33 s and 1 s the maximum attained DI was 0.13 and 0.1 respectively.

When resonance took place, i.e. excitation period equal to 0.2 s, substantially higher damage was reached. Interestingly, for the higher acceleration values, i.e. 0.05, 0.075 and 0.1 g, the same values maximum DI_{open}, DI_{slip} were reached. This behaviour implied that the failure mechanism was fully activated, and any further damage was expressed as further opening

or sliding of the already formed cracks. On the other hand, the measured DI_{drift} steadily increased for higher accelerations. When the excitation period was 0.2 s, it was the only case where non-negligible residual damage was recorded. For the cases of the acceleration equal to 0.05 and 0.075 g, the residual damage was mostly expressed through cracks (opening or sliding). For the highest acceleration considered, that is 0.1 g, residual drift was noticed.
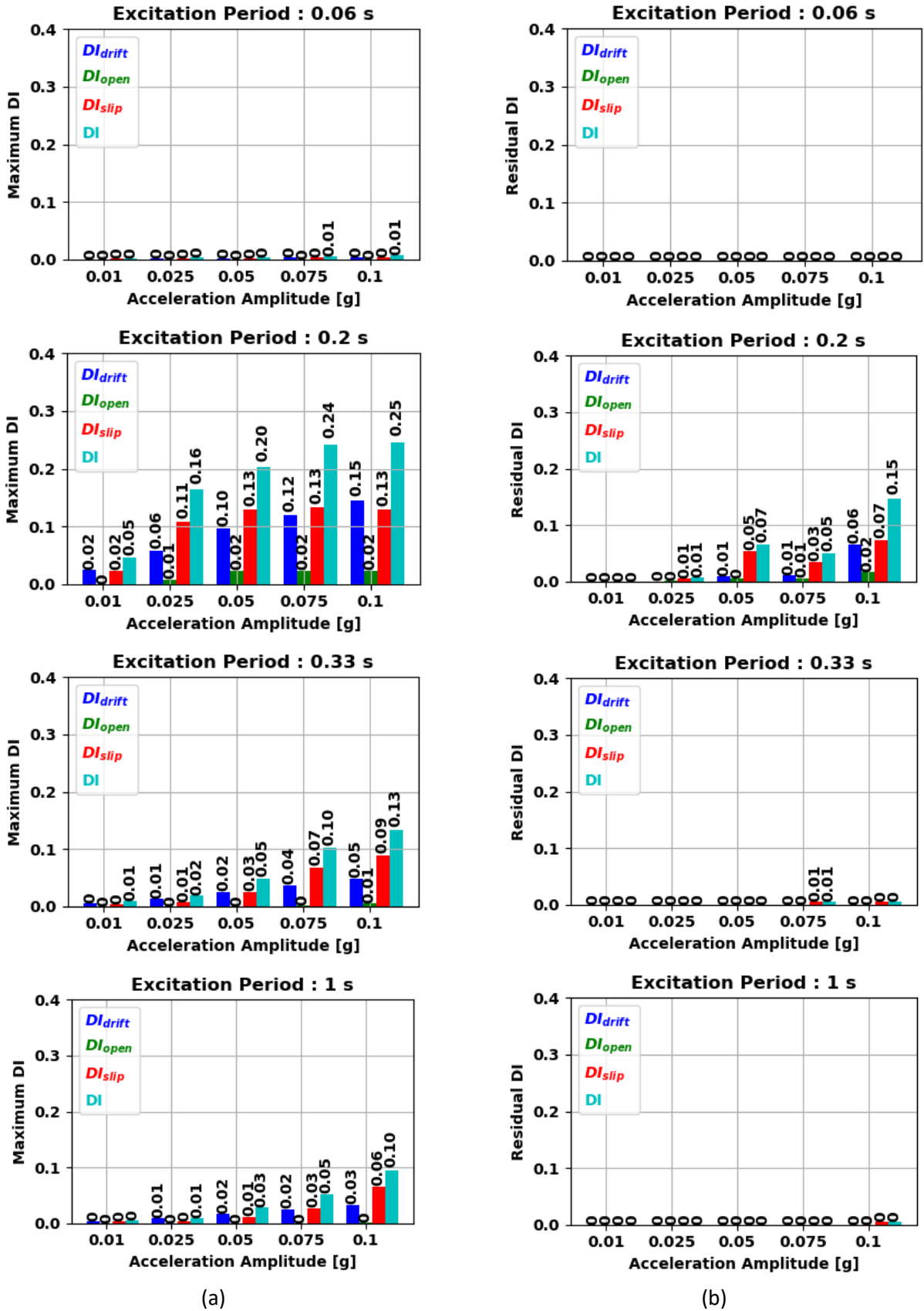
Figure 5-8: (a) Maximum and (b) residual values of the damage indices DI_{drift}, DI_{open}, DI_{slip} and DI presented for the wall with symmetric opening. From top to bottom the graphs correspond to excitation period 0.06 s, 0.2 s, 0.33 s and 1 s respectively.

In Figure 5-9, the drift ratio as obtained from the analyses with the wall with symmetric opening for excitation period 0.2 s is presented. One should mention that this excitation period matches the natural period of the walls with opening. The last full cycle is shown with red dashed lines and its duration T is displayed too (Figure 5-9). From Figure 5-9, it is noticed that the duration of the last full cycle increased when higher acceleration amplitudes were applied. For accelerations 0.01 g and 0.025 g, the duration T equalled 0.2 s. On the other hand, this duration reached 0.24 s, 0.32 s and 0.39 s for accelerations 0.05 g, 0.075 g and 0.1 g respectively (Figure 5-9). This response is related to the period elongation that took place due to the accumulated damage; as the excitation amplitude increased extra joints opened or slipped which reduced the effective stiffness of the modelled walls. Therefore, the considered computational model based on DEM was able to reproduce the propagation of damage along the mortar joints and its effect on period elongation.
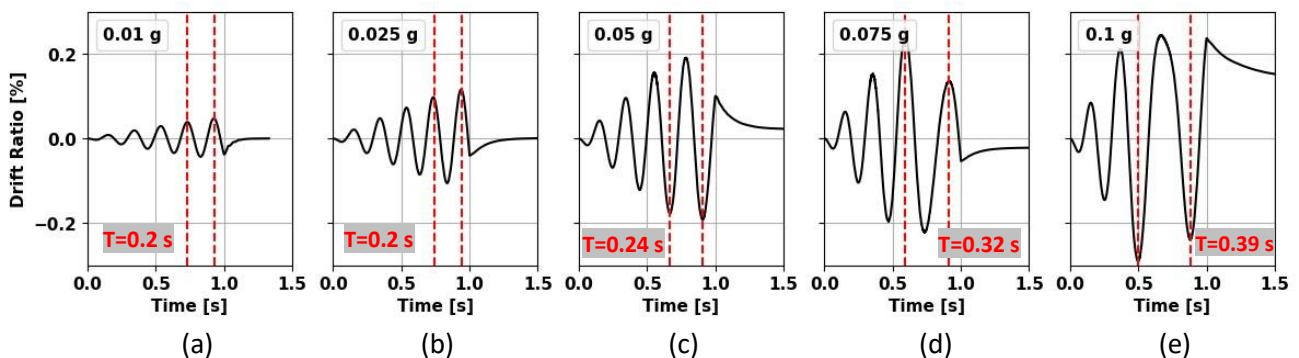
Figure 5-9: The drift ratio time-history as obtained from the analyses with the wall with symmetric opening for excitation period 0.2 s is presented for acceleration amplitudes (a) 0.01 g, (b) 0.025 g, (c) 0.05 g, (d) 0.075 g and (e) 0.1 g. For each subplot, with red dashed lines is denoted the last full cycle as observed in the drift ratio time-history and its duration T is displayed as well.

5.1.4 Application of damage indexing to walls under seismic loading

In order to further evaluate the damage propagation on the modelled masonry walls, an IDA was performed (Vamvatsikos and Cornell 2002). To this end, two records from the Groningen region that produced the highest PGA values were selected (Bal et al. 2019b). The North component of the MID1 record from the August 2012 Huizinge Earthquake (ML 3.6) (Figure 5-10a) and the East component of the BGAR record from the January 2018 Zeerijp Earthquake (ML 3.4) (Figure 5-10b) were used for the analyses. The Huizinge and Zeerijp Earthquakes had PGA values 0.08 and 0.11 g respectively (Sarhosis et al. 2019b). Both records produce spectral acceleration close to 0.15 g for period equal with the natural period of the perforated walls, that is 0.2 s. The records were scaled with factors 0.5, 0.75, 1., 1.2, 1.4, 1.6, 1.8 and 2 and an IDA was performed. During the dynamic analysis, no viscous damping was assumed; instead the only dissipation being due to frictional sliding on the joints.
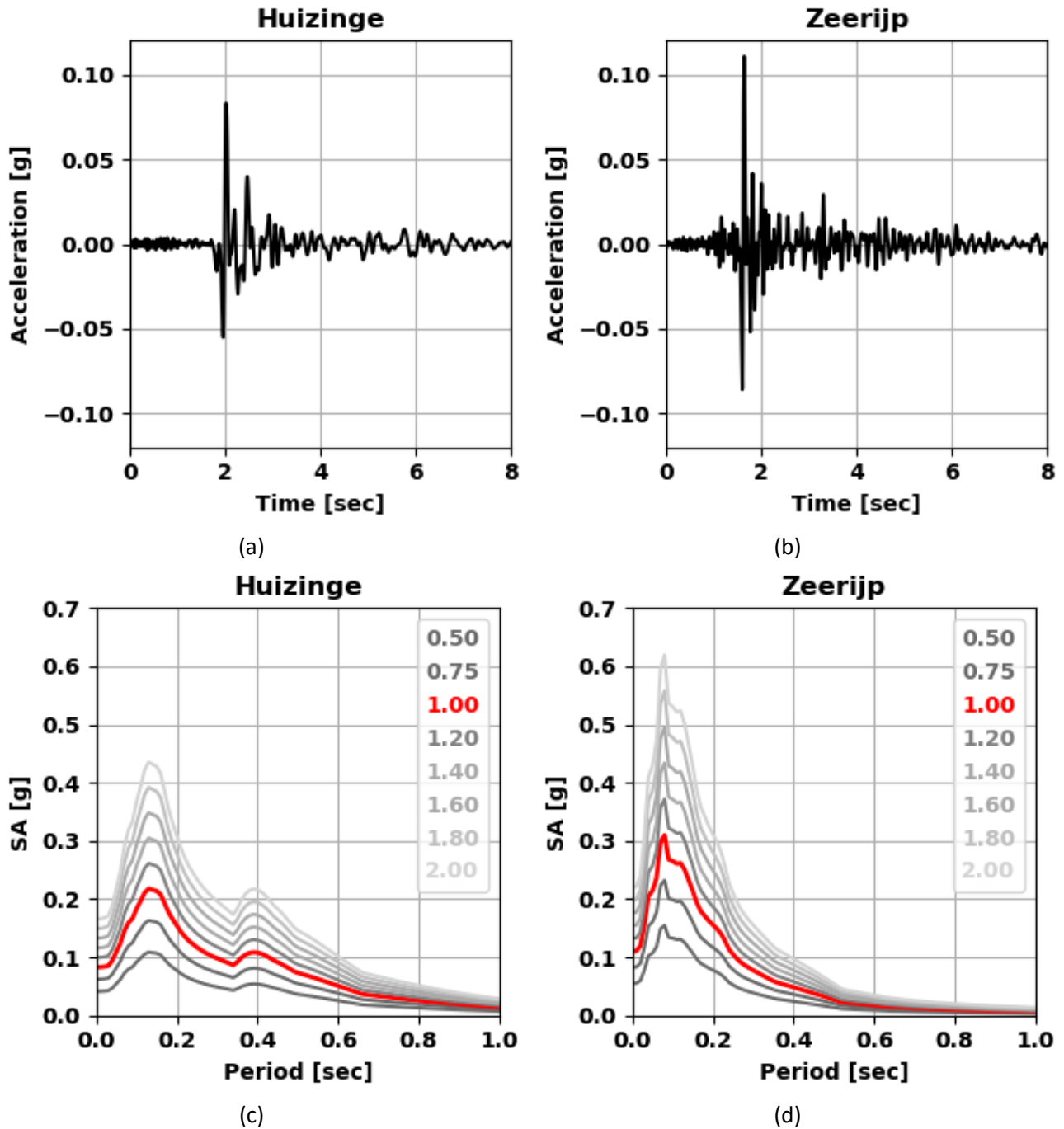
Figure 5-10: Acceleration time-history (top) and the corresponding response spectra (bottom) generated for the IDA are displayed for the Huizinge (left) and Zeerijp (right) records. The legend of graphs with the response spectra denotes the scaling factor used for the IDA.

From the literature review, when no monitoring scheme exists or when testing is unavailable, the inspection process relies on residual signs of damage, that is cracks and drift. In order to provide a better insight of the inflicted damage at the end of the IDAs, the residual DI and its components are presented in Figure 5-11 for the wall with symmetric opening. The results shown in Figure 5-11 correspond to the IDA with the Huizinge record. The residual DI was negligible for the lower PGA values and reached 0.11 for the maximum PGA. It is highlighted

that the observed residual DI was attributed to the components related to cracks, that is DI_{open} and DI_{slip}, while DI_{drift} remained insignificant. Thus, it can be inferred that even though no residual drift was recorded damage could be still observed as cracks. Similar results were also presented by Graziotti et al. (2017) where an incremental dynamic shaking table test was performed on a full scale URM house, typical example of the Groningen building stock. In particular, after applying excitations of low amplitude, the residual drift was negligible, but cracks could still be observed on the structure (Graziotti et al. 2017).
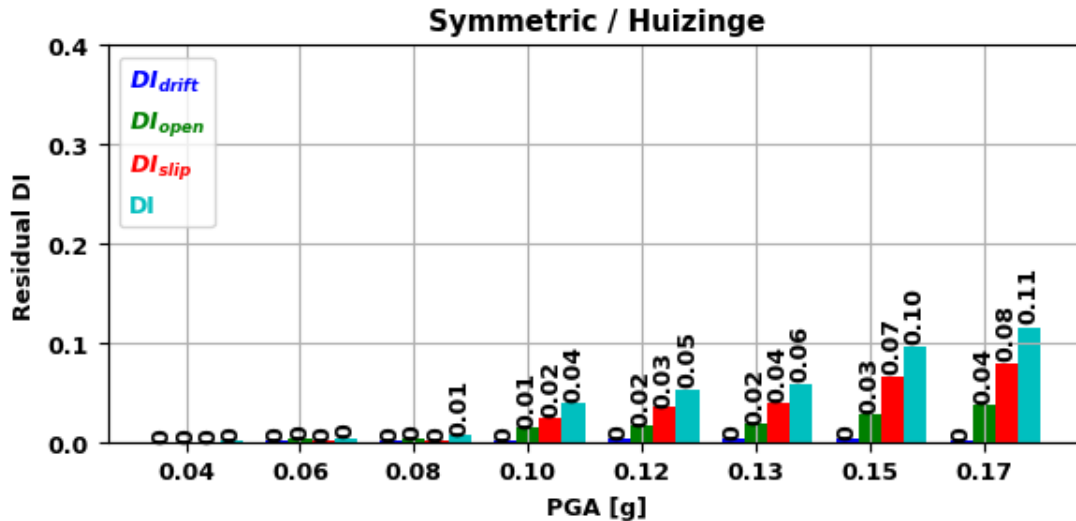
Figure 5-11: Residual values of the damage indices DI_{drift}, DI_{open}, DI_{slip} and DI presented for the wall with symmetric opening over the corresponding PGA. The results correspond to the IDA with the Huizinge record.

In Figure 5-12 the maximum and residual values of the damage index DI as obtained from the IDA results are presented over the maximum attained drift ratios during the analyses. A second order polynomial regression analysis was performed and the produced trendline is shown with blue line in Figure 5-12. The data corresponding to the maximum DI followed an almost linear increase over the maximum drift ratio as shown from the corresponding trendline (Figure 5-12a). The residual DI increased linearly before approaching a plateau towards higher drifts.
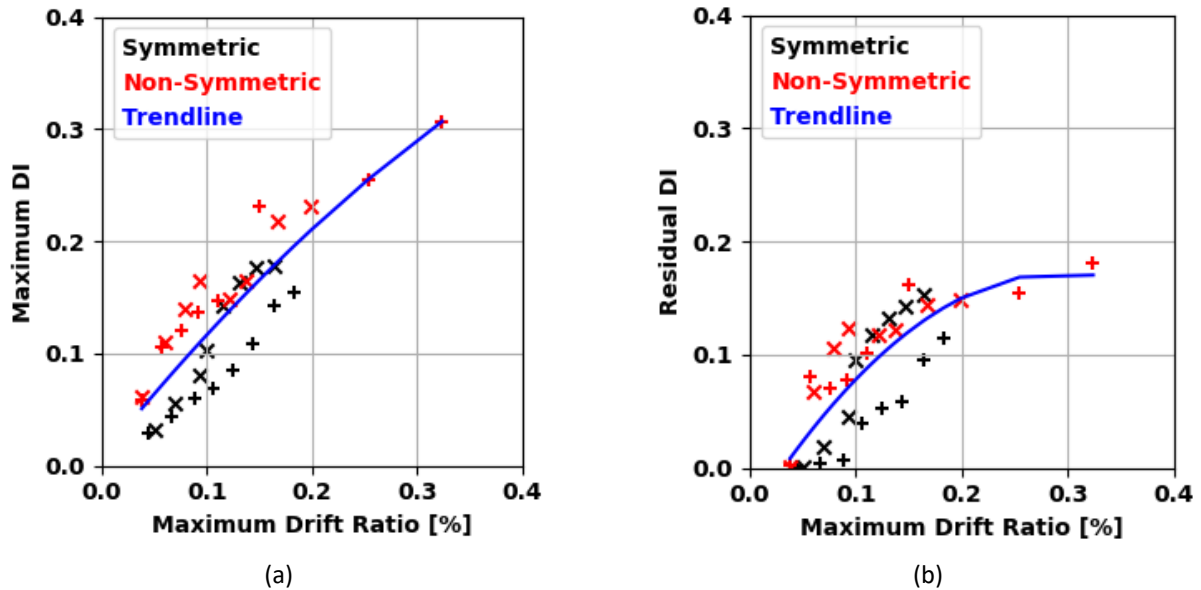
Figure 5-12: (a) Maximum and (b) residual values of the damage index DI as obtained from the IDA results. The results for the IDA based on the Huizinge and Zeerijp records are shown with '+' and 'x' markers respectively. The trendline obtained from a second order polynomial regression analysis is denoted with blue line.

5.1.5 Conclusions

So far, damage in masonry structures subjected to dynamic loading is assessed based on post-earthquake observations. However, during earthquake loading, cracks can open and close in a masonry structure. Such open and closing of cracks is not possible to be identified by post-earthquake observations. The aim of this study was to investigate the quantification of damage in URM structures which takes into consideration the initiation and propagation of damage due to recursive earthquake excitations. A dataset of experimental results from in-plane quasi-static cyclic tests on masonry walls was considered. The experimentally obtained crack patterns were investigated and their correlation with damage propagation was studied. Using software based on the DEM, a numerical model was developed and validated against a series of full-scale experimental tests obtained from the literature. Wall panels representing common typologies of house façades of URM buildings in the Northern European region i.e. Groningen gas field, the Netherlands, were numerically investigated. The accumulated damage within the seismic response of the masonry walls was investigated by means of representative harmonic load excitations and an IDA based on induced seismicity records from Groningen. A damage index based on cracking formation and drift ratio was proposed and applied to the numerical findings while common trends between the numerical and experimental data were highlighted. Using the results of the developed DEM numerical model, the suitability of the proposed DI equation to realistically represent the level of damage and its sensitivity to low amplitude loading was highlighted. The adopted numerical approach was able to capture any residual damage expressed as cracks even when the residual drift was zero at the end of an excitation. Based on the analyses with harmonic loads, the effect

of the load amplitude and the period of excitation on the damage propagation was elucidated; when no period resonance took place, the damage was limited even for moderate load amplitude while for the cases that the walls were excited with their natural period, damage was recorded even for lower load amplitudes. Although the proposed approach has been applied to masonry structures subjected to induced seismicity, the methodology could be applied when masonry structures subjected to earthquakes with high aftershock activity.

Additional experimental data with proper documentation of crack propagation are required to provide a generic quantification of damage for different configurations of masonry walls in terms of geometry, boundary conditions, material properties, overload, etc. The proposed damage index needs to be further calibrated based on experimental findings to correlate the obtained values with damage levels.

5.2 Quantification of crack propagation based on experimental studies

In Section 5.1 a numerical exercise on the quantification of damage evolution with the DEM was presented. Whilst interesting conclusions could be drawn on the evolution of cracking on masonry walls, limitations were encountered as well. The quantification of damage was on the consideration of drift ratio and cracking level. In the DEM analysis cracking was expressed as crack opening and sliding corresponding to tensile and shear failure at the mortar joints respectively. This representation of cracking through its two components (i.e. mortar joint opening and sliding) was examined numerically with the DEM model developed. However, when assessing the damage in real structures or experimental results it is not possible to obtain such detailed information. Therefore, the verification of numerical findings against experimental measurements would be a difficult task. In this Section, a further elaboration on the quantification of damage in masonry walls due to recursive load focusing on the crack propagation was attempted based on results from experimental studies. In particular, a damage index accounting for the total failed mortar joints on masonry walls is introduced (Section 5.2.1). This damage index can be easily computed by visually inspecting a cracked masonry wall providing an intuitive characterization of the damage extent. The evolution of cracking was evaluated based on an extensive set of experimental studies making use of a newly introduced damage index (Section 5.2.2). Finally a discussion (Section 5.2.3) and drawn conclusions (Section 5.2.4) are presented.

5.2.1 Damage index for the quantification of crack propagation

An insight into the crack propagation obtained from the slender wall specimen EC-COMP2-1 tested at EUCENTRE (Graziotti et al. 2016b) is presented. The crack distribution at the top part of the wall at the end of the test is shown in Figure 5-13a. Time-history of drift ratio (Figure 5-13b), crack opening (Figure 5-13c) and sliding (Figure 5-13d) at the left top part of the wall (Figure 5-13a) are displayed additionally. The EC-COMP2-1 pier exhibited pure rocking behaviour with horizontal cracks along the mortar bed joints at the top and bottom of

the wall (Figure 5-15). The maximum crack opening and sliding increased upon attainment of greater drift levels while residual cracking (shown with black line in Figure 5-13c and Figure 5-13d) was observed for the final cycles. Although the specimen returns to its zero position at the end of each cycle, permanent damage can be traced through the formed cracks. Thus, it was deemed meaningful to examine the connection between the recorded cracks and the inflicted damage. To this end, a new damage index DI_{crack} is proposed for the quantification of crack propagation on masonry walls and is defined as follows:

$$DI_{crack} = \frac{Total\ Length\ of\ failed\ mortar\ joints}{Total\ length\ of\ mortar\ joints} \tag{5.12}$$

DI_{crack} represents the ratio of failed mortar joints over the total mortar joints of a masonry wall. The introduced damage index was deemed suitable since it can be easily computed by visually inspecting a cracked masonry wall providing an intuitive characterization of the damage extent. The evolution of DI_{crack} was evaluated through an extensive dataset of experiments on masonry walls (refer to Section 5.2.2). It is noted that DI_{crack} was calculated based on the crack patterns as reported in the corresponding publications.

| (a) | (b) | (c) | (d) |
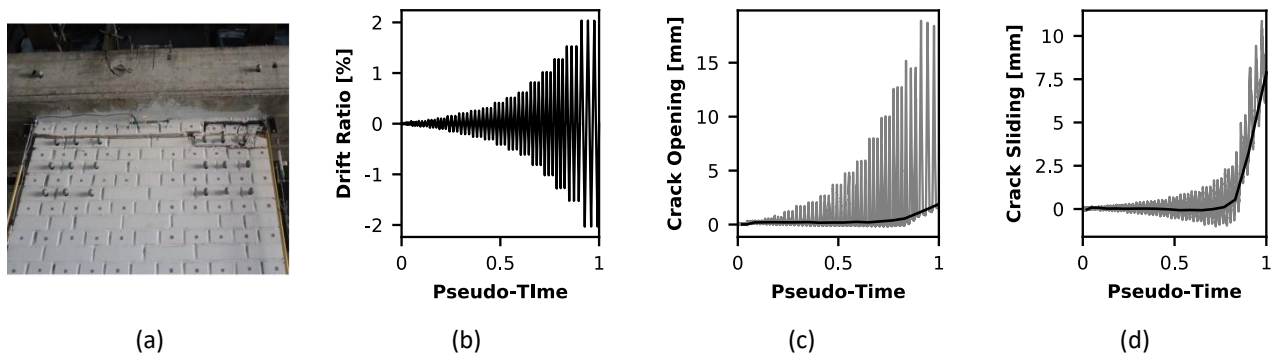
Figure 5-13: Experimental results from the tested wall EC-COMP2-1 (Graziotti et al. 2016b). (a) Crack pattern at the top part of the wall at the end of the test. Time-history of (b) drift ratio; (c) crack opening and (d) crack sliding as measured with monitoring markers at the top left corner of the wall. For the sub-figures (c) and (d) the residual values at the end of each cycle are shown with black line.

5.2.2 Experimental background of crack propagation in masonry walls

Significant research has been devoted on the interpretation of the response of URM walls under horizontal load by considering results from different experimental campaigns. These studies mainly focus on the estimation of the in-plane lateral strength and displacement capacity (Frumento et al. 2009; Salmanpour et al. 2013; Vanin et al. 2017; Messali and Rots 2018; Morandi et al. 2018). An extensive experimental campaign with cyclic shear tests on 75 masonry walls built with different types of clay masonry units, bond characteristics and mortar properties was considered for the evaluation of the deformation capacity, the effective elastic "cracked" stiffness and the shear strength (Frumento et al. 2009). Furthermore, a dataset of rocking URM piers typical for Dutch or similar buildings was considered and the relevance of geometry, material properties, and boundary and loading conditions on the drift

capacity was studied (Messali and Rots 2018). Morandi et al. (2018) derived a database of in-plane cyclic tests on URM piers from different research projects to investigate their in-plane lateral strength and displacement capacity. While these studies consider extensive datasets and provide insights on the response of URM piers, the damage propagation as expressed through the evolution of cracks is commonly disregarded. Vintzileou et al. (2020) argued that limited quantitative information can be found in the literature about cracking patterns and evolution of crack width with increasing loading. These data are necessary to enable a correct definition of damage limits and correlation with drift levels. This is extremely important when cracks form at the service level and reliable assessment of the damage and the repair costs are required.

To bridge this gap, a dataset of experiments was prepared by collecting data not only focusing on the displacement – force loops but also on crack distribution for different drift levels. Since measurements regarding cracks are not explicitly reported, data were extracted from deformed shapes as presented in different reports and publications. In particular, results from in-plane quasi-static cyclic tests on 32 masonry walls were considered (Table 5-3). The evolution of DI_{crack} for the different wall types is presented in Figure 5-14. The examined walls are representative of different types of real-case masonry piers since various aspect ratios, boundary conditions and values of overload were covered (see Table 5-3). It is noted that the considered walls are representative of masonry with low bond strength. Low bond strength masonry refers to masonry in which the tensile and shear bond at the unit-mortar interface is so low that it has a dominant effect on the mechanical behaviour of masonry; any cracks are expected to predominantly appear along the mortar joints and less likely on the brick units (Sarhosis and Sheng 2014; Giamundo et al. 2014). Regarding the mortar properties of the examined walls, maximum bond wrench strength and cohesion were 0.43 MPa and 0.75 MPa respectively (Table 5-3).

Eight calcium silicate (Ravenshorst and Messali 2016; Messali et al. 2020) (Figure 5-16 and Figure 5-21) and two clay (Korswagen et al. 2020b) walls were tested at the Macrolab/Stevinlaboratory at TUD in Delft, the Netherlands and three calcium silicate (Graziotti et al. 2015, 2016a; Grottoli et al. 2019) and five clay walls (Graziotti et al. 2016b; Kallioras et al. 2018) were tested at EUCENTRE in Pavia, Italy (Figure 5-15 and Figure 5-20). Furthermore, six clay shear walls, solid or with a central opening, were tested at Eindhoven University of Technology (TUE) under monotonic horizontal load considering different vertical precompression levels (Vermeltfoort et al. 1993) (Figure 5-24). Two clay walls of two-leaf thickness with different height/length ratio, that is 2 and 1.35, were tested at the Joint Research Centre in Ispra, Italy (Anthoine et al. 1995; Magenes and Calvi 1997) (Figure 5-17). The slender wall, HW, only rocked without further damage and it was re-tested with higher level of precompression. The second test will be referred to as HW*. In order to further expand the considered dataset, experiments on masonry walls with opening, two calcium silicate

(Korswagen et al. 2020a) (Figure 5-22) and two clay (Drougkas et al. 2020) (Figure 5-23) walls tested at TUD and one clay-brick veneer wall (Heath et al. 2008) were examined (Figure 5-22). In particular for the work by Drougkas et al. (2020), one of the two considered walls was retrofitted with bed joint reinforced re-pointing (TUD-Strengthened) and its response under in-plane cyclic load was compared with the unstrengthened counterpart (TUD-Unstrengthened). It is highlighted that for the veneer wall tested by Heath et al. (2008) special care was taken to ensure that the timber frame built behind the wall did not influence the in-plane response of the tested specimen. The structural response of the walls with opening was dictated by two piers connected with spandrels at the bottom and top. The masonry walls tested at TUD, EUCENTRE and TUE represented common URM houses found in the Netherlands while the work by Heath et al. (2008) reproduced a typical Australian residential construction. The material properties of the walls tested at Ispra were representative of old URM buildings from Italy (Magenes et al. 1995)

Table 5-3: Characteristics of the examined experimental dataset examined.

Specimen name	Length, L	Height, H	Thickness, t	Aspect ratio, H/L	Shear span ratio, H_0/L	Wall type	Boundary conditions	Failure mode	Precompression, σ_v	Material	f_w	c	$tan\varphi$	$f_{c,m}$	Source
	[m]	[m]	[m]	[-]	[-]				[MPa]		[MPa]	[MPa]	[-]	[MPa]	
TUD-COMP-0a	1.10	2.76	0.10	2.5	1.25	SL	DF	H	0.7	CS	0.27	0.14	0.43	5.93	[a]
TUD-COMP-1	1.10	2.76	0.10	2.5	2.51	SL	C	H	0.7	CS	0.27	0.14	0.43	5.93	[a]
TUD-COMP-2	1.10	2.76	0.10	2.5	2.51	SL	C	F	0.5	CS	0.27	0.14	0.43	5.93	[a]
TUD-COMP-3	1.10	2.76	0.10	2.5	1.25	SL	DF	H	0.4	CS	0.27	0.14	0.43	5.93	[a]
TUD-COMP-4	4.00	2.76	0.10	0.7	0.35	SQ	DF	S (DC)	0.5	CS	0.27	0.14	0.43	5.93	[a]
TUD-COMP-5	4.00	2.76	0.10	0.7	0.35	SQ	DF	S (HS)	0.3	CS	0.27	0.14	0.43	5.93	[a]
TUD-COMP-6	4.00	2.76	0.10	0.7	0.69	SQ	C	S (DC)	0.5	CS	0.27	0.14	0.43	5.93	[a]
TUD-COMP-20	1.10	2.76	0.10	2.5	2.51	SL	C	F	0.63	CS	0.12	0.13	0.52	6.35	[a]
EC-COMP-1	1.10	2.75	0.10	2.5	1.25	SL	DF	F	0.52	CS	0.24	0.21	0.42	6.2	[b]
EC-COMP-3	4.00	2.75	0.10	0.7	0.69	SQ	C	S (DC)	0.3	CS	0.24	0.21	0.42	6.2	[b]
EC-COMP2-1	1.20	2.71	0.21	2.3	1.13	SL	DF	F	0.52	CL	0.23	0.15	0.55	11.22	[c]
EC-COMP2-2	1.20	2.71	0.21	2.3	1.13	SL	DF	H	1.2	CL	0.23	0.15	0.55	11.22	[c]
EC-COMP2-3	1.20	2.71	0.21	2.3	1.13	SL	DF	H	0.86	CL	0.23	0.15	0.55	11.22	[c]
EC-COMP2-4	2.74	2.71	0.21	1.0	0.49	SQ	DF	S (DC)	0.3	CL	0.23	0.15	0.55	11.22	[c]
EC-COMP2-5	2.74	2.71	0.21	1.0	0.49	SQ	DF	S (HS)	0.3	CL	0.23	0.15	0.55	11.22	[c]
EUC-S-Flat-IP	0.66	1.86	0.10	2.8	1.42	SL	DF	F	1.8	CS	0.4	0.62	0.71	9.2	[d]
UoM	3.00	2.40	0.11			WwO	C	F	0	CL		0.75	0.68		[e]
HW	1.00	2.00	0.25	2.0	1.00	SL	DF	F	0.6	CL	0.04	0.23	0.58	6.2	[f]
LW	1.00	1.35	0.25	1.35	0.68	SQ	DF	S (DC)	0.6	CL	0.04	0.23	0.58	6.2	[f]
HW*	1.00	2.00	0.25	2.0	1.00	SL	DF	H	0.8	CL	0.04	0.23	0.58	6.2	[f]
TUD-Unstrengthened	3.07	2.70	0.10			WwO	C	FRB	0.12	CL	0.08	0.13	0.82	12.93	[g]
TUD-Strengthened	3.07	2.70	0.10			WwO	C	FRB	0.12	CL	0.08	0.13	0.82	12.93	[g]
TUD-COMP-47	3.07	2.69	0.10	0.9	0.44	SQ	DF	S (DC)	0.46	CL	0.16	0.13	0.82	12.93	[h]
TUD-COMP-48	3.07	2.69	0.10	0.9	0.44	SQ	DF	S (DC)	0.46	CL	0.16	0.13	0.82	12.93	[h]
TUD-COMP-49	3.13	2.70	0.10			WwO	C	FRB	0.12	CS	0.43	0.33	0.64	7.66	[i]
TUD-COMP-50	3.13	2.70	0.10			WwO	C	FRB	0.12	CS	0.43	0.33	0.64	7.66	[i]
J4D	0.99	1.14	0.10	1.2	0.58	SQ	DF	S (DC)	0.3	CL		0.287	0.75	11.5	[j]
J5D	0.99	1.14	0.10	1.2	0.58	SQ	DF	S (DC)	0.3	CL		0.287	0.75	11.5	[j]

J6D	0.99	1.14	0.10	1.2	0.58	SQ	DF	S (DC)	1.21	CL	0.287	0.75	11.5	[j]
J7D	0.99	1.14	0.10	1.2	0.58	SQ	DF	S (DC)	2.12	CL	0.287	0.75	11.5	[j]
J2G	0.99	1.14	0.10			WwO	DF	FRB	0.3	CL	0.287	0.75	11.5	[j]
J3G	0.99	1.14	0.10			WwO	DF	FRB	0.3	CL	0.287	0.75	11.5	[j]

Wall type: SL: slender wall; SQ: squat wall; WwO: wall with opening
Boundary conditions: DF: double fixed; C: cantilever
Failure mode: F: flexure, H: hybrid; S (DC): shear (diagonal cracking); S (HS): shear (horizontal sliding); FRB: four rigid bodies (for clarification refer to Section 5.2.2.3)
Material: CS: calcium silicate; CL: clay
Source: [a] (Ravenshorst and Messali 2016; Messali et al. 2020); [b] (Graziotti et al. 2015, 2016a); [c](Graziotti et al. 2016b; Kallioras et al. 2018); [d] (Grottoli et al. 2019); [e] (Heath et al. 2008); [f] (Anthoine et al. 1995; Magenes and Calvi 1997); [g] (Drougkas et al. 2020); [h] (Korswagen et al. 2020b); [i] (Korswagen et al. 2020a); [j] (Vermeltfoort et al. 1993)
f_w: bond strength; c: cohesion; $tan\varphi$: internal friction coefficient; $f_{c,m}$: compressive strength of masonry perpendicular to the bed joints
[1] For the walls with opening (WwO) the geometrical characteristics refer to the external dimensions of the walls
[2] Mechanical properties that were not reported in the corresponding publication were left blank

For the considered tested walls, DI_{crack} was calculated for different drift levels. The distribution of cracks was reported at the end of a loading cycle while the given drift corresponded to the maximum value imposed during a cycle. The distribution of DI_{crack} over drift is displayed separately for slender, squat and walls with opening in Figure 5-14 in order to better highlight trends observed for the different wall types. The walls were categorized as slender or squat according to their aspect ratio and are presented in Section 5.2.2.1and Section 5.2.2.2 respectively. The shear walls from TUE have aspect ratio 1.1 and the solid ones were considered as squat. Both the solid and the ones with opening are presented in Section 5.2.2.4. The rest of the walls with opening and height 2.4 to 2.7 m are displayed in Section 5.2.2.3.
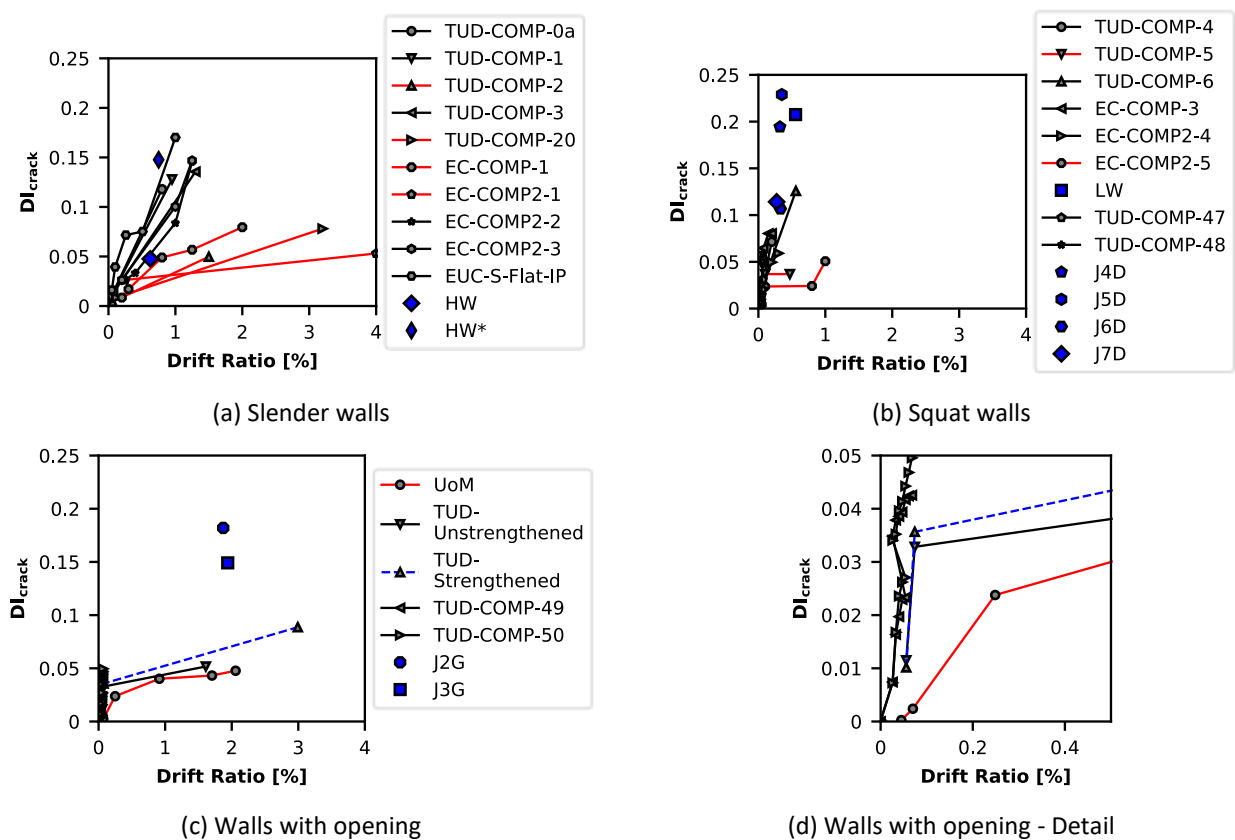
Figure 5-14: The distribution of DI_{crack} over drift ratio for the (a) slender walls, (b) squat walls, (c) walls with opening, and (d) detail of the graph regarding the walls with opening for low drift values.

5.2.2.1 Slender walls

The failure modes of the slender walls were flexure-governed (Figure 5-15, Figure 5-16 and Figure 5-17). In particular, the walls TUD-COMP-2, TUD-COMP-20, EC-COMP-1, EC-COMP2-1 and HW (the first four specimens are shown with red line while the latter with blue marker in Figure 5-14a) were characterized by pure rocking behaviour. For the first four piers, flexure cracks along the bed joints appeared at the constrained edges and toe crushing was reported at the later stages of the experiments. The HW wall was tested up to 0.63% drift ratio and experienced pure rocking without any further damage. For this reason, the HW wall

was re-tested with higher precompression level (HW*) and failure related with the formation of "trapezoidal cracking" (Anthoine et al. 1995; Magenes and Calvi 1997) as shown in Figure 5-17. It is noted that, since the HW wall could be further tested, it can be inferred that it could reach drift ratio higher than 0.63% and most likely the test was deliberately stopped at this drift level. This explains the low drift value that the HW wall attained in comparison to the rest of the rocking walls (Figure 5-14a). The rest of the slender walls (shown with grey line in Figure 5-14a) experienced a hybrid failure mechanism consisting of flexural and shear cracks. For the slender walls TUD-COMP-0a, TUD-COMP-1, TUD-COMP-3 (Figure 5-16) and EUC-S-Flat-IP (Figure 5-15) the damage initiated as horizontal flexural cracks at the mortar bed joints close to the constrained edges. Further on, damage propagated to extra bed joints while shear sliding and toe crushing took place as well. Particularly for the slender walls EC-COMP2-2 and EC-COMP2-3 (Figure 5-15), the onset of damage was observed as horizontal cracks due to rocking. For greater drift, diagonal shear cracks formed and finally dictated the failure mechanism of these walls. Based on the graphs of DI_{crack} over drift, the slope for the slender walls with pure rocking behaviour was gentle (Figure 5-14a). On the other hand, the curves of the slender walls exhibiting hybrid failure mechanisms fall between the curves corresponding to squat (Figure 5-14b) and slender walls with rocking (Figure 5-14a). The onset of damage corresponds to DI_{crack} in the range of 0 up to 0.03 and was attained for drift ratio up to 0.25%. The slender walls which exhibited pure rocking behaviour ranked DI_{crack} up to 0.08 when failure was reached. On the other hand, the slender walls with hybrid failure mechanism reached higher levels of DI_{crack} at the final stage due to the different failure mode. Failure with rocking mechanism can be realized with cracking of limited horizontal bed joints while the hybrid mode is expressed as horizontal flexural cracking and sliding of extra joints.
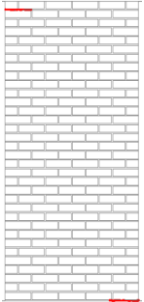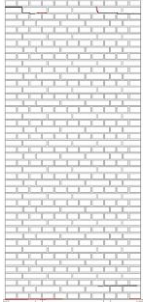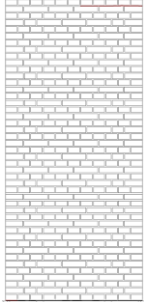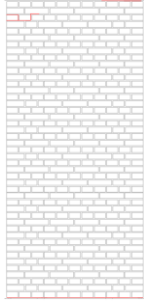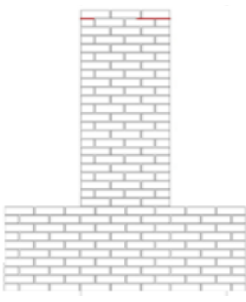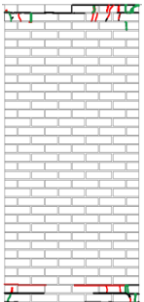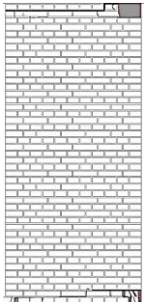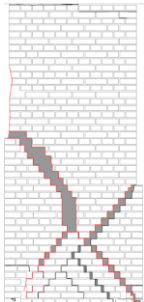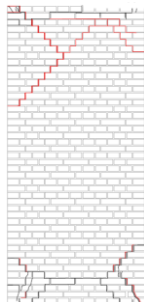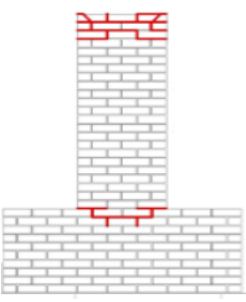
EC-COMP-1	EC-COMP2-1	EC-COMP2-2	EC-COMP2-3	EUC-S-Flat-IP
δ: 0.2% | DI_{crack}: 0.01	δ: 0.25% | DI_{crack}: 0.03	δ: 0.25% | DI_{crack}: 0.03	δ: 0.2% | DI_{crack}: 0.03	δ: 0.05% | DI_{crack}: 0.02
δ: 2% | DI_{crack}: 0.08	δ: 4% | DI_{crack}: 0.05	δ: 1.25% | DI_{crack}: 0.15	δ: 1.25% | DI_{crack}: 0.15	δ: 1% | DI_{crack}: 0.17

Figure 5-15: Crack patterns observed for the slender masonry walls as reported in (Graziotti et al. 2015, 2016a, b; Kallioras et al. 2018; Grottoli et al. 2019). The crack patterns, the drift ratio δ and the corresponding DI_{crack} are displayed for the onset of cracking (top) and the end of the tests (bottom).
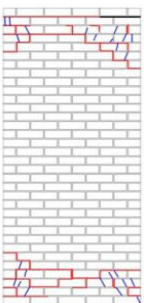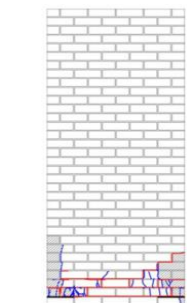
TUD-COMP-0a	TUD-COMP-1	TUD-COMP-2	TUD-COMP-3	TUD-COMP-20
δ: 0.02% | DI_{crack}: 0.01	δ: 0.03% | DI_{crack}: 0.01	δ: 0.06% | DI_{crack}: 0.00	δ: 0.07% | DI_{crack}: 0.01	δ: 0.12% | DI_{crack}: 0.01
δ: 0.8% | DI_{crack}: 0.12	δ: 0.95% | DI_{crack}: 0.13	δ: 1.5% | DI_{crack}: 0.05	δ: 1.3% | DI_{crack}: 0.14	δ: 3.2% | DI_{crack}: 0.08

Figure 5-16: Crack patterns observed for the slender masonry walls as reported in (Ravenshorst and Messali 2016; Messali et al. 2020). The crack patterns correspond to the end of the tests. The first cracks appeared are shown in black. The drift ratio δ and the corresponding DI_{crack} are displayed for the onset of cracking and the end of the tests.

HW	HW*	LW
δ: 0.63% | DI_{crack}: 0.05	δ: 0.75% | DI_{crack}: 0.15	δ: 0.56% | DI_{crack}: 0.21

Figure 5-17: Schematic representation of the crack pattern at the end of the tests as reported in (Anthoine et al. 1995; Magenes and Calvi 1997). The drift ratio δ and the corresponding DI_{crack} are displayed for the end of the tests.

The in-plane drift capacity of URM piers depends on factors like: precompression level, geometry, boundary conditions and material properties (Petry and Beyer 2015a; Vintzileou et al. 2020). The ultimate drift capacity for walls that fail by flexure/rocking has been found to be high, whereas, on the other hand, the maximum drift for walls that fail by shear or by hybrid mechanisms is rather limited. This distinctive performance in terms of drift capacity that characterizes the different failure modes was validated from the response of the examined slender piers (Figure 5-14a). Taking this into consideration, different drift limits are provided for rocking and shear failure by the Eurocode, the American, the New Zeeland, and Italian Codes; a discussion on this topic is provided by Messali & Rots (2018). According to Eurocode 8 – Part 3 (EC8-3 2005), the force capacity of an URM wall is dictated by different equations whether the wall is controlled by flexure or shear and the minimum of these values yields an analytical identification of the failure mode. Following the EC8-3 guidelines, Morandi et al. (Morandi et al. 2018) determined the expected failure mode for an extensive dataset and it was found that 25% were misclassified as compared to the experimental failure type. In a similar way, Frumento et al. (2009) compared the experimentally obtained maximum horizontal force with the lateral strength evaluated based on the mechanical model proposed by Magenes & Calvi (1997) to identify the collapse mechanism (i.e. flexure or shear) but the classifications were incorrect in many cases. To further elaborate on the identification of the collapse mechanism a combination of available data, such as photographs/sketches of damage sequence, the shape of the hysteresis loop (thin or wide cycles), ultimate drift ratio etc., was additionally regarded (Frumento et al. 2009). In cases where the failure type was not defined in the research reports, the choice of the damage type based on the aforementioned data could be subjective and difficult to determine (Frumento et al. 2009). Wilding & Beyer (2018) examined 79 full scale shear - compression tests of in-plane loaded modern URM walls and it was concluded that the shear span ratio (H_0/L) and the axial load ratio ($\sigma_v/f_{c,m}$) are rather good indicators of the failure mode. Nevertheless, it was highlighted that there is a range of values of these two parameters that both modes could be expected; that is for shear span ratios close to one accompanied by low to moderate axial load ratio.

Although it is important to correctly predict the failure mode in order to evaluate reliably the response of URM piers, so far there is no objective way to accurately identify the failure mechanism based on characteristics such as geometry, boundary conditions, precompression level, and material properties. In order to address this, the characteristics of the examined slender walls were investigated for any relationships with the failure mode (flexure or hybrid). In Figure 5-18a, the shear span ratio H_0/L was plotted against the axial load ratio $\sigma_v/f_{c,m}$ for the slender walls; the flexure and hybrid failure modes are shown in red and blue respectively. The shear span H_0 is computed as half or the entire height H in case of double fixed or cantilever boundary conditions respectively. Based on Figure 5-18a, no distinctive pattern could be extracted. Subsequently, the axial load ratio was normalized over cohesion and friction coefficient to the third power (c^3 and $(tan\varphi)^3$ respectively) (Figure 5-18b). This time a line can be drawn to split two areas where different failure modes take place and is given by the following equation:

$$f = y - 0.0034x - 0.8200 \qquad (5.13)$$

where y is H_0/L and x is $\sigma_v/f_{c,m}/c^3/(tan\varphi)^3$; H_0 and L in meters; σ_v, $f_{c,m}$, and c in MPa. When f is positive and negative the expected failure mode is flexure and hybrid respectively (Figure 5-18b).

By taking a closer look in Figure 5-18b, HW and HW* are expectedly very close to the borderline. It is reminded that it is the same wall, initially tested with axial load 0.6 MPa and upon rocking failure, the precompression was increased to 0.8 MPa leading to hybrid failure. Thus, for a specific wall with certain geometry, boundary conditions and material properties, there is a threshold value of axial load that a shift from pure rocking to hybrid failure mode takes place.

As presented in Figure 5-19, no relationship between friction coefficient and cohesion can be observed for the examined walls. Thus, both were used to normalize the axial load ratio (Figure 5-18b). In order to highlight the role of the shear strength, as expressed by cohesion and friction coefficient, the walls TUD-COMP-3 and EC-COMP-1 are presented in more detail. These two walls have almost identical characteristics, but they experience different failure mode. In particular, the two walls have same geometry, boundary conditions and axial load (see Table 5-3). Regarding the material properties both have similar friction coefficient $tan\varphi$ and compressive strength of masonry $f_{c,m}$. The only distinctive difference is regarding cohesion; TUD-COMP-3 and EC-COMP-1 have 0.14 MPa and 0.21 MPa respectively. Therefore, it can be inferred that for the EC-COMP-1 wall due to high cohesion, flexure failure precedes the formation of any shear cracks. On the other hand, TUD-COMP-3 has lower cohesion and consequently a hybrid failure mechanism occurs. Consequently, higher

cohesion, friction coefficient or both, appears to inhibit shear failure in favour of rocking response.
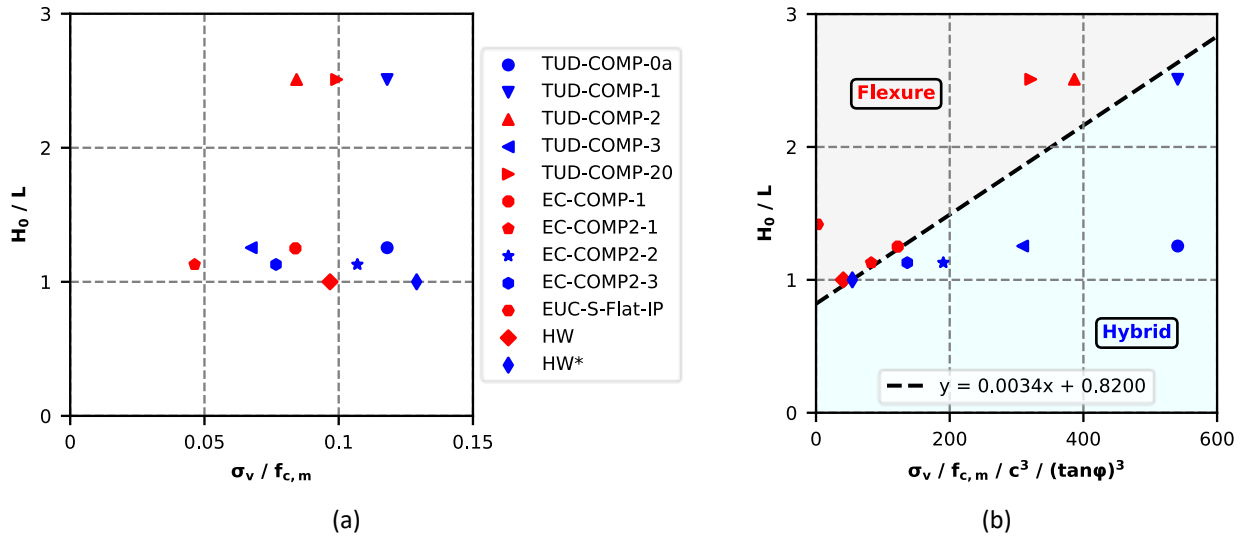
Figure 5-18: Shear span ratio (H_0/L) against (a) axial load ratio ($\sigma_v/f_{c,m}$) and (b) axial load ratio normalized over cohesion and friction coefficient to the third power (c^3 and $(tan\varphi)^3$ respectively) for the slender walls. The specimens with flexural and hybrid failure are displayed with red and blue markers respectively. In sub-figure (b), the dashed line signifies the limit between flexure and hybrid failure mode.
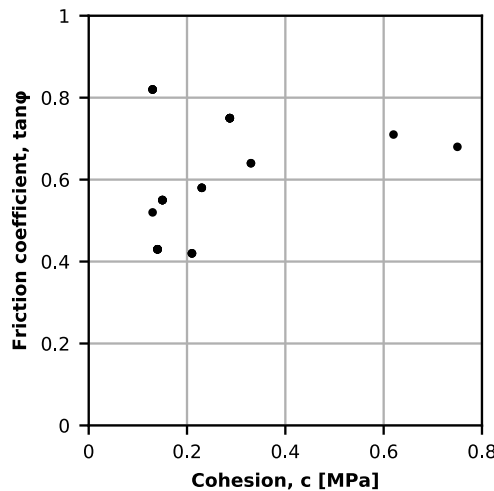
Figure 5-19: Friction coefficient ($tan\varphi$) vs cohesion (c) for the examined wall specimens (Table 5-3).

5.2.2.2 Squat walls

In this section the results for the squat walls with height either 1.35 m or close to 2.7 m are presented (Figure 5-17, Figure 5-20 and Figure 5-21). The squat walls (Figure 5-24) with lower height, that is 1.14 m, tested at TUE, are displayed in Section 5.2.2.4.

For the squat walls, the failure mechanism was shear-dominated (Figure 5-17, Figure 5-20 and Figure 5-21). The walls EC-COMP2-4, EC-COMP3, TUD-COMP-4 and TUD-COMP-6 (shown with grey line in Figure 5-14b) exhibited stepped diagonal cracks along the mortar

joints while unit failure was recorded as well for higher drift levels. The failure of these walls was attained for limited drift and thus is characterized as brittle (Figure 5-14b). The walls TUD-COMP-47 and TUD-COMP-48 were tested under repetitive cycles of low drift amplitude to examine the initiation of light damage and the experiments reached up to 0.08% drift ratio. Therefore, only stepped diagonal cracks were formed without any further propagation of damage. DI_{crack} values for the walls TUD-COMP-47 and TUD-COMP-48 were reproduced from graphs regarding the length of the observed cracks; for additional information refer to Korswagen et al. (2020b). The LW wall with low aspect ratio, i.e. 1.35, exhibited brittle failure with diagonal cracks typical to shear behaviour as explained in (Anthoine et al. 1995; Magenes and Calvi 1997) (Figure 5-17). It is noted that the LW wall experiences higher DI_{crack} value, 0.21, than the squats walls with height approximately 2.7 m. This difference could be attributed either to size effects or to the higher precompression level; LW is loaded with 0.8 MPa while the rest of the squat walls account for overload up to 0.5 MPa. This peculiarity is further discussed in Section 5.2.2.4.

For the squat specimen EC-COMP2-5 a horizontal crack along the whole length of the wall was observed at the bottom part (Figure 5-20). During the test, any applied displacements were accommodated as sliding along this formed crack. This failure mechanism led to higher drift in comparison to the rest of the squat walls (Figure 5-14b). At the final cycles of the experiment, shear failure took place at the top part of the wall which led to partial collapse of the wall and termination of the test. Similar failure mechanism was observed for the TUD-COMP-5 (Figure 5-21). Sliding as failure pattern was observed two times among the examined squat walls. It is noted that no reasoning was provided by the corresponding references (Graziotti et al. 2016b; Ravenshorst and Messali 2016; Kallioras et al. 2018; Messali et al. 2020). In particular, EC-COMP2-4 and EC-COMP2-5 had the same geometry, boundary conditions, precompression level, and were built with the same material. The only difference was on the loading protocol; for EC-COMP2-4 each cycle was repeated three times while for EC-COMP2-5 each cycle was applied only once. The two walls experienced different failure mode but it was not possible to associate the failure type to the different loading protocol (Graziotti et al. 2016b). Further investigation is needed to understand the parameters that dictate the expected failure mechanism for the squat walls. More experimental data need to be examined in order to reliably assess whether the sliding failure can be attributed to the experimental setup and considerations, such as boundary conditions or precompression level, or it is linked to the inherent discrepancy of the material properties along the URM walls (Sarhosis et al. 2020).

The squat walls were characterized by a steep increase of the attained DI_{crack} over drift attributed to their brittle behaviour (Figure 5-14b). When failure was attributed to horizontal sliding, i.e. EC-COMP2-5 and TUD-COMP-5 walls, the maximum DI_{crack} was 0.05. The squat walls that experienced stepped diagonal cracks, apart from the wall TUD-COMP-6, scored

higher DI_{crack}, that is 0.09, at the maximum drift level. The squat wall TUD-COMP-6 reached a rather high value of DI_{crack} at the ultimate drift. The distribution of damage for the aforementioned wall was reported when excessive damage had taken place along the mortar joints and unit failure was extensive as well. The crack onset for the squat walls was observed for limited drift values in the range of 0.01% to 0.10%. Failure took place at drift 0.2% to 056% and 0.47% to 1% for the squat walls experiencing shear cracking and horizontal sliding respectively. It is noted that the walls failing with sliding could attain higher drift levels and they were terminated due to limitations imposed by the actuators.
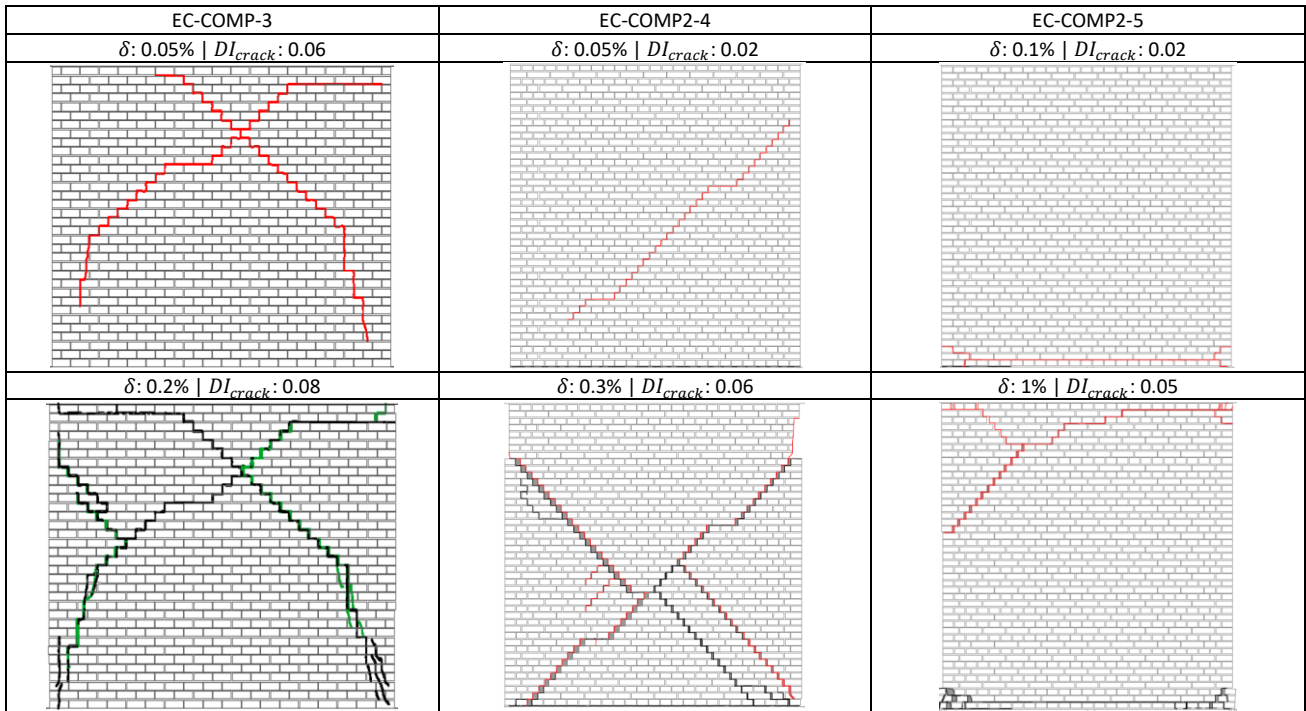
Figure 5-20: Crack patterns observed for the squat masonry walls as reported in (Graziotti et al. 2015, 2016a, b; Kallioras et al. 2018). The crack patterns, the drift ratio δ and the corresponding DI_{crack} are displayed for the onset of cracking (top) and the end of the test (bottom).
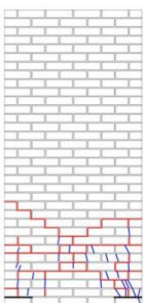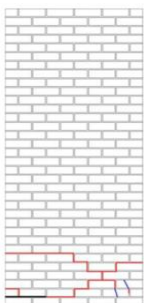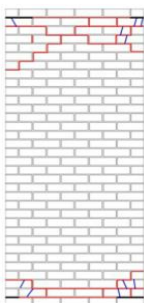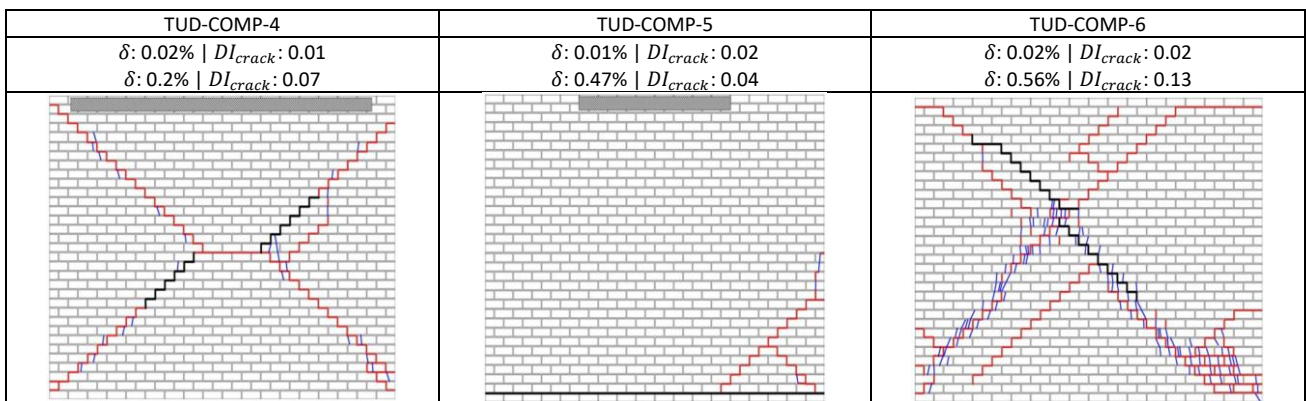

Figure 5-21: Crack patterns observed for the squat masonry walls as reported in (Ravenshorst and Messali 2016; Messali et al. 2020). The crack patterns correspond to the end of the tests. The first cracks appeared are shown in black. The drift ratio δ and the corresponding DI_{crack} are displayed for the onset of cracking and the end of the tests.
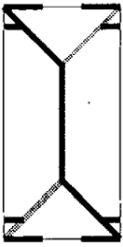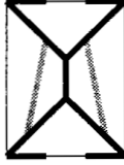
5.2.2.3 Walls with opening

In this section the results for the walls with opening and height close to 2.7 m are presented (Figure 5-22 and Figure 5-23). The shear walls (Figure 5-24) with opening and lower height, that is 1.14 m, tested at TUE, are displayed in Section 3.4.

For the TUD-COMP-49 and TUD-COMP-50 specimens (Korswagen et al. 2020a) the crack onset was observed around the corners of the window opening where the piers interconnect with the spandrels (Figure 5-22). At greater drift, the already formed cracks further propagated either horizontally or diagonally towards the corners of the walls. The walls ultimately decomposed in four rigid bodies with no signs of damage and these rigid bodies slid and rotated against each other (Korswagen et al. 2020a). Similar failure mechanism was recorded for the veneer wall with opening tested by Heath et al. (2008). The crack patterns experimentally obtained match well the response observed in shaking table tests on full scale URM houses (Graziotti et al. 2017; Kallioras et al. 2018). It terms of DI_{crack} the walls with opening from the two experimental campaigns (Heath et al. 2008; Korswagen et al. 2020a) yielded comparable values. The crack initiation corresponded to DI_{crack} in the range of 0.01 while the maximum attained DI_{crack} was approximately 0.05.

Drougkas et al. (2020) investigated the response of two walls with opening with (TUD-Strengthened) and without strengthening (TUD-Unstrengthened) (Figure 5-23). The considered loading protocol was split in three phases; phase 1 and phase 2 consisted of low amplitude top displacements (i.e. drift ratio up to 0.07%) while phase 3 accounted for high amplitude top displacements reaching the capacity of the walls. Phase 1 and 2 corresponded to Damage Limitation (DL) state while phase 3 regarded the NC state. The two walls by Drougkas et al. (2020) behaved similarly up to the DL state as can be noticed from the obtained crack patterns (Figure 5-23) and DI_{crack} (0.03 to 0.04) while similar was also the response in terms of stiffness and strength. In other words, for low amplitude drift values the two walls are expected to suffer similar degree of damage in terms of cracks. Apparently, difference could be seen for the NC state. The strengthened wall reached higher drift due to the increased ductility provided by the strengthening elements; drift capacity was increased from 1.61% to 2.99%. Moreover, the strengthened wall is able to tolerate greater extent of damage since it reaches DI_{crack} 0.09, higher than the 0.05 of the unstrengthened wall. In overall, it can be inferred that the strengthened wall is expected to have cracks for small drift. This type of strengthening does not change the failure mechanism and thus it is not possible to avoid the formation of cracks; it only offers greater ductility which delays the collapse of the structure. Therefore, this strengthening solution could be chosen when the aim is the avoidance of collapse; for lower damage limits (i.e. DL state) any enhancement is not significant. Consequently, if the avoidance of any damage is the goal, different retrofitting schemes should be evaluated.

TUD-COMP-49	TUD-COMP-50	UoM
δ: 0.03% | DI_{crack}: 0.01	δ: 0.03% | DI_{crack}: 0.01	δ: 0.07% | DI_{crack}: 0.00
δ: 0.07% | DI_{crack}: 0.04	δ: 0.07% | DI_{crack}: 0.05	δ: 2.06% | DI_{crack}: 0.05
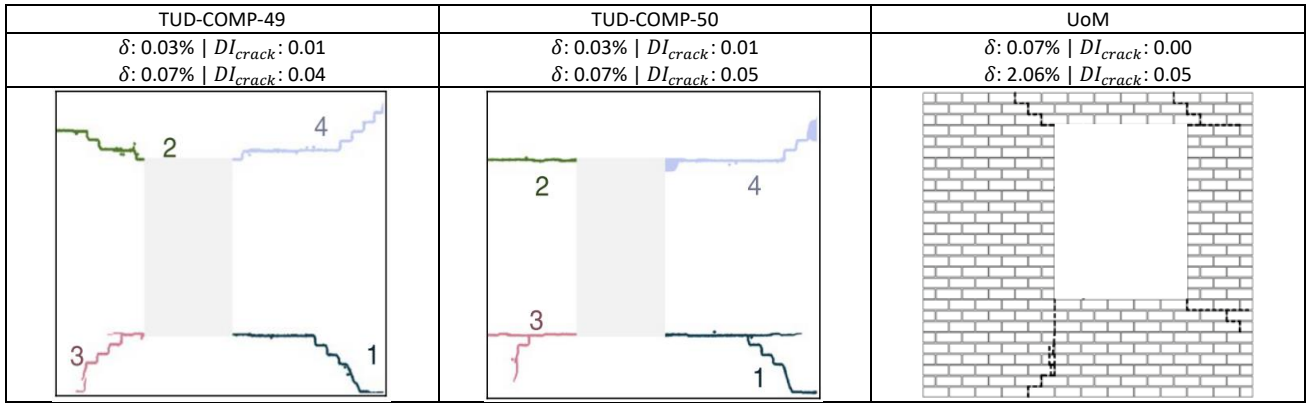
Figure 5-22: Crack patterns observed for the masonry walls with openings as reported in (Heath et al. 2008; Korswagen et al. 2020a). The crack patterns correspond to the end of the tests. The drift ratio δ and the corresponding DI_{crack} are displayed for the onset of cracking and the end of the tests.

TUD-Unstrengthened	TUD-Strengthened
δ: 0.07% | DI_{crack}: 0.03	δ: 0.07% | DI_{crack}: 0.04
δ: 1.61% | DI_{crack}: 0.05	δ: 2.99% | DI_{crack}: 0.09
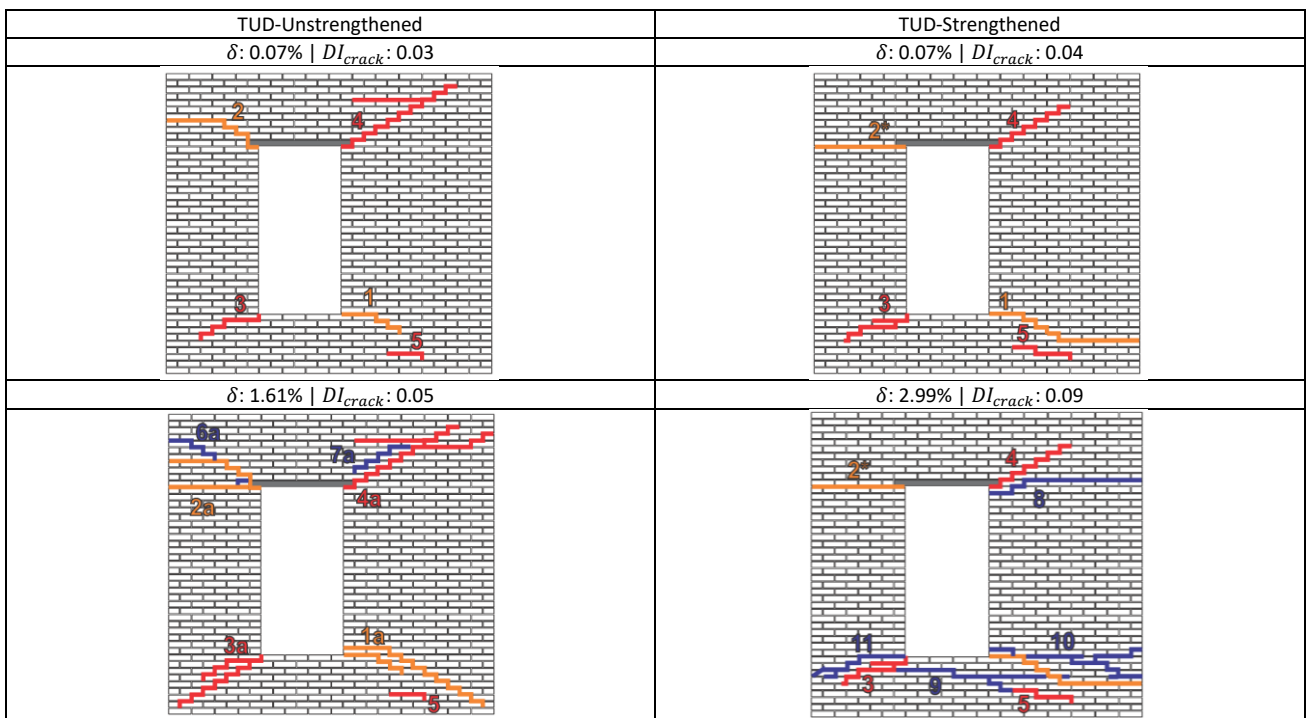
Figure 5-23: Crack patterns observed for the masonry walls with opening as reported in (Drougkas et al. 2020). The crack patterns, the drift ratio δ and the corresponding DI_{crack} are displayed for the Damage Limitation state (top) and the Near Collapse state (bottom).

The walls with opening resemble the response of the rocking slender walls; the failure mechanism is expressed through limited cracking (DI_{crack} is up to 0.05; the TUD-Strengthened wall reaches DI_{crack} 0.09) while high values of drift are attained (Figure 5-14). The TUD-COMP-49 and TUD-COMP-50 specimens (Korswagen et al. 2020a) were tested up to 0.07% drift ratio since the scope of the study was the propagation of light damage. Moreover, the walls with opening tested at TUD (TUD-COMP-49, TUD-COMP-50, TUD-Unstrengthened and TUD-Strengthened) reached values of DI_{crack} 0.04 to 0.05 for very limited drift. This could be attributed to two reasons. High resolution DIC techniques were used for crack mapping and therefore the crack onset could be recorded for crack widths less

than 0.1 mm which is the limit for damage to be visible to the naked eye. Moreover, for the specimens tested at TUD the considered loading protocols included numerous cycles while the UoM wall was tested with only a limited number of loading cycles, that is 5. Beyer & Mergos (2015) and Godio et al. (2019) studied the implications of loading protocols on the drift capacity of URM walls and it was concluded that applying numerous loading cycles does not alter the damage pattern, but damage takes places at lower drift. The loading history influences the drift capacity while force capacity is insensitive; when cyclic load was applied the deformation capacity was half the maximum drift attained for monotonic test (Beyer and Mergos 2015).

5.2.2.4 TUE shear walls

Six shear walls with 0.99 m length and 1.14 m height were tested at TUE under different precompression load keeping the bottom and top boundaries horizontal while precluding any vertical movement (Vermeltfoort et al. 1993); four walls were solid and two had a central opening (Figure 5-24). The crack patterns for the TUE walls were available only for the final stage of the experiments, therefore in Figure 5-14 they are represented only as a single marker per specimen; no line could be drawn to display the evolution of DI_{crack}.

J6D and J7D, solid walls from TUE with higher overload, that is 1.21 MPa and 2.12 MPa respectively, recorded values of DI_{crack}, i.e. 0.11, similar to the rest of the squat walls presented in Section 5.2.2.2 while J4D and J5D with 0.3 MPa precompression reached higher values of DI_{crack}, that is 0.19 to 0.23 (Figure 5-14b). All the solid walls experienced a stepped diagonal crack through perpend and bed joints and additionally for the walls with low precompression bending cracks at the bottom and top of the wall were possible due to the lower confinement. The drift ratio at failure was in the range of 0.3% for the solid shear walls tested at TUE, matching the response of the squat walls with greater height presented in Section 5.2.2.2 (Figure 5-14b).

The crack pattern of the TUE shear walls with opening comprised of diagonal zigzag cracks around the corners of the opening and tensile cracks at the base and top of the small piers leading to a collapse mechanism with four hinged rigid blocks (Figure 5-24), similar to the walls with opening presented in Section 5.2.2.3 (Figure 5-22 and Figure 5-23). The TUE walls with opening attained high drift capacity close to 2% and the obtained DI_{crack}, that is 0.15 to 0.18, was higher than the counterparts with greater height. It cannot be certainly said whether the higher DI_{crack} is due to size effects or can be attributed to the higher precompression levels of the TUE walls. In particular, the TUE specimens with opening had 0.3 MPa overload while the rest of the walls with opening (presented in Section 5.2.2.3) had vertical load up to 0.12 MPa.
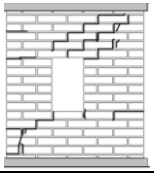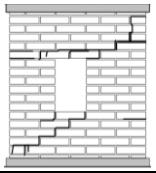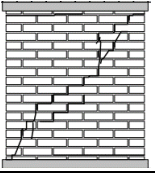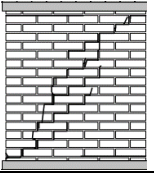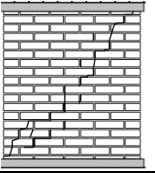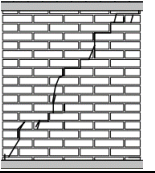
J2G	J3G	J4D	J5D	J6D	J7D
δ: 1.87%	δ: 1.94%	δ: 0.32%	δ: 0.35%	δ: 0.33%	δ: 0.27%
DI_{crack}: 0.18	DI_{crack}: 0.15	DI_{crack}: 0.19	DI_{crack}: 0.23	DI_{crack}: 0.11	DI_{crack}: 0.11

Figure 5-24: Crack patterns observed for the shear masonry walls as reported in (Vermeltfoort et al. 1993) (reproduced from Lourenço (1996)). The drift ratio δ and the corresponding DI_{crack} are displayed for the end of the tests.

5.2.3 Discussion

EC8-3 (EC8-3 2005) defines three limit states for the assessment of structures under horizontal loads: (a) DL, (b) Significant Damage (SD), and (c) NC. In particular for the DL limit state EC8-3 prescribes that the structure suffers only light damage and no repair measures are needed. For the NC limit state the structure is heavily damaged, with low residual lateral strength and stiffness, although vertical elements are still capable of sustaining vertical loads (EC8-3 2005). The values of DI_{crack} and drift ratio are displayed for DL and NC (Table 5-4). These two limit states were associated with the experimental findings; DL and NC correspond to the crack onset as reported from the experimental campaigns and to the ultimate drift during the experiments, respectively. It is noted that the ultimate drift was considered at the latest loading cycle of the experiments without partial or total collapse of the specimens. For most of the examined walls no data could be extracted for the intermediate stages of the experiments, thus it is not possible to define the DI_{crack} and the corresponding drift values for the SD limit state.

In Table 5-4, the walls are categorized as slender, squat and walls with opening. The drift values corresponding to crack initiation, i.e. DL, as reported from experiments on full scale URM structures (Magenes et al. 1995; Esposito et al. 2016; Tomassetti et al. 2017; Graziotti et al. 2017; Kallioras et al. 2018, 2020; D'Altri et al. 2019a) are listed in Table 5-4 as well. It is noted that the slender and squat walls account for aspect ratio 2 to 2.8 and 0.7 to 1.4, respectively. The examined walls are presented separately for each failure mode while the results are reported for different height ranges. As explained in Section 5.2.2.4, walls with lower height experienced higher DI_{crack}, but it is not clear if this behaviour can be attributed to size effects or other parameters, such as level of axial load, due to limited data.

Table 5-4: The values of DI_{crack} and drift ratio are displayed for the limit states Damage Limitation and Near Collapse.

Specimen type	Failure mode	Height, H [m]	Damage Limitation		Near Collapse	
			DI_{crack}	Drift ratio [%]	DI_{crack}	Drift ratio [%]
Slender	F	$2 \leq H \leq 2.76$	0.01 - 0.03	0.06 - 0.25	0.05 - 0.08	1.5 - 4[1]
	H	$2 \leq H \leq 2.76$	0.01 - 0.03	0.02 - 0.25	0.12 - 0.17	0.75 - 1.3
Squat	S (DC)	$2.75 \leq H \leq 2.76$	0.01 - 0.06	0.02 - 0.05	0.06 - 0.13	0.2 - 0.56
	S (DC)	$1.14 \leq H \leq 1.35$	-	-	0.11 - 0.21	0.27 - 0.56
	S (HS)	$2.75 \leq H \leq 2.76$	0.02	0.01 - 0.1	0.04 - 0.05	0.47 - 1
Walls with opening[2]	FRB	$2.4 \leq H \leq 2.76$	0.01 - 0.03	0.03 - 0.07	0.05	1.61 - 2.06
	FRB	$H = 1.14$	-	-	0.15 - 0.18	1.87 - 1.94
Full scale[3]	-	-	-	0.05 - 0.15	-	-

F: flexure; H: hybrid; S (DC): shear (diagonal cracking); S (HS): shear (horizontal sliding); FRB: four rigid bodies (for clarification refer to Section 5.2.2.3)

[1] The drift value for the HW wall was not regarded since the experiment was stopped before reaching the deformation capacity

[2] The strengthened wall TUD-Strengthened was not considered

[3] Experiments on full scale masonry structures from the literature (Magenes et al. 1995; Esposito et al. 2016; Tomassetti et al. 2017; Graziotti et al. 2017; Kallioras et al. 2018, 2020; D'Altri et al. 2019a)

According to EC8-3 (EC8-3 2005), the attainment of the DL limit state is considered when the maximum force of the individual walls is reached while no drift limits are provided. Calvi (Calvi 1999) set as 0.1% and 0.3% the drift limit for the LS1 limit state (i.e. no damage) and LS2 (minor structural damage easily repairable) respectively. The Italian Code NTC 2008 limits the drift at DL for URM buildings to 0.3%, whereas the latest NTC 2018 reduced this value to 0.2% (Morandi et al. 2018). Morandi et al. (2018) found appropriate the drift threshold proposed in NTC 2018 for DL. The considered experimental results agree with the conclusion of Morandi et al. (2018). In particular, DL corresponds to drift values 0.02% - 0.25%, 0.01% - 0.1%, and 0.03% - 0.07% for slender, squat, and walls with opening respectively while crack initiation was reported for drift levels 0.05% to 0.15% based on experiments on full scale URM structures (Magenes et al. 1995; Esposito et al. 2016; Tomassetti et al. 2017; Graziotti et al. 2017; Kallioras et al. 2018, 2020; D'Altri et al. 2019a) (Table 5-4). Therefore, the consideration of a drift value linked to the DL limit state is suggested and the value prescribed by NTC 2018 is deemed suitable.

Regarding the NC limit state, the drift threshold set by EC8-3 defines distinct drift boundaries for flexure and shear, that is $1.07 \cdot H_0/L\%$ and 0.53% respectively. For instance, for the slender calcium silicate walls tested at TUD and EUCENTRE, according to EC8-3 when flexural failure mode is considered, the drift limit at NC is calculated as 1.3% and 2.7% for double fixed and cantilever boundary conditions respectively. It is noted that the experimentally derived NC drift of the slender walls was 1.5% to 4% and 0.8% to 1.3% when failing with flexural and hybrid mode respectively. Therefore, the limits set by EC-8 could be considered acceptable for flexural failure but appear inadequate for the hybrid cases. Moreover, the EC8-3 drift limit for shear, i.e. 0.53%, is considered overconservative to be applied for the slender walls. Therefore, as pointed out also in Section 5.2.2.1, it is essential to define an objective way to reliably predict the failure mode of slender walls and the

incorporation to EC8-3 of an additional drift limit for hybrid failure mode is advised. Based on the considered experimental data, a threshold value between the limits defined for shear and flexure seems appropriate.

Being able to accurately identify the expected mode of slender walls would enable the better design of strengthening solutions. Vanin et al. (2017) reported that stone piers retrofitted with light interventions, such as mortar injections, the ultimate drift capacity could increase by a factor of 3 to 6 while this enhancement was even more profound when the failure mode shifted from shear to flexure. This could be very useful when designing for a retrofit solution. Appropriate considerations could be taken to avoid hybrid failure mechanism. In this way higher drift capacity is achieved and the expected cracks will be bounded to a minimum extent since rocking response is linked with lower DI_{crack}. This would render any repairs easier and less costly.

By examining the crack propagation from experiments on URM walls under in-plane load meaningful observations could be made. For the squat wall EC-COMP-3 DI_{crack} recorded at the crack onset was 0.06 while for the rest of the walls the value of DI_{crack} scored up to 0.03. Based on this, it could be inferred that a value of 0.03 for the DI_{crack} could be related to the DL limit state. Further on, the slender walls with rocking response reach a plateau for increasing drift while DI_{crack} increases linearly with drift for the slender walls with hybrid failure and the squat specimens characterized by shear failure with diagonal cracks. In other words, each failure mode and wall type is characterized by a distinctive evolution of DI_{crack}. Therefore, similar to drift, DI_{crack} values cannot be universally correlated with damage states; for each failure mechanism and specimen type different limit values need to be defined per limit state. While certain trends were observed, additional experimental data are required to further generalize any findings and reliably correlate the DI_{crack} values with certain damage states. Nevertheless, as pointed out by Vintzileou et al. (2020), quantitative data for crack characteristics for different drift levels are ill reported in experimental campaigns found in the literature which hinders the extraction of more reliable conclusions and thus the inclusion of such data in future studies is recommended.

Petry & Beyer (2014) highlighted that tests on walls with smaller height lead to higher drift capacities than full storey height walls. Morandi et al. (2018) argued that URM walls of low height, that is less than 1.5 m, could be subjected to "size effects"; the boundary conditions could affect the results of the cyclic tests, in terms of lateral strength, failure mechanism and drift capacity. For the examined walls with smaller height, that is 1.14 m or 1.35 m, no striking differences could be observed in terms of drift capacity in comparison to walls with greater height. On the other hand, variations could be noticed regarding the DI_{crack} values. Nevertheless, due to limited available data it could not be confidently argued whether these

differences are due to size effects or are related to other parameters, such as higher axial load. Extra experimental data need to be considered to draw any solid conclusions.

5.2.4 Conclusions

Cumulative damage due to subsequent ground motions is expected to have an effect on the seismic capacity of a structure. The most common practice for the evaluation of the structural condition of buildings is the visual inspection of any signs of damage expressed as residual cracks. Crack-based assessment has attracted the interest of the research community, although relevant studies for masonry are rather limited. The quantification of crack propagation based on experimental studies was attempted for masonry structures. Experimentally obtained crack patterns were investigated and their correlation with damage accumulation was examined. A damage index accounting for the total failed mortar joints on masonry walls was introduced. This damage index can be easily computed by visually inspecting a cracked masonry wall providing an intuitive characterization of the damage extent. The evolution of cracking was evaluated based on an extensive set of experimental studies making use of the newly introduced damage index.

The main contributions are:

- The lack of any drift limit for URM walls at the DL limit state in the EC8-3 (EC8-3 2005) was highlighted. The threshold value of 0.2% prescribed by the recent Italian Code NTC 2018 was found suitable based on the examined experimental results from this PhD and other studies in the literature.
- Slender walls display distinctive response in terms of drift capacity and DI_{crack} levels when failing with flexural or hybrid mechanism. Thus, in order to reliably assess slender masonry piers it is essential to define an objective way to reliably predict the failure mode of these walls. A preliminary formula was proposed but additional experimental data are required for a more accurate calibration. The influence of shear properties, i.e. cohesion and friction coefficient, on the failure mode and the expected crack patterns was elucidated.
- When slender URM walls with hybrid mode are assessed with the EC8-3, the drift capacity defined for flexure was found inadequate while the one for shear is deemed overconservative. The incorporation to EC8-3 of an additional drift limit for hybrid failure mode was advised. Based on the considered experimental data, a threshold value between the limits defined for shear and flexure is reckoned appropriate.
- Being able to accurately identify the expected mode (flexural or hybrid) of slender walls would enable the better design of strengthening solutions. Hybrid failure mechanism was associated with lower drift capacity and higher damage extent. Therefore, when possible, appropriate considerations could be taken to avoid hybrid failure mechanism

to achieve higher drift capacity and limit the expected cracking which would render any repairs easier and less costly.

- Limits of DI_{crack} values corresponding to the damage levels DL and NC were introduced. This was not possible for the SD limit state due to limited data regarding the intermediate stages of the experiments.

- Walls of lower height were examined and higher cracking distribution expressed through values of DI_{crack} were attained than taller piers while the drift capacity was similar. Due to limited available data, it could not be confidently argued whether these differences are due to size effects or are related to other parameters, such as higher axial load. Extra experimental data need to be considered to draw any solid conclusions and possible correction factors could be produced to tackle any size effects.

In order to be able to further generalize any conclusions further experimental data are required. It is advised that future experimental campaigns report in a more systematic way quantitative data regarding crack propagation (crack patterns, length and width for different drift levels). These data could enrich the dataset already collected in order to reliably define damage states for masonry structures. As next step, data from full scale tests will be additionally investigated to further enrich any drawn conclusions.

5.3 Numerical investigation of the quantification of crack propagation with the micro-modelling approach

Along the numerical exercises with the DEM (refer to Section 5.1) certain limitations were encountered. The numerical model with the DEM considered elastic rigid blocks for the representation of masonry units neglecting any failure or degradation under compression while the verification of the mechanical parameters was made against a single wall specimen. Moreover, the numerical results for cracking could be extracted on the basis of two mechanisms (tensile opening and shear sliding) which made difficult the correlation of any findings with experimental measurements; from visual inspection of damaged walls the differentiation between tensile and shear failure is not possible.

In order to address these issues, a micro-modelling solution was developed in the computational software ABAQUS (ABAQUS 2013) to reliably reproduce and quantify the damage accumulation in masonry structures (Section 5.3.1). The numerical model was verified against a challenging set of experimental studies and a comprehensive methodology for the calibration of the required mechanical properties is presented (Section 5.3.2). It was possible for the numerical results regarding cracking propagation to be manipulated suitably in order to be directly compared with corresponding measurements from experimental

studies. In particular, the quantification of crack propagation with the use of the damage index DI_{crack}, introduced in Section 5.2.1, was numerically scrutinized.

Furthermore, the damage classification system for masonry buildings based on maximum crack width (Table 5-5) proposed by Burland et al. (1977) was evaluated numerically. The aim of this classification scheme was to relate the damage extent described by the maximum measured crack width to ease of repair. Although such a damage classification based solely on crack width appears convenient, Burland et al. (1977) highlighted that to assess the degree of damage account must be taken of its location; crack width is only one aspect of damage and should not be used on its own as a direct measure of it. Along with the proposed DI_{crack} (refer to Section 5.2.1), the crack width-based classification by Burland et al. (1977) was numerically evaluated for its efficacy to provide a suitable representation of damage propagation in masonry structures. A discussion on the numerical investigation of the quantification of crack propagation for masonry structures is provided in Section 5.3.3, and any conclusions are demonstrated in Section 5.3.4.

Table 5-5: Damage classification of masonry buildings based on maximum crack width according to (Burland et al. 1977).

Damage level	Maximum crack width [mm]
1. Very slight	0.1 to 1
2. Slight	1 to 5
3. Moderate	5 to 15
4. Severe	15 to 25
5. Very severe	> 25

5.3.1 Development of a micro-modelling representation of masonry structures

A simplified micro-modelling approach where expanded units are represented by continuum elements whereas the behaviour of the mortar joints and unit-mortar interface is lumped in discontinuous elements was regarded for the representation of the cyclic behaviour of masonry structures under recursive load. The implementation of the model was realized within the computational software ABAQUS (ABAQUS 2013) suitable for finite element analysis. Due to the lack of suitable constitutive law implemented in ABAQUS, a subroutine was developed for the sake of this study to describe the response of mortar joints under cyclic load. Since the focus of this study was on the in-plane performance of masonry walls their numerical representation was two-dimensional. The continuum elements simulating masonry units were governed by damaged elasticity in combination with tensile and compressive plasticity while cohesive-frictional behaviour was incorporated in the interfaces representing mortar joints. Extra clarification on the simulation of masonry units and mortar joints are provided in Sections 5.3.1.1 and 5.3.1.2 respectively. Any brick faces that may come into contact during an analysis are assigned to contact pairs of master/slave surfaces considering a finite-sliding formulation, allowing any arbitrary motion of the surfaces, along with the node-to-surface discretization method. The subroutine is called at points on the slave surface of a contact pair with the user-defined constitutive model defining the interaction between the

surfaces. The use of direct-integration implicit dynamic analysis was found to resolve any convergence issues while geometric nonlinearity was additionally taken into consideration.

5.3.1.1 Representation of the masonry units in a masonry wall

Since the mortar joints are simulated by a zero-thickness interface, the size of the masonry units has to be to be expanded slightly (i.e. half of the mortar thickness in each direction) to accommodate this. The masonry units were simulated as nonlinear blocks with CPS4R (4-node bilinear plane stress) elements making use of the CDP constitutive law. For extra clarification regarding the CDP model refer to Section 3.3. Although bricks were simulated with the CDP model, which considers isotropic response, the incorporation of horizontal and vertical discontinuities representing mortar joints allows to reliably reproduce the anisotropic behaviour of masonry (see Section 5.3.1.2 for extra details).

The stiffness of masonry units was found to significantly influence the overall stiffness and horizontal force capacity of the masonry walls numerically evaluated (see Section 5.3.2 for a discussion on the calibration of the mechanical properties). This is attributed to the fact that shear strength is linked to the developed compression stress at the interfaces (see Eq. (5.17)). Young's modulus (E_0) values from previous experimental and numerical studies (Riddington and Naom 1994; Lourenço 1996; Nazir and Dhanasekar 2014; Dolatshahi and Aref 2016) were evaluated and the resulted values are reported in Table 5-8; the assumption of rather rigid brick elements yielded the best representation of the experimental response. The Poisson's ratio was assumed as 0.2 following previous studies (Petry and Beyer 2015b; Chácara et al. 2017; Dolatshahi et al. 2018; D'Altri et al. 2019a; Greco et al. 2020; Wilding et al. 2020).

The developed cohesive-frictional behaviour for mortar joints does not consider failure in compression (refer to Section 5.3.1.2 for the characterisation of the response of mortar joints). Therefore any nonlinearities due to compression were accounted for by suitably configuring the compressive strength σ_{c0} for the CDP model. In particular, σ_{c0} was found to affect the shape of the hysteresis loop (see Section 5.3.2.1 for a numerical evaluation of different values considered for σ_{c0}). The calibrated values for σ_{c0} corresponded to 30% to 50% of the compressive strength of masonry measured perpendicular to bed joints (Table 5-8).

Since only limited cracks are expected along brick units, their tensile strength σ_{t0} did not critically change the response of the examined masonry walls. Given the fact that the strength of brick in tension is not always reported, a universal value of 1 MPa was deemed suitable for the numerical analysis carried here based on past studies (Dolatshahi and Aref 2016; Abdulla et al. 2017; D'Altri et al. 2019a; Korswagen et al. 2020a).

Table 5-6: Nonlinear uniaxial response of the Concrete Damaged Plasticity in compression (left) and tension (right).

Compression			Tension		
ε_c^{pl}	σ_c [MPa]	d_c	ε_t^{pl}	σ_t [MPa]	d_t
0	σ_{c0}	0	0	1	0
0.01	1	0.9	0.005	0.1	0.9

Table 5-7: The main parameters for the Concrete Damaged Plasticity model.

Dilatation angle [°]	Eccentricity	σ_{b0}/σ_{c0}	K_c	Viscosity
10	0.1	1.16	0.666	0.0005

Table 5-8: Mechanical properties considered for the Concrete Damaged Plasticity model for the simulation of different experimental campaigns (see Section 5.3.2). The values in parenthesis correspond to the experimental values.

Experimental campaign	Young's modulus, E_0 [MPa]	Compression strength, σ_{c0} [MPa]
Calcium silicate walls - EUCENTRE (Section 5.3.2.1)	30,000	2 (6.2)
Clay walls - EUCENTRE (Section 5.3.2.2)	30,000	5 (11.22)
Calcium silicate walls - TUD (Section 5.3.2.3)	15,000	2 (5.94)
Walls with opening - TUD (Section 5.3.2.4)	15,000	5 (14.02)
Shear walls - TUE (Section 5.3.2.5)	15,000	5 (10.5

5.3.1.2 Representation of mortar joints in a masonry wall

For the discontinuous elements replicating the response of mortar joints the initial linear elastic behaviour was followed by the initiation and evolution of damage. The elastic behaviour is described in terms of an elastic constitutive matrix that relates the normal and shear stresses to the corresponding displacements across the interface. The normal and tangential stiffness components are not coupled; pure normal separation by itself does not give rise to cohesive forces in the shear direction, and pure shear slip with zero normal separation does not give rise to any cohesive forces in the normal direction.

The normal stress σ_n for the elastic region is calculated as follows:

$$\sigma_n = \begin{cases} k_{n,t} \cdot u_n, & u_n \geq 0 \\ k_{n,c} \cdot u_n, & u_n < 0 \end{cases} \qquad (5.14)$$

where $k_{n,c}$ and $k_{n,t}$ the cohesive stiffness in the normal direction for compression and tension respectively, and u_n the normal displacement; positive and negative u correspond to tension and compression respectively. To limit possible surface penetrations while in compression, the compressive normal stiffness was assumed considerably higher than the tensile counterpart (i.e. $k_{n,c} = 10 \, k_{n,t}$). It is assumed that cohesive surfaces do not undergo damage under pure compression. Any compressive failure is accounted for at the masonry unit level.

Regarding the tangential direction, the shear stress τ_s increases linearly with the shear displacement u_s in the elastic region:

$$\tau_s = k_s \cdot u_s \qquad (5.15)$$

where k_s the cohesive stiffness in the tangential direction.

The process of degradation begins when the contact stresses satisfy certain damage initiation criteria. The considered damage initiation criterion is a Mohr-Coulomb failure with tension cut-off (Figure 5-25). The criterion is defined as:

$$max\left\{\frac{\langle\sigma_n\rangle}{f_t},\frac{\tau_s}{f_s}\right\} = 1 \tag{5.16}$$

where the symbol $\langle\rangle$ represents the Macaulay bracket and signifies that a purely compressive stress state does not initiate damage, f_t is the tensile strength, while shear strength f_s is given as follows:

$$f_s = -tan\varphi \cdot \sigma_n + c \tag{5.17}$$

where $tan\varphi$ is the internal friction coefficient and c is the cohesion.
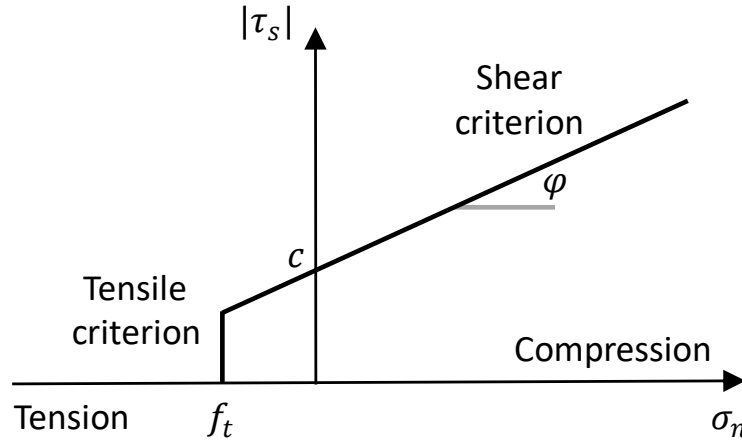
Figure 5-25: Illustration of the Mohr-Coulomb failure with tension cut-off considered as damage initiation criterion for the discontinuous elements.

Once the damage initiation criterion is reached, a damage evolution law describes the rate at which the cohesive stiffness is degraded. In this study linear damage evolution is considered. A damage variable D represents the overall damage at the contact point. It initially has a value of 0 and D monotonically evolves from 0 to 1 upon further loading after the initiation of damage. The damage variable D is defined as follows:

$$D = max\left\{\begin{array}{c}\dfrac{(u_n^{max} - u_n^o)}{(u_n^f - u_n^0)}\\[2mm]\dfrac{(u_s^{max} - u_s^o)}{(u_s^f - u_s^0)}\end{array}\right. \tag{5.18}$$

where u_n^o and u_s^o the displacement at damage initiation, u_n^f and u_s^f the displacement at complete failure, and u_n^{max} and u_s^{max} the maximum normal displacement attained during the

loading history; the "n" and "s" subscripts signify displacement in the normal and shear direction respectively. The damage due to normal and shear stresses are coupled in essence that damage due to normal stresses leads to reduction of the shear strength and vice versa.

Upon damage initiation, the normal stress for tension is defined as:

$$\sigma_n = \begin{cases} (1-D) \cdot f_t, & u_n^o \leq u_n < u_n^f \\ 0 & , & u_n^f \geq u_n \end{cases} \tag{5.19}$$

In Figure 5-26 an illustration of the normal behaviour of discontinuous elements prior to and upon damage initiation is presented. Upon exceedance of the elastic branch, for tensile stresses loading and unloading takes places with the degraded stiffness $(1-D)k_{n,t}$ (Figure 5-26).
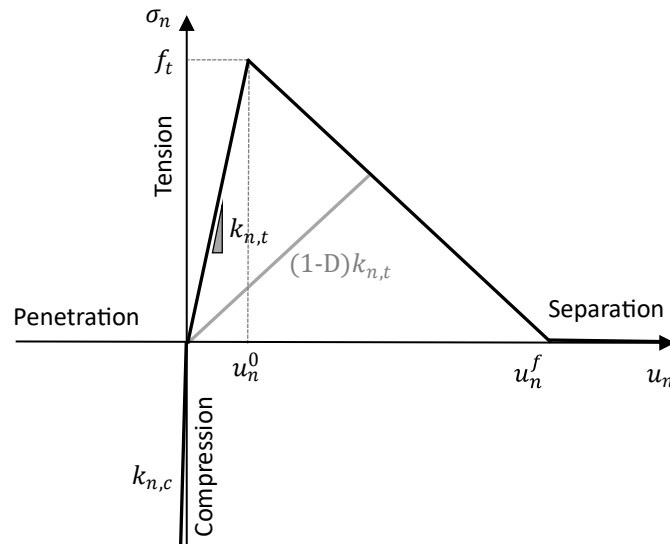
Figure 5-26: Illustration of the normal behaviour of discontinuous elements.

Once the damage criterion is satisfied, shear stress is given:

$$\tau_s = \begin{cases} (1-D) \cdot f_s + D \cdot \mu \cdot \langle -\sigma_n \rangle, & u_s^o \leq u_s < u_s^f \\ \mu \cdot \langle -\sigma_n \rangle & , & u_s^f \geq u_s \end{cases} \tag{5.20}$$

where μ the residual friction coefficient. In particular, cohesive-frictional behaviour in shear is activated; as shear displacement approaches u_s^f, i.e. D tends to 1, the contribution of cohesion decreases and ultimately friction dictates the response in shear (Figure 5-27).
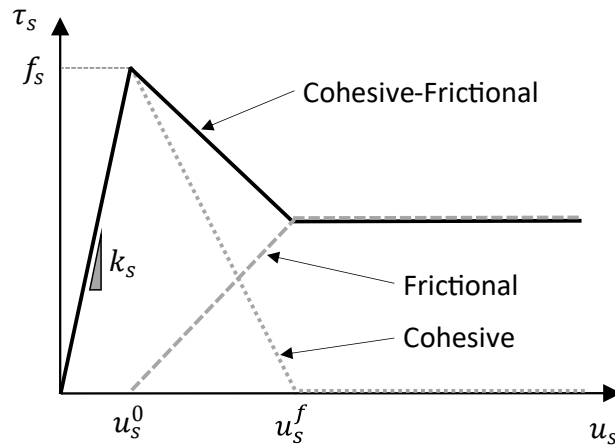
Figure 5-27: Illustration of the shear behaviour of discontinuous elements.

As shown in Eq. (5.17), shear strength is dependent on the normal stress when in compression; tensile normal stress does not contribute to shear stress. In order to visualize the influence of compressive stress on shear stress, the evolution of the latter is given for three different levels of axial stress, that is 0.1, 0.5 and 1.0 MPa (Figure 5-28a). It is noted that the curves in Figure 5-28 correspond to material properties as calculated in the experimental work by Vermeltfoort et al. (1993) for the wall specimens J4D/J5D and J2G/J3G (for more details refer to 5.3.1.2). It is evident that higher compressive stress leads to higher shear stress (Figure 5-28a). Additionally, the cyclic shear response for axial stress of 1.0 MPa is presented in Figure 5-28b. In the post peak branch, degradation takes place until the attainment of u_s^f, i.e. shear displacement at complete failure, and subsequently the response is purely frictional (Figure 5-28b).

(a) (b)
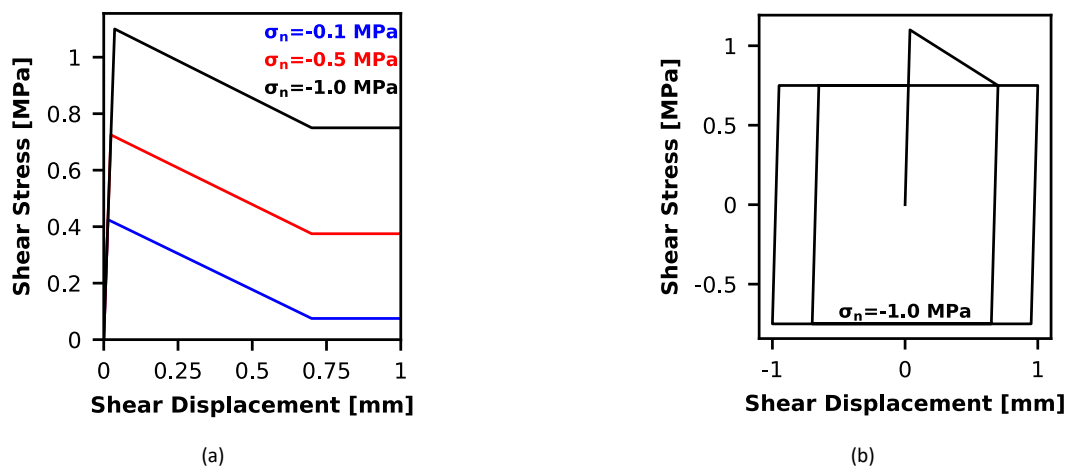
Figure 5-28: (a) Shear behaviour of discontinuous elements for different levels of axial stress. (b) Cyclic shear behaviour of discontinuous elements for axial stress 1.0 MPa. The curves correspond to material properties defined in 5.3.1.2.

Dilatancy was not considered in the behaviour of the discontinuous elements replicating the response of mortar joints. According to van der Pluijm et al. (2000) dilatancy angle decreases to zero with increasing plastic shear slip and confining normal pressure which often makes

its influence almost negligible at the macroscale, especially when masonry is not confined (Malomo et al. 2019b), and thus dilatancy can be neglected (Lourenço 1996). Similar assumption was made in previous numerical studies for masonry (Chaimoon and Attard 2007; Dolatshahi and Aref 2016; Bejarano-Urrego et al. 2018; Sarhosis and Lemos 2018; Malomo et al. 2019b).

Regarding the calibration of the material properties, the tensile strength f_t of mortar joints was set based on the bond strength f_w obtained from bond wrench tests. The parameters to define the initial and residual strength in the tangential direction (i.e. $tan\varphi$, c, and μ) were calculated based on the results of shear tests on masonry triplets. It is noted that by considering the experimentally obtained parameters well match was attained, thus no further calibration of these parameters was essential. The tensile separation u_n^f and shear slip u_s^f upon which cohesive behaviour is completely damaged were set to match the experimental tensile (Mode I) and shear (Mode II) failure respectively (van der Pluijm 1999).

According to Bejarano-Urrego et al. (2018), calculation of the contact stiffness parameters based on small scale tests led to great scatter. The tangential stiffness k_s was calibrated based on shear tests on masonry triplets yielding an accurate representation of the overall stiffness of masonry walls (D'Altri et al. 2019a). Although the latter approach is straightforward, its implementation is not possible when the corresponding experimental data are not reported. Sarhosis (2016) found the determination of numerical material properties problematic and recommended the material identification based on large scale masonry elements. The tangential stiffness k_s was obtained upon calibration over the overall response of the considered masonry walls by evaluating suitable values from the literature (Lourenço 1996; Sarhosis and Sheng 2014; D'Altri et al. 2019a). The normal stiffness in tension $k_{n,t}$ did not affect significantly the response of the analysed masonry walls (Section 5.3.2) and therefore a constant value was regarded for the different cases while for the counterpart in compression $k_{n,c}$ rigid stiffness was assigned to limit possible surface penetrations.

Perpend joints are frequently not properly filled with mortar, may have limited frictional resistance due to lack of vertical compression, and are characterized by lower quality compaction (Bejarano-Urrego et al. 2018; Malomo et al. 2019a). To account for these effects, lower properties were assigned to perpend joints in comparison to bed joints in previous numerical studies (Wilding et al. 2017; Dolatshahi et al. 2018; Korswagen et al. 2020b). In this study it was found that the properties of the perpend joints affect the shear response and thus they were configured suitably to fit the cracking pattern of specimens with shear or hybrid failure mechanism. Refer to Section 5.3.2.1 for a numerical exercise on the effect of the parameters considered for the perpend joints.

5.3.2 Numerical analysis

In this Section, the developed numerical model with the micro-modelling approach was verified over a challenging set of experimental studies. Two calcium silicate (Section 5.3.2.1) and six clay (Section 5.3.2.2) piers tested at EUCENTRE; six calcium silicate solid walls (Section 5.3.2.3) and two clay masonry panel with opening (Section 5.3.2.4) tested at TUD; and four clay shear walls tested at TUE (Section 5.3.2.5) were simulated. For additional information regarding the considered experimental campaigns refer to Section 5.2.2. The examined wall specimens accounted for diverse levels of precompression (σ_v), boundary conditions, masonry types and material (i.e. clay and calcium silicate bricks) to showcase the ability of the numerical model to reliably reproduce the performance of masonry under cyclic in-plane loads. Special interest was devoted on the simulation of the damage evolution associated to crack propagation. Furthermore, a comprehensive methodology for the calibration of the required mechanical properties was presented.

5.3.2.1 Calcium silicate walls - EUCENTRE

Two calcium silicate walls, one slender (EC-COMP-1) (Figure 5-29) and one squat (EC-COMP-3) (Figure 5-32), tested at EUCENTRE (Graziotti et al. 2015, 2016a) were modelled in this Section. The calibrated parameters of the model are presented in Table 5-8 and Table 5-9. The numerical model was able to reproduce with high fidelity the hysteresis loop and the failure mechanisms for both walls. The ability of the developed numerical model to reproduce accurately the crack propagation was verified against experimental findings (refer to Section 5.3.2.2).

For the slender case, good agreement was achieved in terms of the peak force (Figure 5-29) and failure mode; rocking behaviour with toe crushing dominated the response of the wall (Figure 5-30a). Previous numerical studies highlighted that simulations of rocking slender piers with the discrete method have difficulties to reproduce the high dissipation linked to masonry crushing phenomena (D'Altri et al. 2019a; Malomo et al. 2019b). Experimenting with the configuration of the mechanical parameters, it was observed that the compressive strength σ_{c0} of brick units affected significantly the shape of the hysteresis loop. The model calibration led to an optimum value of 2 MPa for σ_{c0} while the results for different values are displayed as well to highlight their impact on the shape of the loop (Figure 5-31). In particular, 5 and 10 MPa were examined for σ_{c0} while modelling of masonry units with elastic behaviour was regarded additionally. Upon increase of the compressive strength, the loop becomes thinner neglecting any energy dissipation due to compressive cracking at the bricks level. When the bricks were considered elastic, any dissipation was completely disregarded. Therefore, considering a rather low value of compressive strength was able to replicate the combination of rocking with the dissipation linked to toe crushing failure. Similar investigation was considered for the squat model. In particular, when elastic behaviour of the bricks was

regarded or different values of compression strength (i.e. 5 and 10 MPa) were evaluated the crack pattern was not affected whereas a thinner hysteresis loop was produced (Figure 5-33b-c).

Moreover, a numerical investigation was performed for the determination of the mechanical properties of the perpend joints. In particular, it was observed that the best match of the experimental response was achieved when inferior strength properties were assigned to the vertical joints. Reduction of the properties of the perpend joints did not affect the response of the slender wall while significantly improved the accuracy of the simulation for the squat case (Figure 5-32). For the latter case, when same properties were considered for all masonry joints, although the peak force was calculated correctly, the cracking pattern was imprecise; sliding along bed joints at the lower part of the wall was falsely predicted (Figure 5-33a). This is attributed to the significant contribution of perpend joints when shear failure expressed as diagonal zig-zag cracks takes place (Figure 5-30b). On the other hand, the properties assigned to perpend joints are not critical for rocking piers; the failure mechanism is dictated by tensile failure of bed joints at the constrained edges of a masonry wall (Figure 5-30a). Consequently, it is deemed beneficial to consider walls with different failure mechanisms in order to achieve a reliable model calibration.

Regarding the quantification of damage, the numerically obtained DI_{crack} was 0.13 approximating well the experimental counterpart (i.e. 0.08) for the slender wall (Figure 5-29). It is noted that in Figure 5-29 the "total" DI_{crack} accounts for the overall crack extent of cracks regardless of the crack width. The DI_{crack} corresponding to each damage level considers the extent of cracks with width falling in a specific range as defined in Table 5-5. For example DI_{crack} denoted as "very slight" accounts for cracks with width 0.1 to 1 mm. The greatest percentage of the cracks at failure were very slight or slight with a limited amount ($DI_{crack} =$ 0.02) reaching the moderate level while cracking initiated for limited drift (i.e. 0.06%). For the squat wall, the crack evolution was reproduced adequately (Figure 5-32). The maximum damage level was very severe with cracks wider than 15 mm accounting for $DI_{crack} = 0.05$. The shear model appears to overestimate the contribution of very slight and slight damage thus leading to a moderately higher DI_{crack} of 0.21 as compared to 0.08 from the tested wall. Similar behaviour was observed for other walls with shear failure as well. In order to calculate DI_{crack} more realistically perhaps the contribution of lower damage levels (that is very slight and slight) could be corrected to reduce their influence on the final score at ultimate failure. This requires further numerical investigation and will not be examined further.

Figure 5-29: Hysteresis loop (left); evolution of DI_{crack} (middle) and damage level (right) against drift ratio for the specimen EC-COMP-1.

Figure 5-30: Experimentally obtained crack pattern (left) (reproduced from Graziotti et al. (2015)) and numerically calculated deformed shape (right) for the specimens (a) EC-COMP-1 and (b) EC-COMP-3. Contours represent magnitude of deformations in m.
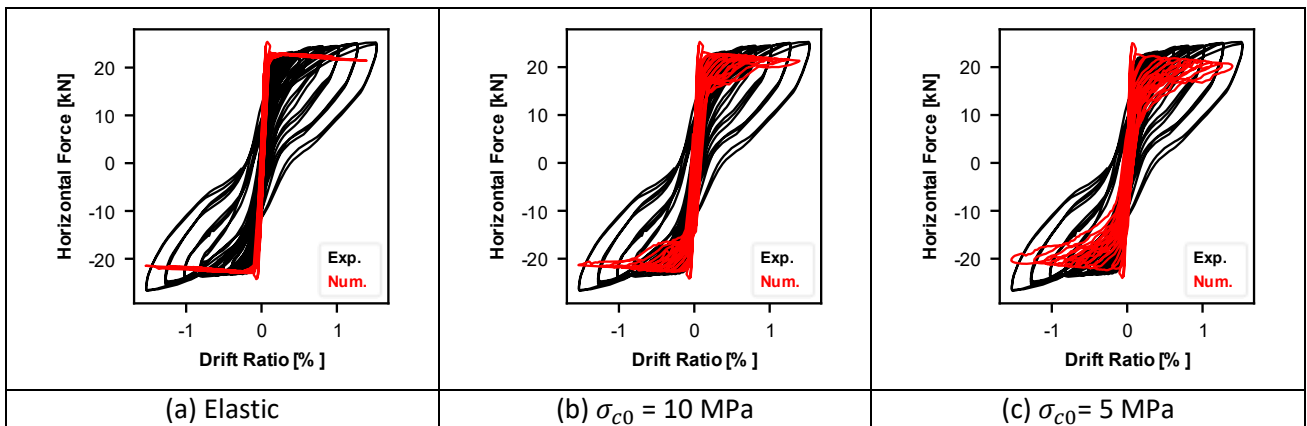
Figure 5-31: Hysteresis loops produced with different numerical configurations of the specimen EC-COMP-1: (a) elastic behaviour for the masonry units; compressive strength σ_{c0} equal to (b) 10 MPa and (c) 5 MPa.
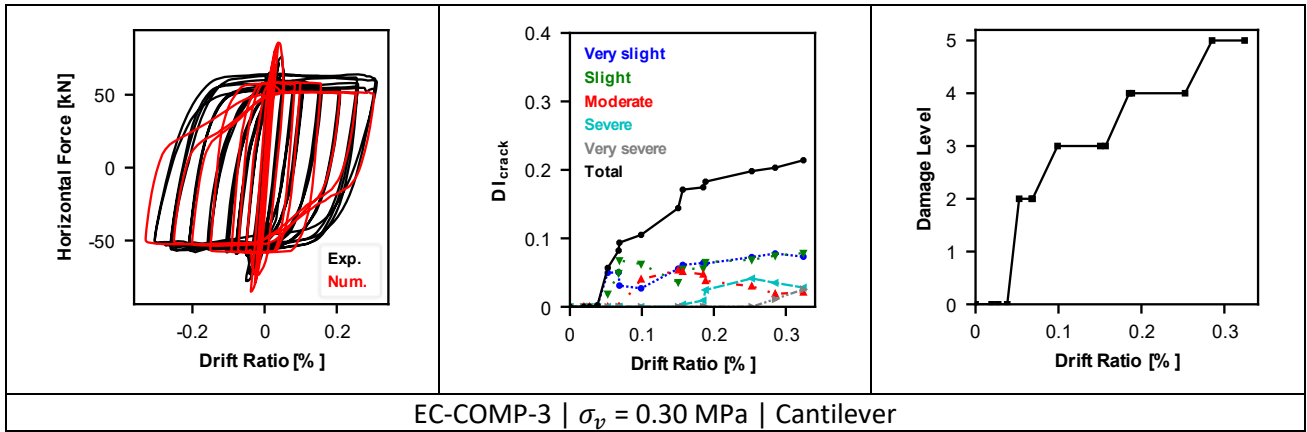
Figure 5-32: Hysteresis loop (left); evolution of DI_{crack} (middle) and damage level (right) against drift ratio for the specimen EC-COMP-3.
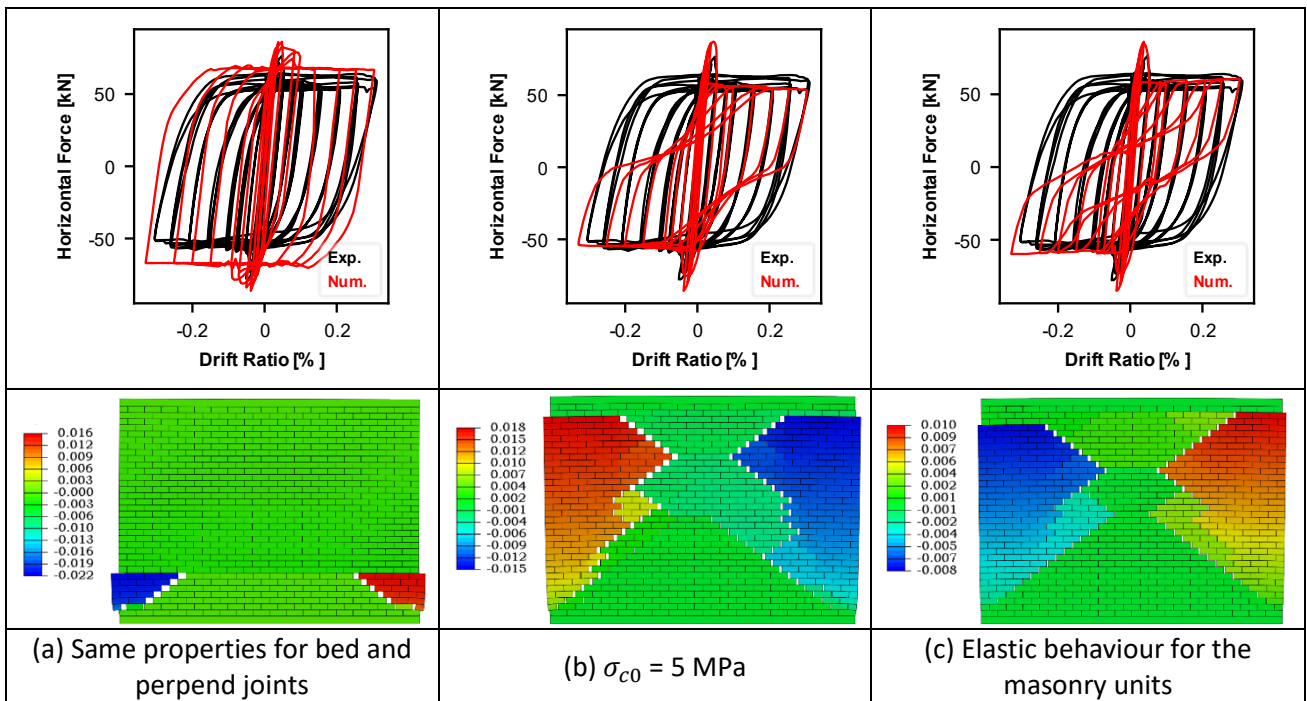
Figure 5-33: Hysteresis loops (top) and deformed shape (bottom) produced with different numerical configurations of the specimen EC-COMP-3: (a) same properties for bed and perpend joints; (b) compressive strength σ_{c0} equal to 5 MPa; and (c) elastic behaviour for the masonry units. Contours represent magnitude of deformations in m.

Table 5-9: Mechanical properties for the definition of the behaviour of the mortar joints for the calcium silicate walls tested at EUCENTRE.

Parameter	Units	Mortar bed joints	Mortar perpend joints
Normal direction			
f_t	[MPa]	0.240	0.060
u_n^f	[mm]	0.6	0.4
$k_{n,t}$	[N/m³]	10^7	
Tangential direction			
c	[MPa]	0.130	0.050
$tan\varphi$	[-]	0.45	0.45
μ	[-]	0.50	0.50
u_s^f	[mm]	0.5	0.3
k_s	[N/m³]	$3 \cdot 10^7$	

5.3.2.2 Clay walls - EUCENTRE

Three slender (Figure 5-34 and Figure 5-35a-c) and one squat (Figure 5-35d and Figure 5-38) clay walls tested at EUCENTRE (Graziotti et al. 2016b; Kallioras et al. 2018) were simulated. The calibrated mechanical parameters are reported in Table 5-8 and Table 5-10. Once again the numerical simulations were able to reliably reproduce the experimental response. The three slender piers accounted for different axial ratio which led to different failure patterns; for low precompression load rocking with toe crushing were observed while upon consideration of higher σ_v the failure shifted to a hybrid mechanism with shear damage dominating the response (Figure 5-35a-c). It is noted that the analysis for the EC-COMP2-1 wall was terminated upon exceedance of 2% drift ratio due to excessive distortion at the crushed brick elements (Figure 5-35a). The numerical model captured well the response under different axial load and the produced hysteresis loops matched the experimental response. For the squat wall, shear diagonal cracks took place leading to high energy dissipation (Figure 5-35d and Figure 5-38).

Regarding the mechanical properties of the perpend joints, it is noted that only reduction of the tensile strength was found suitable while the rest of the parameters were set similar to the bed joints (Table 5-10). For the walls modelled in Section 5.3.2.1, the assumed properties for the perpend joints were substantially lower that the bed joints. This difference could be possibly attributed to the fact that the walls presented in this Section were of two-leaf thickness allowing for better interconnection among the bricks and thus limiting the vulnerability of the perpend joints. Therefore the consideration of a standard reduction factor for the properties of the perpend joints that could be used for different wall typologies does not seem suitable. An incremental reduction of the strength of the perpend joints appears as the recommended practice that would allow for a correct calibration.

In order to evaluate the fidelity of the crack evolution computed from the numerical analysis, measurements from the tested walls were used for comparison. For the slender wall EC-COMP2-1 deformations extracted from monitored markers were considered (see Figure 5-37). The markers were at the top constrained edge where the greatest crack opening was

observed due to rocking response of the wall. The mortar joints experienced incrementally increasing opening up to 18 mm while residual crack opening up to 2 mm was observed for the final loading cycles (Figure 5-36b). Additionally, the horizontal deformation along the brick layers accounting for shear sliding was examined. Joint sliding accumulated along the loading cycles and reached up to 11 mm (Figure 5-36c). The joints that failed in shear did not return to their original position thus leading to permanent damage expressed as residual sliding (Figure 5-36c). Good agreement was achieved between the numerical (Figure 5-36) and experimental (Figure 5-37) evolution of cracks for both failure mechanisms (i.e. flexural joint opening and shear sliding). Therefore the developed numerical model is able to reproduce reliably the accumulation of damage as expressed through cracking evolution.

For the rocking specimen EC-COMP2-1 (Figure 5-34a) upon the activation of the failure mechanism no further crack propagation was recorded (i.e. DI_{crack} increased only slightly for greater drift values) while the already formed cracks became wider around the crushed toes reaching damage level 4. The slender walls with hybrid failure (EC-COMP2-2 and EC-COMP2-3) reached damage level 3 at the ultimate stage (Figure 5-34b-c). For the latter the DI_{crack} was predicted accurately (0.12) while for the former wall this value was higher than the experimental response. This is attributed to the overestimation of the very slight damage accounting for crack width up to 1 mm (Figure 5-34c). The squat model EC-COMP2-4 reached damage level 4 at ultimate failure while crack onset took place for 0.11% drift ratio (Figure 5-38). Mortar joints attained at moderate or severe damage level jointly corresponded to DI_{crack} of 0.07 (Figure 5-38).
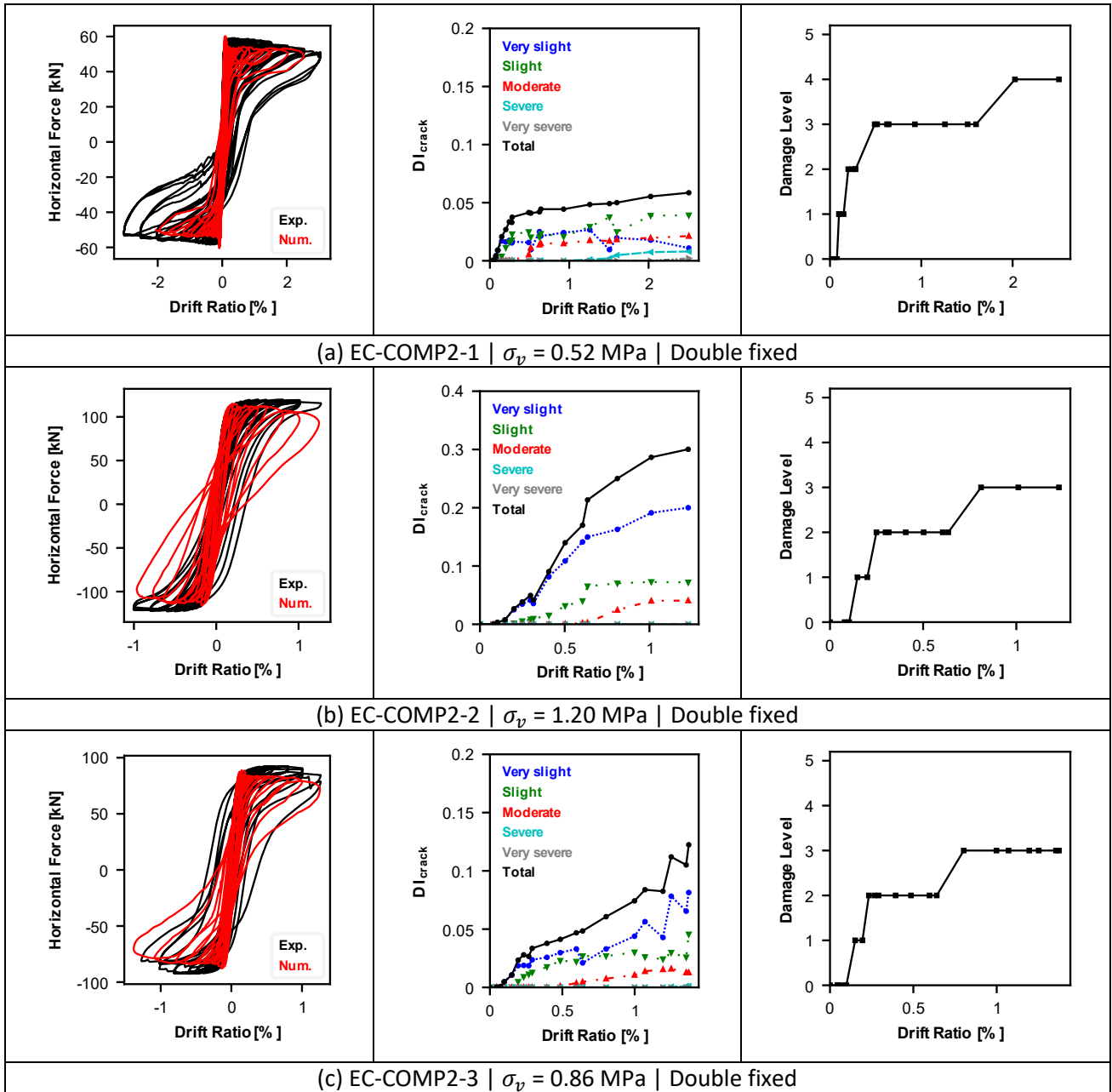
Figure 5-34: Hysteresis loop (left); evolution of DI_{crack} (middle) and damage level (right) against drift ratio for the specimens (a) EC-COMP2-1, (b) EC-COMP2-2, and (c) EC-COMP2-3.
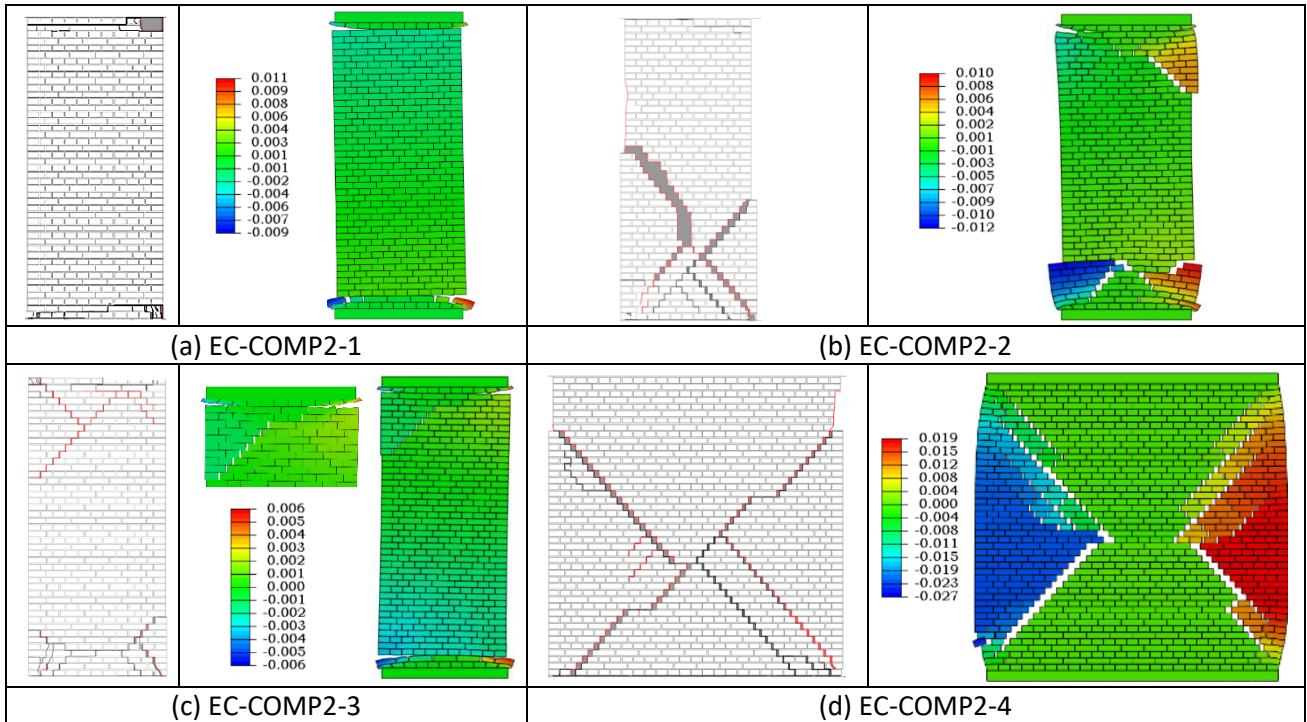
Figure 5-35: Experimentally obtained crack pattern (left) (reproduced from Graziotti et al. (2016)) and numerically calculated deformed shape (right) for the specimens (a) EC-COMP2-1, (b) EC-COMP2-2, (c) EC-COMP2-3, and (d) EC-COMP2-4. Contours represent magnitude of deformations in m.
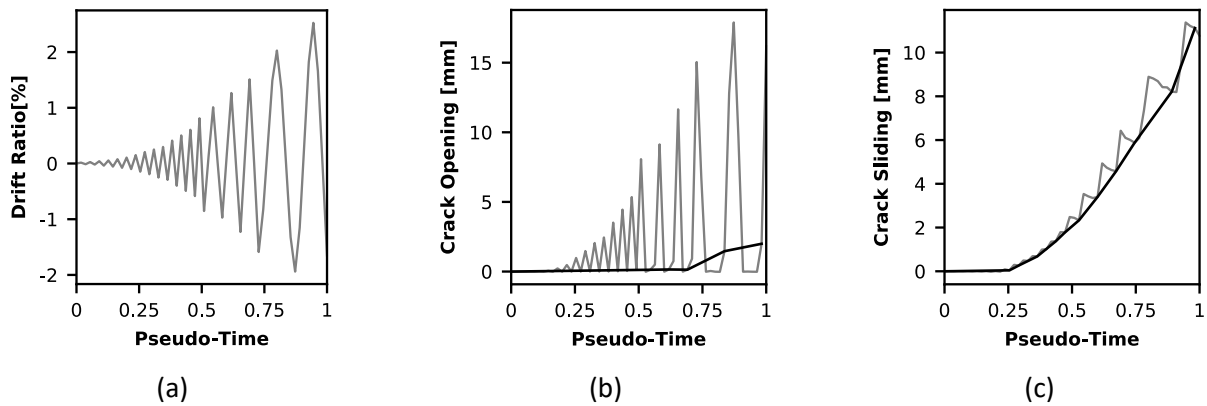
Figure 5-36: Time-history of (a) drift ratio; (b) crack opening and (c) crack sliding as measured at the top left corner of the EC-COMP2-1 specimen. For the sub-figures (b) and (c) the residual values at the end of each cycle are shown with black line.
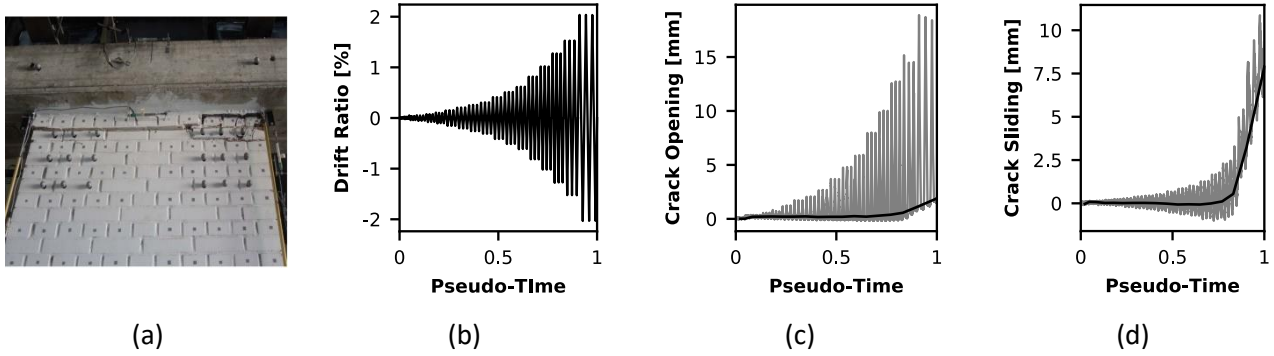
Figure 5-37: Experimental results from the tested wall EC-COMP2-1 (Graziotti et al. 2016b). (a) Crack pattern at the top part of the wall at the end of the test. Time-history of (b) drift ratio; (c) crack opening and (d) crack sliding as measured with monitoring markers at the top left corner of the wall. For the sub-figures (c) and (d) the residual values at the end of each cycle are shown with black line.

EC-COMP2-4 | σ_v = 0.30 MPa | Double fixed
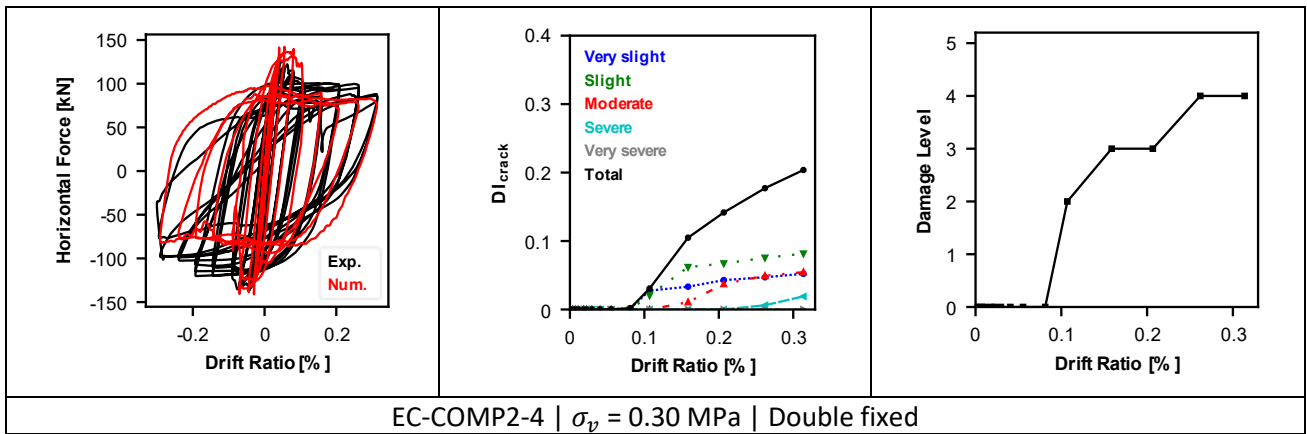
Figure 5-38: Hysteresis loop (left); evolution of DI_{crack} (middle) and damage level (right) against drift ratio for the specimen EC-COMP2-4.

Table 5-10: Mechanical properties for the definition of the behaviour of the mortar joints for the clay walls tested at EUCENTRE.

Parameter	Units	Mortar bed joints	Mortar perpend joints
		Normal direction	
f_t	[MPa]	0.230	0.085
u_n^f	[mm]	0.6	
$k_{n,t}$	[N/m³]	10^7	
		Tangential direction	
c	[MPa]	0.150	
$tan\varphi$	[-]	0.55	
μ	[-]	0.60	
u_s^f	[mm]	0.5	
k_s	[N/m³]	$2 \cdot 10^7$	

5.3.2.3 Calcium silicate walls - TUD

A very demanding experimental set of six calcium silicate walls, four slender (Figure 5-39 and Figure 5-40) and two squat (Figure 5-41 and Figure 5-42), (Ravenshorst and Messali 2016; Messali et al. 2020) was investigated numerically in this Section. The calibrated mechanical parameters are reported in Table 5-8 and Table 5-11. The numerical analyses

simulated accurately the experimental behaviour in terms of hysteresis loops and failure mechanisms. For additional description of the response of the tested piers refer to Sections 5.2.2.1 and 5.2.2.2. Similarly to conclusions from the calibration process presented in Section 5.3.2.1, consideration of low compressive strength σ_{c0} improved the shape of the hysteresis loop for the slender walls (Figure 5-39).

The slender walls TUD-COMP-0a, TUD-COMP-2 and TUD-COMP-3 reached damage level 3, i.e. moderate damage. For the cases with hybrid failure mode, the cracking extent was predicted well for TUD-COMP-2 (Figure 5-39b) whereas the slender wall TUD-COMP-0a was characterized by a steep increase of DI_{crack} (i.e. 0.19) (Figure 5-39a) moderately exceeding the experimental value (i.e. 0.12); as shown above (see Section 5.3.2.1) the hybrid failure mechanism with extensive shear joint sliding was linked with overestimation of the degree of very slight cracks. On the contrary, the damage classification based on maximum crack width increased more gradually reaching up to damage level 3 (Figure 5-39a). The simulation of the rocking TUD-COMP-2 specimen led to limited crack extent (DI_{crack} reached 0.05) reproducing correctly the experimental response. The rocking wall TUD-COMP-20 suffered greater damage as expressed from DI_{crack} value of 0.10 and damage level 4 (i.e. one level higher that the rest of the slender walls) (Figure 5-39d). This wall attained high drift ratio of 3% associated with severe toe crushing (Figure 5-39d and Figure 5-40d).

The cracking pattern was accurately captured for the squat walls TUD-COMP-4 and TUD-COMP-6 (Figure 5-42). The two specimens were loaded with the same precompression level with the former tested under a double fixed configuration while for the latter cantilever conditions were considered leading to more extensive damage, and higher DI_{crack} and damage level. The squat walls were associated with shear cracking resulting to exaggerated DI_{crack}, similarly to the squat walls presented in Section 5.3.2.1 and 5.3.2.2.
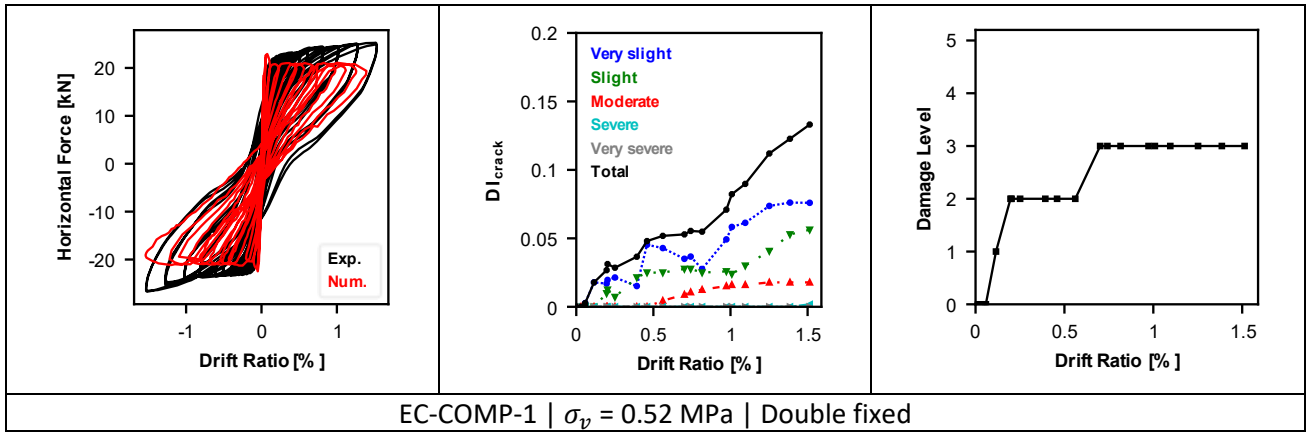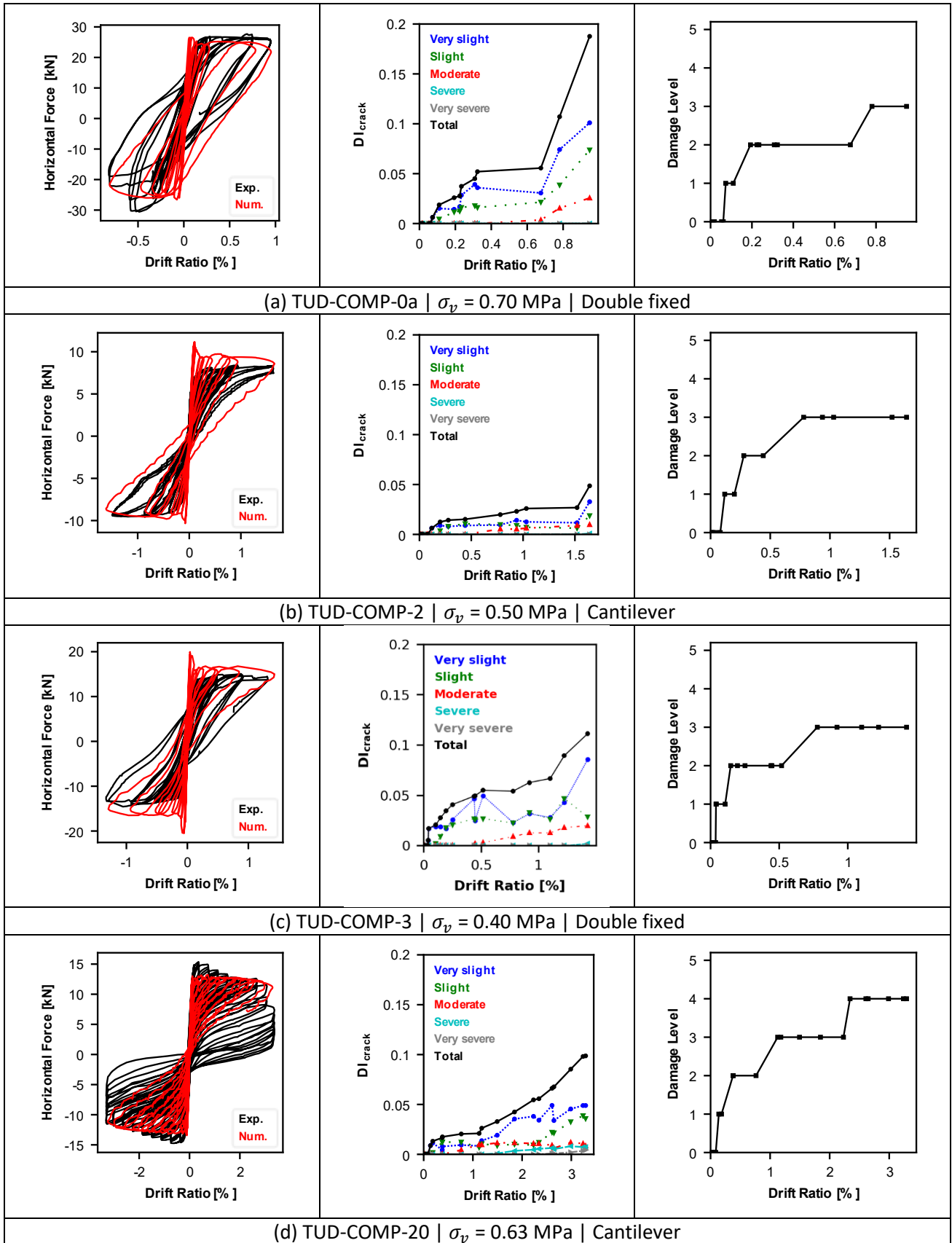
Figure 5-39: Hysteresis loop (left); evolution of DI_{crack} (middle) and damage level (right) against drift ratio for the specimens (a) TUD-COMP-0a, (b) TUD-COMP-2, (c) TUD-COMP-3, and (d) TUD-COMP-20.

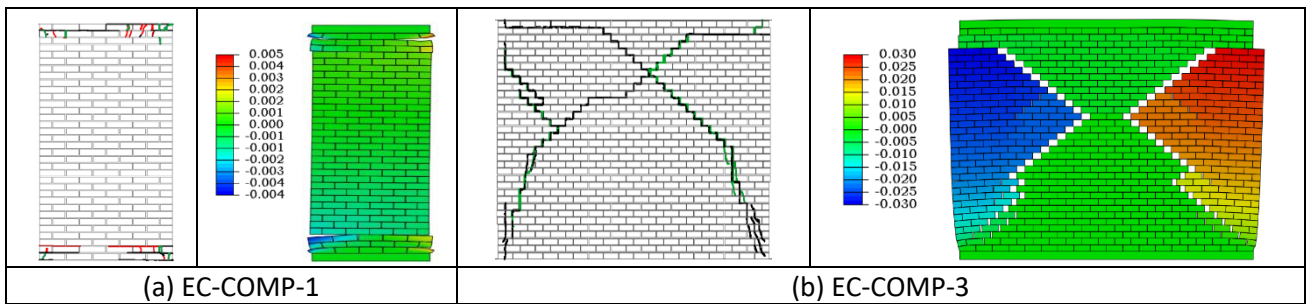(a) TUD-COMP-0a

(b) TUD-COMP-2

(c) TUD-COMP-3
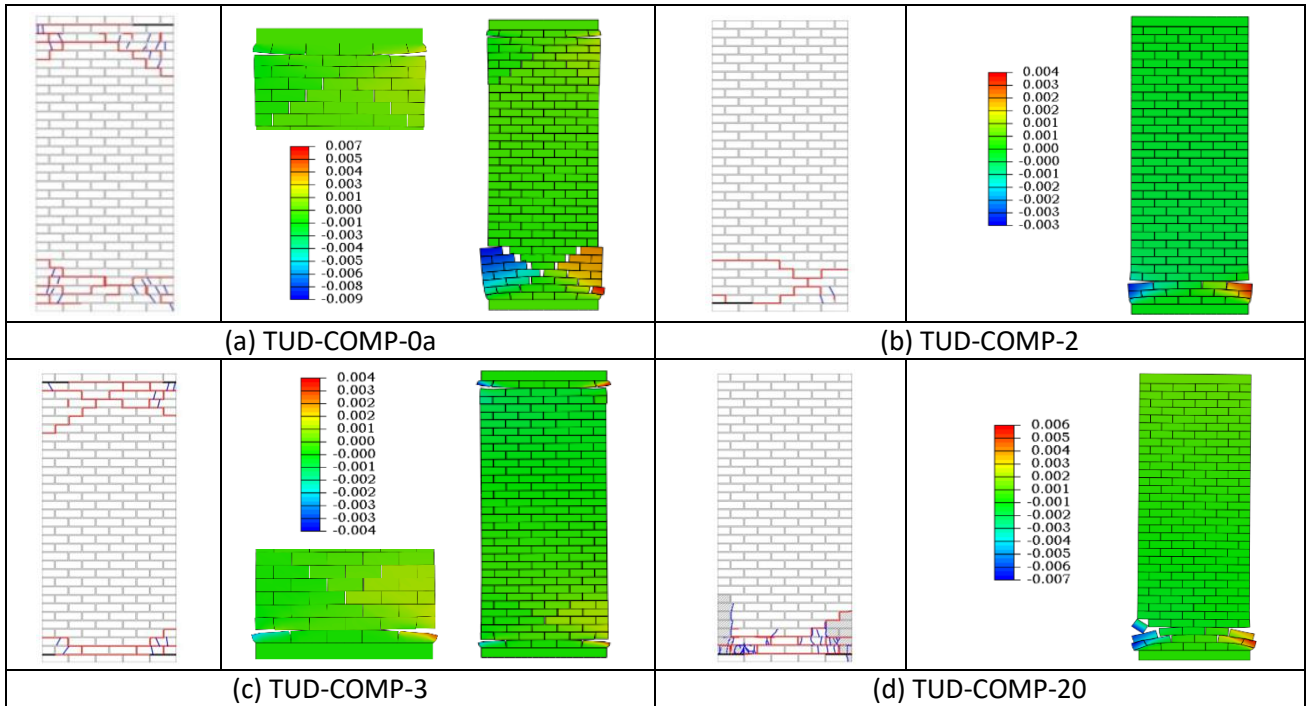
(d) TUD-COMP-20

Figure 5-40: Experimentally obtained crack pattern (left) (reproduced from Messali et al. (2020)) and numerically calculated deformed shape (right) for the specimens (a) TUD-COMP-0a, (b) TUD-COMP-2, (c) TUD-COMP-3, and (d) TUD-COMP-20. Contours represent magnitude of deformations in m.

(a) TUD-COMP-4 | σ_v = 0.50 MPa | Double fixed

(b) TUD-COMP-6 | σ_v = 0.50 MPa | Cantilever
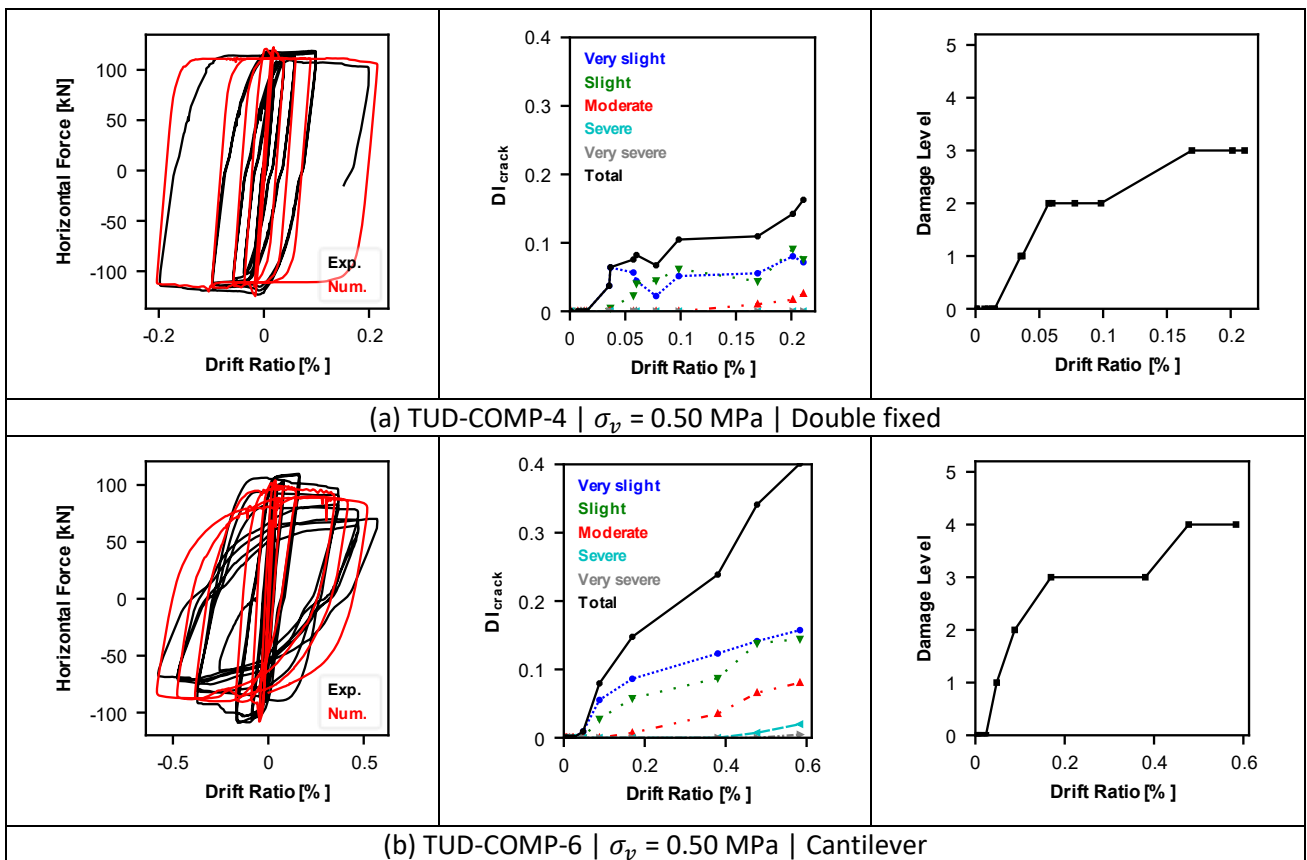
Figure 5-41: Hysteresis loop (left); evolution of DI_{crack} (middle) and damage level (right) against drift ratio for the specimens (a) TUD-COMP-4, and (b) TUD-COMP-6.

(a) TUD-COMP4
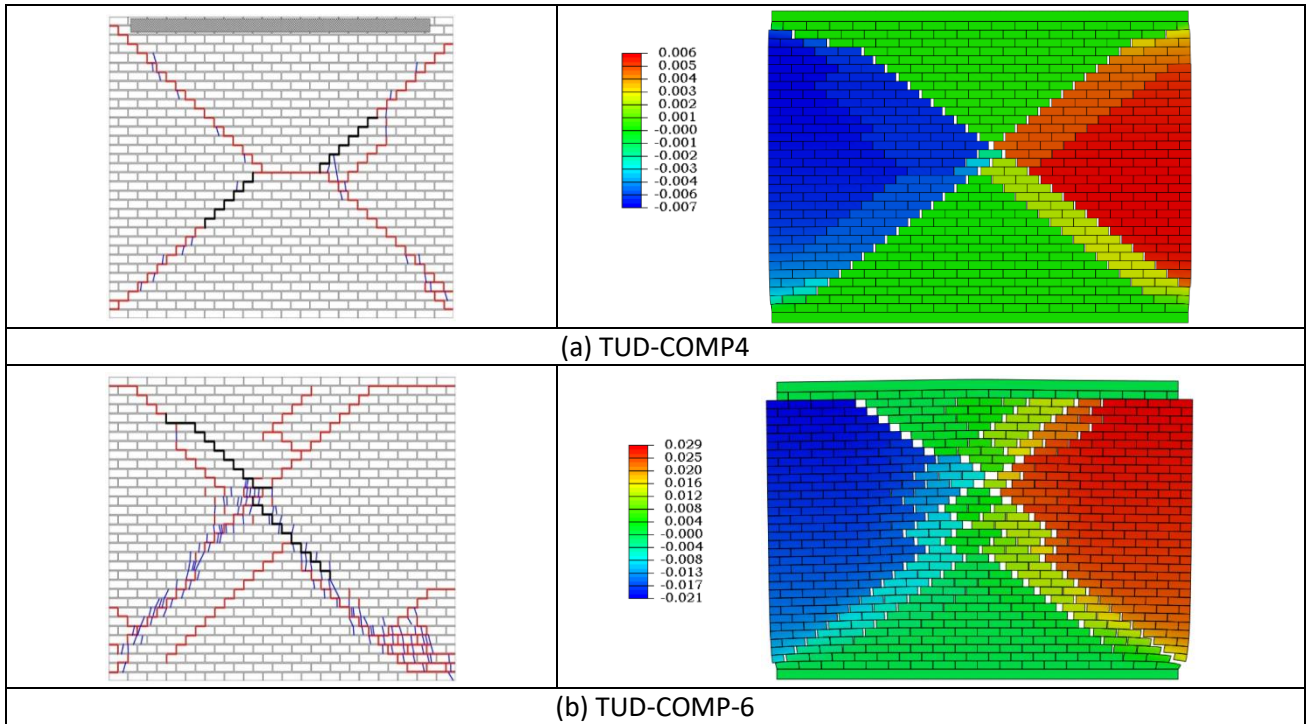
(b) TUD-COMP-6

Figure 5-42: Experimentally obtained crack pattern (left) (reproduced from Messali et al. (2020)) and numerically calculated deformed shape (right) for the specimens (a) TUD-COMP-4, and (b) TUD-COMP-6. Contours represent magnitude of deformations in m.

Table 5-11: Mechanical properties for the definition of the behaviour of the mortar joints for the calcium silicate walls tested at TUD.

Parameter	Units	Mortar bed joints	Mortar perpend joints
Normal direction			
f_t	[MPa]	0.270	0.025
u_n^f	[mm]	0.6	0.2
$k_{n,t}$	[N/m³]	10^7	
Tangential direction			
c	[MPa]	0.110	0.030
$tan\varphi$	[-]	0.55	0.55
μ	[-]	0.55	0.55
u_s^f	[mm]	0.3	0.3
k_s	[N/m³]	$7 \cdot 10^7$	

5.3.2.4 Walls with opening - TUD

Two identical calcium silicate walls with opening tested at TUD (Korswagen et al. 2020a) were numerically investigated (Figure 5-43 and Figure 5-44). The walls were excited under repeated cycles of low level drift ratio (up to 0.07%) in order to examine the evolution of light damage. The calibrated mechanical parameters are reported in Table 5-8 and Table 5-12. The numerical model replicated adequately the hysteresis loop (Figure 5-43) and the cracking pattern (Figure 5-44). The numerical and experimental deformed shapes are presented for maximum negative and positive applied drift and at the end of the test (Figure 5-44). The specimen decomposed in four rigid bodies with no signs of damage and these rigid bodies slid and rotated against each other (Figure 5-44). The simulation correctly replicated the

formed crack patterns for different load directions accounting also for limited residual deformations at the end of the test (Figure 5-44).

The numerical model reproduced limited cracking (DI_{crack} = 0.02) classified as very slight damage level. The experimental cracks (DI_{crack} = 0.05) were detected with a high-resolution DIC technique (Korswagen et al. 2020b). Therefore, it can be argued that part of the detected cracks from the tested specimens would be invisible to the naked eye. The DI_{crack} has been configured to account only for visible cracks corresponding numerically to a minimum crack width of 0.2 mm (see Section 6.3). Therefore, it can be inferred that the model is able to reproduce the crack onset related to light damage. In order to account for micro-damage (below the threshold for a crack to be visible) a limit lower than 0.2 mm could be considered for the calculation of DI_{crack}, but this lays out of the scope of this work and will not be further examined.

For this experimental campaign only one wall type was considered. Consequently it was not possible to validate the numerical properties over a wider range of wall types, precompression levels and boundary conditions. For instance, tensile strength and cohesion were considered at the same level for the bed and perpend joints. As shown in Section 5.3.2.1, the calibration of the mechanical properties of the perpend joints relied on the response of squat walls with shear failure where the contribution of the vertical joints in the collapse mechanism is substantial. Moreover, the specimens were tested only for light damage level, thus the activation of the ultimate failure mechanism was not reached. While the numerical model provided an accurate representation of the experimental response, additional experimental evidence is required to calibrate the numerical representation more reliably.
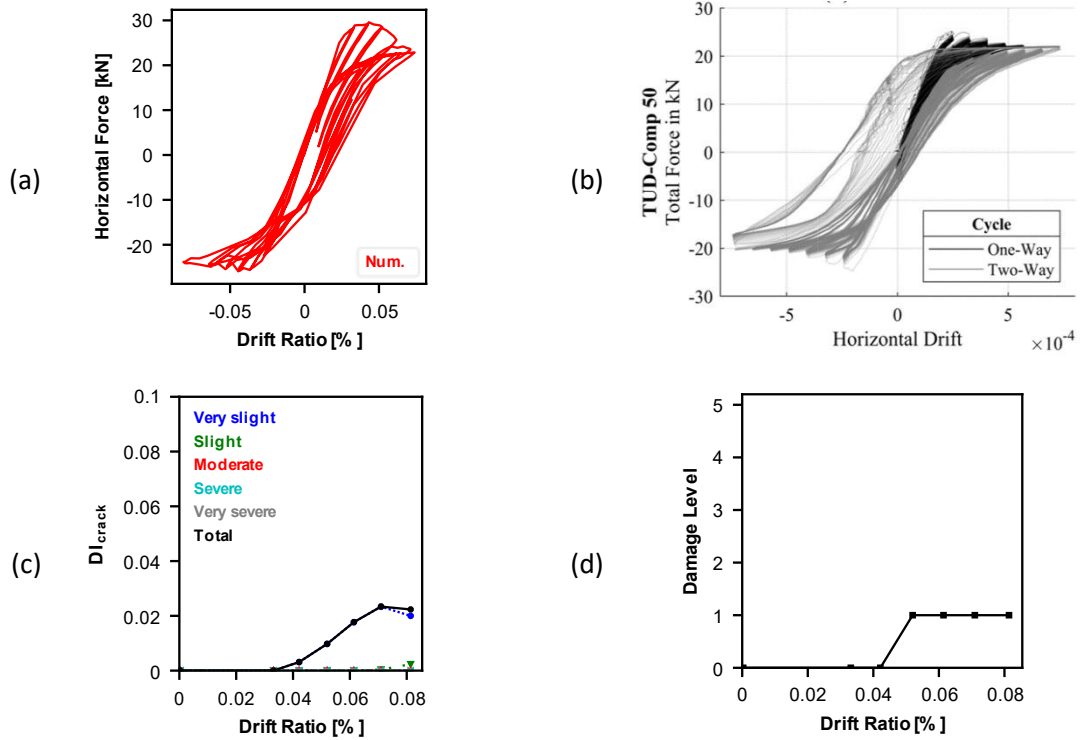
Figure 5-43: (a) Numerical and (b) experimental hysteresis loop (reproduced from Korswagen et al. (2020a)); (c) evolution of DI_{crack} and (d) damage level against drift ratio for the specimens TUD-COMP-49/50.
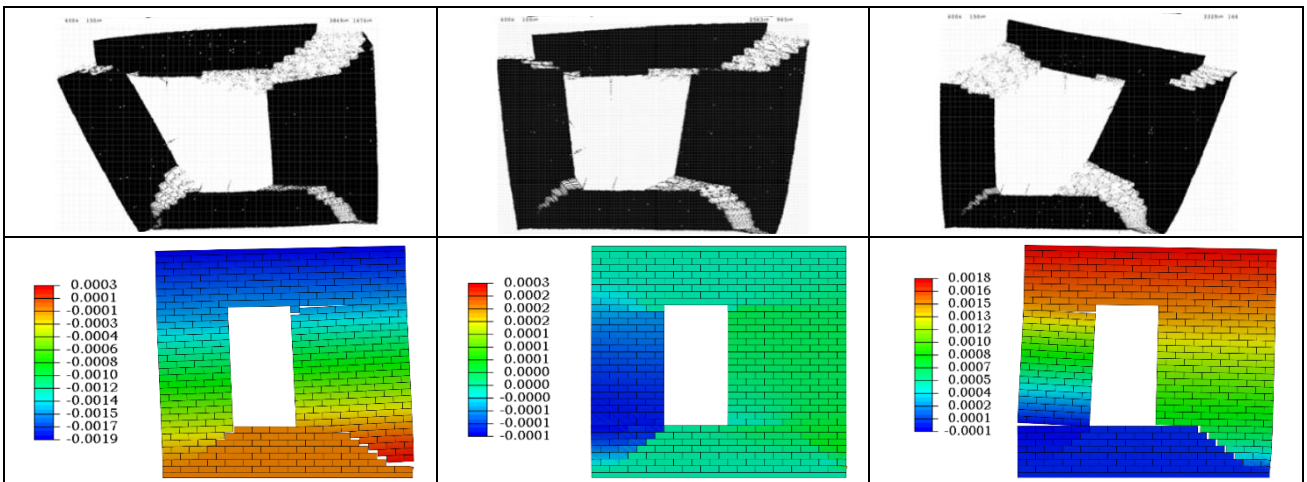
Figure 5-44: Experimental (top) (reproduced from Korswagen et al. (2020a)) and numerical (bottom) deformed shape for the specimens TUD-COMP-49/50 corresponding to maximum negative (left) and positive (right) applied drift and the end of the test (middle). Contours represent magnitude of deformations in m.

Table 5-12: Mechanical properties for the definition of the behaviour of the mortar joints for the calcium silicate walls with opening tested at TUD.

Parameter	Units	Mortar bed joints	Mortar perpend joints
Normal direction			
f_t	[MPa]	0.100	
u_n^f	[mm]	0.6	0.4
$k_{n,t}$	[N/m³]	10^7	
Tangential direction			
c	[MPa]	0.100	
$tan\varphi$	[-]	0.50	
μ	[-]	0.50	
u_s^f	[mm]	0.5	0.3
k_s	[N/m³]	$3 \cdot 10^7$	

5.3.2.5 Shear walls - TUE

Six clay shear walls, solid or with opening, tested under monotonic load at TUE (Vermeltfoort et al. 1993) were simulated (Figure 5-45, Figure 5-46, and Figure 5-47). These walls were of lower height (1.14 m) that the previously considered walls (Sections 5.2.2.1, 5.2.2.2 and 5.2.2.3). The shear walls were tested under double fixed configuration while any vertical displacement was additionally constrained. The calibrated mechanical parameters are reported in Table 5-8 and Table 5-13.

Force - displacement curves (Figure 5-45) and failure modes were replicated accurately (Figure 5-47). The solid walls experienced a stepped diagonal crack through perpend and bed joints and additionally for the walls with low precompression (J4D and J5D) bending cracks at the bottom and top of the wall were possible due to the lower confinement (Figure 5-47a-c). The crack pattern of the specimens with opening (J2G and J3G) comprised of diagonal zigzag cracks around the corners of the opening and tensile cracks at the base and top of the small piers leading to a collapse mechanism with four hinged rigid blocks (Figure 5-47d).

The solid walls accounted for DI_{crack} values in the range of 0.11 to 0.16 (Figure 5-46a-c) matching well the experimental response. These values are higher than the ones computed for walls with greater height presented above. Despite these relative high values of DI_{crack}, the sustained damage was classified as very slight based on the maximum crack width attained; only the specimen J6D reached damage level 2 at the final stage of the test (Figure 5-46b). While maximum drift ratio was in the range of 0.3% the absolute top displacement applied corresponded to approximately 3 mm. Therefore it is deemed logical that the maximum crack width (deformation at the mortar joints) was rather limited (i.e. in the range of 1 mm). For the case of the solid shear walls with lower height investigated, a damage classification solely based on crack width might be not be representative of the real damage extent whereas DI_{crack} was able to reproduce any crack propagation more reliably. For the walls with opening (J2G and J3G), the maximum DI_{crack} was 0.2 which translates to

moderate damage level (Figure 5-46d). It is noted that the latter specimens due to their rocking behaviour could accommodate drift up to 1.94% (Figure 5-45b).

The mechanical parameters used to model the TUE shear walls were in good agreement with the parameters considered by Lourenço (1996) (Table 5-13). No reduction of the properties for the perpend joints was considered differently unrealistically high cracking was predicted. This evidently higher strength of the perpend joints could be attributed to higher confinement provided due to the low height of the walls. Further research is recommended to relate the strength of perpend joints with the confinement level. For a discussion on size effects refer to Section 5.2.3.

| (a) Solid walls | (b) Walls with opening |
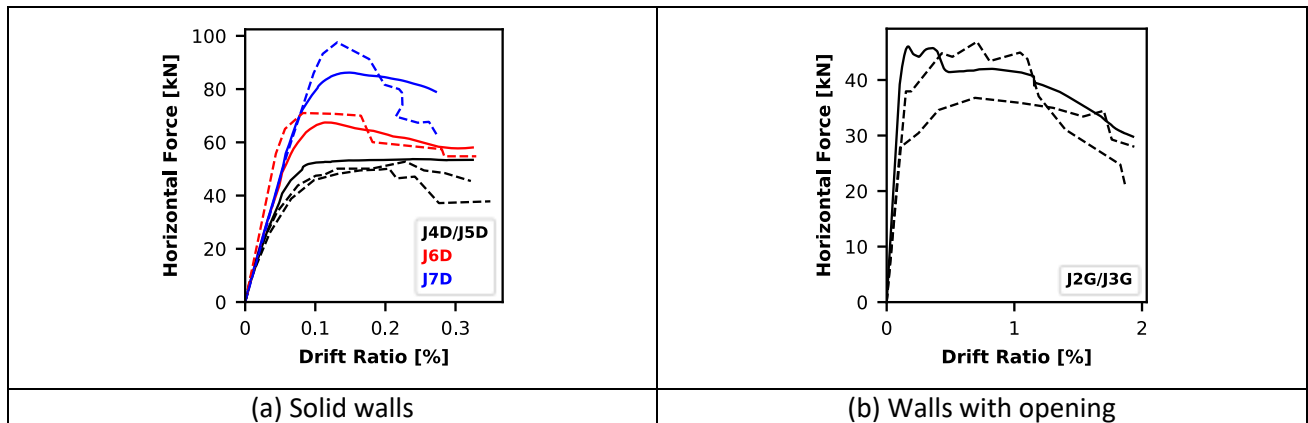
Figure 5-45: Horizontal force vs drift ratio for the (a) solid and (b) with opening shear walls. Solid and dashed lines correspond to numerical and experimental response respectively.
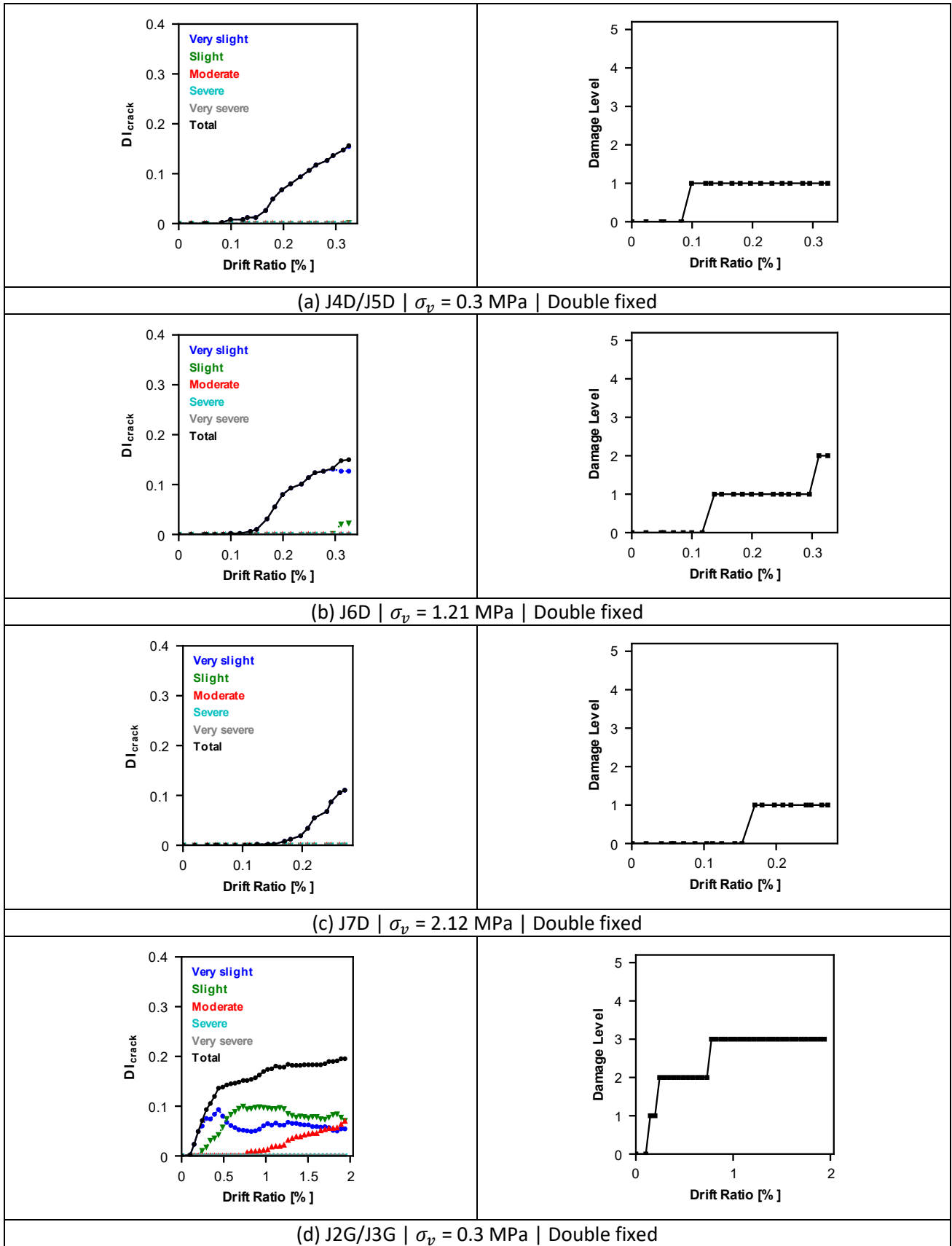
Figure 5-46: Evolution of DI_{crack} (left) and damage level (right) against drift ratio for the specimens (a) J4D/J5D, (b), J6D, (c) J7D, and (d) J2G/J3G.

(a) J4D/J5D
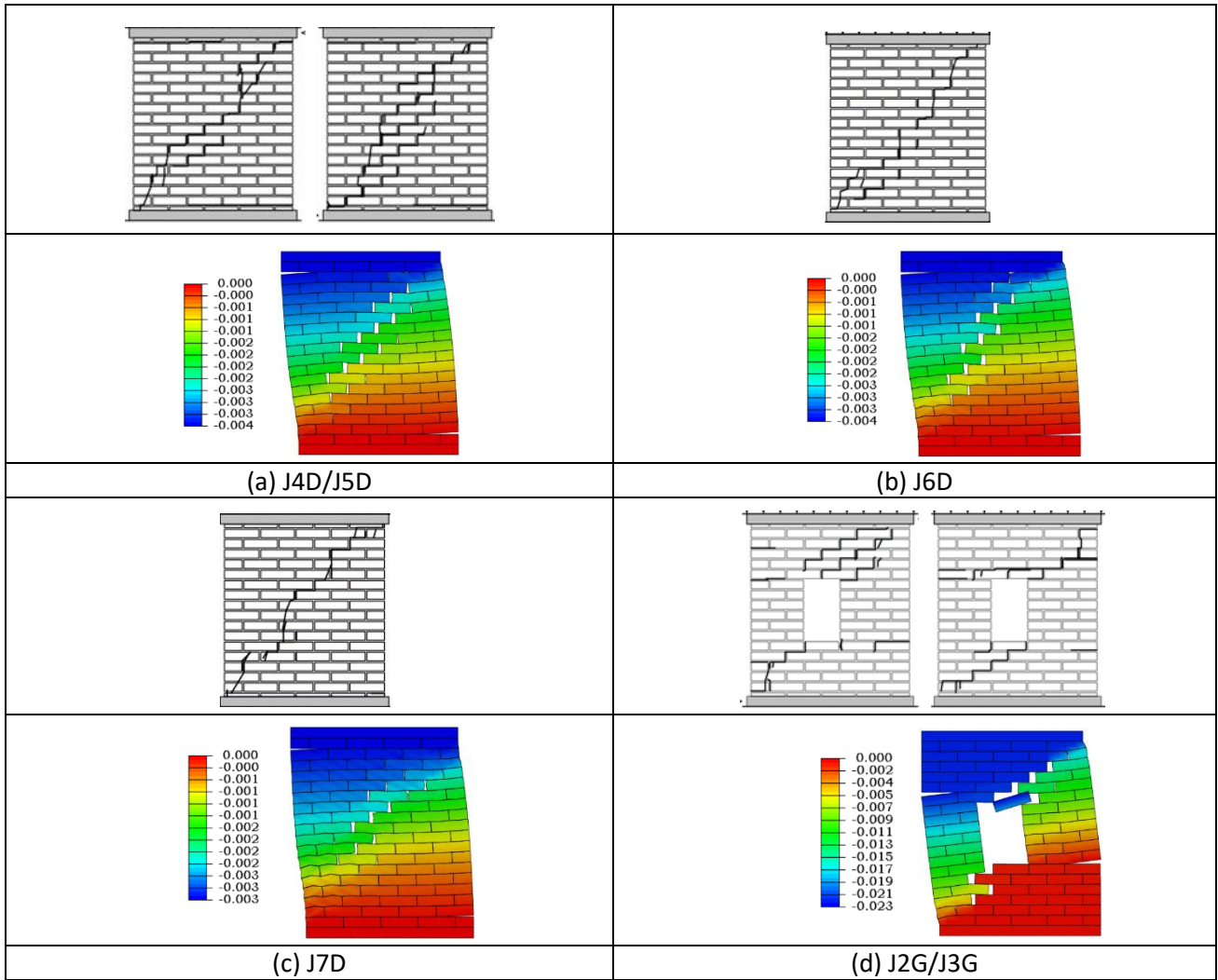
(b) J6D

(c) J7D

(d) J2G/J3G

Figure 5-47: Experimentally obtained crack pattern (top) (reproduced from Lourenço (1996)) and numerically calculated deformed shape (bottom) for the specimens (a) J4D/J5D, (b), J6D, (c) J7D, and (d) J2G/J3G. Contours represent magnitude of deformations in m.

Table 5-13: Mechanical properties for the definition of the behaviour of the mortar joints for the clay shear walls tested at TUE: (a) J4D/J5D and J2G/J3G, and (b) J6D and J7D.

Parameter	Units	Mortar joints[a]	Mortar joints[b]
Normal direction			
f_t	[MPa]	0.250	0.160
u_n^f	[mm]	0.8	
$k_{n,t}$	[N/m³]	10^7	
Tangential direction			
c	[MPa]	0.350	0.224
$tan\varphi$	[-]	0.75	
μ	[-]	0.55	
u_s^f	[mm]	0.7	
k_s	[N/m³]	$3 \cdot 10^7$	

5.3.3 Discussion

In Section 5.3.2 damage propagation in masonry walls was numerically investigated on a set of experimental campaigns. The efficacy of the numerical model to reliably represent the failure mechanism and crack propagation was validated against experimental findings. The

quantification of damage based on two factors (DI_{crack} and crack width) is summarized and discussed for the different wall types considered (slender, squat and short shear walls) (Figure 5-48). For the walls with opening tested at TUD no extra specimens with similar geometry were examined and thus any conclusions were presented in Section 5.3.2.4 and will not be further discussed in this Section.

The numerical model was found able to adequately reproduce the evolution of DI_{crack} as reported from experimental studies (Figure 5-14 and Figure 5-48). In particular for the slender walls, the numerical simulations replicated the different trends observed regarding the evolution of DI_{crack} for specimens with hybrid and flexural failure mechanism, denoted with black and red line respectively in Figure 5-48a. The overestimation of the contribution of slight damage for the specimen EC-COMP-1 falsely led to steeper increase of DI_{crack} resembling the behaviour of slender walls with hybrid failure (Figure 5-48a). The squat walls were associated with an abrupt linear increase of DI_{crack} for limited drift signifying their brittle response (Figure 5-48b). The shear walls tested at TUE presented similar pattern with the walls with opening (J2G and J3G) reaching a plateau for higher drift values (Figure 5-48c).

Along this study, it was possible for the experimental DI_{crack} values to be obtained for different loading stages based on sketches displaying crack patterns provided in the literature (see Section 5.2). On the contrary, the evolution of crack width for different drift levels is not commonly reported from experiments on masonry walls, thus hindering any efforts for damage classification based on crack width. To bridge this gap, the proposed numerical model was validated against tested specimens that such measurements were made available (refer to Section 5.3.2.2), allowing the further investigation of crack width evolution on different wall configurations.

The classification of damage based on crack width led to the correlation of crack initiation, i.e. very slight damage, to drift limits, reported in Table 5-14, for the different wall types considered. The limits numerically obtained compare well with the ones extracted from experimental studies (Table 5-4). In general terms, visible cracks would be expected for drift values in the range of 0.04% to 0.17% (Table 5-14). Therefore, the numerical simulations based on the micro-modelling approach are able to capture any light damage for very limited drift. It is noted that macro-models have been found less sensitive on this matter (see Section 2.8 for a relevant discussion). The continuum models capture well the different failure mechanisms of masonry walls, however fail to reproduce local phenomena, like joint opening and sliding, associated to low damage extent.

The damage levels for the squat walls are characterized by steep increase for limited drift, following similar trend with the corresponding DI_{crack}, accounting for severe and very severe damage at ultimate failure which appears suitable (Figure 5-48b). On the other hand, the shear walls tested at TUE and the slender walls with hybrid failure ranked up to damage level

3 (Figure 5-48a and c). For these walls, damage classification based on crack width appears to underestimate the real extent of cracking since only moderate damage would be considered at the final testing stage where the failure mechanism has been fully activated. This is due to the fact that failure is reached for low drift level, thus cracks wider than 25 mm would not be expected. For the slender walls with flexural failure mode, higher damage level 4, corresponding to severe damage, was only reached upon exceedance of high drift ratio of 2% (Figure 5-48a). Consequently, the attainment of higher damage levels appears to be strongly related with higher drift values which disregards the fact that masonry walls might fail for limited drift as well (Figure 5-48a and c). Moreover, whereas DI_{crack} was able to highlight different trends experienced for slender walls with different failure mode, damage classification entirely based on crack width failed to capture this behaviour. In particular, the curves corresponding to hybrid mode match the counterparts characterized by flexural mechanism (Figure 5-48a).

Consequently, a classification based on crack width appears to be strongly related to the maximum applied drift and fails to take into consideration parameters like different boundary conditions and precompression levels which have been found to critically affect the damage propagation in masonry walls. Burland et al. (1977) and Giardina et al. (2015) stressed out that assessing the degree of damage for real buildings is a complex process that requires judgement and experience; crack width is only one aspect of damage and should not be used on its own as a direct measure. Contemplating the latter argument with conclusions from the numerical investigations, it is concluded that evaluation of the damage degree solely based on one factor, i.e. crack width, might be misleading. On the other hand the suggested DI_{crack} appears to better represent the real extent of damage of masonry walls for different configurations. For further clarification on the use of DI_{crack} for the quantification of damage in masonry walls refer to Section 5.2.
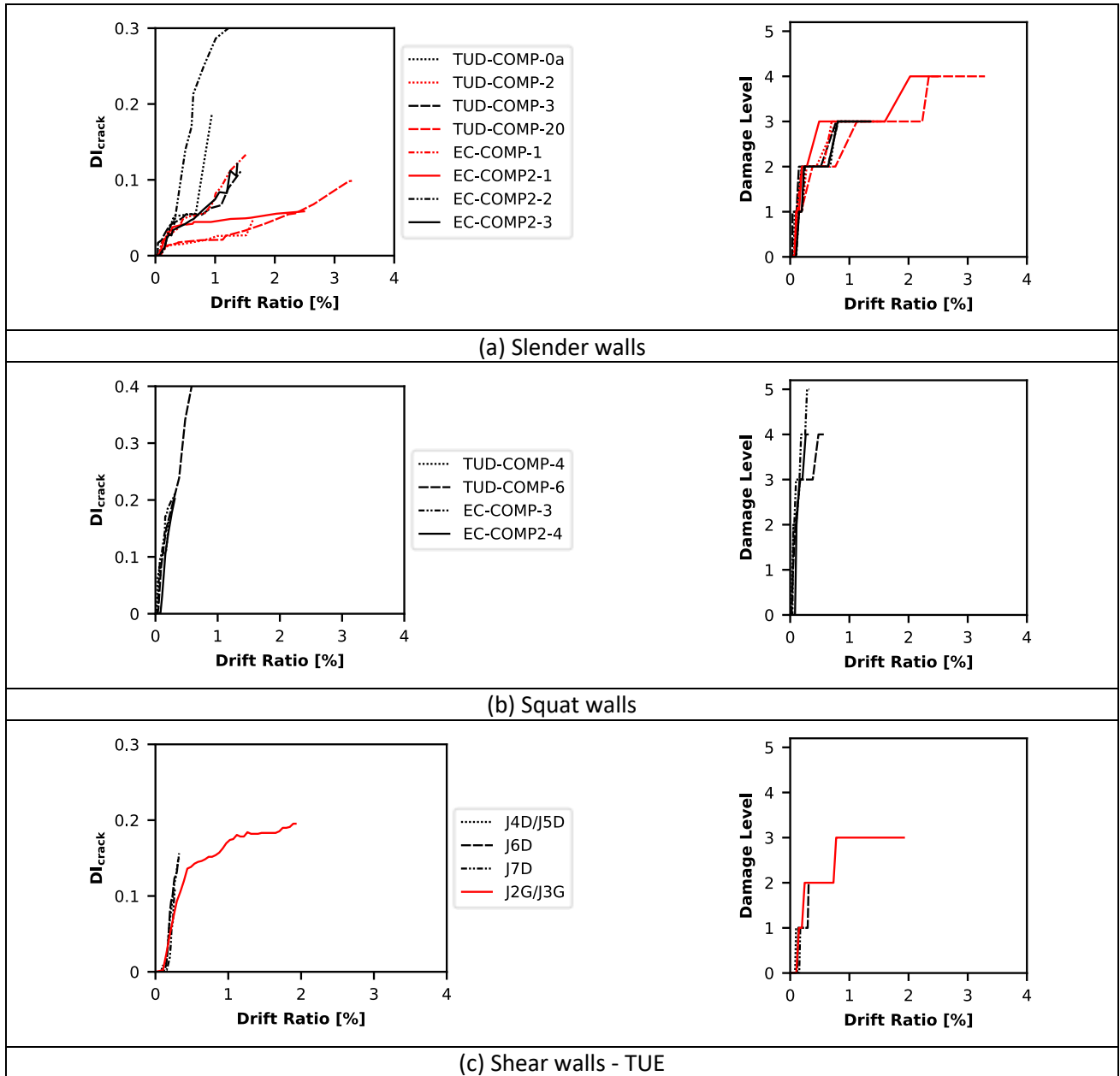
Figure 5-48: Evolution of DI_{crack} (left) and damage level (right) against drift ratio for (a) slender walls (walls associated with hybrid and flexural failure are shown with black and red line respectively), (b) squat walls, and (c) shear walls tested at TUE (solid walls and walls with opening are shown with black and red line respectively).

Table 5-14: Drift ratio ranges corresponding to crack onset (very slight damage) based on the numerical simulations of different wall types.

Wall type	Drift ratio [%]
Slender walls	0.04 – 0.15
Squat walls	0.04 – 0.11
Shear walls - TUE	0.10 – 0.17

5.3.4 Conclusions

A numerical model based on the micro modelling approach was developed to reliably reproduce and quantify the damage accumulation occurring in masonry structures. The

masonry units were considered with continuum elements governed by damaged elasticity in combination with tensile and compressive plasticity while cohesive-frictional behaviour was incorporated in the interfaces representing mortar joints. The model was validated against an extended series of experimental data. The verification of the model was based on the reproduction of the experimental response in terms of hysteresis loop and failure mechanism. Crack patterns and available crack measurements were additionally considered to showcase the efficacy of the numerical model to accurately reproduce the damage propagation as expressed by both crack extent and width.

A concise methodology to correctly calibrate the mechanical properties of the implemented micro-model was proposed. Certain parameters (e.g. bond strength, cohesion, and friction coefficient) could be directly extracted from small scale tests while other properties, such as Young's modulus and compressive strength of masonry units, were calibrated best by considering full scale experiments. It is highly recommended to consider walls with different failure mechanisms in order to reliably define the required parameters. In particular, perpend joints have significant contribution in the cracking pattern of squat walls with shear failure and consideration of inferior properties allowed in some cases to correctly simulate the experimental failure mode. An incremental reduction of the strength of the vertical joints appears as the recommended practice that would allow for a correct calibration. Limited or no reduction of the properties assigned to perpend joints was found suitable for two-leaf specimens or walls with low height. Further research is recommended to better define the strength of perpend joints for different wall thicknesses and confinement levels. Consideration of rather low value of compressive strength for the masonry units predicted well the combination of rocking behaviour with high energy dissipation linked to toe crushing failure.

The evolution of the experimentally calculated DI_{crack} was reproduced adequately due to the high fidelity of the numerical analysis. While the numerical investigations considered account for in-plane recursive load, further research is suggested to expand the quantification of damage under different loading types such as settlements and out of plane excitations.

The developed numerical model was able to reproduce the crack onset related to light damage. In general terms, visible cracks would be expected for drift values in the range of 0.04% to 0.17%. Numerical simulations based on the micro-modelling approach are able to capture any light damage, expressed as joint opening and sliding, for very limited drift outperforming macro-models which have been found less sensitive on this matter.

Measurements of crack width for different drift levels are not commonly reported in experimental studies. The developed numerical model allowed the detailed representation of crack propagation and thus enabled the numerical investigation of crack width evolution for different wall configurations. Damage classification based solely on crack width appears convenient since it requires only one factor, but this simplicity might lead to misleading

damage assessment. Such a crack width-based classification was found to be strongly related to the maximum applied drift and failed to take into consideration parameters like different boundary conditions and precompression levels which critically affect the damage propagation occurring in masonry walls. For instance, for slender walls with hybrid failure mode characterised by limited drift capacity, crack width up to 25 mm would be expected which corresponds to moderate damage level, even though the failure mechanism has been fully activated. On the other hand, quantification of damage based on the suggested DI_{crack} appears to better represent the real extent of cracking of masonry walls for different configurations (refer to Section 5.2).

As future research, the numerical model could be verified over different loading mechanisms, such as settlements and out-of-plane excitations or combination of them, and the damage propagation can be numerically evaluated for various loading scenarios. The extension of the work on full scale structures considering a three-dimensional representation will be evaluated.

Chapter 6
Experimental study on the accumulation of damage in masonry

As discussed in the literature review (refer to Section 2.7), additional research is required to understand better the relationship between load history and damage accumulation for masonry structures. In order to gap the limitations observed in previous studies, an experimental campaign was undertaken. In particular, wall specimens were tested under monotonic and cyclic manner to evaluate any effects of the load history on the behaviour of masonry. The experimental campaign is described in Section 6.1 while the obtained results are presented in Section 6.2. Different numerical approaches were researched for their efficacy to reproduce the experimental response and any limitations were highlighted (Section 6.3). Conclusions and recommendations for future research are provided in Section 6.4.

6.1 Experimental campaign

This experimental campaign investigates the effect of cyclic load on the response of masonry structures focusing on damage propagation as expressed through deformations and crack onset. Six walls representative of spandrel geometry were tested under three-point in-plane bending (Figure 6-1). The walls were single leaf following the running bond pattern and were made of clay bricks and multipurpose mortar, materials commonly used in the Groningen region (Figure 6-2). The tested specimens had dimensions 1.11 m x 0.42 m x 0.1 m and consisted of 7 brick courses (Figure 6-1). The thickness of the mortar layer was 10 mm while the brick units had dimensions 214 x 104 x 50 mm (Table 6-2). The walls were sitting on two steel supporting rollers at the two sides and point load was applied with an electromechanical servo actuator at the middle of the top brick layer (Figure 6-1). In order to avoid any surface anomalies and stress concentrations a thin cork layer was placed on the wall at the point that the load was applied from the actuator.
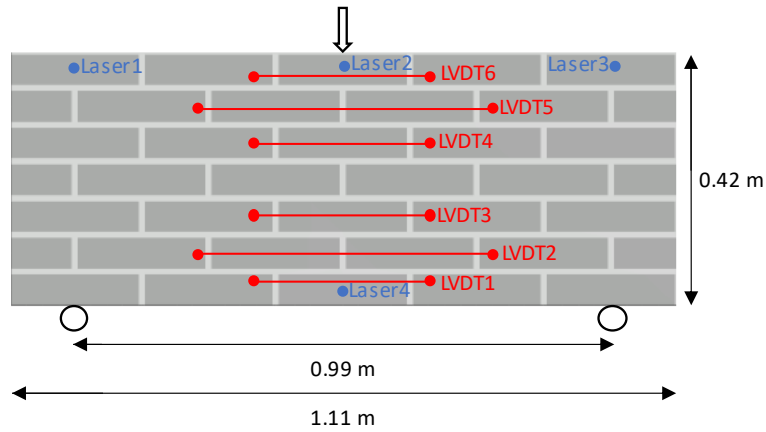
Figure 6-1: Test setup for three-point in-plane bending on masonry spandrels displaying the wall dimensions and the considered instrumentation.

| (a) | (b) |

Figure 6-2: (a) Construction of the wall specimens; (b) multipurpose mortar.

A set of companion tests were undertaken to characterize the mechanical properties of the masonry walls (Figure 6-3) and the results are summarized in Table 6-1. Bricks were tested in compression according to EN 772-1 (EN 772-1 2000) to calculate the mean compressive strength (f_b = 22.1 MPa) of the masonry units while their density was found as p_b = 1,969 kN/m^3 (Table 6-2). Mortar specimens of 160 x 40 x 40 mm were tested to retrieve the flexural (f_t = 3.7 MPa) and compressive (f_c = 12.5 MPa) strength following the guidelines of EN 1015-11 (EN 1015-11 1999) (see

Table 6-3). The bond strength (f_w = 0.7 MPa) of the bed joints was determined with bond wrench experiments on masonry couplets based on EN 1015-5 (EN 1015-5 2005) (Table 6-4). The mortar used for this study is considered as high strength mortar while recent experimental studies in the literature focused on masonry with low bond strength mortar (i.e. f_w ranging from 0.06 to 0.47 MPa) (Graziotti et al. 2017; Kallioras et al. 2018; Korswagen et al. 2019; Messali et al. 2020). It is noted that although triplet specimens were prepared to be tested for shear strength, problems with the actuator did not allow the execution of these tests.

(a) Compression tests on brick units

(b) Bond wrench tests on couplets

(c) Compressive tests on mortar

(d) Tensile tests on mortar
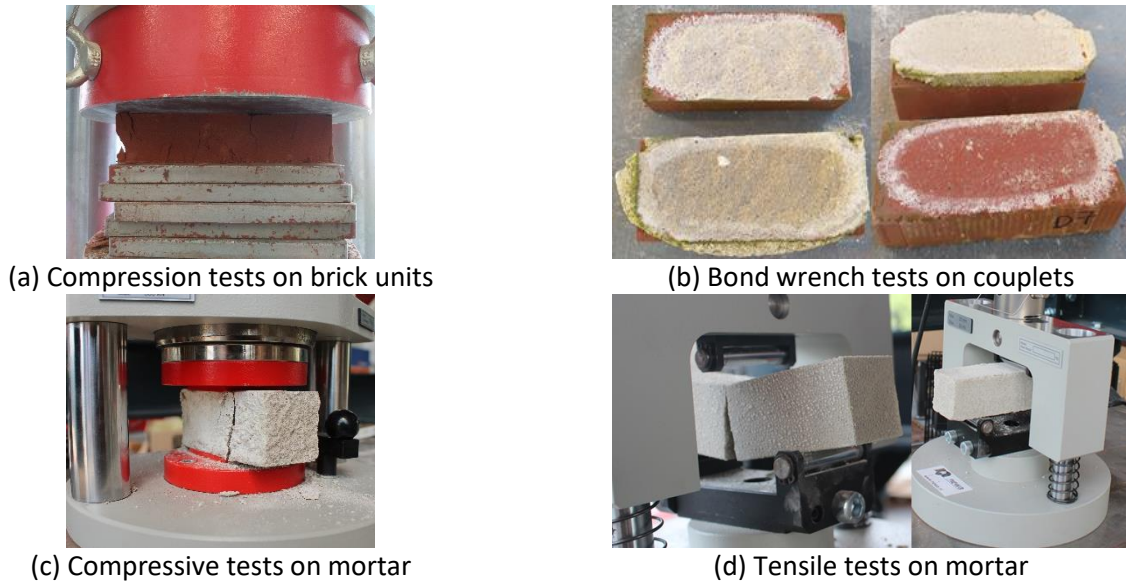
Figure 6-3: Companion tests to retrieve the mechanical properties of the masonry walls.

Table 6-1: Mechanical properties of masonry obtained from companion tests. CoV: coefficient of variation.

Material property	Symbol	Unit	Mean	CoV
Density of bricks	p_b	[kg/m³]	1,969	2%
Density of masonry	p	[kg/m³]	1,900	-
Normalized compressive strength of masonry units	f_b	[MPa]	22.1	21%
Compressive strength of mortar	f_c	[MPa]	12.5	19%
Tensile strength of mortar	f_t	[MPa]	3.7	28%
Bond strength of masonry	f_w	[MPa]	0.7	21%

Table 6-2: Compressive tests on masonry units. StDev: standard deviation; CoV: coefficient of variation.

No	Length	Width	Height	Weight	Density, p_b	Load	Compressive pressure	Shape factor, δ	Normalized compressive strength, f_b
	[mm]	[mm]	[mm]	[g]	[kg/m³]	[kN]	[MPa]	[-]	[MPa]
1	214	102	49	2,173	2,032	401.4	18.4	0.87	16.0
2	214	102	51	2,162	1,942	546.0	25.0	0.87	21.8
3	215	106	50	2,193	1,925	704.7	30.9	0.87	26.9
4	214	104	49	2,155	1,976	610.6	27.4	0.87	23.9
Mean					**1,969**				**22.1**
StDev					**47.2**				**4.6**
CoV					**2%**				**21%**

Table 6-3: Tensile and compressive tests on mortar specimens. StDev: standard deviation; CoV: coefficient of variation.

No	Weight	Tensile strength, f_t	Compressive strength, f_c
	[g]	[MPa]	[MPa]
1	435	4.9	13.8
2	440	4.7	14.0
3	445	4.7	15.3
4	440	5.5	15.5
5	440	2.8	14.3
6	440	3.3	14.5
7	445	2.5	11.3
8	445	3.2	11.1
9	440	3.8	11.4
10	455	3.8	9.4
11	450	2.5	10.5
12	455	2.8	8.9
Mean		**3.7**	**12.5**
StDev		**1.0**	**2.3**
CoV		**28%**	**19%**

Table 6-4: Bond wrench tests on masonry couplets. StDev: standard deviation; CoV: coefficient of variation.

No	Bond strength, f_w [MPa]
1	0.8
2	0.4
3	0.8
4	0.6
5	0.8
6	0.7
7	0.7
8	0.8
9	0.5
10	0.7
Mean	**0.7**
StDev	**0.1**
CoV	**21%**

Regarding the instrumentation, six LVDTs were measuring horizontal deformations along the top three and bottom three brick layers (Figure 6-1). Since a vertical crack was expected to occur around the mid-span of the wall, the LVDTs were placed around that region to measure any deformations that would lead to a crack. Moreover, four lasers were used to measure the vertical displacements at the top (two at the sides and one at the mid-span) and bottom (mid-span) (Figure 6-1). It is noted that the reported vertical displacements correspond to measurements from Laser4 at the mid-span of the bottom brick layer (Figure 6-1).

For the six wall specimens tested, different loading protocols were considered. In particular, the tests were (a) monotonic; (b) cyclic with one cycle per amplitude; and (c) cyclic with multiple cycles per amplitude. Each of the loading protocols was applied on a pair of walls in order to reduce any discrepancies due to the inherent variability of masonry material parameters (Tabbakhha and Deodatis 2017; Bejarano-Urrego et al. 2018; Sarhosis et al. 2020). Details regarding the different loading protocols and the maximum force for each specimen are displayed in Table 6-5.

The specimens W1 and W2 were tested under monotonically increased vertical displacement to obtain the reference maximum force of the examined walls (Figure 6-5). From these two monotonic tests the average maximum force was 19.9 kN (Table 6-5). Based on this, the term "force capacity" of the examined specimens will hereafter refer to a value of 20 kN.

The rest four spandrels were tested under cyclic conditions to investigate how repetitive loads affect their response. For the cyclic tests on the walls W3 and W4, at the beginning a preload in the range of 2 kN was applied, which accounts for 10% of the force capacity, and subsequently numerous cycles followed. For each cycle, the specimen was pushed downwards until a maximum value of displacement and then the applied force would return

to the preload level. The maximum displacement was increased by a constant increment of 0.05 mm per cycle. Failure took place after 15 and 21 cycles for the specimens W3 and W4 respectively (Figure 6-5 and Figure 6-8).

For the cyclic tests on the walls W5 and W6, sets of cycles with different force levels were considered. Each set consisted of multiple cycles of the same force level; the force levels are given as percentage of the walls' force capacity. At the beginning of each set a preload in the range of 2 kN was applied while at the end of each set of cycles the specimens were fully unloaded. Failure was reached after 229 and 585 cycles for the walls W5 and W6 respectively (Figure 6-5 and Figure 6-9). In particular, the applied load for wall W5 accounted for sets of 100 cycles at 60%, 100 cycles at 70%, and 29 cycles at 80% of the walls' force capacity. The loading history for specimen W6 comprised of 150 cycles at 75%, 150 cycles at 80%, 150 cycles at 85%, 100 cycles at 90%, and 35 cycles at 95% of the walls' force capacity (Table 6-5).

Table 6-5: Details regarding the different loading histories and the maximum force for each specimen.

Specimen name	Load type	Loading history	max Force [kN]	average max Force [kN]
W1	Monotonic	Monotonically increasing displacement was applied	19.4	19.9
W2	Monotonic		20.4	
W3	Cyclic	The maximum applied displacement was increased by a constant increment (i.e. 0.05 mm) for each cycle	15.8	17.5
W4	Cyclic		19.1	
W5	Cyclic	Sets of cycles with different load levels were applied: 100 cycles @ 60% FC 100 cycles @ 70% FC 29 cycles @ 80% FC	16	17.5
W6	Cyclic	Sets of cycles with different load levels were applied: 150 cycles @ 75% FC 150 cycles @ 80% FC 150 cycles @ 85% FC 100 cycles @ 90% FC 35 cycles @ 95% FC	19	

FC stands for Force Capacity, as obtained from the monotonic tests and corresponds to 20 kN.

6.2 Experimental results

High consistency was observed regarding the crack patterns obtained along the experimental campaign. Vertical cracks formed passing through the brick units and the perpend joints (Figure 6-4). In very limited cases the crack passed along bed joints as well (Figure 6-4). The formed crack initiated from the bottom brick part of the specimens, which was under tension, and extended up to the top brick layer leading to collapse. At the top, the crack fell into the proximity of the loading point. It is noted that prior to failure no visible cracks were detected and the response can be characterized as brittle. The obtained crack pattern could be attributed to the usage of strong mortar; if weaker mortar were used then zig-zag cracks along

the mortar joints were to be expected while cracks though the brick units would be limited (Graziotti et al. 2016b; Korswagen et al. 2019, 2020a).

(a) W1

(b) W2

(c) W3

(d) W4

(e) W5

(f) W6
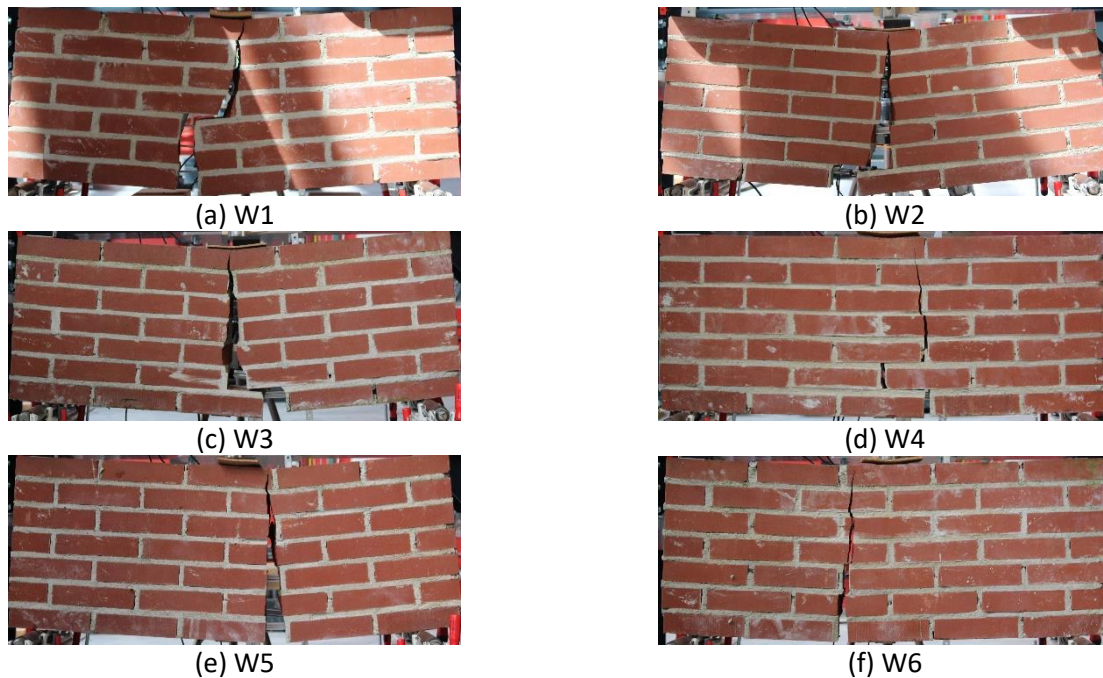
Figure 6-4: Crack patterns obtained at failure of the tested spandrels under three-point in-plane bending.

The force – vertical displacement diagrams for the tested walls are presented in Figure 6-5. The two monotonically tested specimens behaved similarly, and the calculated force capacity was in the range of 20 kN (Figure 6-5a and b). The cyclic tests experienced a progressive fattening of the hysteresis loop along the applied cycles which performs as an indication of damage propagation (Figure 6-5c-f). The damage evolution is better highlighted from the LVDT measurements (Figure 6-7, Figure 6-8, and Figure 6-9).

By comparing the results from the monotonic and cyclic tests, it was evident that the multiple load cycles do affect the response of the masonry structures. In particular, for the walls excited under cyclic load the maximum obtained force was 80% to 95% of the force capacity corresponding to the monotonic cases (Figure 6-6). In other words, the cyclic tests never reached the force capacity of the monotonic counterparts and the decrease in terms of force was from 5% to 20%. These values should not be deemed as established limits, since only limited specimens were considered, but they showcase that, when assessing the condition of masonry structures, the loading history should be taken into consideration and perhaps suitable reduction factors can be implemented. In order to be able to define such reduction factors additional tests are recommended.

Korswagen et al. (2019) in their study of light damage in masonry spandrels did not observe any force reduction under repetitive load in respect to the maximum force obtained for monotonic tests. Korswagen et al. (2019) considered weaker mortar which has been shown

to lead to greater variation on the material properties. In particular, the coefficient of variation, which is indicative of the variability of the experimental response, for the characterization of the bond strength was 21% for this experimental campaign while ranged from 32% to 69% from studies where low strength mortar was considered (Graziotti et al. 2017; Kallioras et al. 2018; Korswagen et al. 2019; Drougkas et al. 2020). Therefore, due to this variation of the mechanical properties the force capacity recorded a wider range of values making it hard to spot different trends between the monotonic and cyclic tests (Korswagen et al. 2019).

Another important finding is that the specimens W5 and W6, which were tested under sets of repetitive load cycles, could initially sustain loads at 80% and 95% of the force capacity, respectively, but repetition of the same load led to failure. This implies that the accumulation of micro-damage can lead to failure even with loads that a structure would normally be expected to carry safely. This is critical especially for cases of masonry structures under recurrent loads of low to medium levels as compared to their capacity. Actions like expansion/shrinkage due to environmental conditions and structural deformations due to soil movements can be considered as recursive load cycles along the life span of a structure. Especially for the case of induced seismicity, structures, usually without any aseismic design, along with the aforementioned loads have to sustain loads due to frequent seismic events. As shown in the case study presented in Chapter 3, low magnitude earthquakes normally would not be expected to cause damage to structures, but the superposition of different load types, i.e. soil effects and earthquake vibrations, have the potential to actually lead to damage at load levels lower than the expected.
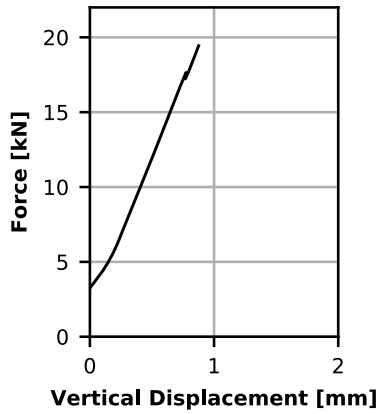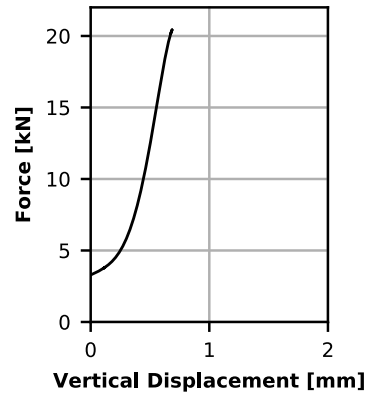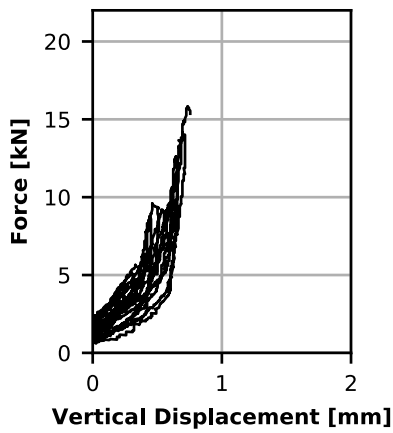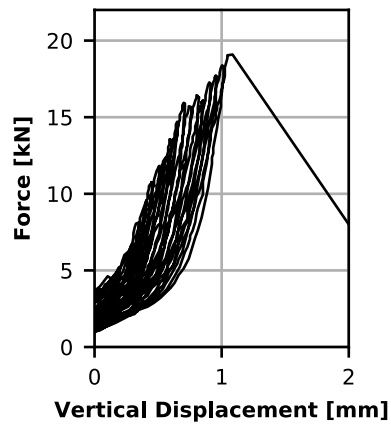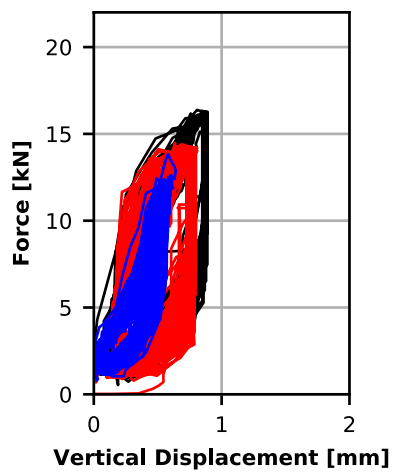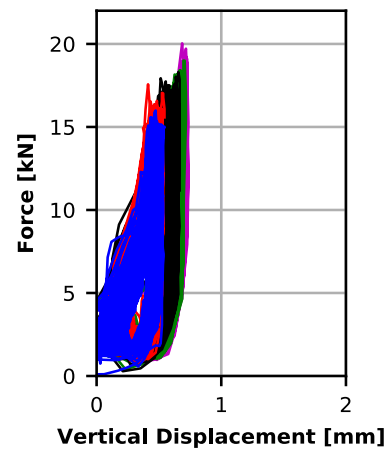
Figure 6-5: Force – vertical displacement diagrams for the tested walls. The specimens (a) W1 and (b) W2 were tested monotonically, while (c) W3, (d) W4, (e) W5, and (f) W6 were loaded cyclically.
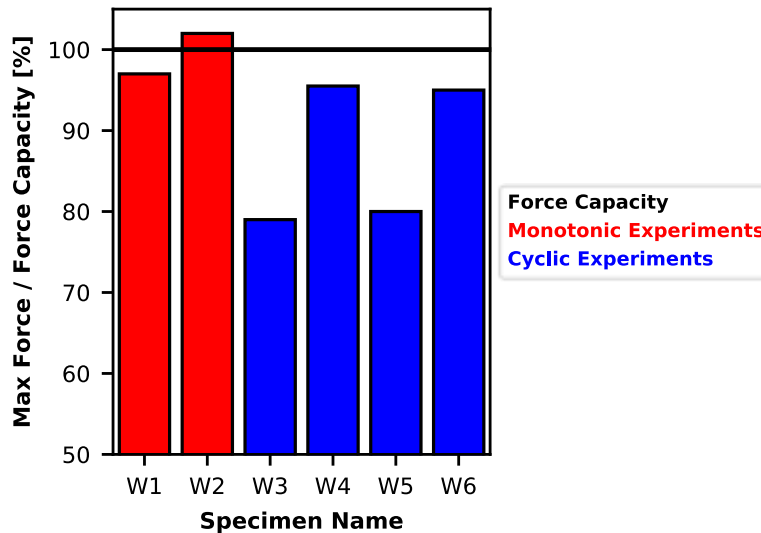
Figure 6-6: For the tested walls the maximum attained force is presented as percentage of the walls' force capacity. The force capacity is defined as the average force obtained from the monotonic experiments.

The measurements of horizontal deformations as recorded with LVDTs are shown in Figure 6-7, Figure 6-8, and Figure 6-9. For the LVDT measurements positive and negative signify tension and compression respectively. The LVDT measurements for the cyclic walls are presented in parallel with the applied vertical displacement for W3 and W4 (Figure 6-8) and the applied force for W5 and W6 (Figure 6-9) for extra clarity.

In general, the highest deformations were recorded from LVDT1 which corresponds to the bottom brick layer being under tension (Figure 6-1). In particular, failure took place for deformations, as obtained from LVDT1, above 0.05 mm and could correspond to deformation values slightly exceeded 0.1 mm. Consequently, for deformations lower than 0.05 mm no visible damage would be expected which is in line with the guidelines by Burland & Wroth (1974). Moreover, since no visible damage could be observed before failure, the conventional limit of 0.1 mm (Burland et al. 1977) regarding the minimum crack width for a crack to be visible to the naked eye appears suitable; for deformations lower than this threshold only micro-damage would be expected on a masonry structure.

At this moment, the deformation measurements from the wall W5 and in particular regarding LVDT2 and LVDT5 are further elucidated. Abrupt increases noticed as jumps in the deformation time-histories were recorded by these two sensors for the first two sets of loading cycles (Figure 6-9). In more detail, for the first cycle at 60% of the force capacity the deformation from LVDT2 reached 0.05 mm while any increase along the next cycles with the same load level was limited and more gradual. Another jump occurred at the first cycle of the next set of load repetitions, i.e. at 70% of the force capacity, without any further increase for this set containing 100 cycles. The response recorded from LVDT5 was likewise (Figure 6-9c). Although these abrupt increases might appear risky for an upcoming failure, the

specimen in fact could sustain increased load level at 80% of the force capacity. On the other hand, the behaviour at the third set was different. For the sensors LVDT1, LVDT2, and LVDT3 placed at the bottom part of the wall the deformation rose with an increasing pace along cycles of same load level (Figure 6-9c). As explained earlier on, the failure initiated from the lower part of the walls which is under tension. This exponential increase of the deformation shows that any micro-damage further propagates and crack formation is possible. Based on the LVDT measurements, it could be concluded that any jumps in the deformation values might not be a clear indication of an upcoming premature failure while exponential increase under same load was found to be related to upcoming failure.

Previous studies have shown that extracting reliably force and displacement capacity for structural components of existing masonry constructions is very challenging due to many uncertainties (Sarhosis and Sheng 2014; de Felice et al. 2016; Sarhosis et al. 2020). This experimental campaign showcased that deformation measurements could perform as a good indicator of the crack onset. Researchers have used monitoring of deformations for masonry structures but only upon the initiation of visible damage in order to record the evolution of cracks (Alessandri et al. 2015; Kita et al. 2019; Blyth et al. 2019; Makoond et al. 2020). Nevertheless, structural elements like tie bars of masonry monuments (Ceravolo et al. 2017; Gentile et al. 2019) or bridge stay cables (Li et al. 2011) have been monitored prior to failure to continuously assess their performance. In a similar manner, monitoring of deformations before visible damage takes places could be considered for critical regions of masonry structures using innovative solutions like fibre-optic cables (Verstrynge et al. 2018; Acikgoz et al. 2021) or strain-sensing piezoresistive bricks (Meoni et al. 2021).

(a) W1   (b) W2
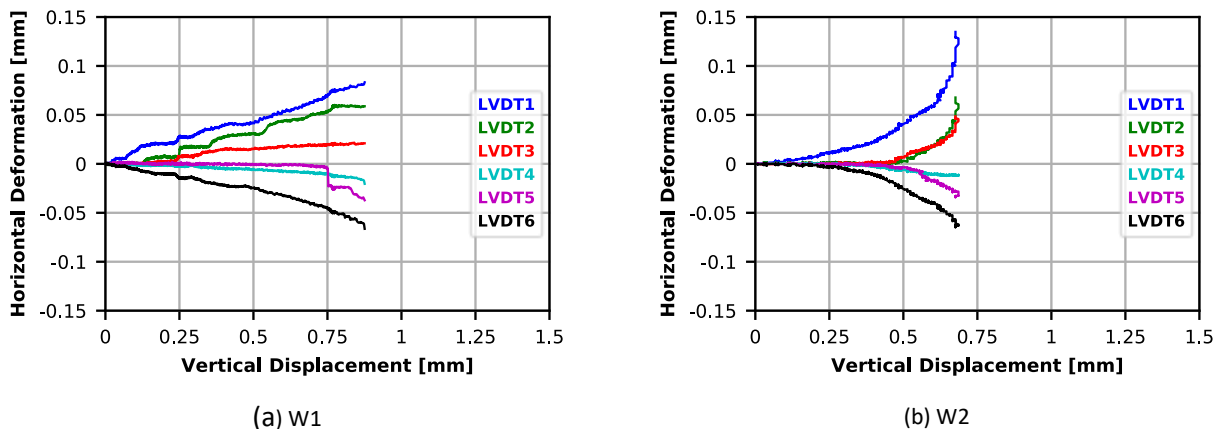
Figure 6-7: Measurements of horizontal deformations as recorded with LVDTs for the specimens (a) W1 and (b) W2 tested under the application of monotonically increasing displacement.
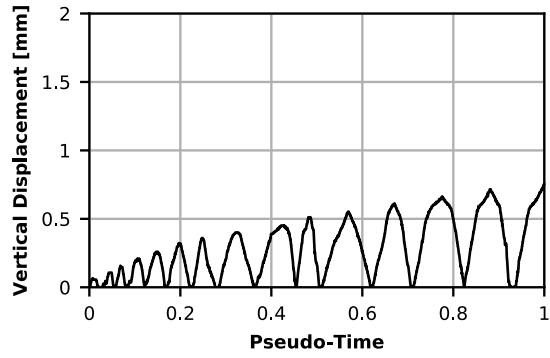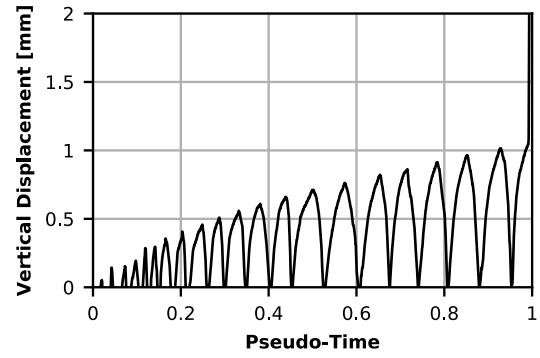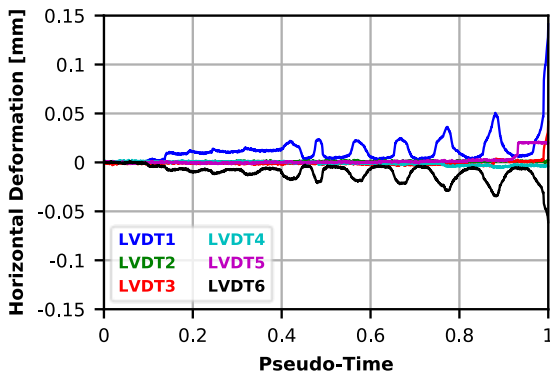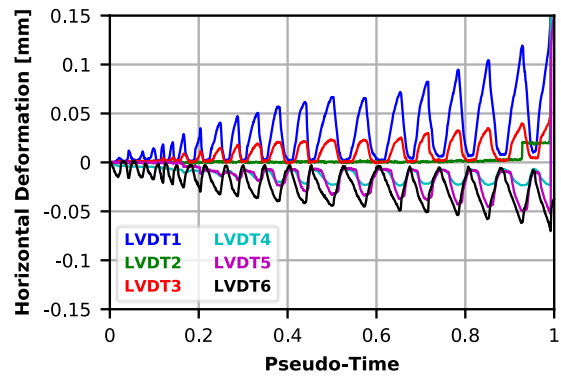
Figure 6-8: Time-history of applied vertical displacements (top) and measurements of horizontal deformations as recorded with LVDTs (bottom) for the specimens W3 (left) and W4 (right). W3 and W4 were tested under the application of incrementally increasing displacement.
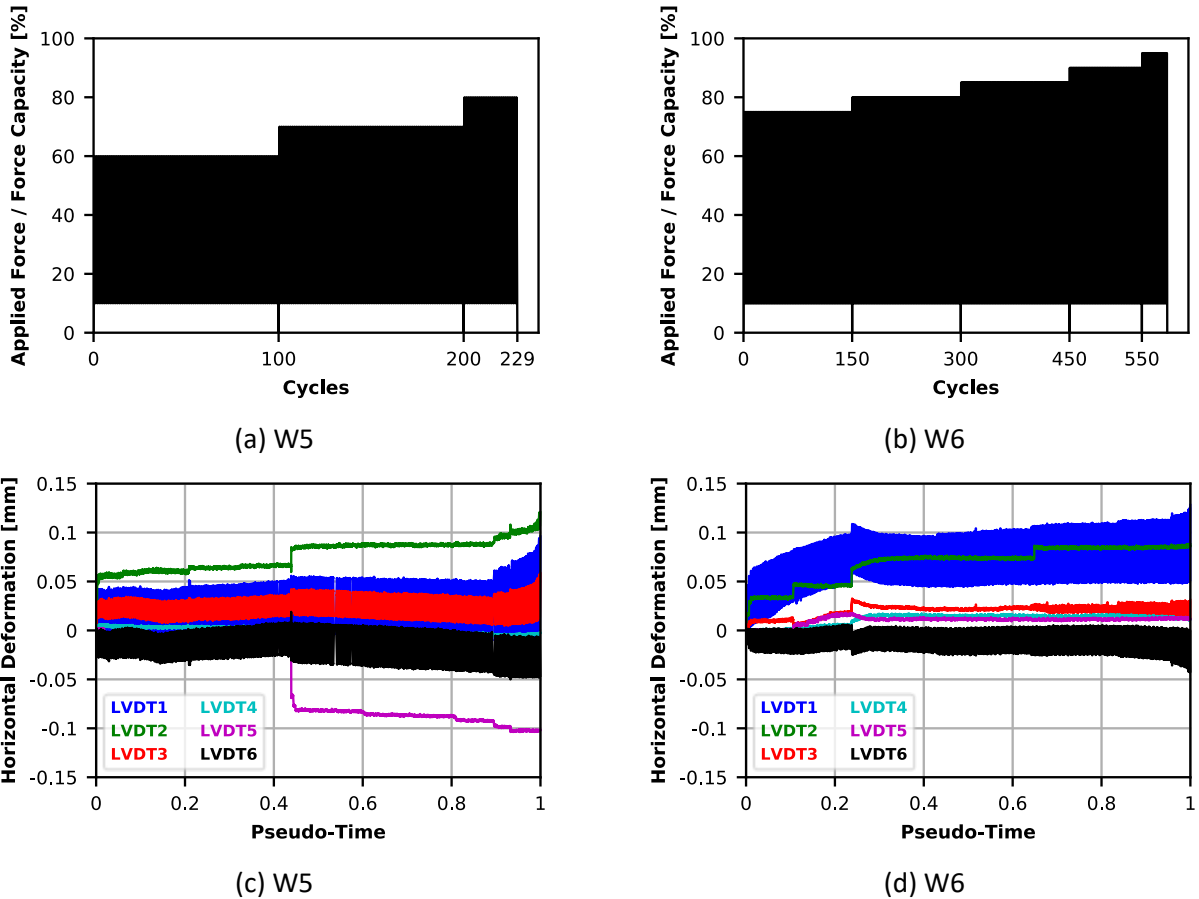
Figure 6-9: Time-history of applied force as ratio of the walls' force capacity (top) and measurements of horizontal deformations as recorded with LVDTs (bottom) for the specimens W5 (left) and W6 (right). W5 and W6 were tested under the application of sets of cycles with different force level.

6.3 Numerical representation of experimental campaign

For the numerical representation of the experimental campaign three different models were considered. First, a macro-modelling simulation was examined where units, mortar, and unit-mortar interface were smeared out in continuum (Lourenço 1996) (Figure 6-10a) (see Section 2.8 for extra details). Moreover, two variations of the simplified micro-modelling approach were regarded; discontinuous elements (i.e. interfaces) reproduced the mortar joints while the expanded brick units were simulated either solely with continuum CPS4R elements (Figure 6-10b) or one vertical interface was considered as well to account for potential cracks along the middle of the units (Figure 6-10c) (for a detailed description of the considered micro-modelling strategy refer to 5.3.1). These three modelling approaches will be referred to as (a) Macro, (b) Micro, and (c) Micro - Crack (Figure 6-10).

(a) Macro   (b) Micro   (c) Micro - Crack
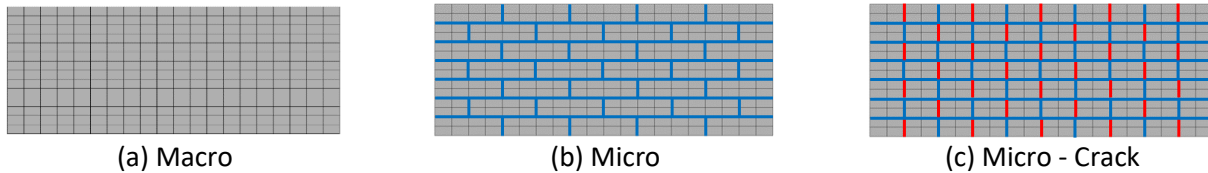
Figure 6-10: Different modelling approaches considered to simulate the response of the tested masonry walls. Mesh, mortar interfaces and interfaces for potential crack along the brick units are shown in black, blue and red respectively.

The three considered models were calibrated over the results of the experimental campaign in terms of force – vertical displacement while the horizontal deformations corresponding to the LVDT measurements were evaluated as well. For the verification of the calibration, the numerical analyses were compared against the response of the monotonic (W1 and W2) and the cyclic with one cycle per amplitude (W3 and W4) specimens. The modelling parameters were extracted from the companion tests, the calibration of the numerical models or from experimental and numerical studies in the literature.

For the Macro model similar approach as the one explained in Section 3.3 was followed. In particular, masonry was regarded as homogeneous continuum and the nonlinear response was simulated with the CDP constitutive law (ABAQUS 2013). For the micro-modelling analyses (Micro and Micro – Crack) the masonry units were simulated using the CDP model (Section 5.3.1.1) while for any discontinuities (that is mortar joints or potential cracks along the bricks) interface elements were considered as shown in Section 5.3.1.2. The cyclic behaviour of the discontinuous elements was defined with a subroutine that was developed for the sake of this study (Section 5.3.1.2). The CDP constitutive law assumes different yield strength in tension and compression and stiffness degradation is incorporated in the post-yield phase (refer to Section 3.3 for additional clarification). The adopted uniaxial response in compression and tension and the evolution of the corresponding damage variable for the different modelling strategies are displayed in Table 6-7 and Table 6-11. Dilation angle, eccentricity, σ_{b0}/σ_{c0} ratio, K_c, and viscosity are configured similar to the values explained in Section 3.3 (Table 6-8). The mechanical properties (i.e. density, Young's modulus, and Poisson's ratio) considered for the numerical representation of the experimental response walls are presented in Table 6-6 and Table 6-10. Poisson's ratio was assumed as 0.2 following previous studies (Petry and Beyer 2015b; Chácara et al. 2017; Dolatshahi et al. 2018; D'Altri et al. 2019a; Greco et al. 2020; Wilding et al. 2020). Different values of Young's modulus were considered for the Macro (Table 6-6) and the two micro models (Table 6-10). It is reminded that the homogeneous properties (i.e. CDP) for the former correspond to the masonry walls as a whole while for the latter are assigned to the brick units. In the Macro model the Young's modulus is a quasi-average of the elasticity of the two masonry components (bricks and mortar) (Giordano et al. 2002). Therefore the Young's modulus for the Marco case (E_0 = 15,000 MPa) is lower than its counterpart for the micro models (E_0 =

20,000 MPa). The adopted values for Young's modulus are in line with values in previous experimental and numerical studies (Riddington and Naom 1994; Lourenço 1996; Nazir and Dhanasekar 2014; Dolatshahi and Aref 2016). See Section 5.3.2 for a discussion on the calibration of the Young's modulus values. For the Macro model the strength in tension (σ_t = 0.6 MPa) and compression (σ_c = 20 MPa) were based on the experimentally obtained bond strength f_w and normalized compressive strength f_b respectively (Table 6-7). For the micro models the tensile strength of the masonry units was defined as σ_t = 1 MPa, higher than the tensile strength of the mortar joints (f_t = 0.7 MPa) which led to the correct reproduction of the experimental crack pattern. Similarly, for the Micro – Crack case the tensile strength of the interface accounting for potential crack in the masonry units was taken as f_t = 1 MPa allowing for the development of cracks along the bricks (Figure 6-11c) as observed in the experiments (Figure 6-4). For the micro models the compressive strength of the masonry units was set as σ_c = 5 MPa following the calibration method explained in Section 5.3.1. Since it was not possible to perform shear tests, the parameters to define the initial and residual strength of the interfaces in the tangential direction (i.e. $tan\varphi$, c, and μ) were adopted from previous experimental and numerical campaigns (Lourenço 1996; Dolatshahi et al. 2018; Bejarano-Urrego et al. 2018; D'Altri et al. 2019a) (Table 6-9). The tensile separation u_n^f and shear slip u_s^f upon which cohesive behaviour is completely damaged were set to match the experimental tensile (Mode I) and shear (Mode II) failure respectively (van der Pluijm 1999) (Table 6-9). The tangential stiffness k_s was appropriately configured to match the experimental response (Table 6-9) by evaluating suitable values from the literature (Lourenço 1996; Sarhosis and Sheng 2014; D'Altri et al. 2019a). The normal stiffness in tension $k_{n,t}$ did not affect significantly the numerical response and its value was considered similar to the one used in Section 5.3.2 (Table 6-9) while for the counterpart in compression $k_{n,c}$ rigid stiffness was assigned to limit possible surface penetrations.

Table 6-6: Summary of mechanical properties adopted for the Macro model.

Material	Density [kg/m³]	Young's modulus [MPa]	Poisson's ratio [-]
Masonry	1,900	15,000	0.2

Table 6-7: Nonlinear uniaxial response of the Concrete Damaged Plasticity in compression (left) and tension (right) for the Macro model.

Compression				Tension		
ε_c^{pl}	σ_c [MPa]	d_c		ε_t^{pl}	σ_t [MPa]	d_t
0	20	0		0	0.6	0
0.06	0.2	0.9		0.001	0.005	0.9

Table 6-8: The main parameters for the Concrete Damaged Plasticity model.

Dilatation angle [°]	Eccentricity	σ_{b0}/σ_{c0}	K_c	Viscosity
10	0.1	1.16	0.666	0.0005

Table 6-9: Mechanical properties considered for the interface elements in the Micro and Micro – Crack models.

Parameter	Units	Mortar joints	Brick/Crack*
Normal direction			
f_t	[MPa]	0.7	1
u_n^f	[mm]	0.3	0.1
$k_{n,t}$	[N/m³]	10^7	10^7
Tangential direction			
c	[MPa]	0.22	0.50
$tan\varphi$	[-]	0.55	0.55
μ	[-]	0.55	0.55
u_s^f	[mm]	0.3	0.1
k_s	[N/m³]	10^8	10^8

*Brick/Crack refers to the interface accounting for potential cracks along the masonry units incorporated in the Micro – Crack model.

Table 6-10: Summary of mechanical properties adopted for the Micro and Micro - Crack models.

Material	Density [kg/m³]	Young's modulus [MPa]	Poisson's ratio [-]
Masonry units	1,900	20,000	0.2

Table 6-11: Nonlinear uniaxial response of the Concrete Damaged Plasticity in compression (left) and tension (right) for the Micro and Micro - Crack models.

Compression				Tension		
ε_c^{pl}	σ_c [MPa]	d_c		ε_t^{pl}	σ_t [MPa]	d_t
0	5	0		0	1	0
0.06	0.2	0.9		0.01	0.1	0.9

The numerical results are presented in terms of force – vertical displacement diagrams (Figure 6-11); deformed shapes with contour plots of plastic strain magnitude (Figure 6-12) and horizontal deformations (Figure 6-13); and horizontal deformation at the bottom brick layer (Figure 6-14).

The Macro approach correctly captured the experimental crack along the mid-span (Figure 6-4), but only crude localization of the damaged region was possible (Figure 6-12a). Moreover, the Macro model correctly predicted the peak force under monotonic load (Figure 6-11a). For the cyclic analysis the maximum force decreased in respect to the monotonic one by 19% (Figure 6-11a). This value lays inside the range of the experimentally obtained force reduction, i.e. 5% to 20% (Figure 6-6). A numerical exercise was considered to investigate the degree of force reduction that could be attained when the Macro model was excited with cyclic load. Different configurations for the evolution of damage variables and inelastic strains were examined based on previous numerical studies for URM structures (Acito et al. 2016; Milani et al. 2018; D'Altri et al. 2019a) and the attained decrease of the ultimate force ranged from 19% to 27%. This load reduction under cyclic load appears to be incorporated in the mechanical behaviour of the considered constitutive model. In particular, CDP considers irreversible damage that occurs during the fracturing process described by the combination of non-associated multi-hardening plasticity and scalar (isotropic) damaged elasticity c. In

order to attempt a more reliable numerical simulation of the damage accumulation expressed as decrease in the peak load, firstly additional experimental work is required to gain a better insight into the mechanism that leads to lower ultimate load under cyclic tests.

One limitation of the Macro model was on the replication of the post-failure response. It is pointed out that for the tested walls the attainment of the peak force was followed by collapse without being able to carry loads any further (Figure 6-5). On the contrary, for monotonic load, the residual strength of the wall decreased gradually in the numerical analysis (Figure 6-11a). Likewise, the cyclic simulation was characterized by unrealistic residual force capacity upon failure (Figure 6-11a). Similar response was observed by Dais et al. (2021) where a masonry monument was investigated under strong earthquake excitations. Even though excessive damage was numerically attained, the structure remained standing while in reality the temple collapsed. Giordano et al. (2002) highlighted the inability of FEM-based macro-modelling approaches to reliably replicate the post-failure response while correctly predicting the initial response and the collapse load. It was argued that geometry changes linked to severe cracking cannot be easily reproduced by a smeared cracking model (Giordano et al. 2002). Therefore, it is recommended that results with the macro-modelling approach are critically evaluated; regions with concentration of damage could signify actual local failure or total collapse of a masonry structure even if the numerical analysis did not lead to collapse.

The micro models were able to reproduce the experimental behaviour with high fidelity both in terms of force – vertical displacement (Figure 6-11b-c) and crack pattern (Figure 6-12b-c). For cyclic load, the micro simulations captured the accumulation of micro-damage through the incremental fattening of the hysteresis loop while brittle failure took place upon the attainment of the peak force. The Micro and the Micro – Crack analyses accurately reproduced the cracking pattern; the former overestimated the contribution of bed joints in the failure mechanism while the latter precisely reproduced the crack expanding through bricks and mortar joints. For this experimental campaign, high strength mortar was used and as a result the formed crack passed through brick units and perpend joints while only in limited cases bed joints contributed. For such cases, it is concluded that incorporating interfaces along the bricks to account for potential cracks allow the accurate simulation of the expected failure mechanism.

Regarding the post-failure behaviour, the Micro – Crack model led to complete strength loss while the Micro simulation incorrectly accounted for limited residual load capacity. For the latter model, no discontinuities were considered along the masonry units that would allow the formed crack to pass through the upper mid brick and thus it was not possible to reproduce the complete failure of the specimen (Figure 6-12b). For the Micro case, when cyclic load was applied, the maximum force decreased only slightly in comparison to the monotonic response while for the Micro – Crack model no reduction was observed. This is in line with

findings from the literature; when discrete modelling is utilized the monotonic response performs as envelope of the cyclic hysteresis loop without any significant peak load reduction (Aref and Dolatshahi 2013; Minga et al. 2018; D'Altri et al. 2019a; Malomo et al. 2019b). Any non-linearities for the Micro – Crack model took place along the interfaces (mortar or brick crack) (Figure 6-12c) while for the Micro analysis limited plastification occurred at the brick units (Figure 6-12b). It is reminded that the solid bricks were simulated with the CDP model and thus the slight damage along the units of the Micro model led to the limited decrease of the maximum force for the cyclic case.

(a) Macro (b) Micro (c) Micro - Crack
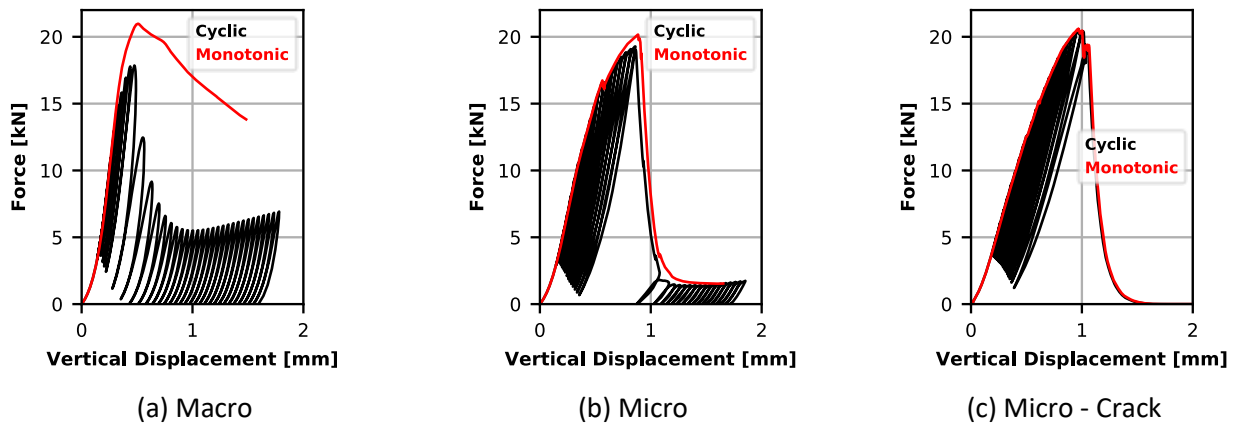
Figure 6-11: Force – vertical displacement diagrams as obtained from the numerical analyses with the different modelling approaches considereded under monotonic and cyclic load.

(a) Macro (b) Micro (c) Micro - Crack
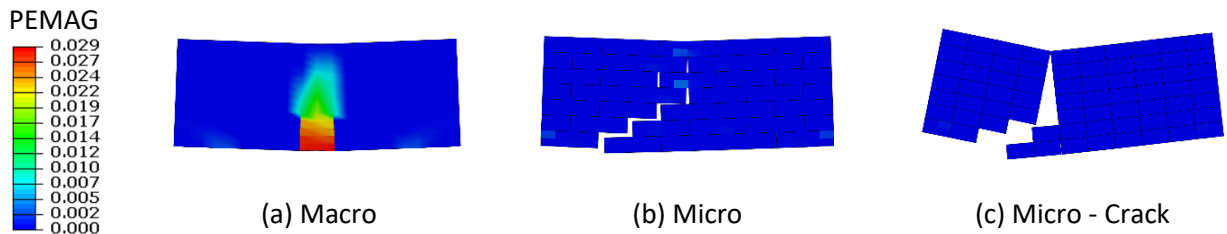
Figure 6-12: Deformed shape at the end of the cyclic analyses obtained from the different modelling approaches considered. The response was the same for monotonic and cyclic load. Contours represent PEMAG, i.e. plastic strain magnitude.

(a) Macro (b) Micro (c) Micro - Crack
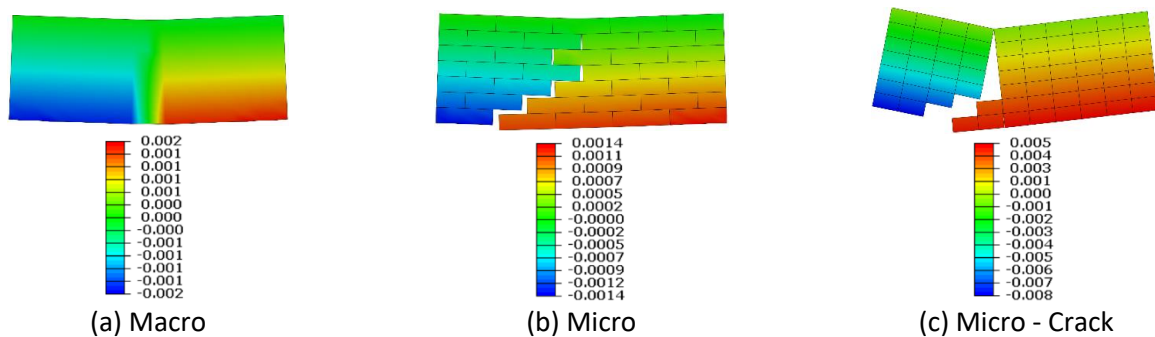
Figure 6-13: Deformed shape at the end of the cyclic analyses obtained from the different modelling approaches considered. The response was the same for monotonic and cyclic load. Contours represent horizontal deformations in m.

The displacement protocol applied for the cyclic analysis is displayed in Figure 6-14a. It is noted that failure was attained prior to the application of the entire protocol (Figure 6-14c, e and g). In Figure 6-14b-g, measurements of horizontal deformation along the bottom brick layer for the different models are shown. These measurements correspond to the values recorded by LVDT1 for the tested walls (Figure 6-1). In particular for the micro analyses, horizontal deformation (Figure 6-14d-g) accounts for normal displacement along the interfaces replicating mortar joints or potential cracks on brick units (for further clarification refer to the definition of the micro-modelling approach in Section 5.3.1.2) with positive values signifying tension (i.e. separation). A correlation between the values of numerical separation and the experimental formation of visible cracks will be attempted below.

For the Macro model, when the wall was loaded monotonically the peak force corresponded to horizontal deformation 0.15 mm while further increase of the horizontal deformation was rather gradual (Figure 6-14b) which is line with the overestimation of the residual force along the post-failure branch under monotonic excitation (Figure 6-11a). On the other hand, for the cyclic analysis the horizontal deformation increased abruptly when approximately 0.1 mm was reached (Figure 6-14c). This abrupt increase of the horizontal deformation steams from the fact that the CDP model considers irreversible damage under cyclic load leading to premature failure and reduction of the force capacity in comparison to the monotonic case (Figure 6-11a).

The two micro models displayed similar response (Figure 6-14d-g). When horizontal deformations exceeded a value in the range of 0.2 mm sharp increase followed leading to failure. Given the brittle response of the tested masonry walls, the failure state was attained upon crack initiation (see Section 6.2). Therefore, 0.2 mm of surface separation could be considered as the threshold value for crack onset in the Micro and Micro – Crack numerical analysis. Moreover, the micro simulations under repetitive load led to accumulation of residual deformations (Figure 6-14e and g). Similar trend was observed along the tested walls (Figure 6-8) but it was less profound that the numerical one.

Based on the experimental findings, initiation of visible cracks corresponded to deformation values ranging between 0.05 mm and slightly exceeding 0.1 mm (see Section 6.2). The numerical results slightly overestimated these values. In particular, as explained above, the threshold value for crack onset in terms of deformations was 0.15 mm and 0.1 mm for the Marco model under monotonic and cyclic load respectively while for the micro cases this limit could be set as 0.2 mm for both load types. Consequently, the assumption considered in Section 5.3 to conventionally set numerical joint separation or sliding of 0.2 mm as threshold for crack onset (Section 5.3) seems suitable.
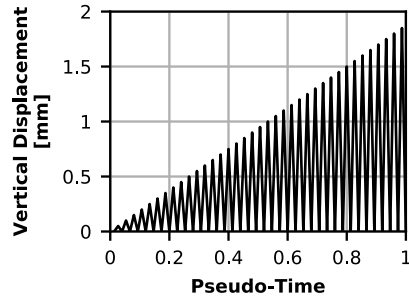
(a) Protocol for cyclic analysis
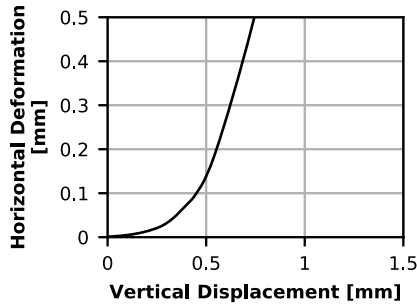
(b) Macro | Monotonic
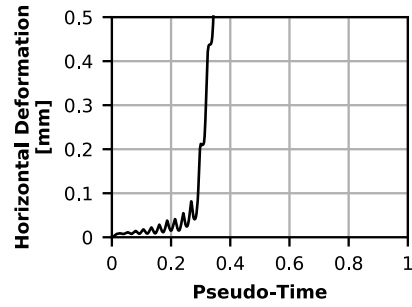
(c) Macro | Cyclic
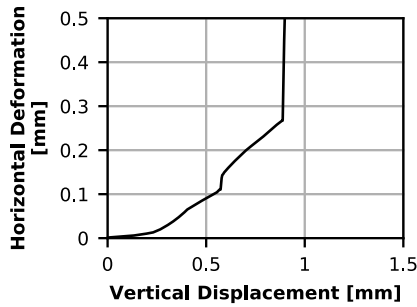
(d) Micro | Monotonic
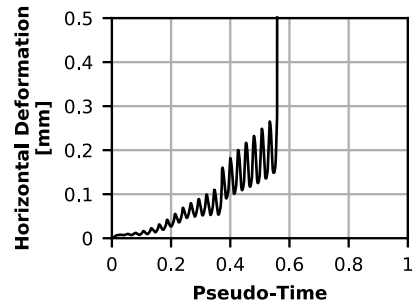
(e) Micro | Cyclic
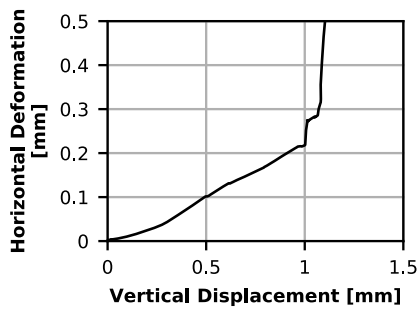
(f) Micro – Crack | Monotonic
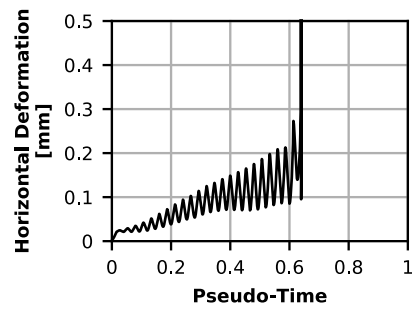
(g) Micro – Crack | Cyclic

Figure 6-14: (a) Displacement protocol applied for the cyclic analysis. (b) – (g) Evolution of horizontal deformation along the bottom brick layer for the different models (Macro; Micro; Micro – Crack) and load types (Monotonic; Cyclic).

6.4 Conclusions

In this Chapter, the undertaken experimental campaign and efforts for its numerical simulation were presented. Six walls representative of spandrel geometry were tested under

three-point in-plane bending to investigate the effect of cyclic load on the response of masonry structures focusing on the damage propagation.

The response of the tested masonry specimens was brittle and damage took place without any prior visible indication. Monitoring of deformations was found able to detect signs of micro-damage (i.e. invisible damage) and provide an early warning of collapse. Exponential increase of deformations for same load levels could signify upcoming failure. Therefore, it is recommended to monitor the deformation levels at critical regions of masonry structures, especially when the required performance level is the avoidance of any visible cracks.

Based on the experimental results, repetitive load cycles have the potential to lead to premature collapse of masonry structures for actions lower that the anticipated capacity. Failure upon repetition of the same load amplitude was recorded which highlights that the accumulation of micro-damage can cause failure even with loads that a structure would normally be expected to carry safely. In particular, the cyclic tests never reached the force capacity of the monotonic counterparts and the decrease in terms of force was from 5% to 20%.

Given the limited experiments performed, it was not possible to determine the mechanism behind the reduction of the force capacity under cyclic load. Additional experimental research is encouraged to study the effects of accumulation of micro-damage in masonry structures and possibly define appropriate strength reduction factors to account for the loading history.

A macro-model and two variations of the simplified micro-modelling approach (i.e. with and without the consideration of discontinuous elements to account for potential cracks along the middle of the masonry units) were evaluated on their efficacy to replicate the experimental response. Load capacity, deformation evolution and failure pattern were captured adequately with all the considered modelling techniques. In particular, the macro approach allowed for a crude localization of the damaged region while both micro models reproduced the cracking pattern with higher fidelity. Therefore, when higher detail is requested and the focus lays on the simulation of local failure types the micro-modelling method is recommended. For cases where high strength mortar is considered, like for this study, cracks are anticipated on both mortar joints and bricks. In such cases the micro approach that accounts for potential discontinuities along the masonry units was found to further improve the simulation of the expected failure mechanism.

Continuous models fail to reproduce geometry changes linked to severe cracking and thus the simulated post-failure response needs to be looked at with a critical eye. The CDP constitutive law that was utilized to simulate the continuum elements considers irreversible damage under cyclic excitation and therefore was able to reproduce the force reduction observed on the cyclically tested walls. On the contrary, the discrete numerical analyses did not account for lower force capacity under cyclic load.

Upon availability of additional experimental interpretation of the accumulation of micro-damage, further calibration of the macro model and elaboration of the behaviour of the micro approach is suggested.

Chapter 7
Concluding remarks

With the pressure to increase local energy supplies by unlocking the energy potential of the ground, induced seismicity in the northern part of Europe has considerably increased. The local building stock, comprising mainly of masonry structures without any aseismic design, has been found susceptible to these induced tremors. Induced seismicity is generally characterized by frequent small-to-medium magnitude earthquakes while structural and non-structural damage have been reported. Since the induced earthquakes are caused by third parties liability issues arise and a damage claim mechanism is activated. Typically, any damage are evaluated by visual inspections. This process has been found rather cumbersome since visual inspections are laborious, slow and expensive while the identification of the causation of any light damage is a challenging task rendering essential the development of a more reliable approach. The aim of this PhD study is to gain a better understanding of the monitoring, modelling and quantification of accumulation of damage in masonry structures due to recursive loads. Any concluding remarks are presented below for each of the objectives.

1. Showcase the potential of seismic events of low magnitude to cause damage to the built environment

Fraeylemaborg, the most emblematic monument in the Groningen region, was selected as a case study in order to investigate possibilities to monitor the accumulation of damage. Fraeylemaborg experienced damage due to the induced seismic activity in the region in the recent years. Initially, a thorough structural condition assessment of the monument was regarded and any signs of damage were highlighted (T1.1). At the moment that the monument was first visited no cracks could be detected along the structure since they had been repaired during the previous restoration courses. Nevertheless, visual inspections around the monument and its retaining walls revealed traces of damage. The existing evidence of damage could be attributed to soil movements and/or differential settlement and were taken into account in the structural assessment of the monument. Soil investigations were also conducted and clay/pot-clay layers were identified. This soil type is characterized by shrinking or/and the expansive behaviour which could possibly lead to soil deformations. Thus such a behaviour was considered in the scenarios that were numerically evaluated.

A novel monitoring approach was adopted to detect damage accumulation in Fraeylemaborg masonry (T1.2). The monitoring results of this historical building were presented to create a basis of discussion on what would be the main differences when monitoring historical buildings in case of induced earthquakes. The SHM scheme applied at Fraeylemaborg comprised various information channels, i.e. accelerometers, a tiltmeter, analogue crack rulers, meteorological data as well as ground water level measurements. The simultaneous

use of multiple channels of information is necessitated by the nature of the induced earthquakes so that reliable conclusions are drawn. Although the increased seismic activity went hand in hand with increased number of cracks on the monument, the shape and location of the latter did not resemble earthquake-related cracks. The existing cracks were more reminiscent of cracks that tend to occur with ground movements rather than with seismic load. The structure underwent two restoration phases in 2015 and 2017, and the manifestation of new cracks in the summer of 2018 was a puzzlement given the relative limited seismic activity in the respective period. Monitoring data from the structure along two earthquakes were presented to provide a better insight. Slight damage was reported after the first earthquake of small magnitude, whereas the second earthquake with much higher recorded accelerations did not lead to any damage. In order to provide plausible scenarios for the causation of damage all the available monitoring data were evaluated. In this way, it was shown that measurements that are based on a single source of sensors, such as only tiltmeters or only accelerometers, would not be enough to provide reasonable explanations. Furthermore, it was also highlighted that the meteorological data play a critical role in developing damage scenarios in case of induced seismicity.

A numerical model was calibrated based on experimental findings and different loading scenarios were compared with the actual damage patterns observed on the structure (T1.3). It was concluded that the in-plane cracks would not be expected in this structure during such small earthquakes. One explanation could be that the soil parameters, such as shrinking of water-sensitive soil layers and/or response of piles, in combination with a small distant earthquake, caused settlements and/or increased the stress levels on foundations. The soil effects might have superimposed with the earthquake effects causing small cracks.

In the future, the work in Fraeylemaborg will continue to better understand the nature of the damage. As part of that effort, a nonlinear numerical model with a properly modelled soil box is prepared and will be run to investigate further the soil-structure interaction phenomena associated with induced seismicity events. To better understand the effect of soil and foundation, measurements of soil movements will be collected and will be correlated with structural damage and the rest of monitoring data is highly recommended.

2. Monitor the damage initiation and propagation in masonry structures with the use of remote sensing

Within this objective the automatic crack detection with the use of artificial intelligence (T2.1) and crack width monitoring with invisible markers (T2.2) were evaluated. While SHM can provide a reliable assessment of structures it is not possible to install such systems to every structure. Therefore, currently the condition of such structures is still predominantly visually inspected which is a laborious, costly and subjective process. The inspection process mainly entails the mapping of any cracks to assess the damage level. With developments in

computer vision, there is an opportunity to use digital images to automate the visual inspection process.

Previous studies have investigated computer vision solutions for the detection of cracks for concrete and asphalt surfaces whereas research on masonry is rather limited. To bridge this gap, deep learning techniques were evaluated on their efficacy to automatically detect cracks from images of real masonry surfaces. In order to address the lack of data in the literature, a dataset with photographs from masonry structures was produced containing complex backgrounds and various crack types and sizes (T2.1.1). In particular, photographs were collected from different sources. Various images of masonry walls containing cracks were obtained from the Internet. Additionally, photographs were taken from different masonry buildings in the Groningen region, the Netherlands. A wide range of scales and resolutions was considered. The crack patches depicture from small (couple of bricks) to larger (whole masonry walls) field of views. The collected images included different types of noisy background for the trained model to learn to negate them efficiently. Since for masonry structures little work has been done for crack detection it was deemed beneficial to train networks both for patch classification and pixel-level segmentation (T2.1.2). To the author's best knowledge, this is the first implementation of deep learning for pixel-level crack segmentation on masonry surfaces. Different deep learning networks were considered and by leveraging the effect of transfer learning crack detection on masonry surfaces was performed on patch level with 95.3% accuracy and on pixel level with 79.6% F1 score. Although the proposed deep learning algorithms achieved promising results, further improvements are required to achieve a fully automated vision-based assessment of masonry surfaces. To this end, the expansion of the current masonry dataset is highly recommended with special care for the inclusion of even broader background types. Further studies are advised to evaluate whether semantic segmentation could be utilized to preliminarily detect objects like doors, ornaments, etc. and negate them so that the network would search for defects only on masonry surfaces. Implementation of the most recent state of the art CNN is encouraged to explore their potential to improve the accuracy of crack detection. Moreover, the accuracy of the trained model against different types of masonry other than brickwork, such as rubble walling, needs to be verified and it is suggested for the masonry dataset to be enriched with relevant data.

Although the developed methods for automatic crack detection from photographs capture with acceptable accuracy the length of the detected cracks, the predictions regarding the crack width fail to reliably measure the actual value, especially in the sub-millimetre region. To overcome these limitations and complement the automatic detection of cracks, two different types of novel invisible markers were introduced for the monitoring of cracks (T2.2.1). The first type is a retroreflective marker covered by a special tape that is opaque in visible light but translucent in NIR, while the second marker is a paint produced from infrared

reflective pigments. The reflection of these markers is captured by a special camera-flash combination and processed using image processing algorithms. With the use of computer vision and photogrammetry it was made possible to take accurate measurements keeping the camera in hand without having it fixed to a constant point (T2.2.2). In this way revisiting a location multiple times to extract measurements for crack monitoring is feasible. A series of experiments were conducted to verify their potential to monitor crack development. A proof of concept for crack monitoring on masonry structures using two different types of markers which are not easily noticeable by human eye but exhibit high reflection when subjected to NIR wavelength of light was displayed. The obtained accuracy could be in the range of 0.05 mm which is below the threshold value of 0.1 mm, i.e. crack widths noticeable by the human eye, which verifies the suitability of the approach to measure cracks in masonry walls or plastered and painted masonry surfaces. The method is especially useful for historical buildings and could also be used by non-technical people allowing citizen involvement in collecting data from the field. Although the accuracy of the method was validated, the markers need to be further tested on actual sites with the aim to assess reliability and durability of the markers to weathering and improve their efficiency. Further development is suggested to improve the detectability of the markers.

It is noted that for neither of the vision-based techniques (i.e. crack detection and crack width monitoring) was possible to be tested on the case study and the tested walls (T2.1.3 and T2.2.3). The cracks that appeared in Fraeylemaborg in 2018 were soon covered during the restoration of the monument. Photographs from the cracks with and without markers were captured from the tested walls during the experimental campaign. Nevertheless, it was not possible to process the collected data due to time restraints. The experimental campaign was initially planned for the third year of the PhD, but due to the Covid pandemic, it was undertaken only at the last months.

3. Investigate and quantify the damage evolution in masonry walls subjected to in-plane recursive load

Upon the establishment of ways to monitor damage accumulation in masonry structures, options to quantify and model this accumulation were explored. This objective was addressed by considering a numerical exercise on the quantification of damage evolution with the DEM (T3.1) and evaluating an extensive database of in plane quasi static cyclic experiments on masonry walls found in the literature for the quantification of damage (T3.2).

The vast majority of research on masonry provides only indirect information about the accumulation of damage as it does not constitute the main topic in those studies. Within the literature review (Chapter 2) traces of cumulative damage from the available, though limited, experimental evidence in the literature were highlighted. It was demonstrated that for masonry nonlinear response initiates for very small amplitude of deformations. This

behaviour so far is being overlooked or ill reported, since the focus of the experimental campaigns is the response of the URM specimens close to their ultimate state. Moreover, it was concluded that by using the data of the full-scale shake table tests the cumulative damage does not monotonically increase in case overall structural parameters, such as top displacement or floor displacements, are monitored. For instance, the damage level corresponding to minor structural might be reached (i.e. formation of hairline cracks along the structure) while the residual inter-storey drift remains zero. Thus, it can be inferred that using only the residual ISD as damage indicator would be misleading since the already inflicted cracks would not be accounted for. In conclusion, evaluating crack distribution and evolution appears to provide invaluable information for the reliable assessment of the condition of a structure. For masonry constructions limited research has been undertaken and information about cracks are usually not reported at all or ill-documented in experimental studies hindering thus the development of a crack-based assessment procedure. Taking all these in consideration, the quantification and modelling of damage in masonry structures was attempted by taking into consideration the initiation and propagation of damage due to earthquake excitations.

Moreover, within the literature review the available modelling tools were scrutinized in terms of their pros and cons in modelling cumulative damage in masonry. Depending on the level of accuracy and the simplicity desired, different modelling strategies can be adopted. In overall, SDOF models can be useful for detecting tendencies in cases that more complicated analyses are not feasible. The major drawback of using SDOF models is that the simulated cumulative damage is sensitive to the degradation parameters, which require calibration against experimental data. To address these limitations, more elaborate analyses were considered in this study for the simulation of damage accumulation in masonry structures.

Wall panels representing common typologies of house façades of URM buildings in the Northern European region, i.e. Groningen gas field, were numerically investigated under dynamic load (T3.1.1). A numerical model was developed with the DEM and was validated against a series of full-scale experimental tests obtained from the literature. The accumulated damage within the seismic response of the masonry walls was investigated by means of representative harmonic load excitations and an IDA based on induced seismicity records from Groningen. A damage index based on cracking formation and drift ratio was proposed and applied to the numerical findings while common trends between the numerical and experimental data were highlighted (T3.1.2). Using the results of the developed DEM numerical model, the suitability of the proposed damage indexing equation to realistically represent the level of damage and its sensitivity to low amplitude loading was highlighted. The adopted numerical approach was able to capture any residual damage expressed as cracks even when the residual drift was zero at the end of an excitation. Based on the analyses with harmonic loads, the effect of the load amplitude and the period of excitation on

the damage propagation was elucidated; when no period resonance took place, the damage was limited even for moderate load amplitude while for the cases that the walls were excited with their natural period, damage was recorded even for lower load amplitudes.

The numerical exercise on the quantification of damage evolution with the DEM provided interesting conclusions, although limitations were encountered as well. It was found that additional experimental data with proper documentation of crack propagation are required to provide a generic quantification of damage for different configurations of masonry walls in terms of geometry, boundary conditions, material properties, overload, etc. The proposed damage index needs to be further calibrated based on experimental findings to correlate the obtained values with damage levels. Moreover, the quantification of damage was on the consideration of drift ratio and cracking level. In the DEM analysis cracking was expressed as crack opening and sliding corresponding to tensile and shear failure at the mortar joints respectively. This representation of cracking through its two components (i.e. mortar joint opening and sliding) was examined numerically with the DEM model developed. However, when assessing the damage in real structures or experimental results it is not possible to obtain such detailed information. Therefore, the verification of numerical findings against experimental measurements would be a difficult task.

To address these limitations, experimentally obtained crack patterns were investigated and their correlation with damage propagation was examined. In particular, results from in-plane quasi-static cyclic tests on 32 masonry walls were considered. The examined walls account for different types of real-case masonry piers since various aspect ratios, boundary conditions and values of overload were covered (T3.2.1). It is noted that the considered walls are representative of masonry with low bond strength. Low bond strength masonry refers to masonry in which the tensile and shear bond at the unit-mortar interface is so low that it has a dominant effect on the mechanical behaviour of masonry; any cracks are expected to predominantly appear along the mortar joints and less likely on the brick units.

The collected experimental data enabled a further elaboration on the quantification of damage in masonry walls due to recursive load focusing on the crack propagation. In particular, a damage index accounting for the total failed mortar joints on masonry walls was introduced (T3.2.2). This damage index can be easily computed by visually inspecting a cracked masonry wall providing an intuitive characterization of the damage extent. It was concluded that factors such as geometry, boundary conditions, precompression level, and material properties appear to affect the evolution and distribution of cracking. Moreover, different trends associated with different failure modes were highlighted while cracking levels were correlated with the DL and NC limit states. A preliminary formula to reliably predict the failure mode of slender masonry piers was introduced. Additionally, the incorporation of drift limit for the DL limit state in the Eurocodes was suggested. In order to be able to further

generalize any conclusions additional experimental data are required. It is noted that it was intended to evaluate the damage quantification based on the crack evolution for spandrel elements as well. Nevertheless, such data could not be obtained from the literature and therefore experimental work on spandrels was not studied. It is advised that future experimental campaigns report in a more systematic way quantitative data regarding crack propagation (crack patterns, length and width for different drift levels). These data could enrich the dataset already collected for this study in order to reliably define damage states for masonry structures. As future research, data from full scale tests could be additionally investigated to further any drawn conclusions.

4) Reproduce numerically the accumulation of damage in masonry under repetitive load

Along the numerical exercises with the DEM certain limitations were encountered. In particular, the numerical model with the DEM considered elastic rigid blocks for the representation of masonry units neglecting any failure or degradation under compression while the verification of the mechanical parameters was made against a single wall specimen. Moreover, the numerical results for cracking could be extracted on the basis of two mechanisms (tensile opening and shear sliding) which made difficult the correlation of any findings with experimental measurements; from visual inspection of damaged walls the differentiation between tensile and shear failure is not possible.

In order to address these issues, a micro-modelling solution was developed in the computational software ABAQUS to reliably reproduce and quantify the damage accumulation in masonry structures. Due to the lack of suitable constitutive law implemented in ABAQUS, a subroutine was developed for the sake of this study to describe the response of mortar joints under cyclic load (T4.1). The numerical model was verified against a challenging set of experimental studies (T4.2). The verification of the model laid on the reproduction of the experimental response in terms of hysteresis loop and failure mechanism. Crack patterns and available crack measurements were additionally considered to showcase the efficacy of the numerical model to accurately reproduce the damage propagation as expressed by both crack extent and width. Furthermore, it was possible for the numerical results regarding cracking propagation to be manipulated suitably in order to be directly compared with corresponding measurements from experimental studies. In particular, the quantification of crack propagation was numerically scrutinized with the use of the introduced DI_{crack} and a crack width-based classification from the literature (T4.3). A concise methodology to correctly calibrate the mechanical properties of the implemented micro-model was proposed. Certain parameters (e.g. bond strength, cohesion, and friction coefficient) was possible to be directly extracted from small scale tests while other properties, such as Young's modulus and compressive strength of masonry units, were calibrated best by

considering full scale experiments. It is highly recommended to consider walls with different failure mechanisms in order to reliably define the required parameters.

The developed numerical model was able to reproduce the crack onset related to light damage. In general terms, visible cracks would be expected for drift values in the range of 0.04% to 0.17%. Measurements of crack width for different drift levels are not commonly reported in experimental studies. The developed numerical model allowed the detailed representation of crack propagation and thus enabled the numerical investigation of crack width evolution for different wall configurations. Damage classification based solely on crack width appears convenient since it requires only one factor, but this simplicity might lead to misleading damage assessment. On the other hand, quantification of damage based on the suggested DI_{crack} appears to better represent the real extent of cracking of masonry walls for different configurations. As future research, the numerical model could be verified over different loading mechanisms, such as settlements and out-of-plane excitations or combination of them, and the damage propagation can be numerically evaluated for various loading scenarios. The extension of the work on full scale structures considering a three-dimensional representation is highly recommended.

5. Evaluate the effect of repetitive load on damage evolution and numerically reproduce any findings

The building stock in Groningen, mainly consisting of masonry constructions, has been proven vulnerable to the recent induced seismicity of the region. These structures along the last decade received multiple load cycles due to the frequent low to medium earthquakes. Therefore, it is critical to investigate the effect of load history on the performance of these masonry structures. To this end, an experimental campaign was undertaken to investigate the accumulation of damage in masonry under repetitive load (T5.1). Six wall specimens resembling the configuration of a spandrel element were tested under three-point in-plane bending considering different loading protocols. The walls were prepared adopting materials and practices followed in the Groningen region. Based on the experimental results, repetitive load cycles have the potential to lead to premature collapse of masonry structures for actions lower that the anticipated capacity (T5.2). Failure upon repetition of the same load amplitude was recorded which highlights that the accumulation of micro-damage can cause failure even with loads that a structure would normally be expected to carry safely. In particular, the cyclic tests never reached the force capacity of the monotonic counterparts and the decrease in terms of force was from 5% to 20%. Given the limited experiments, it was not possible to determine the mechanism behind the reduction of the force capacity under cyclic load.

Additional experimental research is encouraged to study the effects of accumulation of micro-damage in masonry structures and possibly define appropriate strength reduction factors to account for the loading history. In this PhD, a spandrel element was chosen to be investigated

due to its simple geometry and structural response. Considering a more complicated configuration such as a pier or a wall with openings is highly recommended to further verify and extend the findings of the current work. The response of the tested masonry specimens was brittle and damage took place without any prior visible indication. Monitoring of deformations was found able to detect signs of micro-damage (i.e. invisible damage) and provide an early warning of collapse. Therefore, it is recommended to monitor the deformation levels at critical regions of masonry structures, especially when the required performance level is the avoidance of any visible cracks.

Furthermore, different numerical approaches were researched for their efficacy to reproduce the experimental response and any limitations were highlighted (T5.3). In particular, a macro-model and two variations of the simplified micro-modelling approach (i.e. with and without the consideration of discontinuous elements to account for potential cracks along the middle of the masonry units) were evaluated on their efficacy to replicate the experimental response. Load capacity, deformation evolution and failure pattern were captured adequately with all the considered modelling techniques. In particular, the macro approach allowed for a crude localization of the damaged region while both micro models reproduced the cracking pattern with higher fidelity. Therefore, when higher detail is requested and the focus lays on the simulation of local failure types the micro-modelling method is recommended. For cases where high strength mortar is considered, like for this study, cracks are anticipated on both mortar joints and bricks. In such cases the micro approach that accounts for potential discontinuities along the masonry units was found to further improve the simulation of the expected failure mechanism. Continuous models fail to reproduce geometry changes linked to severe cracking and thus the simulated post-failure response needs to be looked at with a critical eye. The CDP constitutive law that was utilized to simulate the continuum elements considers irreversible damage under cyclic excitation and therefore was able to reproduce the force reduction observed on the cyclically tested walls. On the contrary, the discrete numerical analyses did not account for lower force capacity under cyclic load.

Upon availability of additional experimental interpretation of the accumulation of micro-damage, further calibration of the macro model and elaboration of the behaviour of the micro approach is suggested. As future research a similar experimental campaign is suggested considering lower strength mortar to simulate historical masonry structures and perhaps some sort of pre-damage could be applied in order to account for any effects of deterioration. Due to the inherent variation of the properties of masonry, discrepancies are to be expected. Therefore, consideration of stochastic approaches are highly recommended to propose appropriate reduction factors.

References

Abadi M, Agarwal A, Barham P, et al (2016) TensorFlow: Large-Scale Machine Learning on Heterogeneous Distributed Systems. ArXiv

ABAQUS (2013) Analysis user's manual, 6.13-3. RI, USA: Dassault Systems Providence

Abbiati G, Broccardo M, Didier M, et al (2018) A probabilistic damage model for predicting plaster cracks on unreinforced masonry walls. In: 16th European Conference on Earthquake Engineering (ECEE 2018). Thessaloniki, Greece

Abdelmoneim Elamin Mohamad A-B, Chen Z (2016) Experimental and Numerical Analysis of the Compressive and Shear Behavior for a New Type of Self-Insulating Concrete Masonry System. Applied Sciences 6:245. https://doi.org/10.3390/app6090245

Abdulla KF, Cunningham LS, Gillie M (2017) Simulating masonry wall behaviour using a simplified micro-model approach. Engineering Structures 151:349–365. https://doi.org/10.1016/j.engstruct.2017.08.021

Abrams DP, Noland JL, Atkinson RH, Waugh P (1985) Response of Clay-Unit Masonry to Repeated Compressive Forces. In: 7th International Brick and Block Masonry Conference. Melbourne, Australia, pp 565–576

Acikgoz S, DeJong MJ., Kechavarzi C, Soga K (2018a) Dynamic response of a damaged masonry rail viaduct: Measurement and interpretation. Engineering Structures 168:544–558. https://doi.org/10.1016/j.engstruct.2018.04.054

Acikgoz S, DeJong MJ, Soga K (2018b) Sensing dynamic displacements in masonry rail bridges using 2D digital image correlation. Structural Control and Health Monitoring 25:e2187. https://doi.org/10.1002/stc.2187

Acikgoz S, Fidler PRA, Pascariello MN, et al (2021) A Fibre-optic Strain Measurement System to Monitor the Impact of Tunnelling on Nearby Heritage Masonry Buildings. International Journal of Architectural Heritage 1–19. https://doi.org/10.1080/15583058.2021.1884318

Acito M, Chesi C, Milani G, Torri S (2016) Collapse analysis of the Clock and Fortified towers of Finale Emilia, Italy, after the 2012 Emilia Romagna seismic sequence: Lesson learned and reconstruction hypotheses. Construction and Building Materials 115:193–213. https://doi.org/10.1016/j.conbuildmat.2016.03.220

Adhikari RK, D'Ayala D (2020) 2015 Nepal earthquake: seismic performance and post-earthquake reconstruction of stone in mud mortar masonry buildings. Bulletin of Earthquake Engineering 18:3863–3896. https://doi.org/10.1007/s10518-020-00834-y

Alberto A, Antonaci P, Valente S (2011) Damage analysis of brick-to-mortar interfaces. Procedia Engineering 10:1151–1156. https://doi.org/10.1016/j.proeng.2011.04.191

Alessandri C, Garutti M, Mallardo V, Milani G (2015) Crack Patterns Induced by Foundation Settlements: Integrated Analysis on a Renaissance Masonry Palace in Italy. International Journal of Architectural Heritage 9:111–129. https://doi.org/10.1080/15583058.2014.951795

Ali L (2019) Damage Detection and Localization in Masonry Structure Using Faster Region Convolutional Networks. International Journal of GEOMATE 17:98–105. https://doi.org/10.21660/2019.59.8272

Alipour M, Harris DK (2020) Increasing the robustness of material-specific deep learning

models for crack detection across different materials. Engineering Structures 206:110157. https://doi.org/10.1016/j.engstruct.2019.110157

Alipour M, Harris DK, Miller GR (2019) Robust Pixel-Level Crack Detection Using Deep Fully Convolutional Neural Networks. Journal of Computing in Civil Engineering 33:04019040. https://doi.org/10.1061/(ASCE)CP.1943-5487.0000854

Andreotti G, Graziotti F, Magenes G (2018) Detailed micro-modelling of the direct shear tests of brick masonry specimens: The role of dilatancy. Engineering Structures 168:929–949. https://doi.org/10.1016/j.engstruct.2018.05.019

Andreotti G, Graziotti F, Magenes G (2019) Expansion of mortar joints in direct shear tests of masonry samples: implications on shear strength and experimental characterization of dilatancy. Materials and Structures 52:64. https://doi.org/10.1617/s11527-019-1366-5

Anthoine A, Magonette G, Magenes G (1995) Shear-compression testing and analysis of brick masonry walls. In: Gerald Duma E (ed) Proceedings of 10th European Conference on Earthquake Engineering. pp 1657–1662

Aref AJ, Dolatshahi KM (2013) A three-dimensional cyclic meso-scale numerical procedure for simulation of unreinforced masonry structures. Computers & Structures 120:9–23. https://doi.org/10.1016/j.compstruc.2013.01.012

Arslan O, Messali F, Smyrou E, et al (2021) Experimental characterization of the axial behavior of traditional masonry wall metal tie connections in cavity walls. Construction and Building Materials 266:121141. https://doi.org/10.1016/j.conbuildmat.2020.121141

ARTEMIS (2016) Software for Operational Modal Analysis and Experimental Modal Analysis. https://svibs.com/. Accessed 30 Jun 2021

ASCE (2017) Minimum Design Loads and Associated Criteria for Buildings and Other Structures, ASCE/SEI 7. American Society of Civil Engineers, Reston, VA

Aschheim M, Black E (1999) Effects of Prior Earthquake Damage on Response of Simple Stiffness-Degrading Structures. Earthquake Spectra 15:1–24. https://doi.org/10.1193/1.1586026

Asteris PG, Sarhosis V, Mohebkhah A, et al (2015) Numerical Modeling of Historic Masonry Structures. In: Asteris PG, Plevris V (eds) Handbook of Research on Seismic Assessment and Rehabilitation of Historic Structures. IGI Global, pp 213–256

Baisch S, Koch C, Muntendam-Bos A (2019) Traffic Light Systems: To What Extent Can Induced Seismicity Be Controlled? Seismological Research Letters 90:1145–1154. https://doi.org/10.1785/0220180337

Bal İE (2018) Myths and fallacies in the Groningen earthquake problem

Bal İE, Dais D, Smyrou E (2018) 'Differences' Between Induced and Natural Seismic Events. In: 16th European Conference on Earthquake Engineering (ECEE 2018). Thessaloniki, Greece

Bal İE, Dais D, Smyrou E, Sarhosis V (2021a) Monitoring of a Historical Masonry Structure in Case of Induced Seismicity. International Journal of Architectural Heritage 15:187–204. https://doi.org/10.1080/15583058.2020.1719230

Bal İE, Dais D, Smyrou E, Sarhosis V (2021b) Novel invisible markers for monitoring cracks on masonry structures. Construction and Building Materials 300:124013. https://doi.org/10.1016/j.conbuildmat.2021.124013

Bal İE, Smyrou E (2019a) Unprocessed Accelerometer Data from Fraeylemaborg, Slochteren, during 22.05.2019 Westerwijtwerd Earthquake of ML3.4

Bal İE, Smyrou E (2019b) Unprocessed Accelerometer and Tiltmeter Data from Fraeylemaborg, Slochteren, during 08.08.2018 Appingedam Earthquake of ML1.9

Bal İE, Smyrou E, Bulder E (2019a) Liability and damage claim issues in induced earthquakes: case of Groningen. In: SECED 2019 Conference. Greenwich, UK

Bal İE, Smyrou E, Dais D (2019b) Comparison of polarity in Groningen data with that of other natural and induced seismicity records, and implications in hazard and risk models. Bulletin of Earthquake Engineering 17:4457–4474. https://doi.org/10.1007/s10518-018-0517-3

Bang S, Park S, Kim H, Kim H (2019) Encoder–decoder network for pixel-level road crack detection in black-box images. Computer-Aided Civil and Infrastructure Engineering 34:713–727. https://doi.org/10.1111/mice.12440

Barattucci S, Sarhosis V, Bruno AW, et al (2020) An experimental and numerical study on masonry triplets subjected to monotonic and cyclic shear loadings. Construction and Building Materials 254:119313. https://doi.org/10.1016/j.conbuildmat.2020.119313

Basma AA, Al-Homoud AS, Husein A (1995) Laboratory assessment of swelling pressure of expansive soils. Applied Clay Science 9:355–368. https://doi.org/10.1016/0169-1317(94)00032-L

Bejarano-Urrego L, Verstrynge E, Giardina G, Van Balen K (2018) Crack growth in masonry: Numerical analysis and sensitivity study for discrete and smeared crack modelling. Engineering Structures 165:471–485. https://doi.org/10.1016/j.engstruct.2018.03.030

Bertolesi E, Milani G, Fagone M, et al (2018) Micro-mechanical FE numerical model for masonry curved pillars reinforced with FRP strips subjected to single lap shear tests. Composite Structures 201:916–931. https://doi.org/10.1016/j.compstruct.2018.06.111

Beyer K, Mergos P (2015) Sensitivity of drift capacities of URM Walls to Cumulative Damage Demands and Implication on Loading Protocols for Quasi-Static Cyclic Tests. In: 12th North American Masonry Conference. Denver, Colorado, USA

Beyer K, Petry S, Tondelli M, Paparo A (2014) Towards Displacement-Based Seismic Design of Modern Unreinforced Masonry Structures. In: Ansal A (ed) Perspectives on European Earthquake Engineering and Seismology. Geotechnical, Geological and Earthquake Engineering. Springer International Publishing, Cham, pp 401–428

Blyth A, Napolitano R, Glisic B (2019) Documentation, structural health monitoring and numerical modelling for damage assessment of the Morris Island Lighthouse. Philosophical Transactions of the Royal Society A: Mathematical, Physical and Engineering Sciences 377:20190002. https://doi.org/10.1098/rsta.2019.0002

Bolhassani M, Hamid AA, Rajaram S, et al (2017) Failure analysis and damage detection of partially grouted masonry walls by enhancing deformation measurement using DIC. Engineering Structures 134:262–275. https://doi.org/10.1016/j.engstruct.2016.12.019

Bouma J (1980) Field measurement of soil hydraulic properties characterizing water movement through swelling clay soils. Journal of Hydrology 45:149–158. https://doi.org/10.1016/0022-1694(80)90011-6

Brackenbury D, Brilakis I, DeJong M (2019) Automated Defect Detection For Masonry Arch Bridges. In: International Conference on Smart Infrastructure and Construction 2019

(ICSIC). ICE Publishing, pp 3–9

Brincker R, Zhang L, Andersen P (2001) Modal identification of output-only systems using frequency domain decomposition. Smart Materials and Structures 10:441–445. https://doi.org/10.1088/0964-1726/10/3/303

Bui TT, Limam A, Sarhosis V, Hjiaj M (2017) Discrete element modelling of the in-plane and out-of-plane behaviour of dry-joint masonry wall constructions. Engineering Structures 136:277–294. https://doi.org/10.1016/j.engstruct.2017.01.020

Burland JB, Broms BB, De Mello VFB (1977) Behaviour of foundations and structures. In: 9th International Conference on Soil Mechanics and Foundation Engineering. Tokyo, Japan, pp 495–546

Burland JB, Wroth CP (1974) Settlement of Buildings and Associated Damage. In: British Geotechnical Society's Conference on the settlement of structures. Cambridge, UK, pp 611–654

Çaktı E, Şafak E (2019) Structural Health Monitoring: Lessons Learned. In: Kasimzade AA, Şafak E, Ventura CE, et al. (eds) Seismic Isolation, Structural Health Monitoring, and Performance Based Seismic Design in Earthquake Engineering. Springer International Publishing, Cham, pp 145–164

Çaktı E, Saygılı Ö, Lemos J V., Oliveira CS (2016) Discrete element modeling of a scaled masonry structure and its validation. Engineering Structures 126:224–236. https://doi.org/10.1016/j.engstruct.2016.07.044

Çaktı E, Saygılı Ö, Lemos J V., Oliveira CS (2020) Nonlinear dynamic response of stone masonry minarets under harmonic excitation. Bulletin of Earthquake Engineering 18:4813–4838. https://doi.org/10.1007/s10518-020-00888-y

Calderini C, Abbati SD, Cotič P, et al (2015) In-plane shear tests on masonry panels with plaster: correlation of structural damage and damage on artistic assets. Bulletin of Earthquake Engineering 13:237–256. https://doi.org/10.1007/s10518-014-9632-y

Calvi GM (1999) A displacement-based approach for vulnerability evaluation of classes of buildings. Journal of Earthquake Engineering 3:411–438. https://doi.org/10.1080/13632469909350353

Carrillo J, Alcocer SM (2012) Acceptance limits for performance-based seismic design of RC walls for low-rise housing. Earthquake Engineering & Structural Dynamics 41:2273–2288. https://doi.org/10.1002/eqe.2186

Carrillo J, Dominguez D, Prado N (2017) Seismic Damage Index Based on Fractal Dimension of Cracking on Thin Reinforced Concrete Walls. ACI Structural Journal 114:. https://doi.org/10.14359/51700919

Casolo S (2017) A numerical study on the cumulative out-of-plane damage to church masonry façades due to a sequence of strong ground motions. Earthquake Engineering & Structural Dynamics 46:2717–2737. https://doi.org/10.1002/eqe.2927

Castellazzi G, D'Altri AM, de Miranda S, Ubertini F (2017) An innovative numerical modeling strategy for the structural analysis of historical monumental buildings. Engineering Structures 132:229–248. https://doi.org/10.1016/j.engstruct.2016.11.032

Ceravolo R, De Marinis A, Pecorelli ML, Zanotti Fragonara L (2017) Monitoring of masonry historical constructions: 10 years of static monitoring of the world's largest oval dome. Structural Control and Health Monitoring 24:e1988. https://doi.org/10.1002/stc.1988

Cha Y-J, Choi W, Büyüköztürk O (2017) Deep Learning-Based Crack Damage Detection Using Convolutional Neural Networks. Computer-Aided Civil and Infrastructure Engineering 32:361–378. https://doi.org/10.1111/mice.12263

Cha Y-J, Choi W, Suh G, et al (2018) Autonomous Structural Visual Inspection Using Region-Based Deep Learning for Detecting Multiple Damage Types. Computer-Aided Civil and Infrastructure Engineering 33:731–747. https://doi.org/10.1111/mice.12334

Chácara C, Mendes N, Lourenço PB (2017) Simulation of Shake Table Tests on Out-Of-Plane Masonry Buildings. Part (IV): Macro and Micro FEM Based Approaches. International Journal of Architectural Heritage 11:103–116. https://doi.org/10.1080/15583058.2016.1238972

Chai YH (2005) Incorporating low-cycle fatigue model into duration-dependent inelastic design spectra. Earthquake Engineering & Structural Dynamics 34:83–96. https://doi.org/10.1002/eqe.422

Chaimoon K, Attard MM (2007) Modeling of unreinforced masonry walls under shear and compression. Engineering Structures 29:2056–2068. https://doi.org/10.1016/j.engstruct.2006.10.019

Chambon S, Moliard J-M (2011) Automatic Road Pavement Assessment with Image Processing: Review and Comparison. International Journal of Geophysics 2011:1–20. https://doi.org/10.1155/2011/989354

Chen H, Lin H, Yao M (2019) Improving the Efficiency of Encoder-Decoder Architecture for Pixel-Level Crack Detection. IEEE Access 7:186657–186670. https://doi.org/10.1109/ACCESS.2019.2961375

Chen L-C, Papandreou G, Kokkinos I, et al (2018a) DeepLab: Semantic Image Segmentation with Deep Convolutional Nets, Atrous Convolution, and Fully Connected CRFs. IEEE Transactions on Pattern Analysis and Machine Intelligence 40:834–848. https://doi.org/10.1109/TPAMI.2017.2699184

Chen L-C, Zhu Y, Papandreou G, et al (2018b) Encoder-Decoder with Atrous Separable Convolution for Semantic Image Segmentation. In: Ferrari V, Hebert M, Sminchisescu C, Weiss Y (eds) Computer Vision – ECCV 2018. ECCV 2018. Lecture Notes in Computer Science. Springer, Cham, pp 833–851

Cho H, Yoon H-J, Jung J-Y (2018) Effects of the Ground Resolution and Thresholding on Crack Width Measurements. Sensors 18:2644. https://doi.org/10.3390/s18082644

Choi W, Cha Y-J (2020) SDDNet: Real-Time Crack Segmentation. IEEE Transactions on Industrial Electronics 67:8016–8025. https://doi.org/10.1109/TIE.2019.2945265

Chollet F (2017) Deep Learning with Python. Manning Publications Co.

Chollet F (2015) Keras. https://keras.io. Accessed 1 Oct 2020

Cigada A, Corradi Dell'Acqua L, Mörlin Visconti Castiglione B, et al (2017) Structural Health Monitoring of an Historical Building: The Main Spire of the Duomo Di Milano. International Journal of Architectural Heritage 11:501–518. https://doi.org/10.1080/15583058.2016.1263691

Coïsson E, Blasi C (2015) Monitoring the French Panthéon: From Rondelet's Historical Surveys to the Modern Automatic System. International Journal of Architectural Heritage 9:48–57. https://doi.org/10.1080/15583058.2013.793437

Crowley H, Pinho R (2017) Report on the v5 fragility and consequence models for the

Groningen Field

Crowley H, Pinho R, Polidoro B, van Elk J (2017) Developing fragility and consequence models for buildings in the Groningen field. Netherlands Journal of Geosciences 96:s247–s257. https://doi.org/10.1017/njg.2017.36

Cundall PA (1971) A computer model for simulating progressive large scale movements in blocky rock systems. In: Proc. Symp. Int. Soc. Rock Mech, Nancy

Cundall PA, Hart RD (1993) Numerical Modeling of Discontinua. In: Analysis and Design Methods. Elsevier, pp 231–243

D'Altri AM, de Miranda S, Castellazzi G, Sarhosis V (2018a) A 3D detailed micro-model for the in-plane and out-of-plane numerical analysis of masonry panels. Computers & Structures 206:18–30. https://doi.org/10.1016/j.compstruc.2018.06.007

D'Altri AM, Messali F, Rots J, et al (2019a) A damaging block-based model for the analysis of the cyclic behaviour of full-scale masonry structures. Engineering Fracture Mechanics 209:423–448. https://doi.org/10.1016/j.engfracmech.2018.11.046

D'Altri AM, Milani G, de Miranda S, et al (2018b) Stability analysis of leaning historic masonry structures. Automation in Construction 92:199–213. https://doi.org/10.1016/j.autcon.2018.04.003

D'Altri AM, Sarhosis V, Milani G, et al (2019b) Modeling Strategies for the Computational Analysis of Unreinforced Masonry Structures: Review and Classification. Archives of Computational Methods in Engineering. https://doi.org/10.1007/s11831-019-09351-x

D'Altri AM, Sarhosis V, Milani G, et al (2020) Modeling Strategies for the Computational Analysis of Unreinforced Masonry Structures: Review and Classification. Archives of Computational Methods in Engineering 27:1153–1185. https://doi.org/10.1007/s11831-019-09351-x

Dais D, Bal İE, Smyrou E (2017) DISCUSSION ON THE RESPONSE OF UNREINFORCED MASONRY TO LOW-AMPLITUDE RECURCIVE LOADS: CASE OF GRONINGEN GAS FIELD. In: Proceedings of the 6th International Conference on Computational Methods in Structural Dynamics and Earthquake Engineering (COMPDYN 2015). Institute of Structural Analysis and Antiseismic Research School of Civil Engineering National Technical University of Athens (NTUA) Greece, Athens, pp 5084–5092

Dais D, Bal İE, Smyrou E, Sarhosis V (2021a) Automatic crack classification and segmentation on masonry surfaces using convolutional neural networks and transfer learning. Automation in Construction 125:103606. https://doi.org/10.1016/j.autcon.2021.103606

Dais D, Sarhosis V, Smyrou E, et al (2019a) Investigations On The Restoration And Seismic Enhancement Options For The Jaisedewal Temple After The Gorkha Earthquake In Nepal. In: SECED 2019 Conference. Greenwich, UK

Dais D, Sarhosis V, Smyrou E, Bal İE (2021b) Seismic intervention options for multi-tiered Nepalese Pagodas: The case study of Jaisedewal temple. Engineering Failure Analysis 123:105262. https://doi.org/10.1016/j.engfailanal.2021.105262

Dais D, Smyrou E, Bal IE, Pama J (2019b) Monitoring, Assessment and Diagnosis of Fraeylemaborg in Groningen, Netherlands. In: Aguilar R., Torrealva D., Moreira S., Pando M.A., Ramos L.F. (eds) Structural Analysis of Historical Constructions. RILEM Bookseries, vol 18. Springer, Cham. pp 2188–2196

David Jenkins M, Carr TA, Iglesias MI, et al (2018) A Deep Convolutional Neural Network for Semantic Pixel-Wise Segmentation of Road and Pavement Surface Cracks. In: 2018 26th European Signal Processing Conference (EUSIPCO). IEEE, Rome, Italy, pp 2120–2124

Davoudi R, Miller GR, Kutz JN (2018) Data-driven vision-based inspection for reinforced concrete beams and slabs: Quantitative damage and load estimation. Automation in Construction 96:292–309. https://doi.org/10.1016/j.autcon.2018.09.024

de Felice G, De Santis S, Lourenço PB, Mendes N (2016) Methods and Challenges for the Seismic Assessment of Historic Masonry Structures. International Journal of Architectural Heritage 11:1–18. https://doi.org/10.1080/15583058.2016.1238976

Di Sarno L (2013) Effects of multiple earthquakes on inelastic structural response. Engineering Structures 56:673–681. https://doi.org/10.1016/j.engstruct.2013.05.041

Didier M, Abbiati G, Broccardo M, et al (2017) Quantification of non-structural damage in unreinforced masonry walls induced by geothermal reservoir exploration using quasi-static cyclic tests. In: 13th Canadian Masonry Symposium. Halifax, Canada

Dolatshahi KM, Aref AJ (2016) Multi-directional response of unreinforced masonry walls: experimental and computational investigations. Earthquake Engineering & Structural Dynamics 45:1427–1449. https://doi.org/10.1002/eqe.2714

Dolatshahi KM, Aref AJ, Yekrangnia M (2014) Bidirectional behavior of unreinforced masonry walls. Earthquake Engineering & Structural Dynamics 43:2377–2397. https://doi.org/10.1002/eqe.2455

Dolatshahi KM, Beyer K (2019) Stiffness and Strength Estimation of Damaged Unreinforced Masonry Walls Using Crack Pattern. Journal of Earthquake Engineering. https://doi.org/10.1080/13632469.2019.1693446

Dolatshahi KM, Nikoukalam MT, Beyer K (2018) Numerical study on factors that influence the in-plane drift capacity of unreinforced masonry walls. Earthquake Engineering & Structural Dynamics 47:1440–1459. https://doi.org/10.1002/eqe.3024

Dorafshan S, Thomas RJ, Maguire M (2018) Comparison of deep convolutional neural networks and edge detectors for image-based crack detection in concrete. Construction and Building Materials 186:1031–1045. https://doi.org/10.1016/j.conbuildmat.2018.08.011

Drougkas A, Licciardello L, Rots JG, Esposito R (2020) In-plane seismic behaviour of retrofitted masonry walls subjected to subsidence-induced damage. Engineering Structures 223:111192. https://doi.org/10.1016/j.engstruct.2020.111192

Dung CV, Anh LD (2019) Autonomous concrete crack detection using deep fully convolutional neural network. Automation in Construction 99:52–58. https://doi.org/10.1016/j.autcon.2018.11.028

Ebrahimkhanlou A, Athanasiou A, Hrynyk TD, et al (2019) Fractal and Multifractal Analysis of Crack Patterns in Prestressed Concrete Girders. Journal of Bridge Engineering 24:04019059. https://doi.org/10.1061/(ASCE)BE.1943-5592.0001427

EC8-3 (2005) Eurocode 8: Design of structures for earthquake resistance – Part 3: Assessment and retrofitting of buildings. EN 1998-3:2005

Ehresman R, Taylor N, Pulatsu B, Erdogmus E (2021) Discrete Rigid Block Analysis to Assess Settlement Induced Damage in Unreinforced Masonry Façades. CivilEng 2:541–

555. https://doi.org/10.3390/civileng2030030

Elnashai AS, Di Sarno L (2008) Fundamentals of Earthquake Engineering. Wiley

EN-1998-1 (2005) Eurocode 8, Design of Structures for Earthquake Resistance, Part 1: General rules, seismic actions and rules for buildings. European Committee for Standardization, Brussels

EN 1015-11 (1999) European standard: Methods of test for mortar for masonry - Part 11: Determination of flexural and compressive strength of hardened mortar. CEN, Brussels

EN 1015-5 (2005) European standard: Methods of test for masonry units - Part 11: Determination of bond strength by the bond wrench method. CEN, Brussels.

EN 772-1 (2000) European standard: Methods of test for masonry units - Part 1: Determination of compressive strength. CEN, Brussels

Erdik M (2019) Seismic Isolation, Structural Health Monitoring, and Performance Based Seismic Design in Earthquake Engineering. Springer International Publishing, Cham

Erdogmus E, Pulatsu B, Gaggioli A, Hoff M (2020) Reverse Engineering a Fully Collapsed Ancient Roman Temple through Geoarchaeology and DEM. International Journal of Architectural Heritage 00:1–21. https://doi.org/10.1080/15583058.2020.1728593

Esposito R, Messali F, Ravenshorst GJP, et al (2019) Seismic assessment of a lab-tested two-storey unreinforced masonry Dutch terraced house. Bulletin of Earthquake Engineering 17:4601–4623. https://doi.org/10.1007/s10518-019-00572-w

Esposito R, Terwel K, Ravenshorst G, et al (2016) Cyclic pushover test on an unreinforced masonry structure resembling a typical Dutch terraced house. In: 16th World Conference on Earthquake. Santiago, Chile

Falconer K (2003) Fractal Geometry: Mathematical Foundations and Applications. John Wiley & Sons, Ltd, Chichester, UK

Fang DL, Napolitano RK, Michiels TL, Adriaenssens SM (2019) Assessing the stability of unreinforced masonry arches and vaults: a comparison of analytical and numerical strategies. International Journal of Architectural Heritage 13:648–662. https://doi.org/10.1080/15583058.2018.1463413

Farhidzadeh A, Dehghan-Niri E, Moustafa A, et al (2013) Damage Assessment of Reinforced Concrete Structures Using Fractal Analysis of Residual Crack Patterns. Experimental Mechanics 53:1607–1619. https://doi.org/10.1007/s11340-013-9769-7

FEMA (2000) FEMA-356: Prestandard and Commentary for the Seismic Rehabilitation of Buildings. FEMA, Washington, D.C.

FEMA 307 (1998) Evaluation of Earthquake Damaged Concrete and Masonry Wall Buildings: Technical Resources. The Applied Technology Council

Feng C, Zhang H, Wang S, et al (2019) Structural Damage Detection using Deep Convolutional Neural Network and Transfer Learning. KSCE Journal of Civil Engineering 23:4493–4502. https://doi.org/10.1007/s12205-019-0437-z

Ferrante A, Giordano E, Clementi F, et al (2021a) FE vs. DE Modeling for the Nonlinear Dynamics of a Historic Church in Central Italy. Geosciences 11:189. https://doi.org/10.3390/geosciences11050189

Ferrante A, Loverdos D, Clementi F, et al (2021b) Discontinuous approaches for nonlinear dynamic analyses of an ancient masonry tower. Engineering Structures 230:111626.

https://doi.org/10.1016/j.engstruct.2020.111626

Foulger GR, Wilson MP, Gluyas JG, et al (2018) Global review of human-induced earthquakes. Earth-Science Reviews 178:438–514. https://doi.org/10.1016/j.earscirev.2017.07.008

Fragiacomo M, Amadio C, Macorini L (2004) Seismic response of steel frames under repeated earthquake ground motions. Engineering Structures 26:2021–2035. https://doi.org/10.1016/j.engstruct.2004.08.005

Frumento S, Magenes G, Morandi P, Calvi GM (2009) Interpretation of experimental shear tests on clay brick masonry walls and evaluation of q-factors for seismic design

Fugro (2018) Geotechnisch onderzoek FRAEYLEMABORG TE SLOCHTEREN. Report No.: 1318-0270-000

Gambarotta L, Lagomarsino S (1997a) Damage models for the seismic response of brick masonry shear walls. Part II: The continuum model and its applications. Earthquake Engineering and Structural Dynamics 26:423–439

Gambarotta L, Lagomarsino S (1997b) Damage models for the seismic response of brick masonry shear walls. Part I: The mortar joint model and its applications. Earthquake Engineering and Structural Dynamics 26:423–439

Gao Y, Mosalam KM (2018) Deep Transfer Learning for Image-Based Structural Damage Recognition. Computer-Aided Civil and Infrastructure Engineering 33:748–768. https://doi.org/10.1111/mice.12363

Garcia-Garcia A, Orts-Escolano S, Oprea S, et al (2018) A survey on deep learning techniques for image and video semantic segmentation. Applied Soft Computing 70:41–65. https://doi.org/10.1016/j.asoc.2018.05.018

Gentile C, Ruccolo A, Canali F (2019) Long-term monitoring for the condition-based structural maintenance of the Milan Cathedral. Construction and Building Materials 228:117101. https://doi.org/10.1016/j.conbuildmat.2019.117101

Germanese D, Leone G, Moroni D, et al (2018) Long-Term Monitoring of Crack Patterns in Historic Structures Using UAVs and Planar Markers: A Preliminary Study. Journal of Imaging 4:99. https://doi.org/10.3390/jimaging4080099

Ghorbani R, Matta F, Sutton MA (2015) Full-Field Deformation Measurement and Crack Mapping on Confined Masonry Walls Using Digital Image Correlation. Experimental Mechanics 55:227–243. https://doi.org/10.1007/s11340-014-9906-y

Giamundo V, Sarhosis V, Lignola GP, et al (2014) Evaluation of different computational modelling strategies for the analysis of low strength masonry structures. Engineering Structures 73:160–169. https://doi.org/10.1016/j.engstruct.2014.05.007

Giardina G, Hendriks MAN, Rots JG (2015) Sensitivity study on tunnelling induced damage to a masonry façade. Engineering Structures 89:111–129. https://doi.org/10.1016/j.engstruct.2015.01.042

Gilbert M (2009) Fatigue in railway bridges. In: Robinson M, Kapoor A (eds) Fatigue in Railway Infrastructure. Elsevier, pp 58–95

Giordano A, Mele E, De Luca A (2002) Modelling of historical masonry structures: comparison of different approaches through a case study. Engineering Structures 24:1057–1069. https://doi.org/10.1016/S0141-0296(02)00033-0

Godio M, Vanin F, Zhang S, Beyer K (2019) Quasi-static shear-compression tests on stone masonry walls with plaster: Influence of load history and axial load ratio. Engineering Structures 192:264–278. https://doi.org/10.1016/j.engstruct.2019.04.041

Gonçalves LMS, Rodrigues H, Gaspar F (2017) Nondestructive Techniques for the Assessment and Preservation of Historic Structures. CRC Press, Boca Raton

Graziotti F, Penna A, Magenes G (2019) A comprehensive in situ and laboratory testing programme supporting seismic risk analysis of URM buildings subjected to induced earthquakes. Bulletin of Earthquake Engineering 17:4575–4599. https://doi.org/10.1007/s10518-018-0478-6

Graziotti F, Rossi A, Mandirola M, et al (2016a) Experimental characterisation of calcium-silicate brick masonry for seismic assessment. CRC Press, Padova, Italy

Graziotti F, Tomassetti U, Kallioras S, et al (2017) Shaking table test on a full scale URM cavity wall building. Bulletin of Earthquake Engineering 15:5329–5364. https://doi.org/10.1007/s10518-017-0185-8

Graziotti F, Tomassetti U, Rossi A, et al (2015) Experimental campaign on cavity walls systems representative of the Groningen building stock. In: Report EUC318/2015U, EUCENTRE. www.eucentre.it/nam-project. Accessed 10 Oct 2020

Graziotti F, Tomassetti U, Rossi A, et al (2016b) Experimental campaign on a clay URM full-scale specimen representative of the Groningen building stock. In: Report EUC128/2016U, EUCENTRE. www.eucentre.it/nam-project. Accessed 10 Oct 2020

Greco F, Leonetti L, Luciano R, et al (2020) A detailed micro-model for brick masonry structures based on a diffuse cohesive-frictional interface fracture approach. Procedia Structural Integrity 25:334–347. https://doi.org/10.1016/j.prostr.2020.04.038

Grimaz S, Malisan P (2017) How could cumulative damage affect the macroseismic assessment? Bulletin of Earthquake Engineering 15:2465–2481. https://doi.org/10.1007/s10518-016-0016-3

Grottoli L, Kallioras S, Korswagen P, Graziotti F (2019) In-plane and out-of-plane quasi-static cyclic tests on unreinforced calcium-silicate masonry walls under high compressive load. Pavia, Italy

Hartley R, Zisserman A (2004) Multiple View Geometry in Computer Vision. Cambridge University Press

Hatzigeorgiou GD, Beskos DE (2009) Inelastic displacement ratios for SDOF structures subjected to repeated earthquakes. Engineering Structures 31:2744–2755. https://doi.org/10.1016/j.engstruct.2009.07.002

Hatzivassiliou M, Hatzigeorgiou GD (2015) Seismic sequence effects on three-dimensional reinforced concrete buildings. Soil Dynamics and Earthquake Engineering 72:77–88. https://doi.org/10.1016/j.soildyn.2015.02.005

He K, Gkioxari G, Dollar P, Girshick R (2017) Mask R-CNN. In: 2017 IEEE International Conference on Computer Vision (ICCV). IEEE, Venice, Italy, pp 2980–2988

He K, Zhang X, Ren S, Sun J (2016) Deep Residual Learning for Image Recognition. In: 2016 IEEE Conference on Computer Vision and Pattern Recognition (CVPR). IEEE, Las Vegas, NV, USA, pp 770–778

He M, Li Q, Li X (2020) Injection-Induced Seismic Risk Management Using Machine Learning Methodology – A Perspective Study. Frontiers in Earth Science 8:1–18.

https://doi.org/10.3389/feart.2020.00227

Heath DJ, Gad EF, Wilson JL (2008) Damage Thresholds in Unreinforced Masonry. Australian Journal of Structural Engineering 8:145–158. https://doi.org/10.1080/13287982.2008.11464994

Heerema P, Ashour A, Shedid M, El-Dakhakhni W (2015) System-Level Displacement- and Performance-Based Seismic Design Parameter Quantifications for an Asymmetrical Reinforced Concrete Masonry Building. Journal of Structural Engineering 141:04015032. https://doi.org/10.1061/(ASCE)ST.1943-541X.0001258

Hoskere V, Narazaki Y, Hoang TA, Spencer BF (2020) MaDnet: multi-task semantic segmentation of multiple types of structural materials and damage in images of civil infrastructure. Journal of Civil Structural Health Monitoring 10:757–773. https://doi.org/10.1007/s13349-020-00409-0

Howard AG, Zhu M, Chen B, et al (2017) MobileNets: Efficient Convolutional Neural Networks for Mobile Vision Applications. ArXiv

Huang G, Liu Z, Van Der Maaten L, Weinberger KQ (2017a) Densely Connected Convolutional Networks. In: 2017 IEEE Conference on Computer Vision and Pattern Recognition (CVPR). IEEE, Honolulu, HI, USA, pp 2261–2269

Huang J, Rathod V, Sun C, et al (2017b) Speed/Accuracy Trade-Offs for Modern Convolutional Object Detectors. In: 2017 IEEE Conference on Computer Vision and Pattern Recognition (CVPR). IEEE, Honolulu, HI, USA, pp 3296–3297

Ibrahim Y, Nagy B, Benedek C (2019) CNN-Based Watershed Marker Extraction for Brick Segmentation in Masonry Walls. In: Karray F, Campilho A, Yu A (eds) Image Analysis and Recognition. ICIAR 2019. Springer, Cham, pp 332–344

Iervolino I, Chioccarelli E, Suzuki A (2020) Seismic damage accumulation in multiple mainshock–aftershock sequences. Earthquake Engineering & Structural Dynamics 49:1007–1027. https://doi.org/10.1002/eqe.3275

Iervolino I, Giorgio M, Chioccarelli E (2013) Gamma degradation models for earthquake-resistant structures. Structural Safety 45:48–58. https://doi.org/10.1016/j.strusafe.2013.09.001

ITASCA (2011) UDEC—universal distinct element code manual: theory and background. Itasca Consulting Group, Minneapolis

Kalfarisi R, Wu ZY, Soh K (2020) Crack Detection and Segmentation Using Deep Learning with 3D Reality Mesh Model for Quantitative Assessment and Integrated Visualization. Journal of Computing in Civil Engineering 34:04020010. https://doi.org/10.1061/(ASCE)CP.1943-5487.0000890

Kallioras S, Correia AA, Graziotti F, et al (2020) Collapse shake-table testing of a clay-URM building with chimneys. Bulletin of Earthquake Engineering 18:1009–1048. https://doi.org/10.1007/s10518-019-00730-0

Kallioras S, Guerrini G, Tomassetti U, et al (2018) Experimental seismic performance of a full-scale unreinforced clay-masonry building with flexible timber diaphragms. Engineering Structures 161:231–249. https://doi.org/10.1016/j.engstruct.2018.02.016

Kang D, Benipal SS, Gopal DL, Cha Y (2020) Hybrid pixel-level concrete crack segmentation and quantification across complex backgrounds using deep learning. Automation in Construction 118:103291. https://doi.org/10.1016/j.autcon.2020.103291

Kassotakis N, Sarhosis V, Peppa MV, Mills J (2021) Quantifying the effect of geometric uncertainty on the structural behaviour of arches developed from direct measurement and Structure-from-Motion (SfM) photogrammetry. Engineering Structures 230:111710. https://doi.org/10.1016/j.engstruct.2020.111710

Kassotakis N, Sarhosis V, Riveiro B, et al (2020) Three-dimensional discrete element modelling of rubble masonry structures from dense point clouds. Automation in Construction 119:103365. https://doi.org/10.1016/j.autcon.2020.103365

Kim I-H, Jeon H, Baek S-C, et al (2018) Application of Crack Identification Techniques for an Aging Concrete Bridge Inspection Using an Unmanned Aerial Vehicle. Sensors 18:1881. https://doi.org/10.3390/s18061881

Kingma DP, Ba JL (2015) Adam: A method for stochastic optimization. In: 3rd International Conference on Learning Representations (ICLR 2015). San Diego, USA

Kita A, Cavalagli N, Masciotta MG, et al (2020) Rapid post-earthquake damage localization and quantification in masonry structures through multidimensional non-linear seismic IDA. Engineering Structures 219:110841. https://doi.org/10.1016/j.engstruct.2020.110841

Kita A, Cavalagli N, Ubertini F (2019) Temperature effects on static and dynamic behavior of Consoli Palace in Gubbio, Italy. Mechanical Systems and Signal Processing 120:180–202. https://doi.org/10.1016/j.ymssp.2018.10.021

KNMI (1993) Netherlands seismic and acoustic network. Royal Netherlands Meteorological Institute (KNMI)

Konig J, David Jenkins M, Barrie P, et al (2019) A Convolutional Neural Network for Pavement Surface Crack Segmentation Using Residual Connections and Attention Gating. In: 2019 IEEE International Conference on Image Processing (ICIP). IEEE, Taipei, Taiwan, pp 1460–1464

Korswagen PA, Longo M, Meulman E, Rots JG (2019) Crack initiation and propagation in unreinforced masonry specimens subjected to repeated in-plane loading during light damage. Bulletin of Earthquake Engineering 17:4651–4687. https://doi.org/10.1007/s10518-018-00553-5

Korswagen PA, Longo M, Rots JG (2020a) Calcium silicate against clay brick masonry: an experimental comparison of the in-plane behaviour during light damage. Bulletin of Earthquake Engineering 18:2759–2781. https://doi.org/10.1007/s10518-020-00803-5

Korswagen PA, Longo M, Rots JG (2020b) High-resolution monitoring of the initial development of cracks in experimental masonry shear walls and their reproduction in finite element models. Engineering Structures 211:110365. https://doi.org/10.1016/j.engstruct.2020.110365

Kouris LAS, Penna A, Magenes G (2019) Dynamic Modification and Damage Propagation of a Two-Storey Full-Scale Masonry Building. Advances in Civil Engineering 2019:1–21. https://doi.org/10.1155/2019/2396452

Kumar N, Barbato M (2019) New Constitutive Model for Interface Elements in Finite-Element Modeling of Masonry. Journal of Engineering Mechanics 145:04019022. https://doi.org/10.1061/(asce)em.1943-7889.0001592

Laefer DF, Gannon J, Deely E (2010) Reliability of Crack Detection Methods for Baseline Condition Assessments. Journal of Infrastructure Systems 16:129–137.

https://doi.org/10.1061/(ASCE)1076-0342(2010)16:2(129)

Larbi JA (2004) Microscopy applied to the diagnosis of the deterioration of brick masonry. Construction and Building Materials 18:299–307. https://doi.org/10.1016/j.conbuildmat.2004.02.002

Lattanzi D, Miller GR, Eberhard MO, Haraldsson OS (2016) Bridge Column Maximum Drift Estimation via Computer Vision. Journal of Computing in Civil Engineering 30:04015051. https://doi.org/10.1061/(ASCE)CP.1943-5487.0000527

Lemos J V. (2007) Discrete Element Modeling of Masonry Structures. International Journal of Architectural Heritage 1:190–213. https://doi.org/10.1080/15583050601176868

Li D, Zhou Z, Ou J (2011) Development and sensing properties study of FRP–FBG smart stay cable for bridge health monitoring applications. Measurement 44:722–729. https://doi.org/10.1016/j.measurement.2011.01.005

Li, Ma, He, et al (2020) Automatic Tunnel Crack Detection Based on U-net and a Convolutional Neural Network with Alternately Updated Clique. Sensors 20:717. https://doi.org/10.3390/s20030717

Li S, Zhao X, Zhou G (2019) Automatic pixel-level multiple damage detection of concrete structure using fully convolutional network. Computer-Aided Civil and Infrastructure Engineering 34:616–634. https://doi.org/10.1111/mice.12433

Li Y, Li H, Wang H (2018) Pixel-Wise Crack Detection Using Deep Local Pattern Predictor for Robot Application. Sensors 18:3042. https://doi.org/10.3390/s18093042

Lin E, Chen Q, Ozdemir OC, et al (2019) Effects of Interface Bonding on the Residual Stresses in Cold-Sprayed Al-6061: A Numerical Investigation. Journal of Thermal Spray Technology 28:472–483. https://doi.org/10.1007/s11666-019-00827-7

Lin T-Y, Dollar P, Girshick R, et al (2017) Feature Pyramid Networks for Object Detection. In: 2017 IEEE Conference on Computer Vision and Pattern Recognition (CVPR). IEEE, Honolulu, HI, USA, pp 936–944

Lin T-Y, Goyal P, Girshick R, et al (2020) Focal Loss for Dense Object Detection. IEEE Transactions on Pattern Analysis and Machine Intelligence 42:318–327. https://doi.org/10.1109/TPAMI.2018.2858826

Liu S, Deng W (2015) Very deep convolutional neural network based image classification using small training sample size. In: 2015 3rd IAPR Asian Conference on Pattern Recognition (ACPR). IEEE, San Diego, USA, pp 730–734

Liu W, Anguelov D, Erhan D, et al (2016) SSD: Single Shot MultiBox Detector. In: Leibe B, Matas J, Sebe N, Welling M (eds) Computer Vision – ECCV 2016. ECCV 2016. Lecture Notes in Computer Science. Springer, Cham, pp 21–37

Liu Y, Yao J, Lu X, et al (2019a) DeepCrack: A deep hierarchical feature learning architecture for crack segmentation. Neurocomputing 338:139–153. https://doi.org/10.1016/j.neucom.2019.01.036

Liu Z, Cao Y, Wang Y, Wang W (2019b) Computer vision-based concrete crack detection using U-net fully convolutional networks. Automation in Construction 104:129–139. https://doi.org/10.1016/j.autcon.2019.04.005

Liu Z, Crewe A (2020) Effects of size and position of openings on in-plane capacity of unreinforced masonry walls. Bulletin of Earthquake Engineering 18:4783–4812. https://doi.org/10.1007/s10518-020-00894-0

Long J, Shelhamer E, Darrell T (2015) Fully convolutional networks for semantic segmentation. In: 2015 IEEE Conference on Computer Vision and Pattern Recognition (CVPR). IEEE, Boston, MA, USA, pp 3431–3440

Lourenço PB (1996) Computational strategies for masonry structures

Maeda H, Sekimoto Y, Seto T, et al (2018) Road Damage Detection and Classification Using Deep Neural Networks with Smartphone Images. Computer-Aided Civil and Infrastructure Engineering 33:1127–1141. https://doi.org/10.1111/mice.12387

Magenes G, Calvi GM (1997) In-plane seismic response of brick masonry walls. Earthquake Engineering & Structural Dynamics 26:1091–1112. https://doi.org/10.1002/(SICI)1096-9845(199711)26:11<1091::AID-EQE693>3.0.CO;2-6

Magenes G, Kingsley GR, Calvi GM (1995) Seismic testing of a full-scale, two-story masonry building: test procedure and measured experimental response. Pavia

Makoond N, Pelà L, Molins C, et al (2020) Automated data analysis for static structural health monitoring of masonry heritage structures. Structural Control and Health Monitoring 27:1–25. https://doi.org/10.1002/stc.2581

Malena M, Portioli F, Gagliardo R, et al (2019) Collapse mechanism analysis of historic masonry structures subjected to lateral loads: A comparison between continuous and discrete models. Computers & Structures 220:14–31. https://doi.org/10.1016/j.compstruc.2019.04.005

Malomo D, DeJong MJ (2021) A Macro-Distinct Element Model (M-DEM) for simulating the in-plane cyclic behavior of URM structures. Engineering Structures 227:111428. https://doi.org/10.1016/j.engstruct.2020.111428

Malomo D, DeJong MJ, Penna A (2019a) Influence of Bond Pattern on the in-plane Behavior of URM Piers. International Journal of Architectural Heritage 1–20. https://doi.org/10.1080/15583058.2019.1702738

Malomo D, DeJong MJ, Penna A (2019b) Distinct element modelling of the in-plane cyclic response of URM walls subjected to shear-compression. Earthquake Engineering & Structural Dynamics 48:1322–1344. https://doi.org/10.1002/eqe.3178

Mandelbrot BB, Wheeler JA (1983) The Fractal Geometry of Nature. American Journal of Physics 51:286–287. https://doi.org/10.1119/1.13295

MATLAB (2019) Natick, Massachusetts: The MathWorks Inc. www.mathworks.com

Mei Q, Gül M, Azim MR (2020) Densely connected deep neural network considering connectivity of pixels for automatic crack detection. Automation in Construction 110:103018. https://doi.org/10.1016/j.autcon.2019.103018

Meoni A, D'Alessandro A, Cavalagli N, et al (2019) Shaking table tests on a masonry building monitored using smart bricks: Damage detection and localization. Earthquake Engineering & Structural Dynamics 48:910–928. https://doi.org/10.1002/eqe.3166

Meoni A, D'Alessandro A, Kruse R, et al (2021) Strain field reconstruction and damage identification in masonry walls under in-plane loading using dense sensor networks of smart bricks: Experiments and simulations. Engineering Structures 239:112199. https://doi.org/10.1016/j.engstruct.2021.112199

Messali F, Esposito R, Jafari S, et al (2018) A multiscale experimental characterisation of Dutch unreinforced masonry buildings. In: 16th European Conference on Earthquake Engineering (ECEE 2018). Thessaloniki, Greece

Messali F, Esposito R, Ravenshorst GJP, Rots JG (2020) Experimental investigation of the in-plane cyclic behaviour of calcium silicate brick masonry walls. Bulletin of Earthquake Engineering. https://doi.org/10.1007/s10518-020-00835-x

Messali F, Rots JG (2018) In-plane drift capacity at near collapse of rocking unreinforced calcium silicate and clay masonry piers. Engineering Structures 164:183–194. https://doi.org/10.1016/j.engstruct.2018.02.050

Miglietta PC, Bentz EC, Grasselli G (2017) Finite/discrete element modelling of reversed cyclic tests on unreinforced masonry structures. Engineering Structures 138:159–169. https://doi.org/10.1016/j.engstruct.2017.02.019

Milani G (2011) Simple homogenization model for the non-linear analysis of in-plane loaded masonry walls. Computers & Structures 89:1586–1601. https://doi.org/10.1016/j.compstruc.2011.05.004

Milani G, Lourenço PB (2010) Monte Carlo homogenized limit analysis model for randomly assembled blocks in-plane loaded. Computational Mechanics 46:827–849. https://doi.org/10.1007/s00466-010-0514-0

Milani G, Tralli A (2011) Simple SQP approach for out-of-plane loaded homogenized brickwork panels, accounting for softening. Computers & Structures 89:201–215. https://doi.org/10.1016/j.compstruc.2010.09.005

Milani G, Valente M, Alessandri C (2018) The narthex of the Church of the Nativity in Bethlehem: A non-linear finite element approach to predict the structural damage. Computers & Structures 207:3–18. https://doi.org/10.1016/j.compstruc.2017.03.010

Minga E, Macorini L, Izzuddin BA (2018) A 3D mesoscale damage-plasticity approach for masonry structures under cyclic loading. Meccanica 53:1591–1611. https://doi.org/10.1007/s11012-017-0793-z

Mohtasham Khani M, Vahidnia S, Ghasemzadeh L, et al (2020) Deep-learning-based crack detection with applications for the structural health monitoring of gas turbines. Structural Health Monitoring 19:1440–1452. https://doi.org/10.1177/1475921719883202

Morandi P, Albanesi L, Graziotti F, et al (2018) Development of a dataset on the in-plane experimental response of URM piers with bricks and blocks. Construction and Building Materials 190:593–611. https://doi.org/10.1016/j.conbuildmat.2018.09.070

Mordanova A, de Felice G (2020) Seismic Assessment of Archaeological Heritage Using Discrete Element Method. International Journal of Architectural Heritage 14:345–357. https://doi.org/10.1080/15583058.2018.1543482

Morris PH, Graham J, Williams DJ (1992) Cracking in drying soils. Canadian Geotechnical Journal 29:263–277. https://doi.org/10.1139/t92-030

Mouyiannou A, Penna A, Rota M, et al (2014) Implications of cumulated seismic damage on the seismic performance of unreinforced masonry buildings. Bulletin of the New Zealand Society for Earthquake Engineering 47:157–170. https://doi.org/10.5459/bnzsee.47.2.157-170

Mulder M, Perey P (2018) Gas Production and Earthquakes in Groningen; Reflection on Economic and Social Consequences. Centre for Energy Economics Research (CEER), Policy Papers No. 3. University of Groningen, The Netherlands

Munjiza A (2004) The Combined Finite-Discrete Element Method. John Wiley & Sons, Ltd, Chichester, UK

Naciri K, Aalil I, Chaaba A, Al-Mukhtar M (2021) Detailed Micromodeling and Multiscale Modeling of Masonry under Confined Shear and Compressive Loading. Practice Periodical on Structural Design and Construction 26:04020056. https://doi.org/10.1061/(ASCE)SC.1943-5576.0000538

Najimi A, Jonas D, McCormick NJ, Kimkeran SA (2014) Assessing the condition of railway assets using DIFCAM: Results from tunnel examinations. In: 6th IET Conference on Railway Condition Monitoring (RCM 2014). Institution of Engineering and Technology, Birmingham, UK, pp 1–6

NAM (2016) Technical Addendum to the Winningsplan Groningen 2016: Production, Subsidence, Induced Earthquakes and Seismic Hazard and Risk Assessment in the Groningen Field

Napolitano R, Glisic B (2019) Methodology for diagnosing crack patterns in masonry structures using photogrammetry and distinct element modeling. Engineering Structures 181:519–528. https://doi.org/10.1016/j.engstruct.2018.12.036

Napolitano R, Hess M, Glisic B (2019) The Foundation Walls of the Baptistery Di San Giovanni: A Combination of Laser Scanning and Finite-Distinct Element Modeling to Ascertain Damage Origins. International Journal of Architectural Heritage 13:1180–1193. https://doi.org/10.1080/15583058.2019.1582726

Nasiri E, Liu Y (2020) Effect of prior in-plane damage on the out-of-plane performance of concrete masonry infills. Engineering Structures 222:111149. https://doi.org/10.1016/j.engstruct.2020.111149

Nazir S, Dhanasekar M (2013) Modelling the failure of thin layered mortar joints in masonry. Engineering Structures 49:615–627. https://doi.org/10.1016/j.engstruct.2012.12.017

Nazir S, Dhanasekar M (2014) A non-linear interface element model for thin layer high adhesive mortared masonry. Computers & Structures 144:23–39. https://doi.org/10.1016/j.compstruc.2014.07.023

Nelson JD, Miller DJ (1992) Expansive Soils – Problems and Practice in Foundation and Pavement Engineering. Wiley Professional Paperback Series, John Wiley & Sons, Hoboken, NJ, USA

Nghiem H-L, Al Heib M, Emeriault F (2015) Method based on digital image correlation for damage assessment in masonry structures. Engineering Structures 86:1–15. https://doi.org/10.1016/j.engstruct.2014.12.021

Ni F, Zhang J, Chen Z (2019) Pixel-level crack delineation in images with convolutional feature fusion. Structural Control and Health Monitoring 26:e2286. https://doi.org/10.1002/stc.2286

Nian G, Li Q, Xu Q, Qu S (2018) A cohesive zone model incorporating a Coulomb friction law for fiber-reinforced composites. Composites Science and Technology 157:195–201. https://doi.org/10.1016/j.compscitech.2018.01.037

Nichols JM (2000) A Study of the Progressive Degradation of Masonry Shear Walls Subjected to Harmonic Loading. PhD Thesis. University of Newcastle. Department of Civil, Surveying and Environmental Engineering

Nievas CI, Bommer JJ, Crowley H, et al (2020) A database of damaging small-to-medium magnitude earthquakes. Journal of Seismology 24:263–292. https://doi.org/10.1007/s10950-019-09897-0

Nishiyama S, Minakata N, Kikuchi T, Yano T (2015) Improved digital photogrammetry technique for crack monitoring. Advanced Engineering Informatics 29:851–858. https://doi.org/10.1016/j.aei.2015.05.005

Novelli VI, D'Ayala D (2015) LOG-IDEAH: LOGic trees for identification of damage due to earthquakes for architectural heritage. Bulletin of Earthquake Engineering 13:153–176. https://doi.org/10.1007/s10518-014-9622-0

Novelli VI, D'Ayala D (2019) Use of the Knowledge-Based System LOG-IDEAH to Assess Failure Modes of Masonry Buildings, Damaged by L'Aquila Earthquake in 2009. Frontiers in Built Environment 5:1–19. https://doi.org/10.3389/fbuil.2019.00095

Oggu P, Gopikrishna K (2020) Assessment of three-dimensional RC moment-resisting frames under repeated earthquakes. Structures 26:6–23. https://doi.org/10.1016/j.istruc.2020.03.039

Oliveira DV, Lourenço PB (2004) Implementation and validation of a constitutive model for the cyclic behaviour of interface elements. Computers & Structures 82:1451–1461. https://doi.org/10.1016/j.compstruc.2004.03.041

Özgenel ÇF, Sorguç AG (2018) Performance Comparison of Pretrained Convolutional Neural Networks on Crack Detection in Buildings. In: Teizer J (ed) Proceedings of the 35th International Symposium on Automation and Robotics in Construction (ISARC). Berlin, Germany, pp 693–700

Page A (1978) Finite Element Model for Masonry. Journal of the Structural Division 104:1267–1285

Pelà L, Cervera M, Roca P (2011) Continuum damage model for orthotropic materials: Application to masonry. Computer Methods in Applied Mechanics and Engineering 200:917–930. https://doi.org/10.1016/j.cma.2010.11.010

Pepe M, Sangirardi M, Reccia E, et al (2020) Discrete and Continuous Approaches for the Failure Analysis of Masonry Structures Subjected to Settlements. Frontiers in Built Environment 6:. https://doi.org/10.3389/fbuil.2020.00043

Petracca M, Pelà L, Rossi R, et al (2017) Micro-scale continuous and discrete numerical models for nonlinear analysis of masonry shear walls. Construction and Building Materials 149:296–314. https://doi.org/10.1016/j.conbuildmat.2017.05.130

Petry S, Beyer K (2015a) Limit states of modern unreinforced clay brick masonry walls subjected to in-plane loading. Bulletin of Earthquake Engineering 13:1073–1095. https://doi.org/10.1007/s10518-014-9695-9

Petry S, Beyer K (2014) Influence of boundary conditions and size effect on the drift capacity of URM walls. Engineering Structures 65:76–88. https://doi.org/10.1016/j.engstruct.2014.01.048

Petry S, Beyer K (2015b) Cyclic Test Data of Six Unreinforced Masonry Walls with Different Boundary Conditions. Earthquake Spectra 31:2459–2484. https://doi.org/10.1193/101513EQS269

Phares BM, Washer GA, Rolander DD, et al (2004) Routine Highway Bridge Inspection Condition Documentation Accuracy and Reliability. Journal of Bridge Engineering 9:403–413. https://doi.org/10.1061/(ASCE)1084-0702(2004)9:4(403)

Popescu ME (1986) A comparison between the behaviour of swelling and of collapsing soils. Engineering Geology 23:145–163. https://doi.org/10.1016/0013-7952(86)90036-0

Pulatsu B, Erdogmus E, Bretas EM (2018) Parametric Study on Masonry Arches Using 2D Discrete-Element Modeling. Journal of Architectural Engineering 24:04018005. https://doi.org/10.1061/(ASCE)AE.1943-5568.0000305

Pulatsu B, Erdogmus E, Lourenço PB, et al (2020a) Simulation of the in-plane structural behavior of unreinforced masonry walls and buildings using DEM. Structures 27:2274–2287. https://doi.org/10.1016/j.istruc.2020.08.026

Pulatsu B, Erdogmus E, Lourenço PB, et al (2020b) Discontinuum analysis of the fracture mechanism in masonry prisms and wallettes via discrete element method. Meccanica 55:505–523. https://doi.org/10.1007/s11012-020-01133-1

Pulatsu B, Erdogmus E, Lourenço PB, Quey R (2019) Simulation of uniaxial tensile behavior of quasi-brittle materials using softening contact models in DEM. International Journal of Fracture 217:105–125. https://doi.org/10.1007/s10704-019-00373-x

Pulatsu B, Gencer F, Erdogmus E (2020c) Study of the effect of construction techniques on the seismic capacity of ancient dry-joint masonry towers through DEM. European Journal of Environmental and Civil Engineering 1–18. https://doi.org/10.1080/19648189.2020.1824823

Pulatsu B, Gonen S, Erdogmus E, et al (2021) In-plane structural performance of dry-joint stone masonry Walls: A spatial and non-spatial stochastic discontinuum analysis. Engineering Structures 242:112620. https://doi.org/10.1016/j.engstruct.2021.112620

Pulatsu B, Gonen S, Erdogmus E, et al (2020d) Tensile Fracture Mechanism of Masonry Wallettes Parallel to Bed Joints: A Stochastic Discontinuum Analysis. Modelling—International Open Access Journal of Modelling in Engineering Science 1:78–93. https://doi.org/10.3390/modelling1020006

Putrino V, D'Ayala D (2019a) NORCIA AND AMATRICE: A COMPARISON OF THE TWO HISTORIC CENTRES' PERFORMANCE UNDER THE CENTRAL ITALY EARTHQUAKE SEQUENCE. In: Proceedings of the 7th International Conference on Computational Methods in Structural Dynamics and Earthquake Engineering (COMPDYN 2015). Institute of Structural Analysis and Antiseismic Research School of Civil Engineering National Technical University of Athens (NTUA) Greece, Athens, pp 2636–2648

Putrino V, D'Ayala D (2019b) Effectiveness of seismic strengthening to repeated earthquakes in historic urban contexts. Disaster Prevention and Management: An International Journal 29:47–64. https://doi.org/10.1108/DPM-07-2018-0230

Ramos LF, De Roeck G, Lourenço PB, Campos-Costa A (2010a) Damage identification on arched masonry structures using ambient and random impact vibrations. Engineering Structures 32:146–162. https://doi.org/10.1016/j.engstruct.2009.09.002

Ramos LF, Marques L, Lourenço PB, et al (2010b) Monitoring historical masonry structures with operational modal analysis: Two case studies. Mechanical Systems and Signal Processing 24:1291–1305. https://doi.org/10.1016/j.ymssp.2010.01.011

Ravenshorst G, Messali F (2016) In-plane tests on replicated masonry walls

Redmon J, Farhadi A (2018) YOLOv3: An Incremental Improvement. ArXiv

Rezaie A, Mauron AJP, Beyer K (2020) Sensitivity analysis of fractal dimensions of crack maps on concrete and masonry walls. Automation in Construction 117:103258. https://doi.org/10.1016/j.autcon.2020.103258

Riddington JR, Naom NF (1994) Finite element prediction of masonry compressive strength. Computers & Structures 52:113–119. https://doi.org/10.1016/0045-7949(94)90261-5

Riveiro B, DeJong MJ, Conde B (2016) Automated processing of large point clouds for structural health monitoring of masonry arch bridges. Automation in Construction 72:258–268. https://doi.org/10.1016/j.autcon.2016.02.009

Roca P, Cervera M, Gariup G, Pela' L (2010) Structural Analysis of Masonry Historical Constructions. Classical and Advanced Approaches. Archives of Computational Methods in Engineering 17:299–325. https://doi.org/10.1007/s11831-010-9046-1

Ronneberger O, Fischer P, Brox T (2015) U-Net: Convolutional Networks for Biomedical Image Segmentation. Medical Image Computing and Computer-Assisted Intervention (MICCAI) 9351:234–241. https://doi.org/10.1007/978-3-319-24574-4_28

Rosebrock A (2017) Deep Learning for Computer Vision with Python

Rossi PP, Rossi C (2015) Monitoring of Two Great Venetian Cathedrals: San Marco and Santa Maria Gloriosa Dei Frari. International Journal of Architectural Heritage 9:58–81. https://doi.org/10.1080/15583058.2013.793435

Rots JG, Messali F, Esposito R, et al (2017) Multi-Scale Approach towards Groningen Masonry and Induced Seismicity. Key Engineering Materials 747:653–661. https://doi.org/10.4028/www.scientific.net/KEM.747.653

Saisi A, Gentile C (2015) Post-earthquake diagnostic investigation of a historic masonry tower. Journal of Cultural Heritage 16:602–609. https://doi.org/10.1016/j.culher.2014.09.002

Salmanpour A, Mojsilovic N, Schwartz J (2013) Deformation capacity of unreinforced masonry walls subjected to in-plane loading: a state-of-the-art review. International Journal of Advanced Structural Engineering 5:. https://doi.org/10.1186/2008-6695-5-22

Salmanpour A, Mojsilović N, Schwartz J (2015) Displacement capacity of contemporary unreinforced masonry walls: An experimental study. Engineering Structures 89:1–16. https://doi.org/10.1016/j.engstruct.2015.01.052

Sandler M, Howard A, Zhu M, et al (2018) MobileNetV2: Inverted Residuals and Linear Bottlenecks. In: 2018 IEEE/CVF Conference on Computer Vision and Pattern Recognition. IEEE, Salt Lake City, UT, USA, pp 4510–4520

Sarhosis V (2016) Optimisation procedure for material parameter identification for masonry constitutive models. International Journal of Masonry Research and Innovation 1:48. https://doi.org/10.1504/IJMRI.2016.074735

Sarhosis V, Asteris P, Wang T, et al (2016) On the stability of colonnade structural systems under static and dynamic loading conditions. Bulletin of Earthquake Engineering 14:1131–1152. https://doi.org/10.1007/s10518-016-9881-z

Sarhosis V, Baraldi D, Lemos J V., Milani G (2019a) Dynamic behaviour of ancient freestanding multi-drum and monolithic columns subjected to horizontal and vertical excitations. Soil Dynamics and Earthquake Engineering 120:39–57. https://doi.org/10.1016/j.soildyn.2019.01.024

Sarhosis V, Dais D, Smyrou E, et al (2021) Quantification of damage evolution in masonry walls subjected to induced seismicity. Engineering Structures 243:112529. https://doi.org/10.1016/j.engstruct.2021.112529

Sarhosis V, Dais D, Smyrou E, Bal İE (2019b) Evaluation of modelling strategies for

estimating cumulative damage on Groningen masonry buildings due to recursive induced earthquakes. Bulletin of Earthquake Engineering 17:4689–4710. https://doi.org/10.1007/s10518-018-00549-1

Sarhosis V, Dais D, Smyrou E, Bal İE (2019c) Computational modelling of damage accumulation in unreinforced masonry Dutch constructions subjected to induced seismicity. In: SECED 2019 Conference. Greenwich, UK

Sarhosis V, Forgacs T, Lemos JV (2020) Stochastic strength prediction of masonry structures: a methodological approach or a way forward? RILEM Technical Letters 4:122–129. https://doi.org/10.21809/rilemtechlett.2019.100

Sarhosis V, Garrity SW, Sheng Y (2015) Influence of brick–mortar interface on the mechanical behaviour of low bond strength masonry brickwork lintels. Engineering Structures 88:1–11. https://doi.org/10.1016/j.engstruct.2014.12.014

Sarhosis V, Lemos JV (2018) A detailed micro-modelling approach for the structural analysis of masonry assemblages. Computers & Structures 206:66–81. https://doi.org/10.1016/j.compstruc.2018.06.003

Sarhosis V, Sheng Y (2014) Identification of material parameters for low bond strength masonry. Engineering Structures 60:100–110. https://doi.org/10.1016/j.engstruct.2013.12.013

Schijve J (2009) Fatigue of Structures and Materials. Springer Netherlands, Dordrecht

Schultz R, Beroza G, Ellsworth W, Baker J (2020) Risk-Informed Recommendations for Managing Hydraulic Fracturing–Induced Seismicity via Traffic Light Protocols. Bulletin of the Seismological Society of America 110:2411–2422. https://doi.org/10.1785/0120200016

Senaldi IE, Guerrini G, Comini P, et al (2020) Experimental seismic performance of a half-scale stone masonry building aggregate. Bulletin of Earthquake Engineering 18:609–643. https://doi.org/10.1007/s10518-019-00631-2

Serpieri R, Albarella M, Sacco E (2017) A 3D microstructured cohesive–frictional interface model and its rational calibration for the analysis of masonry panels. International Journal of Solids and Structures 122–123:110–127. https://doi.org/10.1016/j.ijsolstr.2017.06.006

Shadlou M, Ahmadi E, Kashani MM (2020) Micromechanical modelling of mortar joints and brick-mortar interfaces in masonry Structures: A review of recent developments. Structures 23:831–844. https://doi.org/10.1016/j.istruc.2019.12.017

Shafiei Dizaji M, Alipour M, Harris DK (2018) Leveraging Full-Field Measurement from 3D Digital Image Correlation for Structural Identification. Experimental Mechanics 58:1049–1066. https://doi.org/10.1007/s11340-018-0401-8

Shetty N, Livitsanos G, Van Roy N, et al (2019) Quantification of progressive structural integrity loss in masonry with Acoustic Emission-based damage classification. Construction and Building Materials 194:192–204. https://doi.org/10.1016/j.conbuildmat.2018.10.215

Shi Y, Cui L, Qi Z, et al (2016) Automatic Road Crack Detection Using Random Structured Forests. IEEE Transactions on Intelligent Transportation Systems 17:3434–3445. https://doi.org/10.1109/TITS.2016.2552248

Smoljanović H, Nikolić Ž, Živaljić N (2015a) A finite-discrete element model for dry stone masonry structures strengthened with steel clamps and bolts. Engineering Structures

90:117–129. https://doi.org/10.1016/j.engstruct.2015.02.004

Smoljanović H, Nikolić Ž, Živaljić N (2015b) A combined finite–discrete numerical model for analysis of masonry structures. Engineering Fracture Mechanics 136:1–14. https://doi.org/10.1016/j.engfracmech.2015.02.006

Smoljanović H, Živaljić N, Nikolić Ž (2013) A combined finite-discrete element analysis of dry stone masonry structures. Engineering Structures 52:89–100. https://doi.org/10.1016/j.engstruct.2013.02.010

Smoljanović H, Živaljić N, Nikolić Ž, Munjiza A (2018) Numerical analysis of 3D dry-stone masonry structures by combined finite-discrete element method. International Journal of Solids and Structures 136–137:150–167. https://doi.org/10.1016/j.ijsolstr.2017.12.012

Song Q, Wu Y, Xin X, et al (2019) Real-Time Tunnel Crack Analysis System via Deep Learning. IEEE Access 7:64186–64197. https://doi.org/10.1109/ACCESS.2019.2916330

Spencer BF, Hoskere V, Narazaki Y (2019) Advances in Computer Vision-Based Civil Infrastructure Inspection and Monitoring. Engineering 5:199–222. https://doi.org/10.1016/j.eng.2018.11.030

StabiAlert (2019) Structural Health Sensor. Report available at https://www.stabialert.nl/fileadmin/stabialert2017/downloads/Specsheet__Safety_from_every_angle_-_Structural_Health_Sensor.pdf. Accessed 14 Jul 2019

Stavridis A, Shing PB (2010) Finite-Element Modeling of Nonlinear Behavior of Masonry-Infilled RC Frames. Journal of Structural Engineering 136:285–296. https://doi.org/10.1061/(ASCE)ST.1943-541X.116

Stephenson V, D'Ayala D (2019) Structural Response of Masonry Infilled Timber Frames to Flood and Wind Driven Rain Exposure. Journal of Performance of Constructed Facilities 33:04019028. https://doi.org/10.1061/(ASCE)CF.1943-5509.0001281

Szegedy C, Vanhoucke V, Ioffe S, et al (2016) Rethinking the Inception Architecture for Computer Vision. In: 2016 IEEE Conference on Computer Vision and Pattern Recognition (CVPR). IEEE, Las Vegas, NV, USA, pp 2818–2826

Szeliski R (2011) Computer Vision. Springer London, London

Tabbakhha M, Deodatis G (2017) Effect of Uncertainty of Tensile Strength of Mortar Joints on the Behavior of Masonry Walls under Lateral Loads. Journal of Structural Engineering 143:04016166. https://doi.org/10.1061/(ASCE)ST.1943-541X.0001640

Tabernik D, Šela S, Skvarč J, Skočaj D (2020) Segmentation-based deep-learning approach for surface-defect detection. Journal of Intelligent Manufacturing 31:759–776. https://doi.org/10.1007/s10845-019-01476-x

Takeda T, Sozen MA, Nielsen NN (1970) Reinforced Concrete Response to Simulated Earthquakes. Journal of the Structural Division 96:2557–2573. https://doi.org/10.1061/JSDEAG.0002765

Tavafi E, Mohebkhah A, Sarhosis V (2019) Seismic Behavior of the Cube of Zoroaster Tower Using the Discrete Element Method. International Journal of Architectural Heritage 1–16. https://doi.org/10.1080/15583058.2019.1650135

Taylor OS, Lester AP, Lee TA, McKenna MH (2018) Can Repetitive Small Magnitude-Induced Seismic Events Actually Cause Damage? Advances in Civil Engineering 1–5. https://doi.org/10.1155/2018/2056123

Thompson JAF, Schonwiesner M, Bengio Y, Willett D (2019) How transferable are features in deep neural networks? In: Ghahramani Z, Welling M, Cortes C, et al. (eds) Advances in Neural Information Processing Systems 27. Curran Associates, Inc., Montreal, Canada, pp 3320–3328

Tomassetti U, Correia AA, Candeias PX, et al (2019) Two-way bending out-of-plane collapse of a full-scale URM building tested on a shake table. Bulletin of Earthquake Engineering 17:2165–2198. https://doi.org/10.1007/s10518-018-0507-5

Tomassetti U, Correia AA, Marques A, et al (2017) Dynamic collapse testing of a full-scale URM cavity-wall structure. In: Atti del XVII Convegno ANIDIS L'ingegneria Sismica. Pistoia, Italy

Tomazevic M (1999) Earthquake-Resistant Design of Masonry Buildings. Imperial College Press

Tomor AK, De Santis S, Wang J (2013) Fatigue deterioration process of brick masonry. Masonry International 26:41–48

Tóth AR, Orbán Z, Bagi K (2009) Discrete element analysis of a stone masonry arch. Mechanics Research Communications 36:469–480. https://doi.org/10.1016/j.mechrescom.2009.01.001

Ulrich T, Negulescu C, Ducellier A (2015) Using the discrete element method to assess the seismic vulnerability of aggregated masonry buildings. Bulletin of Earthquake Engineering 13:3135–3150. https://doi.org/10.1007/s10518-015-9754-x

Valente M, Milani G (2016a) Non-linear dynamic and static analyses on eight historical masonry towers in the North-East of Italy. Engineering Structures 114:241–270. https://doi.org/10.1016/j.engstruct.2016.02.004

Valente M, Milani G (2016b) Seismic assessment of historical masonry towers by means of simplified approaches and standard FEM. Construction and Building Materials 108:74–104. https://doi.org/10.1016/j.conbuildmat.2016.01.025

Valente M, Milani G (2019) Damage assessment and collapse investigation of three historical masonry palaces under seismic actions. Engineering Failure Analysis 98:10–37. https://doi.org/10.1016/j.engfailanal.2019.01.066

Valero E, Forster A, Bosché F, et al (2019) Automated defect detection and classification in ashlar masonry walls using machine learning. Automation in Construction 106:102846. https://doi.org/10.1016/j.autcon.2019.102846

Vamvatsikos D, Cornell CA (2002) Incremental dynamic analysis. Earthquake Engineering & Structural Dynamics 31:491–514. https://doi.org/10.1002/eqe.141

van den Beukel J, van Geuns L (2019) Groningen gas: the loss of a social license to operate. Report for The Hauge Centre for Strategic Studies, HCSS Geo-economics, The Hauge, Netherlands

van der Pluijm R (1999) Out-of-plane bending of masonry: behaviour and strength

van der Pluijm R, Rutten H, Ceelen M (2000) Shear behaviour of bed joints. In: 12th International Brick/Block Masonry Conference. Madrid, Spain, pp 1849–1862

van Elk J, Doornhof Di, Bommer JJ, et al (2017) Hazard and risk assessments for induced seismicity in Groningen. Netherlands Journal of Geosciences 96:s259–s269. https://doi.org/10.1017/njg.2017.37

van Thienen-Visser K, Breunese JN (2015) Induced seismicity of the Groningen gas field: History and recent developments. The Leading Edge 34:664–671. https://doi.org/10.1190/tle34060664.1

Vanin F, Zaganelli D, Penna A, Beyer K (2017) Estimates for the stiffness, strength and drift capacity of stone masonry walls based on 123 quasi-static cyclic tests reported in the literature. Bulletin of Earthquake Engineering 15:5435–5479. https://doi.org/10.1007/s10518-017-0188-5

Vanniamparambil PA, Bolhassani M, Carmi R, et al (2014) A data fusion approach for progressive damage quantification in reinforced concrete masonry walls. Smart Materials and Structures 23:015007. https://doi.org/10.1088/0964-1726/23/1/015007

Vasconcelos G, Lourenço PB (2009) Experimental characterization of stone masonry in shear and compression. Construction and Building Materials 23:3337–3345. https://doi.org/10.1016/j.conbuildmat.2009.06.045

Vermeltfoort AT, Naninck CFP, Raijmakers TMJ (1993) Vervormingsgestuurde meso-schuifproeven op metselwerk: Deel II (meetrapport)

Verstrynge E, De Wilder K, Drougkas A, et al (2018) Crack monitoring in historical masonry with distributed strain and acoustic emission sensing techniques. Construction and Building Materials 162:898–907. https://doi.org/10.1016/j.conbuildmat.2018.01.103

Vintzileou E, Tselios I, Karagiannaki D (2020) Quantification of damage to masonry structures under seismic conditions. In: Brick and Block Masonry - From Historical to Sustainable Masonry. CRC Press, pp 451–458

Vlek C (2018) Induced Earthquakes from Long-Term Gas Extraction in Groningen, the Netherlands: Statistical Analysis and Prognosis for Acceptable-Risk Regulation. Risk Analysis 38:1455–1473. https://doi.org/10.1111/risa.12967

Wang N, Zhao X, Zhao P, et al (2019) Automatic damage detection of historic masonry buildings based on mobile deep learning. Automation in Construction 103:53–66. https://doi.org/10.1016/j.autcon.2019.03.003

Wilding BV, Beyer K (2018) The effective stiffness of modern unreinforced masonry walls. Earthquake Engineering & Structural Dynamics 47:1683–1705. https://doi.org/10.1002/eqe.3035

Wilding BV, Dolatshahi KM, Beyer K (2017) Influence of load history on the force-displacement response of in-plane loaded unreinforced masonry walls. Engineering Structures 152:671–682. https://doi.org/10.1016/j.engstruct.2017.09.038

Wilding BV, Godio M, Beyer K (2020) The ratio of shear to elastic modulus of in-plane loaded masonry. Materials and Structures 53:. https://doi.org/10.1617/s11527-020-01464-1

Wojnarowski AE, Leonteva AB, Tyurin S V., et al (2019) Photogrammetric Technology for Remote High-Precision 3d Monitoring of Cracks and Deformation Joints of Buildings and Constructions. ISPRS - International Archives of the Photogrammetry, Remote Sensing and Spatial Information Sciences XLII-5/W2:95–101. https://doi.org/10.5194/isprs-archives-XLII-5-W2-95-2019

Xiao X-S, Jiang D-H (1994) Fractal Characterization of Fracture Surface in Brick Masonry. In: 10th International Brick and Block Masonry Conference, (IB2Mac 1994). Calgary, Canada

Xu H, Su X, Wang Y, et al (2019) Automatic Bridge Crack Detection Using a Convolutional

Neural Network. Applied Sciences 9:2867. https://doi.org/10.3390/app9142867

Yakubovskiy P (2019) Segmentation Models. In: GitHub. https://github.com/qubvel/segmentation_models. Accessed 1 Oct 2020

Yang F, Zhang L, Yu S, et al (2020a) Feature Pyramid and Hierarchical Boosting Network for Pavement Crack Detection. IEEE Transactions on Intelligent Transportation Systems 21:1525–1535. https://doi.org/10.1109/TITS.2019.2910595

Yang Q, Shi W, Chen J, Lin W (2020b) Deep convolution neural network-based transfer learning method for civil infrastructure crack detection. Automation in Construction 116:103199. https://doi.org/10.1016/j.autcon.2020.103199

Yang X, Li H, Yu Y, et al (2018) Automatic Pixel-Level Crack Detection and Measurement Using Fully Convolutional Network. Computer-Aided Civil and Infrastructure Engineering 33:1090–1109. https://doi.org/10.1111/mice.12412

Yuen TYP, Kuang JS, Ali BSM (2016) Assessing the effect of bi-directional loading on nonlinear static and dynamic behaviour of masonry-infilled frames with openings. Bulletin of Earthquake Engineering 14:1721–1755. https://doi.org/10.1007/s10518-016-9899-2

Zaborac J, Athanasiou A, Salamone S, et al (2020) Crack-Based Shear Strength Assessment of Reinforced Concrete Members Using a Fixed-Crack Continuum Modeling Approach. Journal of Structural Engineering 146:04020024. https://doi.org/10.1061/(ASCE)ST.1943-541X.0002564

Zhang A, Wang KCP, Fei Y, et al (2018a) Deep Learning–Based Fully Automated Pavement Crack Detection on 3D Asphalt Surfaces with an Improved CrackNet. Journal of Computing in Civil Engineering 32:04018041. https://doi.org/10.1061/(ASCE)CP.1943-5487.0000775

Zhang A, Wang KCP, Li B, et al (2017) Automated Pixel-Level Pavement Crack Detection on 3D Asphalt Surfaces Using a Deep-Learning Network. Computer-Aided Civil and Infrastructure Engineering 32:805–819. https://doi.org/10.1111/mice.12297

Zhang C, Chang CC, Jamshidi M (2018b) Bridge Damage Detection using a Single-Stage Detector and Field Inspection Images. ArXiv

Zhang J, Lu C, Wang J, et al (2019) Concrete Cracks Detection Based on FCN with Dilated Convolution. Applied Sciences 9:2686. https://doi.org/10.3390/app9132686

Zhang K, Zhang Y, Cheng H-D (2020) CrackGAN: Pavement Crack Detection Using Partially Accurate Ground Truths Based on Generative Adversarial Learning. IEEE Transactions on Intelligent Transportation Systems 1–14. https://doi.org/10.1109/TITS.2020.2990703

Zhao Z-Q, Zheng P, Xu S-T, Wu X (2019) Object Detection With Deep Learning: A Review. IEEE Transactions on Neural Networks and Learning Systems 30:3212–3232. https://doi.org/10.1109/TNNLS.2018.2876865

Zonno G, Aguilar R, Boroschek R, Lourenço PB (2019a) Analysis of the long and short-term effects of temperature and humidity on the structural properties of adobe buildings using continuous monitoring. Engineering Structures 196:109299. https://doi.org/10.1016/j.engstruct.2019.109299

Zonno G, Aguilar R, Boroschek R, Lourenço PB (2019b) Environmental and Ambient Vibration Monitoring of Historical Adobe Buildings: Applications in Emblematic Andean Churches. International Journal of Architectural Heritage 1–17. https://doi.org/10.1080/15583058.2019.1653402

Zou Q, Zhang Z, Li Q, et al (2019) DeepCrack: Learning Hierarchical Convolutional Features for Crack Detection. IEEE Transactions on Image Processing 28:1498–1512. https://doi.org/10.1109/TIP.2018.2878966

Zucchini A, Lourenço PB (2009) A micro-mechanical homogenisation model for masonry: Application to shear walls. International Journal of Solids and Structures 46:871–886. https://doi.org/10.1016/j.ijsolstr.2008.09.034

Zuzulock ML, Taylor O-DS, Maerz NH (2021) Understanding the multiple small magnitude induced seismic soil fatigue potential on hazard assessments. Case Studies in Construction Materials 15:e00570. https://doi.org/10.1016/j.cscm.2021.e00570